Dipl. -Ing. Sarah Krainer, BSc

# Investigation of Liquid Penetration and Wetting on Paper in the High Speed Inkjet Field

**DOCTORAL THESIS**

to achieve the university degree of

Doktorin der technischen Wissenschaften

submitted to

**Graz University of Technology**

Supervisor
Univ. - Prof. Dr. Ulrich Hirn
Institute for Pulp, Paper and Fibre Technology
Graz University of Technology

Prof. DR. IR. H.M.A. (Herman) Wijshoff
Department for Mechanical Engineering
Eindhoven University of Technology

Graz, December 2019

# AFFIDAVIT

I declare that I have authored this thesis independently, that I have not used other than the declared sources/resources, and that I have explicitly indicated all material which has been quoted either literally or by content from the sources used. The text document uploaded to TUGRAZonline is identical to the present doctoral thesis.

_____ _____

Date Signature

Die Theorie ist eine Vermutung mit Hochschulbildung.

---

James Earl Carter
39th President of the United States

# Kurzfassung

Diese Arbeit untersucht das Flüssigkeitsverhalten während des High Speed Inkjet (HSI) Drucks. Es werden hierzu vier Schwerpunkte gesetzt: Evaluierung von Messmethoden, Einfluss von Viskosität und Oberflächenspannung der verwendeten Flüssigkeit, Effekt der Tropfengröße und Verweilzeit am Papier sowie Einfluss des Papiers auf Flüssigkeitspenetration und Benetzung.

Es wurden drei verschiedene Messmethoden evaluiert, die häufig sowohl in der Papierindustrie als auch in der Druckindustrie verwendet werden: Messung mit Ultraschall-Flüssigkeitspenetrationsgerät (ULP), ebenso Kontaktwinkelmessung und Flüssigkeits-Absorptionsmessung (Automatic Scanning Absorptometer, ASA) ähnlich einer Bristow Wheel Testung. Es zeigte sich, dass die Ergebnisse der Ultraschall-Penetrationstestung gut mit der direkten Messung des penetrierten Volumens mit dem Flüssigkeits-Absorptionsmessgerät (Automatic Scanning Absorptometer, ASA) korreliert. Im Gegensatz dazu lieferte die Gegenüberstellung der verschiedenen Benetzungsparameter dieser Messinstrumente keine gute Vergleichbarkeit und das in der Praxis bereits etablierte Kontaktwinkelmessgerät ist daher in der Untersuchung des Benetzungsverhalten vorzuziehen.

In weiterer Folge wurden fünf Testflüssigkeiten mit Hilfe der Ohnesorge-Zahl und der Reynolds-Zahl entwickelt, sodass sie als Modellflüssigkeiten mit einem High Speed Inkjet (HSI) Druckkopf gejettet werden konnten. Diese Testflüssigkeiten wurden so konzipiert, dass sie einen möglichst großen Bereich in Bezug auf Oberflächenspannung und Viskosität abdecken und trotzdem noch von einem Industriedrucker gedruckt werden können. Dies ermöglicht es die Auswirkung der Flüssigkeitseigenschaften auf Spreitung und Penetration zu untersuchen. Vier Papiere mit unterschiedlichen Bulk-Eigenschaften und Oberflächenbehandlungen wurden analysiert, um die Effekte auf das Flüssigkeitsverhalten am Papier zu quantifizieren. Ein Allzweck Office Papier mit Masseleimung, eine ungestrichene High Speed Inkjet Papiersorte, ein pigmentiertes HSI Papier und das Rohpapier dieser drei

Sorten wurden hierzu verwendet. Die verwendeten Papiere repräsentieren die ungestrichenen Papiere auf dem HSI-Markt.

Um den Einfluss der Papiersorte, Flüssigkeitseigenschaft und Tropfengröße während des Drucks zu untersuchen, wurden Einzeltropfenmuster mit 30 *pl* und 120 *pl* Volumen und vollflächige Drucke auf den ausgewählten Papieren mit den Modellflüssigkeiten gedruckt. Es zeigte sich hierbei, dass die Viskosität der Haupteinflussparameter in Bezug auf Tropfenspreitung, Oberflächenbedeckung (Surface Coverage) und Druckfarbenpenetration bei ungeleimten Papieren ist. Verwendet man geleimte Papiere, spielt auch die Oberflächenspannung eine wesentliche Rolle. Eine Verringerung dieser erhöht Tropfenspreitung und Flüssigkeitspenetration auf hydrophobiertem Papier.

Des Weiteren wurde untersucht, inwiefern die apparativen Messmethoden, die im Labor zur Verfügung stehen, in der Lage sind, Spreitung und Penetration des industriellen Drucks vorherzusagen. Es zeigte sich, dass die Ultraschall-Penetrationstestung die Flüssigkeitspenetration im HSI Druck für geleimte Papiere gut vorhersagt. Je stärker allerdings die Absorptionsfähigkeit des verwendeten Papieres war, desto schlechter wurde die erhaltene Korrelation zwischen Durchdruck und ULP-Penetrationsparameter. Ein ähnlicher Korrelationsverlauf wurde beim Vergleich mittels Automatic Scanning Absorptometer ermittelten Penetrationsparameter und dem Durchdruck während des HSI Drucks festgestellt.

Die Tropfenspreitung wurde anhand der gedruckten Tropfenfläche bei 30 *pl* and 60 *pl* gemessen. Dieser Parameter wurde dann mit dem Kontaktwinkel von gleichen Tropfengrößen (30 *pl* und 60 *pl*) sowie von $\mu l$-Tropfen verglichen. Es stellte sich heraus, dass der Kontaktwinkel der Tropfen aller Größenordnungen sich in seiner Vergleichbarkeit mit der gedruckten Tropfenfläche nicht wesentlich unterscheidet. Für stark absorbierende Papiere zeigte der Vergleich zwischen $\mu l$-Tropfen-Kontaktwinkel und Druckergebnis sogar die höchste Korrelation, was darauf hindeutet, dass der Kontaktwinkel an Mikroliter-Tropfen gemessen werden sollte. Des Weiteren wurde festgestellt, dass der Haupteinflussparameter auf die Vorhersagefähigkeit des Kontaktwinkelmessgerätes die Absorptionsfähigkeit des Papieres ist. Eine erhöhte Penetrationsrate zog eine schlechtere Korrelation zwischen Kontaktwinkel bei beliebiger Tropfengröße und der gedruckten Tropfenfläche mit sich. Die höchste Korrelation wurde bei einem Kontaktwinkel unmittelbar nach Tropfenapplikation am Papier gemessen, unabhängig von der verwendeten Flüssigkeit-Papier-Kombination.

Abschließend wurde der Effekt von Oberflächenspannung und Tropfengröße in einem

Bereich zwischen 30 $pl$ und 4 $\mu l$ auf das Flüssigkeitsverhalten auf den verwendeten Papieren evaluiert. Es stellte sich heraus, dass mit steigender Absorptionsrate und Kontaktzeit zwischen Tropfen und Papier die Tropfengrößenabhängigkeit des Kontaktwinkels stark zunimmt. Die Ergebnisse zeigen, dass der Kontaktwinkel zur Bestimmung des Benetzungsverhaltens an $\mu l$-Tropfen gemessen werden sollte, da hier der Einfluss der Penetration auf die Spreitung minimiert wird. Im Fall einer hohen Absorptionsrate des Papieres und/oder einer zu kleinen Tropfengröße sollte der Kontaktwinkel bei gleichem relativ absorbierten Tropfenvolumen gemessen werden. Dieses erfasst den kombinierten Einfluss der Kontaktzeit, der Tropfengröße und der Absorptionsrate des Papieres. Die Untersuchung der Oberflächenspannung zeigt, dass ein hoher Wert zur Folge hat, dass der Kontaktwinkel im $\mu l$-Bereich höher ist als im $pl$-Bereich und für niedrige Oberflächenspannung vice versa.

# Abstract

This work investigates the fluid behaviour during High Speed Inkjet (HSI) printing. It focuses on four aspects: evaluation of testing instruments, influence of viscosity and surface tension on the print result, effect of droplet size and residence time on the paper and influence of the paper on liquid penetration and wetting.

Three commonly used measurement methods in print- and paper industry are evaluated: ultrasonic liquid penetration measurement (ULP), contact angle measurement and similar to the Bristow Wheel, a direct liquid absorption measurement (automatic scanning absorptometer, ASA). The results of the ultrasonic penetration test correlate well with the direct measurement of the penetrated volume detected with the automatic scanning absorptometer (ASA). In contrast to that, none of the wetting parameters obtained from these measurements provided comparability, thus the popular contact angle measurement instrument is recommended for the investigation of wetting behaviour.

Furthermore, five model liquids with maximum range in viscosity and surface tension were developed. The Ohnesorge number and the Reynolds number were employed to guarantee jetability of the liquids using an industrial High Speed Inkjet (HSI) printhead. It was thus possible to investigate the impact of fluid properties on the liquid behaviour on paper. Four paper grades with different bulk and surface treatments were employed to capture the effect on fluid penetration and wetting during the printing process. These grades include an all purpose office paper with AKD bulk sizing, an uncoated HSI paper, a pigmented HSI paper and a base paper, which has been used as the raw material of the other three papers. The paper vary in surface treatment and sizing, representing the most relevant uncoated paper grades on the HSI market.

To investigate the influence of paper grade, liquid property and drop size on the print result, single drop patterns with 30 *pl* and 120 *pl* volume and full-tone prints were jetted with the model liquids. The prints were analysed regarding dot spreading (dot area), surface

coverage and print through. The results show that viscosity is the main impact factor for all three unsized papers. An increase in viscosity reduces dot area and print through. Interestingly, for sized papers (fourth investigated paper grade) also surface tension is relevant, causing a reduction in dot spreading and liquid penetration for higher surface tension.

To evaluate the prediction power of the used laboratory devices we compared the print through value of the HSI printed sheets with the ULP and ASA penetration results and the dot area with the measured contact angle using the same paper-liquid combination.

It was found, that the ULP predicts liquid penetration in HSI printing for sized papers well. However, the stronger the absorbency of the paper, the poorer was the correlation between print through and ULP penetration parameter. A similar correlation was observed, comparing the automatic scanning absorptometer imbibition results with the print through results of the full-tone printed sheets.

The printed liquid spreading was evaluated for 30 *pl* and 60 *pl* HSI printed drops, measuring the dot area. This parameter was then compared with the contact angle of small drops (30 *pl* and 60 *pl*) and $\mu l$ drops. It turned out, that the comparability of contact angles using different drop sizes with the printed dot areas did not differ significantly, despite different absolute contact angle values. The main impact parameter was found to be the absorption rate of the paper. A reduction of the penetration rate resulted in a better correlation between the contact angle (at any drop size) and the printed dot area. The highest correlation was found using the contact angle immediately after drop application on the paper, regardless of the liquid-paper combination and drop size used.

Finally, the effect of absorption rate, surface tension and droplet size in a range between 30 *pl* and 4 $\mu l$ on the contact angle measurement was investigated. The contact angle decreases with an increase of relative absorbed drop volume, independent of contact time, absorption rate of the paper and drop size. It is recommended to use the contact angle of $\mu l$ drops immediately after drop application to quantify wetting, minimising the influence of penetration on the spreading process. However, for substrates with a too high absorption rate and/or small drop volumes the contact angle needs to be measured at same relative absorbed drop volumes V. V captures the combined impact of liquid volume, paper absorption rate and contact time. The investigation of the liquid surface tension showed that in the case of high values, a higher contact angle was observed for droplets in the $\mu l$ range

compared to results of the *pl* range. This behaviour was reversed for liquids with low surface tension.

**List of Publications**

Publication I Sarah Krainer and Ulrich Hirn: The effect of viscosity and surface tension on inkjet printed picoliter dots, RSC Advances, 9(54):31708–31719, 2019.

Publication II Sarah Krainer and Ulrich Hirn: Short timescale wetting and penetration on porous sheets measured with ultrasound, direct absorption and contact angle, RSC Advances, 8(23):12861–12869, 2018.

Manuscript III Sarah Krainer and Ulrich Hirn: Predicting High Speed Inkjet dot spreading and penetration from ultrasonic testing and picoliter contact angle, submitted to Nordic Pulp & Paper Research Journal

Manuscript IV Sarah Krainer and Ulrich Hirn: Contact Angle Measurement on Porous Substrates: Effect of Liquid Absorption and Drop Size

**List of Selected Oral Presentations**

Sarah Krainer and Ulrich Hirn: Short timescale wetting and liquid penetration on porous media, an experimental approach. Interpore 2018, USA, New Orleans, 2018. Appeared in: Book of Abstracts interpore 2018, page: 449, 2018.

Sarah Krainer and Ulrich Hirn: Penetration into paper-industry High Speed Inkjet prints evaluation vs. measurement techniques results. Progress in Paper Physics Seminar 2018, Polen, Lodz, 2018.

Sarah Krainer and Ulrich Hirn: Wetting and penetration on paper. Zellcheming, Deutschland, Frankfurt, 2018.

**List of Selected Posters**

Sarah Krainer and Ulrich Hirn: Impact of time dependent liquid properties on paper wetting, measured with pico-drop contact angle measurement. Interpore 2019, Spain, Valencia, 2019. Appeared in: Book of Abstracts interpore 2019, page: 341, 2019.

Sarah Krainer and Ulrich Hirn: Short timescale wetting and penetration on paper. Interpore 2018, USA, New Orleans, 2018. Appeared in: Book of Abstracts interpore 2018, page: 448, 2018.

Sarah Krainer and Ulrich Hirn: Impact of time dependent liquid properties on paper wetting, measured with pico-drop contact angle measurement. Tappi PaperCon, USA, Indianapolis, 2019.

Sarah Krainer and Ulrich Hirn: Ink penetration into paper. Fundamental Research Symposium, England, Oxford, 2017.

# Contents

Chapter 1

# Introduction

## 1.1 Research Project

This doctoral thesis was done in the Christian Doppler Laboratory (CDL) for fibre swelling and paper performance. Three research groups from different universities (KTH, University of Mines Leoben and Graz University of Technology) and four industrial partners (Kelheim Fibres, Mondi, Océ-Canon and SIG Combiblock) participated in the project of this thesis. This collaboration was created to understand the mechanisms behind the industrial processes. The CDL is separated to three main topics: liquid absorption, dimensional stability of fibre networks and fibre network mechanics.

## 1.2 Aim of the Work

The work focuses on liquid absorption and spreading on paper during High Speed Inkjet (HSI) printing; it can be divided into four main goals.

Laboratory measurements are used to predict liquid behaviour during this industrial process, providing insights into wetting and penetration. The **first goal** of this work was to understand basic mechanisms of three commonly used laboratory measurement techniques: ultrasonic liquid penetration measurement (ULP), contact angle measurement and automatic scanning absorptometer (ASA) measurement. This knowledge helps to compare results of different measurement techniques and creates common ground for discussions.

Five model liquids have been developed to capture fluid property impact on liquid penetration and wetting. The Ohnesorge- and Reynolds number were utilised to ensure jetability of the liquids with a HSI printhead, while exhibiting a maximum range in viscosity and surface tension. The investigated papers had different bulk and surface treatments to capture the paper impact on fluid spreading and penetration. An all purpose office AKD-sized paper, an uncoated HSI paper, a pigmented HSI paper and a completely untreated base paper were investigated. The base paper has been used as the raw material of the other three grades. Importantly, these papers represent the most relevant grades on the current market for uncoated HSI printing papers. The model liquids and papers were employed in all investigations carried out during this work.

The **second goal** was to capture the impact of drop size, liquid viscosity and surface tension on HSI prints. The five model liquids were printed as single dots and full-tone areas on the four utilized paper grades. Dot area, print through and surface coverage were evaluated to characterise the liquid behaviour during High Speed Inkjet printing. This supports the ink- and paper grade development in the industrial application.

The **third goal** was to evaluate the potential of laboratory measurement devices to predict liquid penetration and wetting during HSI printing. The print through of printed sheets was compared with penetration measurements from ULP and ASA. Wetting studies were carried out capturing the contact angle of different drop sizes, ranging from 30 $pl$ to 4 $\mu l$. These contact angles were compared to HSI printed dot areas with a created liquid volume of 30 $pl$ and 60 $pl$.

**Finally**, the impact of paper absorption, liquid surface tension and drop size (ranging from 30 $pl$ to 4 $\mu l$) on the contact angle measurement was investigated. The analysis of contact angles was conducted using the five self-developed model liquids and water on the four investigated paper grades with different absorption rates. This investigation aims to answer the question of how to correctly measure contact angle on absorptive material like paper. It will highlight the impact of drop size, liquid absorption and the change of contact angle over time.

## 1.3 Outline

This doctoral thesis is based on publication I to IV and is a cumulative dissertation. These articles are listed on page v, above, and were written during the work in the CDL project.

Chapter 2 contains a discussion of the fundamentals of liquid penetration and wetting as well as an overview of impact factors on penetration into porous substrates. Chapter 3 describes the HSI printing process itself and relevant process parameters. Chapter 4 gives a review of commonly used measurement techniques to quantify liquid penetration and wetting in the HSI printing field.

Publication I deals with the impact of liquid viscosity, surface tension, drop size and paper type on the print results.

Publication II provides a comparison of different measurement techniques quantifying liquid penetration and spreading on paper. Ultrasonic liquid penetration (ULP) measurement, automatic scanning absorptometer (ASA) and contact angle measurement are investigated and the correlation between the technique outcomes is evaluated.

Manuscript III compares results of inkjet print evaluations to laboratory testing methods (ultrasonic liquid penetration measurement (ULP), automatic scanning absorptometer (ASA) and contact angle measurement). Here, the potential of laboratory testing methods to predict inkjet print results is evaluated.

Manuscript IV quantifies the influence of paper absorption rate, surface tension, relative absorbed drop volume and drop size on contact angle measurements. The size dependency of the contact angle is related to the absorption rate of the paper and to the contact time between fluid drop and substrate.

Finally, the conclusions of the investigations and the main findings are summarized in the last chapter.

Chapter 2

# Liquid Penetration into Paper

Print quality is one of the most relevant aspects defining the value of printed paper [1]. The quality of HSI prints is determined by the penetration of the ink into the substrate and ink spreading on it [2]. It can be observed, that fast fluid imbibition causes fast ink drop drying, accompanied with rapid ink setting. This can be rationalised by an increased liquid transport of the ink vehicle into the paper bulk [3, 4]. Especially in the High Speed Inkjet (HSI) field, rapid ink setting is a fundamental requirement [1, 2, 5–8], as some printing processes attain a velocity up to 300 m/min [1, 9].

One drawback of fast imbibition is the reduced colour density of the print out [10, 11]. Together with the carrier liquid, ink colourants move into the paper bulk, negatively affecting colour appearance by decreasing colour density and increasing print mottle [1, 2, 12]. High ink penetration can also lead to too low ink spreading, increasing print mottle and declining the colour density of half tone prints [12–14]. It can be noted, that this effect is also influenced by other factors, like for example the pigment load of the ink [15]. For production of high quality prints and fast ink setting during the print process, a well-tuned combination of liquid spreading and penetration into the paper is mandatory [14, 16–18].

## 2.1 Wettability

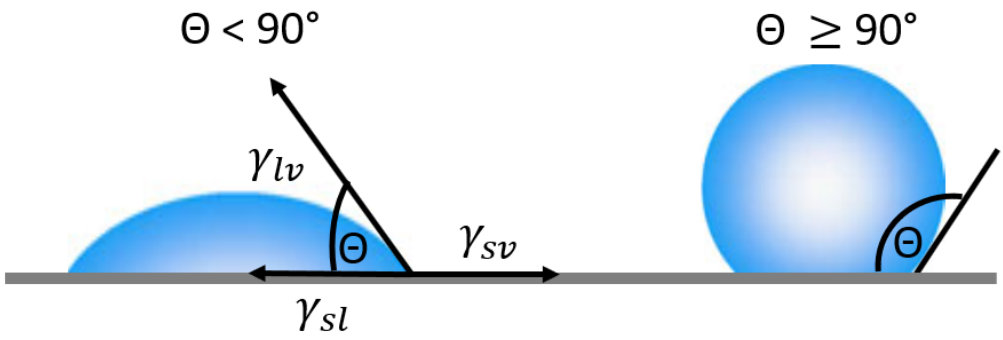


**Figure 2.1** A liquid drop is applied on a flat substrate, triggering interaction between fluid and media. A tangent is drawn to the drops outline at the three-phase contact point and the angle between the tangent and the flat substrate is designated as contact angle Θ, being a measure for the interaction of liquid and substrate. The contact angle is controlled by the surface tension of the liquid ($\gamma_{lv}$), the interface tension between substrate and liquid ($\gamma_{sl}$) and the surface energy of the substrate ($\gamma_{sv}$). High contact angle Θ ($\geq 90°$) can be observed, when bad wetting occurs. Good wetting, and thus high spreading on the surface is indicated by a low contact angle, $\Theta < 90°$. Adapted from Yuan et al. [19].

The liquid behaviour on paper is determined by fluid properties (viscosity, density, surface tension) and paper properties (pore size distribution, roughness, surface energy) [16, 20–23]. An important parameter to quantify fluid wetting is the contact angle Θ of a liquid drop applied on a flat, horizontal substrate, entailing interaction between substrate and liquid. The contact angle Θ is defined as the angle between the tangent of the drops outline in the three-phase contact point and the substrates surface, as illustrated in Figure 2.1, left side. Θ is determined by the liquid surface tension $\gamma_{lv}$, the interfacial tension $\gamma_{sl}$ between the substrate and liquid in equilibrium and by the surface energy of the substrate $\gamma_{sv}$, surrounded by a vapour phase v (= air).

A contact angle below 90° indicates good wetting, favouring drop spreading on the surface as depicted in Figure 2.1. The higher the wetting, the better is the spreading and the lower is the contact angle of a liquid drop on a substrate (Figure 2.1, left side). A contact angle of zero can be observed, when the droplet spreading is so high that a liquid film is created on the surface of the substrate.

In contrast to that, a high contact angle ($\Theta \geq 90°$) can be observed, when the fluid coheres

on the solid [24, 25]. Here, the liquid does not spread on the surface, creating a (hemi) spherical shape and bad wetting occurs.

Young [26] described the equilibrium between contact angle and interface tensions/energy $\gamma$ according to:

$$\cos(\Theta) = \frac{\gamma_{sv} - \gamma_{sl}}{\gamma_{lv}}. \tag{2.1}$$

where $\Theta$ [°] is the contact angle between the tangent of the liquid drops outline in the three-phase contact point and the solid, $\gamma_{sv}$ [N/m] is the surface energy of the substrate, $\gamma_{lv}$ [N/m] is the surface tension of the liquid and $\gamma_{sl}$ [N/m] is the interfacial tension between liquid and substrate.

The difference between the surface energy of the substrate $\gamma_{sv}$ and the interfacial tension $\gamma_{sl}$ between liquid and substrate is denoted as wetting-tension $\gamma_w$, Equation 2.2 [24].

$$\gamma_w = \gamma_{sv} - \gamma_{sl} = \cos(\Theta) * \gamma_{lv} \tag{2.2}$$

A high wetting-tension $\gamma_w$ can be observed, when the liquid drop easily spreads on the paper surface.

Equation 2.1 and 2.2 assume a three-phase system, exhibiting a thermodynamic equilibrium. The drop consists of pure liquid and is applied on a smooth and chemically homogenous substrate [27].

However, in reality, the surface of a substrate is not always perfectly smooth and homogenous, which influences the drop behaviour. Liquid spreading of structured (=rough) surfaces deviates from wetting on idealised substrates [28–30]. Thus, surface roughness affects liquid wetting and complicates capturing the wettability of a solid.

### 2.1.1 Wetting Dynamics on Rough Surfaces

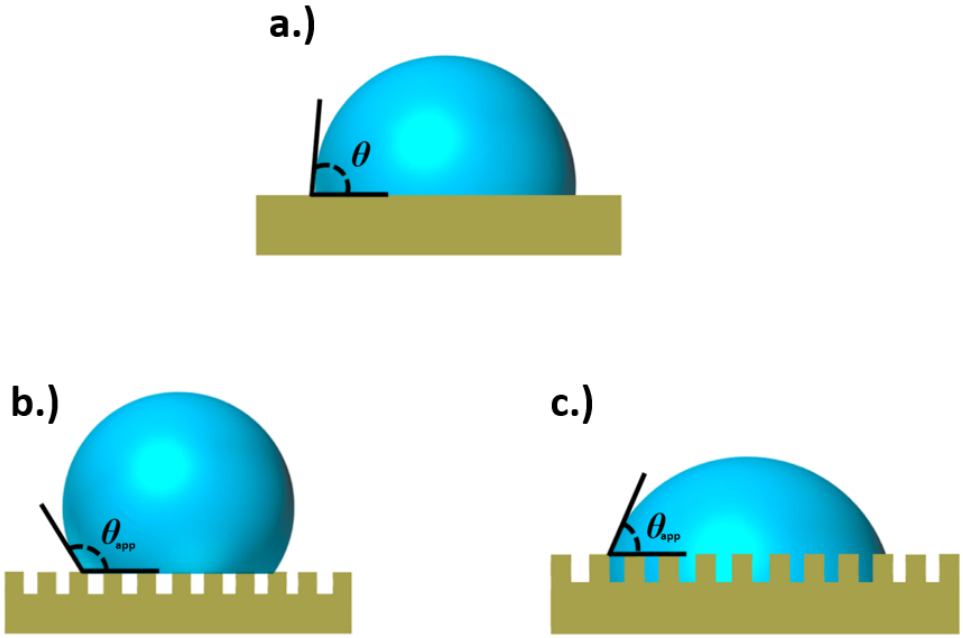


**Figure 2.2** a.) Illustration of the contact angle Θ according to Young [26] on a flat and smooth surface. b.) and c.) illustrate different wetting states on rough surfaces a drop might exhibit. b.) Cassie-Baxter state wetting assumes, that the wetting liquid entraps air, creating a composite-like interface [31]. c.) According to Wenzel the liquid fully adopts to the surface topography and complete wetting takes place. Picture adapted from [32].

Liquid wetting of surfaces, and thus spreading is affected by the interplay between liquid, solid and vapour phase. Roughness is a measure for the unevenness of a surface. The higher the unevenness, the rougher is the surface [32], complicating the quantification of liquid-substrate interaction.

The apparent contact angle is a common parameter for characterising drop spreading on rough surfaces [30, 33, 34]. It can be noted, that the apparent contact angle differs from the contact angle predicted by Young's equation (Equation 2.1), which is only valid for smooth and homogenous surfaces [35–38] (Figure 2.2 a). Researchers tried various approaches to explain the behaviour that drops on real surfaces exhibit to minimize the system free energy. Two predominant states of the liquid-substrate system are referred to as: the Wenzel state [36] and Cassie-Baxter state [35]. Contact angle predicted by Young's equation (Equation 2.1) is only valid for smooth and homogenous surfaces (see Figure 2.2 a).

**Wenzel State**

The Wenzel state is valid for rough surfaces, which are chemically homogeneous. Here, the liquid adapts to the topographical variations of the surface, flowing also into the valleys of the roughness. Thus, the substrate is fully wetted as illustrated in Figure 2.2 c. The increase of roughness creates a higher effective contact area between liquid and solid, causing an exaggeration of the substrates wetting properties [32].

A smooth substrate exhibiting good wettability is easier wetted by increasing the roughness. Almost not-wettable surfaces show enhanced wetting resistance for higher unevenness of the surface, causing an increase in contact angle. The reduction of wettability for almost not-wettable media and rise in wettability of good wettable substrates is based on the increase of interfacial area, created by the roughness of the media. The apparent contact angle $\Theta_{app}$ of fully wetted and rough substrates can be expressed by the Wenzel equation, Equation 2.3.

$$cos(\Theta_{app}) = r * cos(\Theta) \tag{2.3}$$

Here, $\Theta$ is the contact angle on the smooth surface of the same substrate (Figure 2.2 a) and r is a roughness parameter $\geq 1$. This parameter is a measure for the increase in contact area between fluid and media due to higher roughness. r is obtained by dividing the actual surface area by the projected surface area of the substrate [31, 36].

The Wenzel state does not explain the liquid behaviour on rough or smooth substrates, exhibiting inhomogeneities on the surface. Here, the Cassie-Baxter state is often used to describe the wetting behaviour.

**Cassie-Baxter State**

Originally, Cassie and Baxter [35] investigated the wettability of porous surfaces, occurring when rain drops fall on porous clothing, like feathers or textiles. The liquid wets the substrate and trapped air between liquid and solid forms air pockets [31]. This hinders complete contact between liquid and solid, aggravating wetting. Thus, a composite-like interface (consisting of air and solid) is created [31, 32, 35], illustrated in Figure 2.2 b.

Further literature review showed, that the Cassie-Baxter state is often applied for explaining high contact angles on a composite (-like) surface, independent of the origin of the surface heterogeneity.

This inhomogeneity can be caused by chemical or structural differences of the surface [31, 37, 39]. A smooth surface, being chemically inhomogeneous [37, 39], is shown in Figure 2.3 a. Here, the surface consists of hydrophobic and hydrophilic parts impacting the liquid behaviour. A structural heterogeneity of the surface can be seen in Figure 2.3 b, a rough spot is surrounded by a smooth region.

The apparent contact angle $\Theta_{app}$, when a drop wets a composite (-like) surface, according to Cassie-Baxter state, is determined by Equation 2.4.

$$cos(\Theta_{app}) = f_1 * cos(\Theta_1) + f_2 * cos(\Theta_2) \tag{2.4}$$

Here, $f_1$ and $f_2$ are the composite fractions, whereas $f_1 + f_2 = 1$. The contact angles $\Theta_1$ and $\Theta_2$ are measured with the same liquid on each of the two surface components. For surfaces consisting of x fractions, the equation can be extended by introducing x terms of $f * cos(\Theta)$ for each surface part [40].

For wetting on a rough surface, entrapping air, a two composite-like surface is created. The term $cos(\Theta)$ for air becomes $cos(180°)$, and thus is - 1. The fraction $f_2$ between air and liquid can be expressed by 1-$f_1$. Here, the original Cassie-Baxter equation is received [35]:

$$cos(\Theta_{app}) = f_1 * cos(\Theta) + (f_1 - 1) \tag{2.5}$$

The contact area $f_1$ between liquid and surface is reduced by the entrapped air, $0 \leq f_1 \leq 1$. $\Theta$ is the contact angle of the liquid drop on a smooth surface of the same material [31]. High amounts of entrapped air decrease the contact area between liquid and substrate, resulting in a higher $cos(\Theta_{app})$. Thus, air pockets between substrate and liquid inhibit wettability.

It can be noted, that Cassie and Baxter [35], used the advancing contact angle on the porous surface, instead of the $\Theta$ measured on a smooth substrate to calculate the apparent contact angle ($\Theta_{app}$) of an advancing liquid drop [35]. For rough surfaces which entrap air between liquid and solid, the fraction $f_1$ can be calculated utilizing the advancing contact angle in combination with the surface geometry of the substrate [35].

**Applicability of Wenzel and Cassie-Baxter Law**

Extrand [41] investigated the contact angle and the contact angle hysteresis on chemically inhomogeneous surfaces. Gao et al. [38] measured liquid wetting on three types of two-component surfaces. Both encountered deviations between experimental results and predicted contact angle values, calculated with the Wenzel or Cassie-Baxter equation. Here, similar size scale of the surface inhomogeneity and the drop contact area was given, as illustrated in Figure 2.3 [37, 38, 41].

Law et al. [31] concluded that realizing and accepting the weaknesses of these equations is a prominent development in surface science. Furthermore, the thermodynamic investigation of the contact areas might help finding new models for various wetting phenomena.

Also Marmur [37] investigated the applicability of these equations lately. He showed, that the prediction of the most stable contact angle using these approaches might be valid, as long as the drop dimension is larger than the wavelength of roughness or chemical heterogeneity of the substrate surface [37]. Similar behaviour was found by Yong [42] and Grzelak [43].

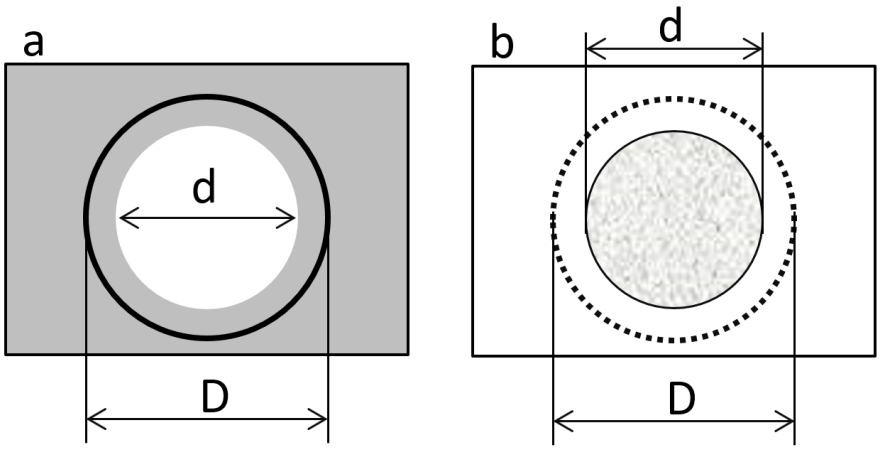


**Figure 2.3** a.) Illustration of a hydrophilic area in a hydrophobic region, b.) a rough area surrounded by a smooth region. d is the area diameter and D represents the liquid droplet diameter. Here, d and D have similar dimensions and the results of the Cassie-Baxter equation are not in accordance with the experimental data [38].

## 2.2 Substrate Surface Energy $\gamma_{sv}$ Quantification by Contact Angle

Young [26] investigated fluid wetting on solid surfaces and observed, that an angle is formed at the three-phase contact line as a result of the mechanical equilibrium between the liquid surface tension $\gamma_{lv}$, solid surface energy $\gamma_{sv}$, and solid-liquid interfacial tension $\gamma_{sl}$. Rearrangement of Young's equation (Equation 2.1) results in:

$$\gamma_{sv} = \cos(\Theta) * \gamma_{lv} + \gamma_{sl} \tag{2.6}$$

where $\gamma_{sv}$ is the surface energy of the substrate, $\Theta$ is the contact angle between liquid and substrate, $\gamma_{lv}$ is the surface tension of the liquid and $\gamma_{sl}$ is the interfacial tension between liquid and substrate. Key drawback of this equation is, that only two parameters out of three, $\Theta$ and $\gamma_{lv}$, can be experimentally measured. However, there are ways to measure the other quantities.

Dupre [44] tackled the problem of capturing the surface energy of substrates by introducing the concept of reversible cohesion work $w^{coh}$ and adhesion work $w^{ad}$ [31, 44].

### 2.2.1 The Concept of Reversible Adhesion and Cohesion Work

Two liquid columns of the same liquid $L_1$ are combined and the change of free energy $\Delta E_{11}^{coh}$ can be equalled to the negative cohesion work, Equation 2.7, illustrated in Figure 2.4.

$$\Delta E_{11}^{coh} = -w_{11}^{coh} = -2 * \gamma_1 \tag{2.7}$$

$\gamma_1$ is the liquid surface tension and $-w_{11}^{coh}$ is the cohesion work between the liquid blocks, needed to cohere the two columns of $L_1$. The work for separating these two columns again is the positive value of $w_{11}^{coh}$.

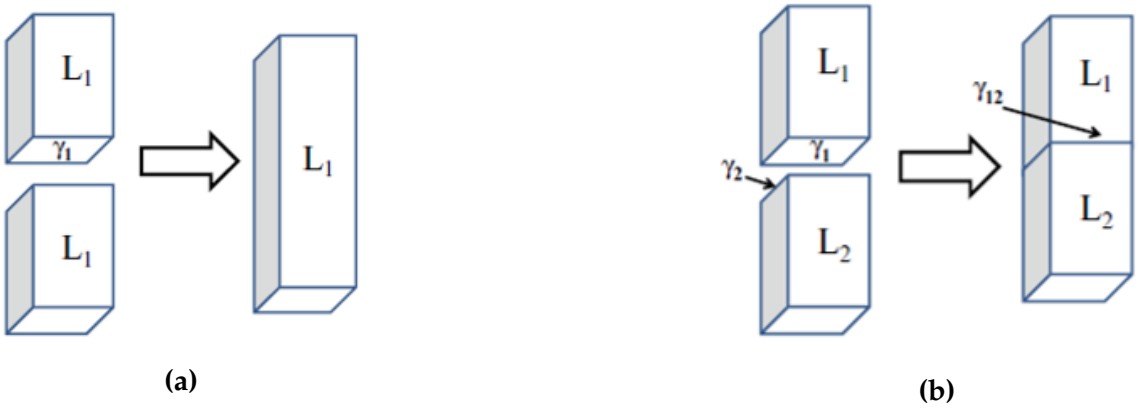


**Figure 2.4** Illustration of cohesion (a) and adhesion (b) [31]. Two cylinders of liquid $L_1$ with surface tension $\gamma_1$ are conjunct, the work to cohere the columns is the negative cohesion work $-w_{11}^{coh}$ (a). Combining liquid blocks of $L_1$ and $L_2$ with corresponding surface tension $\gamma_1$ and $\gamma_2$, the negative adhesion work $-w_{12}^{ad}$ is the work to adhere these two immiscible liquids (b). $\gamma_{12}$ represents the interfacial tension between the two liquid columns.

Two columns of immiscible liquid $L_1$ and $L_2$ are conjunct and the resulting free energy change per unit $\Delta E_{12}^{ad}$ represents the negative of the adhesion work. $\Delta E_{12}^{ad}$ can be expressed by the interface tension $\gamma_{1,2}$ of the contact area, subtracted by the surface tensions $\gamma_1$ and $\gamma_2$ of the two liquids. This expression is also valid, when replacement of one liquid column $L_1$ by a solid substrate $L_s$ is done, shown in Equation 2.8. Here, the relationship between adhesion and wetting can be found.

$$\Delta E_{12}^{ad} = \gamma_{sl} - \gamma_{sv} - \gamma_{lv} = -w_{sl}^{ad} \tag{2.8}$$

Here, $\gamma_{lv}$ represents the surface tension of a liquid block $L_1$ surrounded by air (= vapour) and $\gamma_{sv}$ represents the surface energy of the solid block. $\gamma_{sl}$ is the interfacial surface tension between solid and liquid, assuming an equilibrium between the components. The reversible work of adhesion $w_{sl}^{ad}$ is needed to separate the liquid column from the solid substrate surface [45].

Substituting the expression ($\gamma_{sv}$ - $\gamma_{sl}$) using the Young equation (Equation 2.1), it becomes clear that $\cos(\Theta) * \gamma_{lv}$ is directly linked to the adhesion work, shown in Equation 2.9 [46]. This is the commonly known Young-Dupre equation [31, 47].

$$w_{sl}^{ad} = \gamma_{lv}(1 + cos(\Theta)) \tag{2.9}$$

The surface tension of a liquid $\gamma_{lv}$ is always positive. Thus, this approach predicts a direct linear relation between adhesion and the wetting related expression (1 + cos(Θ)) [45]. For non-wetting conditions, exhibiting a contact angle Θ of 180°, adhesion work $w_{ad}$ is zero [46].

This analysis enables the investigation of the substrate surface energy $\gamma_{sv}$ implementing Equation 2.9 for adhesion work $w_{sl}^{ad}$ by measuring the contact angle Θ between liquid and paper and the liquid surface tension $\gamma_{lv}$ directly. Many approaches try to access the adhesion work $w_{sl}^{ad}$ and the affiliated $\gamma_{sl}$ experimentally [48, 49]. The Owens-Wendt-Rabel-Kaelble (OWRK) method is commonly used in the paper and printing industry, and is thus described in more detail.

### 2.2.2 Derivation of the OWRK Equation

The OWRK Method is a development of the Fowkes approach, based on the assumption, that the surface energy of solids or surface tension of liquids can be divided into partial components, addressing the impact of various molecular interactions, which are independent of each other [50–52]. For example, the liquid surface tensions might be the result of two contributors, as shown in Equation 2.10.

$$\gamma_{lv} = \gamma_{lv}^{d} + \gamma_{lv}^{p} \tag{2.10}$$

Here, the liquid surface tension $\gamma_{lv}$ is the sum of $\gamma_{lv}^{d}$ and $\gamma_{lv}^{p}$, representing the dispersive and polar interactions.

Following the Berthelot mixing rule, a molecular interaction energy $\epsilon_{ij}$ consisting of molecule species i and j, can be calculated by the geometric mean of their affiliated energies $\epsilon_{ii}$ and $\epsilon_{jj}$, Equation 2.11.

$$\epsilon_{ij} = \sqrt{\epsilon_{ii} * \epsilon_{jj}} \tag{2.11}$$

It was thermodynamically proven [51, 53–55], that the effect of dispersive interfacial interactions $\gamma_{sl}$ between solid and liquid molecules on the interfacial tension can be estimated by the geometric mean, $\gamma_{sl} = \sqrt{\gamma_{sv}^d * \gamma_{lv}^d}$.

The forces on the molecules at the interface line are illustrated in Figure 2.5. For a liquid surface molecule (Figure 2.5, left arrows), the liquid surface tension tries to cohere the liquid molecules, acting as counterpart to the interaction at the interfacial area $\sqrt{\gamma_{sv}^d * \gamma_{lv}^d}$. The forces on the solid molecules at the contact line (Figure 2.5, right arrows), are the solid surface energy and the interaction at the interfacial area $\sqrt{\gamma_{sv}^d * \gamma_{lv}^d}$, acting against the solid substrate energy. Thus, the total interaction energy on a liquid surface molecule is $\gamma_{lv} - \sqrt{\gamma_{sv}^d * \gamma_{lv}^d}$ and for a solid molecule $\gamma_{sv} - \sqrt{\gamma_{sv}^d * \gamma_{lv}^d}$.

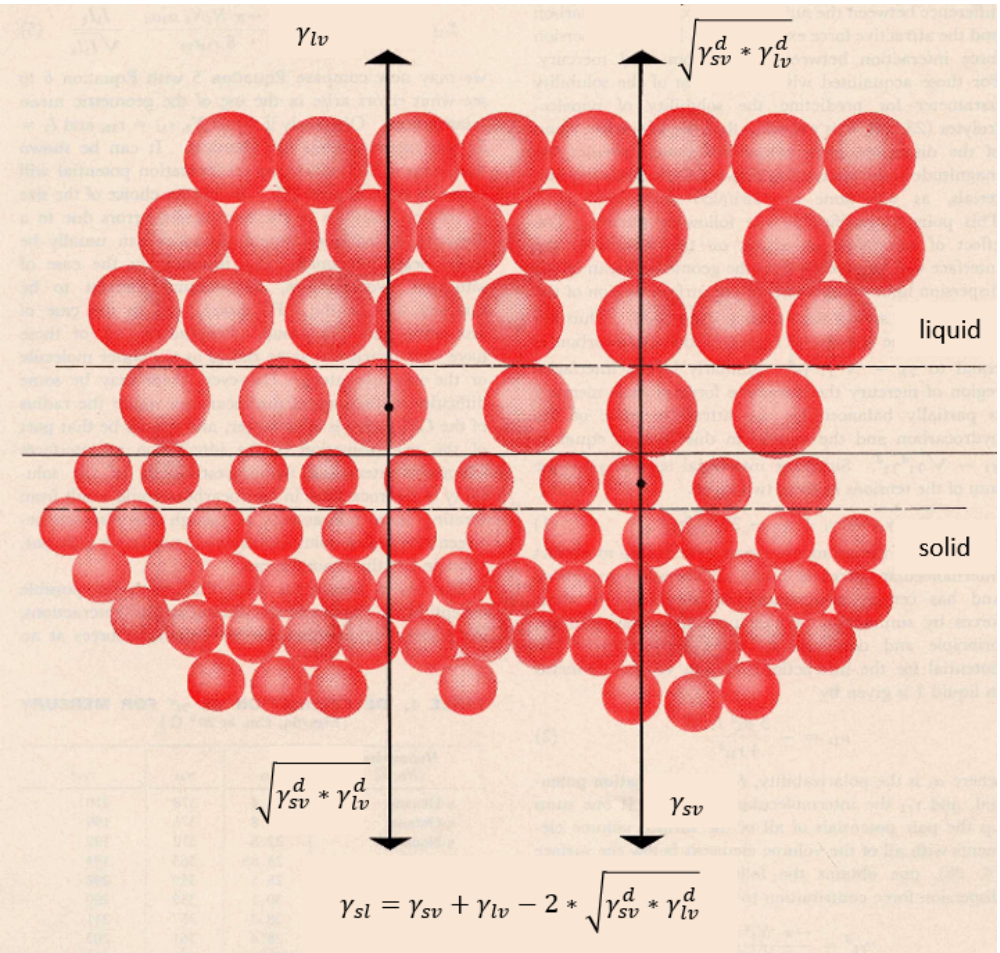


**Figure 2.5** At the interface region between solid and liquid the molecules are affected by the bulk attractive forces of each phase. Here, only dispersive forces ($\sqrt{\gamma_{sv}^d * \gamma_{lv}^d}$) act across the interfacial area. Adapted from Fowkes [51].

Thus, the total interface tension $\gamma_{sl}$ equals the sum

$$\gamma_{sl} = \gamma_{sv} + \gamma_{lv} - 2 * \sqrt{\gamma_{sv}^{d} * \gamma_{lv}^{d}}. \tag{2.12}$$

Here, $\gamma_{sl}$ is the interfacial tension between substrate and liquid, $\gamma_{lv}$ is the liquid surface tension and $\gamma_{sv}$ is the surface energy of the substrate. $d$ indicates the dispersive part of the surface energy and surface tension. For the case, where also polar forces operate at the interfacial area [48], Equation 2.12 can be extended to a more general form:

$$\gamma_{sl} = \gamma_{sv} + \gamma_{lv} - 2 * \sqrt{\gamma_{sv}^{d} * \gamma_{lv}^{d}} - 2 * \sqrt{\gamma_{sv}^{p} * \gamma_{lv}^{p}} \tag{2.13}$$

where $d$ indicates the dispersive fraction and $p$ the polar part of the liquid surface tension $\gamma_{lv}$ and substrate surface energy $\gamma_{sv}$.

Combining Equation 2.8 and Equation 2.9, which both capture the reversible adhesion work $w_{sl}^{ad}$ , the following expression is obtained:

$$-\gamma_{sl} + \gamma_{sv} + \gamma_{lv} = \gamma_{lv}(1 + cos(\Theta)) \tag{2.14}$$

Replacing the interfacial surface tension $\gamma_{sl}$ between solid and liquid with the expression defined in Equation 2.13 for $\gamma_{sl}$, the fundamental equation of the OWRK approach is obtained:

$$\gamma_{lv} * (1 + cos(\Theta)) = 2 * \sqrt{\gamma_{sv}^{d} * \gamma_{lv}^{d}} + 2 * \sqrt{\gamma_{sv}^{p} * \gamma_{lv}^{p}} \tag{2.15}$$

However, there are still two unknown components: the polar part $\gamma_{sv}^{p}$ and the disperse part $\gamma_{sv}^{d}$ of the substrate surface energy. These parameters can be obtained and described in the following section.

### 2.2.3 Application of the OWRK Method

As first step the OWRK equation (Equation 2.15) is rearranged [56], obtaining the following expression:

$$\frac{\gamma_{lv} * (1 + cos(\Theta))}{2 * \sqrt{\gamma_{lv}^d}} = \sqrt{\gamma_{sv}^d} + \sqrt{\gamma_{sv}^p} * \sqrt{\frac{\gamma_{lv}^p}{\gamma_{lv}^d}} \tag{2.16}$$

The second step is the contact angle measurement of at least two known liquids, on the same substrate, the surface energy of which is to be determined. The liquids should have a large difference in polarity. Furthermore, its properties $\gamma_{lv}^p$ (polar fraction of the surface tension) and $\gamma_{lv}^d$ (dispersive fraction of the liquid surface tension) and their sum $\gamma_{lv} = \gamma_{lv}^d + \gamma_{lv}^p$ need to be known.

Then, the contact angle $\Theta$ and surface tensions $\gamma_{lv}$ of the liquids are plugged into $\frac{\gamma_{lv} * (1 + cos(\Theta))}{2 * \sqrt{\gamma_{lv}^d}}$ and $\sqrt{\frac{\gamma_{lv}^p}{\gamma_{lv}^d}}$, delivering y-value and x-value of two points in an OWRK-plot, illustrated in Figure 2.6. Here, the expression $\frac{\gamma_{lv} * (1 + cos(\Theta))}{2 * \sqrt{\gamma_{lv}^d}}$ is plotted versus $\sqrt{\frac{\gamma_{lv}^p}{\gamma_{lv}^d}}$ and a linear regression of the data points is made (third step). The y-intercept is equal to $\sqrt{\gamma_{sv}^d}$ and the slope is equal to $\sqrt{\gamma_{sv}^p}$ [48, 56].

Finally, according to Equation 2.10, the addition of $\gamma_{sv}^d$ and $\gamma_{sv}^p$ results in the desired surface energy $\gamma_{sv}$ of the substrate. Three liquids with known surface tension and measured contact angle are used for the regression line in Figure 2.6, those liquids should have large varieties in polarity (i.e. $\gamma_{lv}^p$) .

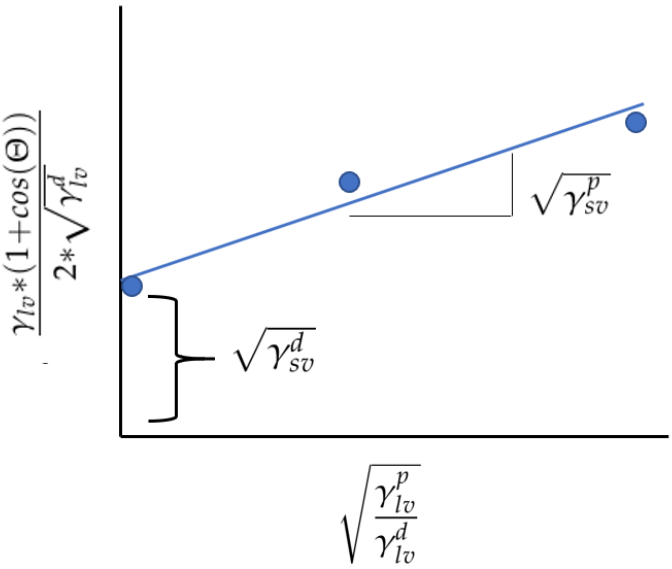


**Figure 2.6** Regression line to determine the surface energy $\gamma_{sv}$ of the substrate. Each point represents another liquid with defined surface tensions $\gamma_{lv}$, $\gamma_{lv}^d$ and $\gamma_{lv}^p$. The measured contact angle $\Theta$ of each liquid on the same substrate changes due to the change of surface tension of the three fluids. The slope and the y-intercept give the polar part $\gamma_{sv}^p$ and dispersive part $\gamma_{sv}^d$ of the substrate surface energy.

## 2.3 Capillary Rise

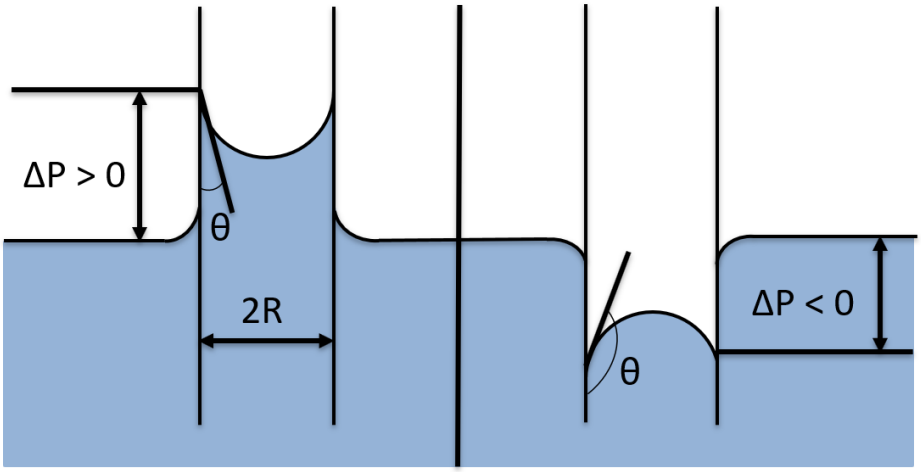


**Figure 2.7** Liquid rise in parallel capillaries. Θ is the contact angle between liquid and wall; R is the radius of the capillary [25]. For a positive Laplace pressure a contact angle $< 90°$ is observed (left). A negative Laplace pressure occurs for contact angles $\geq 90°$ (right) [57].

In a porous paper, liquid travels from the surface into the bulk using pores as pathways. These pores operate as capillaries and transport liquid from the surface into paper bulk. The meniscus is the liquid front curvature of a fluid brought into contact with a small tube (capillary). In capillaries, the angle between liquid meniscus and wall plays an important role, being a measure for liquid meniscus shape. Figure 2.7 a shows a liquid penetrating into the capillary, exhibiting a contact angle $\Theta < 90°$ between wall and fluid. The cohesion between liquid molecules is lower than adhesion forces between capillary and fluid, causing the liquid to penetrate into the tube. This behaviour is reversed for the fluid-capillary combination in Figure 2.7 b, resulting in a convex meniscus ($\Theta \geq 90°$). In this case, an external pressure is required for the liquid to enter the tube. The liquid movement within a capillary is determined by the capillary pressure, defined by the Young-Laplace equation (Equation 2.17).

$$\Delta P = \frac{2\gamma_{lv} cos(\Theta)}{R} \tag{2.17}$$

$\Theta$ [°] is the contact angle between liquid and wall, $\gamma_{lv}$ [N/m] is the surface tension of the

liquid and R [m] is the radius of the capillary [25]. To compensate the pressure difference, the liquid moves up- or downwards in the capillary.

Positive $\Delta P$ causes liquid flow into the capillary. If the pressure difference is negative ($\Delta P < 0$), an external pressure needs to be applied pushing the fluid into the capillary. Another way to force the liquid into the tube is to generate a negative pressure, sucking the fluid into the capillary. The smaller the radius R, the higher will be the capillary pressure $\Delta P$ [25].

## 2.4 Impact of Pore Geometry on Liquid Penetration

The nature of paper is such that bonding of paper fibres creates pores of different size and shape throughout the material. These pores operate as capillaries and transport liquid from the surface into paper bulk. The pores have various shapes, exhibiting also non-parallel pore walls, causing variations in pore geometry. These changes affect liquid movement into the paper bulk. In this section, an overview of some pore shapes and their impact on fluid penetration is given [58, 59].

In a **straight, parallel pore** liquid penetration takes place as long as the contact angle $\Theta$ between capillary wall and fluid is less than 90°, created by a positive Laplace pressure $\Delta P$, explained in Section 2.3. The liquid meniscus is concave and wetting of the pore wall occurs. Fluid movement stops as soon as the contact angle $\Theta$ is $\geq 90°$ and capillary pressure equals zero.

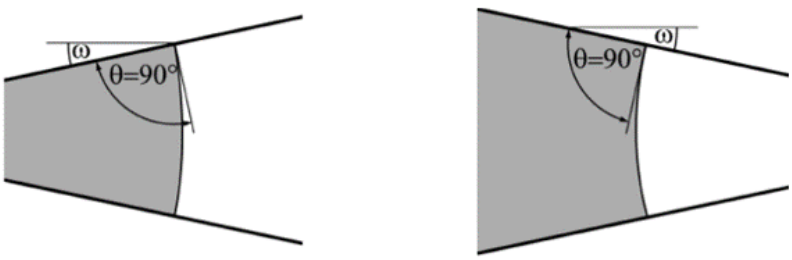


**Figure 2.8** Capillaries with non-parallel walls creating pore divergence (left) and convergence (right). Penetration takes place as long as the contact angle is lower than 90° plus the inclination of the wall, $\Theta \leq \omega + 90°$ [59].

$$\Theta \leq \omega + 90^{\circ} \tag{2.18}$$

In paper, **pores can be convex or concave** (see Figure 2.8), this affects imbibition into the substrate. In order to obtain penetration, the contact angle $\Theta$ between pore wall and liquid needs to be smaller than $90^{\circ}$ plus the converging angle $\omega$ [$^{\circ}$] of the wall [59], as described in Equation 2.18. This results in a concave meniscus, causing liquid wetting of the pore wall, and thus penetration into the pore. In contrast to this, diverging pores hinder liquid imbibition. The increase of the pore radius can decrease the capillary pressure until it equals zero and penetration stops.

Figure 2.9 shows a **pore exhibiting divergence and convergence of the pore wall**, as it occurs in the paper bulk [61]. Figure 2.9 shows three time stages of liquid imbibition. Figure 2.9 a illustrates initial penetration at $\Theta + \omega_1 < 90^{\circ}$. The liquid front reaches a section of the pore with sharp contraction $|\omega_2| > |\omega_1|$ (Figure 2.9 b), which increases the capillary pressure and results in a jump of the fluid into the pore. Penetration slows down for expanding areas and might even stop, if the pore wall divergence is so high that $\Theta + \omega_3 \geq 90^{\circ}$ occurs (Figure 2.9 c) [59, 62]. The different wall slopes occurring in pores, being randomly distributed within the paper, cause variations in liquid penetration and travelled fluid distance into every single pore.

## 2.5 Impact of Pore Network on Liquid Penetration

Researchers [60, 63] investigated the horizontal absorption of fluid into cellulose substrate, observing that in paper, the local capillary pressure is not only affected by geometry of single pores but also by the linkage of single pores, and thus by the nature of the complete pore network.

Figure 2.10 depicts the pore filling process for small and big pores. Figure 2.10 a.) illustrates fibres creating a pore. The liquid imbibition process starts with fluid movement along the channels created by the fibre overlap or along grooves in the fibre wall, operating as half

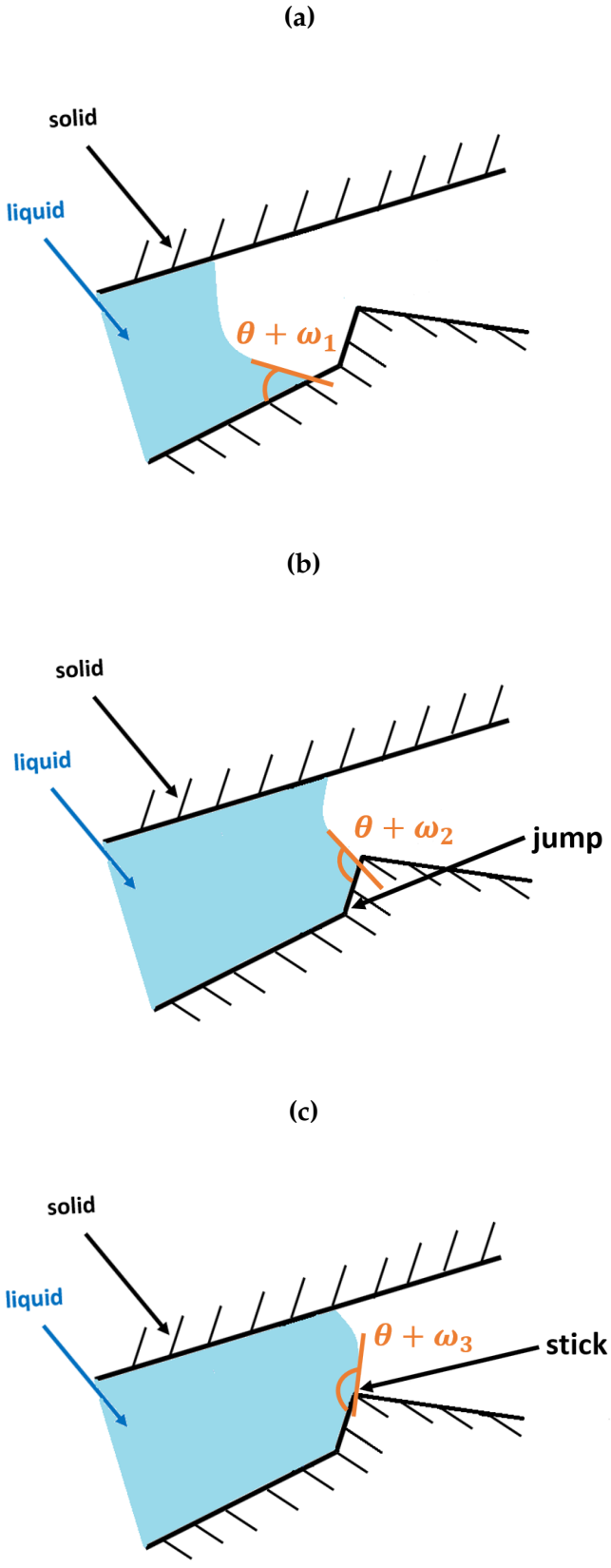


**Figure 2.9** Divergence and convergence [60] in one pore. A high amount of discontinuities can be expected in the paper network due to fibre bonding [61]. a.) Beginning of penetration for $\Theta + \omega_1 < 90°$. b.) Imbibition velocity increases for $\Theta + \omega_2 < \Theta + \omega_1$, causing a jump of the liquid front into the pore. c.) Fluid movement slows down for $\Theta + \omega_3$ and stops if $\Theta + \omega_3 \geq 90°$.

open capillaries (Figure 2.10 b.1). With advancing liquid movement, the fluid fronts of the two fibre channels emerge, travelling now as one fluid front, exhibiting also one meniscus (Figure 2.10 b.2). The liquid enters the created inter-fibre pore as long as the Laplace pressure $\Delta P$ (Equation 2.17) is higher than zero, $\Delta P > 0$ (Figure 2.10 b.3.).

Figure 2.10 c.) illustrates the filling process of small pores. First, initial wetting of the pore wall occurs, followed by the liquid bulk movement behind the wetting front. Further wetting takes place until the two wetting fronts emerge and the liquid bulk of both sides are joined, completely filling the pore with the liquid.

Figure 2.10 d.) shows a large pore with the same initial pore wall wetting as observed for small pores, illustrated in Figure 2.10 c.). Here, the pore filling is stopped due to too low Laplace pressure $\Delta$ P (Equation 2.17), and thus a too small curvature of the liquid meniscus. Only wetting of pore edges can be observed, due to liquid movement along grooves in the fibre walls and fibre-fibre created channels [20, 64, 65].

Danino [63] focused on radial penetration of non-polar liquids into cellulose porous sheets. Liquid supply was either a drop or from unlimited liquid reservoirs. Overall, the penetration rate of a limited amount is slower than for unrestricted quantity of liquid. Here, it is explained by the redistribution of the fully penetrated liquid drop amount, from bigger to smaller pores, as smaller ones are favoured in the selection of the pathway (higher capillary pressure). In comparison, drawing the liquid from infinite reservoirs, once the liquid flows into small pores, the liquid supply refills the emptied space, and no competition between big and small pores is given due to liquid oversupply.

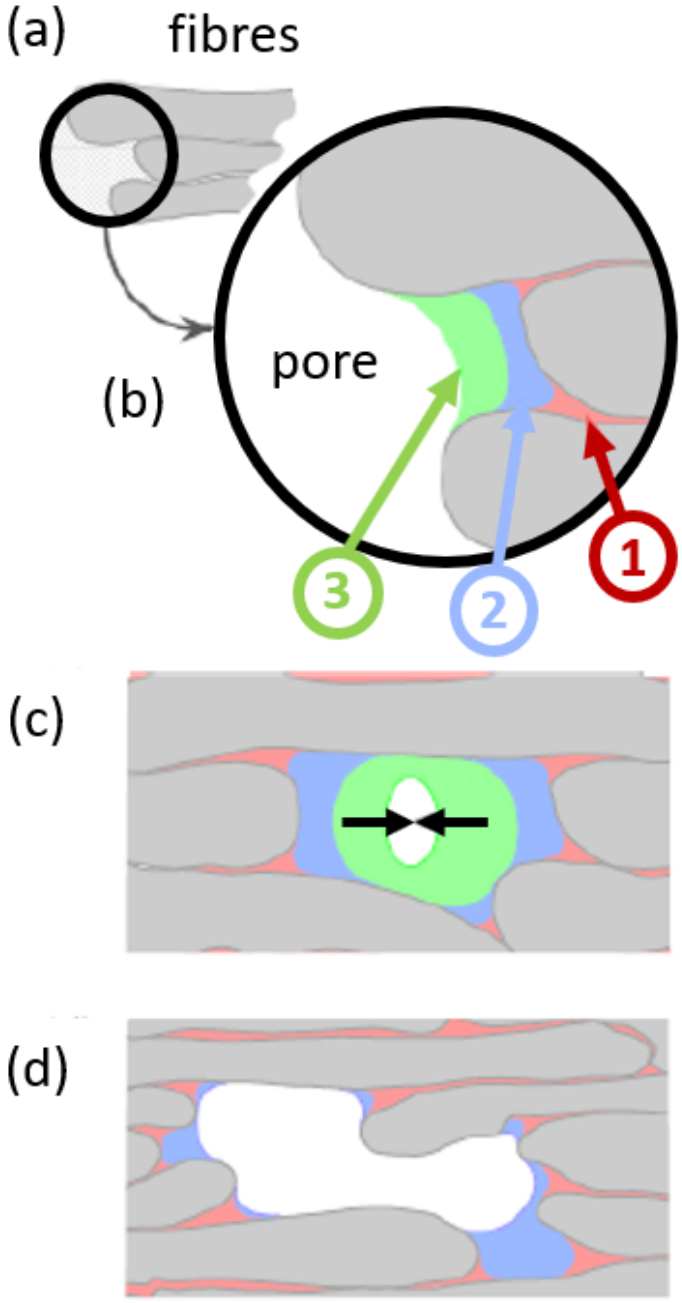


**Figure 2.10** (a) Illustration of fibres creating a pore. b.) liquid wetting at three different progress steps b.1) liquid moves along channels, created by the fibre overlap or along grooves in the fibre wall, operating as half open capillaries b.2) Fluid fronts of the two fibre channels have emerged, travelling now as fluid front, exhibiting one meniscus. b.3) The liquid penetrates into the created inter-fibre pore as long as a curvature of the fluid front is given. c) Small pores can be filled by initial wetting of the pore walls, followed by emerging of the wetting fronts and the liquid bulk, filling the pore. d.) shows a large pore with the same initial pore wall wetting as observed in c.). However, in this case the Laplace pressure is too low for further penetration, thus only partial wetting of pore edges can be observed due to liquid movement along fibres and fibre-fibre created grooves [20, 64, 65]. Picture adapted from Roberts [20].

Besides the shape and the size of the pore, also the overall pore volume affects liquid penetration into the paper [10, 17, 64, 66–68]. The increase of porosity leads to higher imbibition amounts [10, 17, 67] and deeper ink penetration into paper [10]. Special focus needs to be put on extremely large pores, stopping fluid imbibition, caused by a capillary pressure equalling to zero, illustrated in Figure 2.10 d. This decreases the theoretically absorbable liquid volume of the paper [20, 59].

Importantly, it can be noted, that the interlinkage of pores, exhibiting various pore sizes and the degree of this linkage is prominent for liquid movement into the paper. The degree of linkage is called connectivity. High connectivity results in a high liquid absorption of the paper due to easy fluid movement into the highly conjuncted pores [64, 68].

## 2.6 Liquid Movement within Fibrous Layer

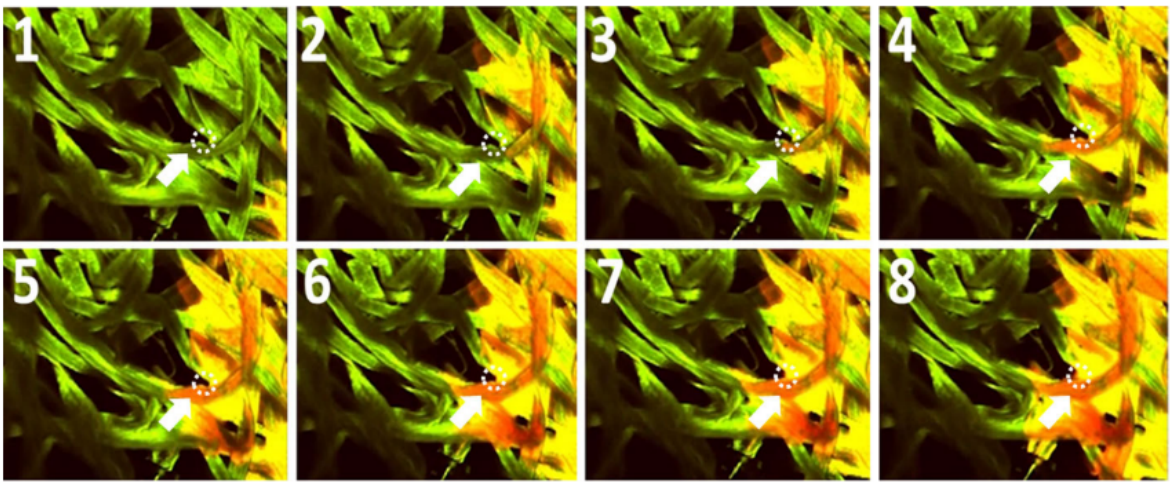


**Figure 2.11** Water with fluorescent particles moving along a fibrous paper layer [69]. The time between the pictures is 3 s. First, liquid wets the fibres and moves along grooves between two bonded fibres, creating a finger-like front. Followed by liquid movement into the pores.

The described impact parameters on liquid penetration into paper focus on pore geometry and pore network structure. However, the overall imbibition is also affected by grooves and furrows of the pore walls and fibre-fibre channels created by fibre-fibre bonding. These structures operate as half open capillaries, exhibiting a smaller radius than the pores, supporting liquid movement. Fluid imbibition is favoured by high capillary pressure according to Equation 2.17, which increases for decreasing pore radius. Thus, the small capillary ra-

dius from channels created by the fibre-fibre bonding or from grooves in the fibre wall, helps overcoming barriers, like pore widening. This increases ink penetration into paper bulk and dot spreading on the surface of the paper [58, 65].

Figure 2.11 shows water movement along a fibrous layer. Fluorescent particles have been added to visualise liquid wetting. The liquid front follows the grooves along the fibre walls and the channels created by fibre-fibre bonding. First, water wets the fibre surface moving along the fibre surface using wall grooves and channels, created between two bonded fibres, resulting in a finger-like front. Second, the liquid behind this wetting front moves into the pores between the fibres, filling them [69].

## 2.7 Modification of Paper Surface Pore Structure - Coating

Liquid behaviour differs for uncoated and coated papers. Uncoated papers have an irregular pore structure. In such cases, first the liquid flows along the fibre surface and/or moves into the fibre. Only then, the liquid penetrates into the pores between fibres [69]. Reduction of ink penetration into paper is achieved by applying coatings. The liquid moves immediately into the coating layer structure. The coating layer creates a homogeneous pore structure on the paper surface, having a mean pore diameter in the size range of around hundreds of nm. This causes a more uniform liquid wetting and penetration of the surface [69, 70].

After ink application, the fluid penetrates into the paper and volatile components evaporate, thus the ink dries on the substrate [71]. The drying process shows a huge impact on the print gloss. High print gloss is created by a smooth ink surface, promoted by slow ink drying. Whereas fast ink drying increases the print velocity, it hinders levelling out the surface inhomogeneity using the remaining ink above the surface. This causes ink drying before a smooth ink dot is created [72, 73].

Different types of ground calcium carbonate (GCC) used in paper coatings, change the initial uptake of fluid into the substrate by creating a pore system above the paper bulk. A refined GCC coating with a broad particle size distribution slows down the initial liquid uptake. In contrast to that, the standard coatings speed up the fluid penetration due to their narrower pore size distribution (PSD). A broad PSD causes a lower void volume of the coating, resulting in lower ink penetration, and thus higher print quality (gloss and

density) [74, 75]. The comparison between broad and narrow pigment size distribution is illustrated in Figure 2.12, showing the effect on dried ink.

The surface homogeneity of the coating itself is crucial for homogenous ink behaviour on the substrate. Also rough paper surface creates a rough ink surface. Furthermore, local variations in surface chemistry and surface porosity of the paper create local varieties in ink setting. Full homogeneity is hard to achieve during industrial processes. For example, a deviation in surface spreading of latex binders used in pigment coatings can cause an increase in variation of the surface energy of the coated substrate [76, 77].

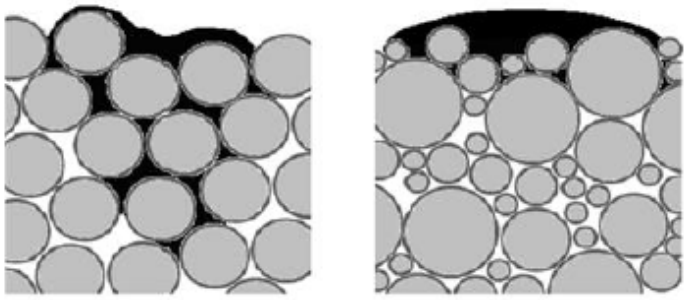

**Figure 2.12** Ink drop penetration into paper coatings having different size distributions. Coatings with narrow pore size distribution have more void volume and allow deeper penetration (left) compared to coatings with high particle size inhomogeneity (right). The rapid imbibition into a layer of similar sized particles causes a decrease in ink gloss due to reduced levelling [71].

## 2.8 Quantitative Models for Liquid Penetration

In contrast to experiential approaches, considering discontinuities of the paper pores, a common way to study porous substrates is the introduction of a **model system**, which mimics the pore structure, reducing complexity of the system [4, 78–90]. This facilitates the study of various mechanisms such as penetration and wetting of the paper, being difficult to investigate on the heterogeneous, cellulose porous sheet. There are numerous studies on liquid flow into porous systems [91–96] and how to quantify it. Two predominant models used in the research approaches are the Lucas-Washburn (LW) equation and the Bosanquet model.

### 2.8.1 The Lucas-Washburn Equation

The Lucas-Washburn (LW) equation is a popular model for describing liquid flow into porous paper, based on a simplified capillary model [97]. It is the fundamental equation of many studies tackling the problem of liquid behaviour characterisation on absorptive substrates. Despite the simplification of penetration mechanisms, this equation is especially in the paper engineering field of importance, highlighting main impact factors of liquid imbibition [98–105].

The Lucas-Washburn equation is based on the Poiseuille law:

$$v = \frac{dH}{dt} = \frac{\Delta P * r^2}{H * \eta * 8} \tag{2.19}$$

Here, the liquid velocity v [m/s], of a laminar flowing fluid into a cylinder with a radius r [m], exhibiting a defined viscosity $\eta$ [Ns/m$^2$] is described, Equation 2.19. $\Delta$P [Pa] is the capillary pressure and pushes the liquid into the capillary, H is the penetration length in [m] and t is the time in [s]. The lower the viscosity and the bigger the pore radius, the higher is the imbibition rate.

Assuming that the only driving force for penetration is the capillary pressure and gravity is neglectable, it is possible to describe $\Delta$P using the Young-Laplace equation (Equation 2.17). Thus, substituting the pressure in Equation 2.19 using the capillary pressure as defined in

Equation 2.17, followed by separation of the variables dH and dt and the integration, the Lucas-Washburn equation is obtained.

$$H = \sqrt{\frac{\gamma * r * cos(\theta)}{\eta * 2}}\sqrt{t} \tag{2.20}$$

Equation 2.20 is the Lucas-Washburn equation, describing liquid penetration into cylindrical capillaries. The penetration length H [m] is the distance travelled by the fluid during penetration time t [s]. H is affected by the capillary radius (pore radius) r [m], surface tension $\gamma$ $[N/m]$ and viscosity $\eta$ $[Ns/m^2]$ of the liquid. The contact angle $\theta$ [°] between liquid and substrate is affected by paper and the liquid properties, see section 2.1, modification of one part always causes a change in contact angle.

Equation 2.20 shows, that according to the LW equation the penetration depth H of the liquid into the substrate is proportional to $\sqrt{t}$. This flow regime is caused by the capillary pressure $\Delta$P (Equation 2.17), which is working against the viscous drag forces given by the Poiseuille law (Equation 2.19) [66, 97].

For penetration times below 1 ms and pore diameters below 1 $\mu$m the LW equation results display big variations from experimentally measured values. Addressing these deviations, the Bosanquet model is adding inertial forces to the Lucas-Washburn equation [17, 21, 106].

### 2.8.2 The Bosanquet Equation

When applying the LW approach, the prediction of liquid penetration behaviour into porous media neglects the inertial forces at the beginning of imbibition. Only viscous drag is counteracting to the capillary pressure. Especially, for large pores and very short contact times this is not a valid assumption.

In contrast to that, the Bosanquet equation considers the viscous drag as well as the inertial forces. The inertial force $F_{intertial} = \frac{d}{dt} * (m * \frac{dH}{dt})$ is determined by the mass of the liquid $m = \pi * r^2 * \rho * H$, where $\rho$ is the density. The friction force $F_{friction} = \frac{8*\pi*\eta*H*dH}{dt}$, with viscosity $\eta$ is based on the Poiseuille law, described in Equation 2.19. $F_{wetting} = 2 * \pi * r * \gamma_{lv} * cos(\Theta)$ is the wetting force. If an external pressure $P_e$ is applied $F_{pressure} = P_e * \pi * r^2$ occurs [21, 58]. The force equilibrium is shown in Equation 2.21.

$$F_{intertial} + F_{friction} = F_{wetting} + F_{pressure} \tag{2.21}$$

Introducing the definition of the forces into Equation 2.21, the Bosanquet equation is received:

$$\frac{d}{dt}(\pi r^2 \rho H \frac{dH}{dt}) + 8\pi\eta H \frac{dH}{dt} = 2\pi r\gamma cos(\theta) + P_e \pi r^2 \tag{2.22}$$

Equation 2.22 gives the Bosanquet equation, describing liquid uptake into porous paper modelled by cylindrical capillaries. Same symbols represent same parameters as designated in the LW equation 2.20 and $\rho$ is the density in $[kg/m^3]$. The parameter r is the capillary radius (pore radius) in [m] and $P_e$ [Pa] is external pressure forcing a fluid into the pore network, as e.g. used in the mercury porosimetry [21, 58].

The inertial forces are prominent at the beginning of the imbibition process, but decrease during advancing penetration to zero [58, 106]. The friction force increases proportional with the penetration length H, starting at a value of zero, where no liquid is in the capillary. Thus, the liquid flow is initially determined by inertial forces acting against the movement of the fluid. The increase of imbibition length H is accompanied with a reduction of inertia impact. The increase of importance of viscous drag causes a transition from inertia controlled flow to a flow mainly affected by viscous forces. Thus, with increasing time the Bosanquet equation converges to the Lucas-Washburn equation, see Figure 2.13.

The Bosanquet equation is valid for both flow regimes: inertia controlled and viscous drag controlled flow.

The integration of Equation 2.22 delivers the following expression, introducing the parameters a and b, which are constant for one liquid-substrate combination [67]:

$$H_1^2 - H_2^2 = \frac{2 * b}{a} * [t - \frac{1}{a} * (1 - e^{-at})] \tag{2.23}$$

with

$$a = \frac{8 * \eta}{\rho * r^2} \tag{2.24}$$

and

$$b = \frac{P_e * r + 2 * \gamma_{vl} * cos(\Theta)}{\rho * r} \tag{2.25}$$

Penetration processes considered in this thesis occur under ambient conditions and without the application of external pressure. Thus, $P_e$ can be equalled to zero. Assuming that the beginning of liquid movement starts at imbibition length zero, $H_1$ can be considered as zero too. The term $\frac{1}{a} * e^{-at}$ accelerates the liquid movement until $-a * t \ll 0$. Here, the Bosanquet equation converges to the Lucas-Washburn equation. Furthermore, looking at early penetration times ($a * t \ll 1$), Equation 2.23 simplifies to

$$H^2 = \frac{2 * \gamma_{vl} * cos(\Theta) * t^2}{\rho * r} \tag{2.26}$$

commonly known as the inertial flow [21]. The inertial flow describes the inertia controlled part of liquid flow entering a capillary. Here, the penetration height H is proportional to t (H$\sim$t). Whereas having viscous flow, described by the Lucas-Washburn equation, the time dependency of the penetration length H is proportional to $\sqrt{t}$ (H $\sim$ $\sqrt{t}$).

Figure 2.13 depicts the calculated penetration length H of 1,3-propanediol within capillaries

of a 1 $\mu m$ or 1 $mm$ diameter. The figure illustrates the inertial flow (circle and triangle), the Bosanquet equation (star and dash) as well as the Lucas-Washburn equation (square and diamond). The contact angle $\Theta$ of 1,3-propanediol on the investigated substrate was 34.5° [21].

Equation 2.23 becomes the LW equation for diameters greater than 1 $\mu m$ and penetration times above 1 ms. For smaller pores the changeover between Bosanquet and Lucas-Washburn equation appears earlier than for bigger pores (1 $\mu m$ vs. 1 $mm$). The beginning of liquid movement into pores is determined by inertial forces, and thus smaller pores are filled. In contrast to that, for viscous flow, described by the LW equation, liquid movement into big pores is faster.

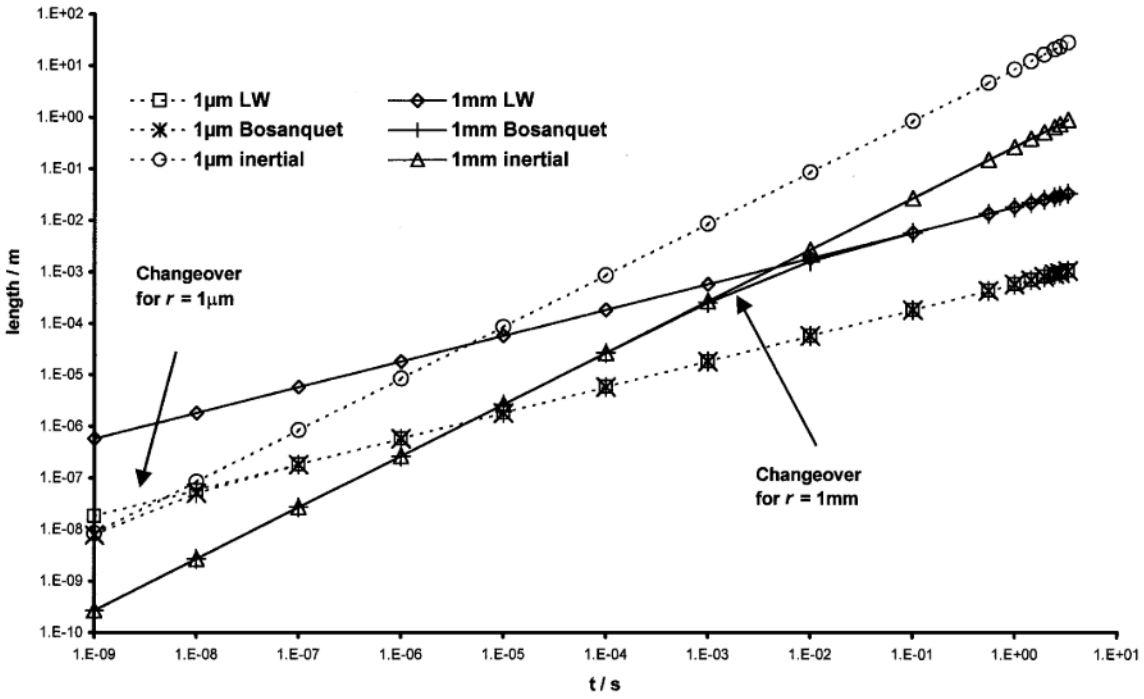


**Figure 2.13** Illustration of 1,3-propanediol penetration length calculated employing Lucas-Wahsburn equation, Bosanquet equation and inertial flow equation for capillary diameters of r = 1 $\mu m$ and r = 1 mm. It shows a changeover for the Bosanquet equation to the LW equation at different process conditions [21].

### 2.8.3 Extension of Lucas-Washburn Equation

Experimental approaches, which were not designed for application of LW Theory, also show a direct proportional relationship between penetration depth and root of time as predicted by the LW-equation [66, 97, 99, 106], ignoring the complex structure of pore network. However, the absolute experimental data often reveal a deviation from the theoretical calculated penetration depth [66, 107].

For liquids consisting of more than one component, during imbibition, they might be separated. This separation of fluid components might also cause a deviation from the simplified theory [86]. Another mechanism, which needs to be considered, especially for small droplet penetration, is the evaporation. Liu et al. [82] introduced a theoretical approach, explaining the limited capillary penetration as a result of evaporation.

Demixing, evaporation, the impact of inertia and several other mechanisms neglected by the LW approach caused the ongoing development of this popular theorem and the underlying experimental work [90, 108–116]. The introduction of new parameters, like the "mobility parameter" [90] or various attempts to introduce a dynamic contact angle factor [79, 108–110, 112, 113, 115, 116] is extending the commonly used theorem to the apparent experimental needs.

## 2.9 Liquid Viscosity and Surface Tension Impact on Penetration and Wetting

The liquid as counterpart of paper in wetting and penetration processes also plays a major role during industrial High Speed Inkjet printing. The liquid behaviour is affected by viscosity, surface tension and the contact angle, which is supported by Equation 2.20. Researchers tried to capture the impact of these parameters experimentally [86, 90, 108, 109, 111] and confirmed the influence on the liquid behaviour.

Han et al. [117] found, that an increase in ratio of surface tension to viscosity causes an increase in penetration. At the beginning of penetration and wetting process, high viscosity aggravates movement into pores [78–80, 99, 118]. Furthermore, Neogi et al. [119] showed

that the spreading rate of a liquid drop depends on the surface tension, viscosity and contact angle, but captured it not quantitatively.

Aslannejad [120] investigated water and an ink-based liquid using simulation. This fluid's viscosity and density are twice as high when compared to water, whereas the opposite is true for the surface tension. He showed, that spreading on paper surface was similar for both. However, water penetrated faster than the ink-based liquid. It seems, that higher viscosity and higher density compared to water decrease the absorption velocity, and thus water reaches the same penetration depth faster [120]. Furthermore, he observed, that low contact angles promote liquid penetration into paper. The highest penetration was found for the lowest contact angle.

The combined effect of viscosity, impact velocity and surface porosity has been investigated by Basit and Asai as well as their respective colleagues [121, 122]. This observation showed that a maximum spreading on the surface was achieved for a maximum drop velocity, minimum liquid viscosity and low substrate porosity. Basit [121] concluded that these findings are also valid for the impact on contact angle.

Alam et al. [123] theoretically investigated liquid viscosities from 0.1 mPas to 100 mPas, showing an increase of the normalized drop spreading diameter. Revealing an exponential increase of drop wetting and penetration in the spreading dominated phase, see Figure 2.14. The surface tension was set to 50 mN/m for all liquids. He concluded, that for drops with high impingement velocity (25 m/s and 50 m/s), the contact angle plays a minor role during the initial phase (until 3 $\mu s$ of contact between liquid and substrate) of drop spreading.

The change in surface tension from 50 mN/m to 73 mN/m had hardly any effect on the spreading [124, 125]. Similar behaviour for contact angle and wettability was shown by Scheller and Zhang [126, 127].

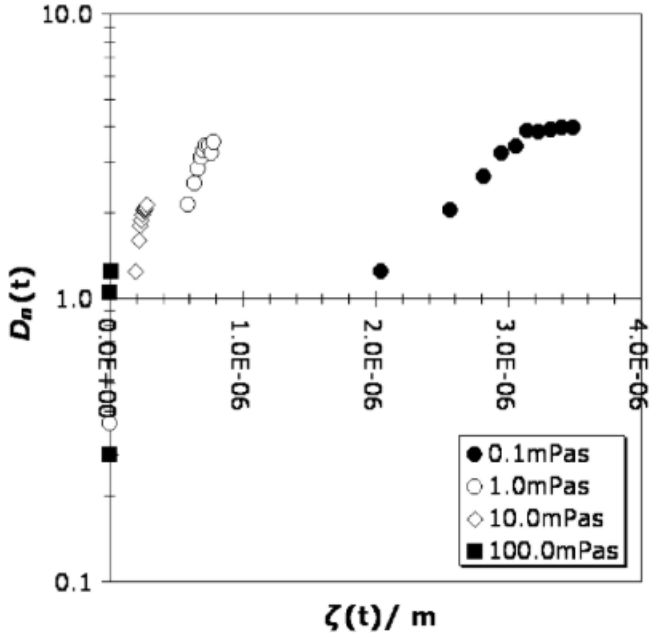


**Figure 2.14** Normalised spreading diameter $D_n(t)$ versus penetration length $\zeta_n(t)$ [m]. (t) indicates, that both parameters change with increasing contact time between drop and substrate. Same symbols represent the same liquid at different contact times. Both parameters decrease with an increase of viscosity, showing worse wetting and lower penetration [123].

Chapter 3

# High Speed Inkjet-Printing

## 3.1 Printer

High Speed Inkjet (HSI) printing gains more and more importance in the printing field [16, 128]. The facile print production, fast production process and the fact that it is a non-contact method are three of the key advantages of this print-method [62]. The ink is applied by shooting droplets onto the substrate surface. The drop production is done either by Drop on Demand (DOD) or the continuous inkjet method (CIJ), they will be shortly explained below. In the HSI industry, where the printing velocity can be up to 5 meter per second, the DOD method is widely used [3, 9].

### 3.1.1 Drop on Demand Method (DOD)

The Drop on Demand (DOD) printhead generates drops only when needed, employing different types of drop production methods. Two prominent methods are the piezoelectric and thermal jetting, illustrated in Figure 3.1.

Thermal jetting uses a heating plate to heat up the ink to 300 °C within microseconds, causing evaporation. A vapour bubble is generated, expanding immediately and squeezing the ink out of the nozzle. The bubble collapses after temperature reduction and the ink chamber is refilled by capillary pressure [14].

The second method uses a piezoelectric element. The deformation of a piezoelectric crystal generates an electric field and an electric field causes a distortion of the crystal. Thus, the

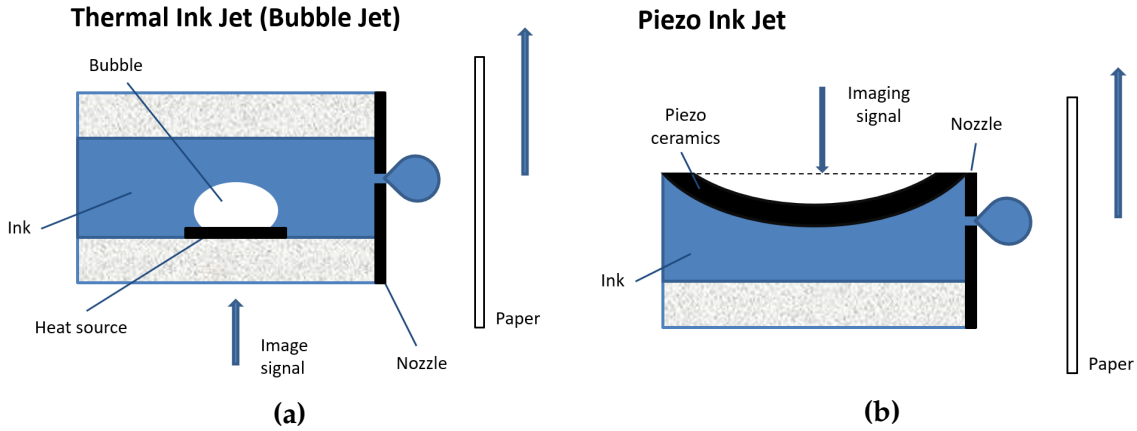


**Figure 3.1** Illustration of drop on demand print heads. The ink is pushed out of the ink chamber either by (a) a bubble created by evaporation or by (b) oscillating of a piezoelectric element [62].

application of an electric field creates a deformation of the piezoelectric element, pushing out the ink.

The DOD method produces prints with high resolution using droplets between 0.1 and 29 pl. The droplet size depends on the firing frequencies (ranging from 5 - 100 kHz), print head settings and liquid properties [15, 129–131].

### 3.1.2 Continuous Inkjet Method (CIJ)

The CIJ method generates drops continuously, and liquid is either applied on the substrate or redirected to a collector. The production of the drops is done by pressure and a piezoelectric element, as illustrated in Figure 3.2. Its oscillation squeezes an ink beam out of the ink chamber, where the liquid beam breaks into individual drops. The generation of the drops depends on the oscillation wavelength of the piezoelectric element [62].

The CIJ method can be further dived into a binary (Figure 3.2 a) and a multiple (Figure 3.2 b) deflected system [132]. Using the binary deflected system, the generated drop is charged by the charge electrodes, followed by a redirection into the gutter using the high voltage deflection plates. The uncharged drop passes straight through the high voltage deflection plates and impinges on the paper surface.

For the multiple deflection method, the uncharged drops are collected in the gutter for reuse. The charged droplets deviate in their charge, and thus can be redirected to different areas on the paper using the high voltage deflection plates [62, 130].

This method is used for low resolution prints and high print velocities. A common nozzle

width is 12 $\mu m$ producing a typical drop size of around 4 - 10 $pl$. The size is strongly depended on the nozzle dimensions and the pressure in the nozzle [62, 130].

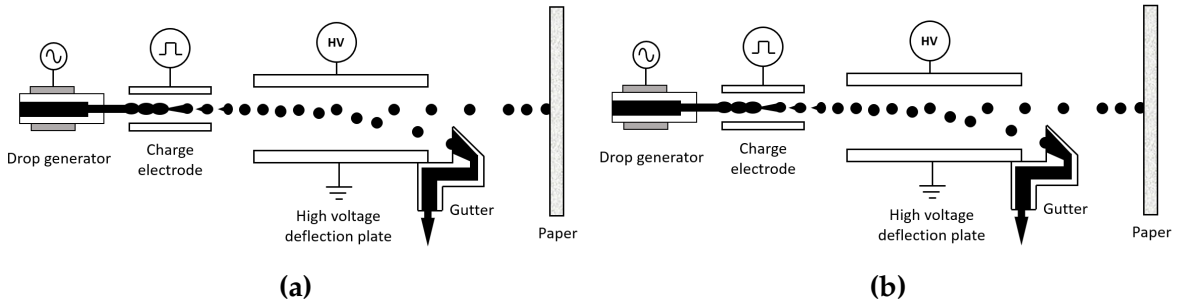


**Figure 3.2** Schematic illustration of a continuous inkjet print head. Droplets are created continuously, either applied on the paper or redirected into a collecting gutter [132]. (a) Illustration of a binary deflected system. Here, the charge electrodes charge the drop to redirect it into the gutter. (b) For a multiple deflected system, the uncharged drops are collected in the gutter for reuse. The droplets exhibit different charges, and thus can be redirected to different areas on the paper using the high voltage deflection plates [62, 130].

## 3.2 Drop Formation of High Speed Inkjet Inks

Stable jetting of inks is crucial for high print quality and reproducible print results. The same amount of ink has to be ejected every time the nozzle fires a drop. The ejection velocity (v) ranges from 5 to 15 $m/s$ [3] and a drop volume between 1 - 30 $pl$ [1] is typically created using a HSI print head. Among others, the two following numbers are often used by ink developers to forecast ink jet ability: Reynolds Number (Re) (Equation 3.1) and Ohnesorge Number (Oh) (Equation 3.2).

$$Re = \frac{\rho v l}{\eta} = \frac{inertia\ forces}{viscous\ forces} \tag{3.1}$$

$$Oh = \frac{\eta}{\sqrt{\gamma \rho l}} = \frac{viscous\ forces}{inertia * surface\ tension} \tag{3.2}$$

The Reynolds Number (Re) (Equation 3.1), relates fluid inertia (density $\rho$ $[kg/m^3]$, velocity v $[m/s]$, nozzle length l $[m]$ and viscous forces (viscosity $\eta$ $[Ns/m^2]$). The Ohnesorge Number (Oh) (Equation 3.2) is mainly influenced by surface tension $\gamma$ $[N/m]$ and viscosity $\eta$. Also the characteristic length l $[m]$ and the fluid density $\rho$ $[kg/m^3]$ are used to calculate this

parameter [3]. Both numbers are dimensionless (balance of two equal entities) [15]. According to literature the Oh should have a value between 0.1 and 1, whereas the Re needs to be between 2 and 150 for liquids exhibiting stable jetting [133].

A typical jetting sequence is depicted in Figure 3.3. First, a liquid beam is squeezed out of the nozzle and the liquid beam breaks into individual drops [62], resulting in a main drop and several smaller satellite drops (see Figure 3.3). Those satellite drops can cause severe problems, if they impinge on different paper regions than the main drop.

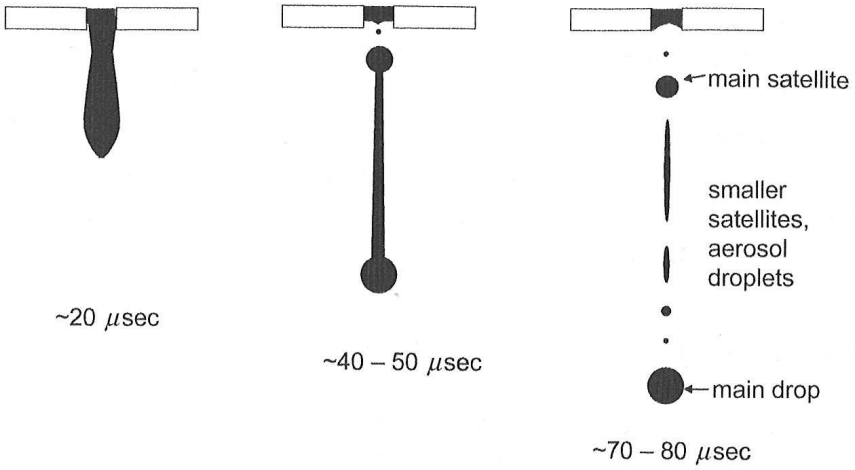


**Figure 3.3** Drop generation by Drop-on-Demand. Liquid is squeezed out of a print head nozzle. The fluid beam breaks-up after ejection. The ink is separated into one main drop and several satellite drops [134].

## 3.3 Ink Behaviour on Paper

The HSI print head creates an ink droplet of a volume of $\sim 12\ pl$, depending on its settings. This drop is shot on the paper surface. As soon as the drop impinges on the substrate the drop wets the surface and penetration starts. Second, it starts to collapse as the ink further penetrates into the paper bulk, and finally volatile components evaporate [122]. The ink setting process is depicted in Figure 3.4. The time intervals of drop penetration and drying vary with the used ink-paper combination, employed during printing. A drop may penetrate into a highly absorbing porous medium and dry within 1 - 50 $ms$, whereas it takes up to 1 second to evaporate and dry on a non-absorbing substrate [3].

An important parameter to quantify the actual coverage of the liquid drop on the paper is

the dot gain. It is the ratio of the printed and dried dot area to the spherical jetted drop before impingement on paper surface [3]. A common dot gain in inkjet printing is $\sim$ 1.5 to 3 [122, 135].

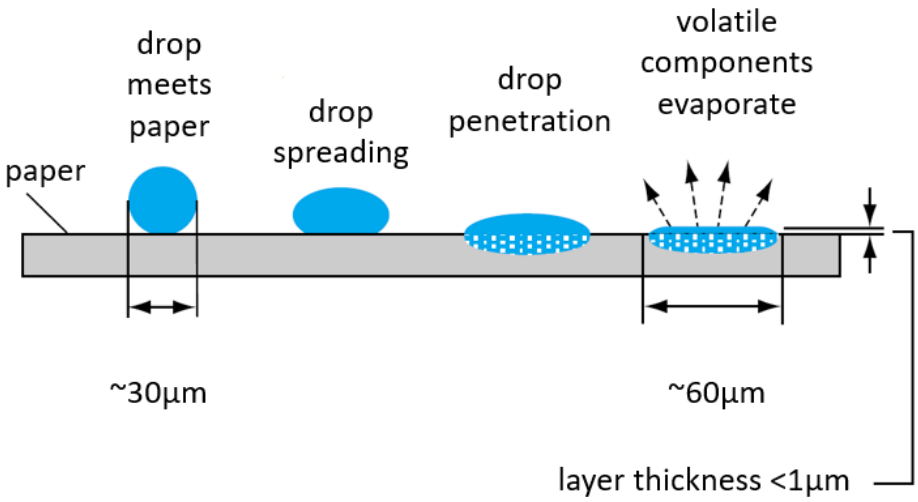


**Figure 3.4** Waterbased ink drop behaviour after impact on paper, adapted from [62]. First, the ink drop spreads on the substrate surface, increasing the dot area. Second, the drop collapses due to liquid imbibition into the paper, starting drop drying. Finally, volatile components evaporate.

## 3.4 Ink Components and Properties

In this study only water-based inks are employed, which are mainly used on the HSI market [130]. This puts the focus on the formulation and properties of waterborne inkjet inks.

Driven by economic pressure, inkjet ink is under constant development. The recipe is a well kept secret as it is one key impact factor for the producers technological and economic success.

However, there are some basic recipes available in the literature. Water serves as carrier liquid, and thus is the biggest component with the largest mass percentage of the ink. Colourants (dyes or pigments) are responsible for the colour of the ink. In commercial inks, pigments or dyes are present in an amount of 0.5 % to 10 % of the ink. Co-solvents ease the printing process, as they ensure that the nozzles do not dry out and enhance ink film formation (5 % to 50 % of the ink). Surfactants ($<$ 2 % of the ink) improve the wetting behaviour of the ink and ease print head maintenances. Polymeric binder ($<$ 10 %) helps

to increase the gloss and the rub-off fastness of the prints. Typical values for water based inkjet ink surface tension are 40 $mN/m$ and 3 $mPas$ for viscosity [3].

The High Speed Inkjet technology uses different drop generation units, ranging from piezo-electric elements to heating plates. Thus, the ink recipe needs special adjustment, depending on the application method. Instead of water as carrier liquid also oil, solvent or methyl ethyl ketone based inks are used in industry. These types of inks and the water based inks dry via absorption into the paper and subsequent also via evaporation. Beside these inks there are also hot melt– and UV inks used for printing [3].

At room temperature, the hot melt ink is originally in a solid state. Before ink application, the ink is heated, and thus liquefied. After drop impingement on the paper, the liquid cools down and solidifies. Thus, the quality of the print out is only slightly affected by the substrate [62, 136].

UV curable inks posses reactive monomers and photo initiators as components [15]. After ink application, the print out is illuminated with UV-light, thus the reactive monomers polymerise and create a solid layer. Similar to the hot-melt inks, the print quality is only slightly substrate dependent [62, 136].

Both inks show very low to zero penetration into the substrate, and thus have a high layer thickness ($> 10\ \mu m$). This layer is sensitive to rub-off, due to the height of the ink film [62]. Printed hot melt– and UV ink dots show a $\sim 1.5$ higher diameter on the paper as the diameter of the printer created liquid sphere [62, 137]. However, the normal dot gain is between 2-3 [15].

The drawbacks of these types of inks are high costs and health, safety and environment based issues [11]. Figure 3.5 gives an overview of typical ink properties for various HSI methods. By implementing different inkjet print heads, the drop size can be adapted accompanied with a change in ink layer thickness on the paper surface after drying [130].

| | Ink type | Viscosity (mPas) | Ink layer thickness (µm) | Drop volume (pl) | Drying |
|---|---|---|---|---|---|
| **Thermal ink jet** | Water-based | 1-5 | < 0.5 | 1-30 | Absorption, evaporation |
| **Piezoelectric ink jet** | Water-, oil-, and solvent-based | 5-20 | < 0.5 | 1-30 | Absorption, evaporation |
| | Hot melt | 10-30 | 12-18 | 10-30 | Solidification through cooling |
| | UV-curing | 10-30 | 10-20 | 10-30 | Radiation cross-linking |
| **Continuous ink jet** | Solvent-, water-, MEK (methyl ethyl ketone)-based | 1-5 | < 0.5 | 5-100 | Absorption, evaporation |

**Figure 3.5** Summary of process parameters applied in different inkjet printing methods. Depending on the drop generation viscosity needs to be adjusted. With different drop production methods the drop size changes, leading to a difference in ink layer thickness on the paper surface after drying [15, 130].

Chapter 4

# Review of Measurement Methods for Liquid Penetration and Wetting

The product value is a crucial impact factor with regards to the price. The evaluation of the product value is done by controlling process relevant parameters and achievement of those requirements. This is fundamental for assessing the suitability of the product [138]. Penetration and wettability are decisive process variables for good print quality and high product value of the paper or ink.

For the paper- and printing industry, liquid penetration and wetting on paper are crucial processes with regard to product quality. Thus, a large number of measurement techniques has been invented to quantify and predict penetration and wetting during the HSI printing. They try to measure process relevant parameters, providing information about the liquid-paper interaction during the industrial liquid application. Some of the most widespread methods are described in this chapter. An overview of these analytical approaches is given in Figure 4.1, highlighting the variation in time resolution and the liquid volume applied by the techniques.

The described methods utilize different measurement principles and apply different liquid volumes on the substrate. For example, whereas the contact angle measurement device creates droplets of 30 $pl$, ultrasonic liquid penetration measurements (ULP) puts the paper in a test liquid bath, providing an unlimited fluid supply.

Besides the variation in liquid amount used to quantify liquid behaviour, also a variation of time between fluid application and first measurement value as well as in time resolution of the measurement itself is high, see Figure 4.1. The Cobb method gives insight in water absorption after 30 seconds of contact time between fluid and paper. The contact angle device used in this work provides results starting directly after liquid applications giving information of drop behaviour every 0.5 *ms*, as this is the duration between single picture acquisition. It can be noted, that image recordings used in the HSI industry can go up to $\mu s$ time resolution [15].

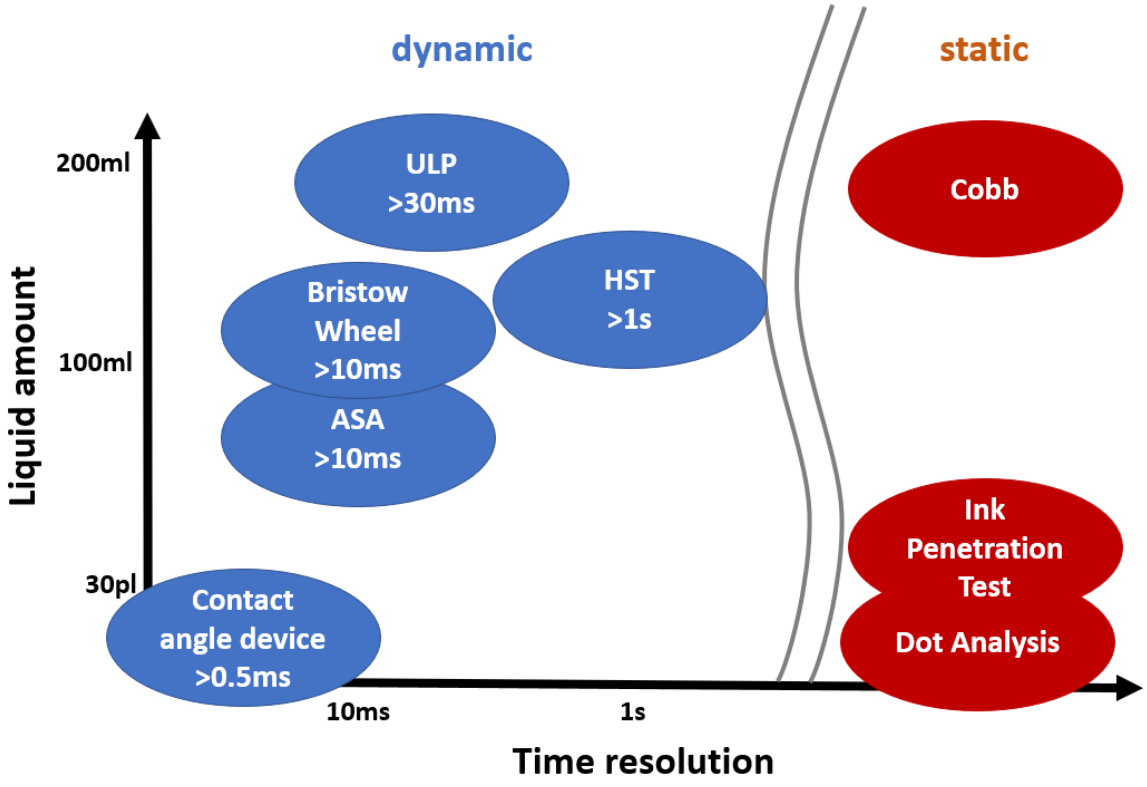


**Figure 4.1** Schematic illustration of measurement methods plotted over liquid amount and time resolution. Static measurements, giving one result value are coloured in red, whereas methods with high time resolution are pictured in blue. In the case of dynamic methods (blue circles), the last line contains the time at which the first measurement value is achieved. ULP is used for ultrasonic liquid penetration test, ASA for automatic scanning absorptometer and HST indicates the Hercules sizing test.

## 4.1 Laboratory Measurement Quantification of Liquid Spreading and Penetration

### 4.1.1 Cobb Absorption Test

The determination of water absorbing capacity according to Cobb is a traditional method quantifying surface absorbency of paper. In this approach, water is applied on a surface area of 100 $cm^2$ at one side of paper, measuring the water volume penetrating into the substrate. Fluid uptake is determined by measuring the sample weight prior and after water application. The contact times vary from 30 seconds for strong absorbing media to 1800 $s$ for heavily sized papers [138]. A detailed description of every single process step accompanied with the required time can be found in DIN EN 20535 [138]. The Cobb technique is a static method providing information about liquid uptake after the chosen contact time as illustrated in Figure 4.1. A high Cobb value can be observed for strong absorbing papers, indicating a high water uptake. The Cobb method fails if the applied water penetrates through the bulk to the backside of the paper. Furthermore, it does not provide results within the High Speed Inkjet (HSI) relevant time scale (up to 50 ms on paper [3]). Thus, this method is not suited for quantification of liquid behaviour during the HSI printing.

### 4.1.2 Ultrasonic Liquid Penetration Test (ULP)

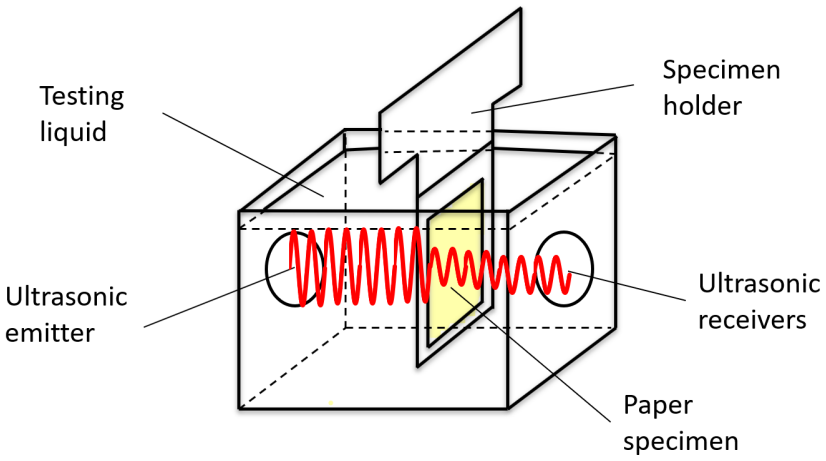


**Figure 4.2** Ultrasonic liquid penetration test-principle: ultrasonic waves are absorbed, reflected and scattered while transmitting through the paper. During the wetting and penetration of liquid, the signal changes, and thus captures penetration and wetting [139].

.

The ultrasonic liquid penetration test (ULP) provides a measure for liquid penetration into porous substrates. As shown in Figure 4.2, an ultrasonic emitter and ultrasonic receiver are positioned opposite to each other. Between them, the sample is immersed into a testing liquid, like e.g. water or ink. The transmitter instantly starts to transmit ultrasonic waves through the sample. These are reflected, scattered or absorbed during the process of liquid imbibition. As absorption proceeds, the receiver records changes in the signal. A typical ULP result curve is illustrated in Figure 4.3. The initial rise of the curve indicates wetting. The time it takes to reach 100 % of intensity is the wetting time ($t_W$ [$s$] in Figure 4.3). High wetting times can be observed for bad wetting. The slope of the curve after the maximum ($\frac{\Delta intensity}{\Delta t}$ [$\%/s$] in Figure 4.3) represents the penetration speed. The faster the liquid penetrates into the paper, the higher is the change in intensity. First values are obtained after $\sim 31$ $ms$ between first contact of liquid and paper [103, 139]. The ULP provides a signal value every $\sim 4$ $ms$.

The results from publication II and manuscript III show, that the ULP is not suited to capture the wetting during HSI printing, but delivers reasonable results quantifying liquid penetration in the HSI related field.

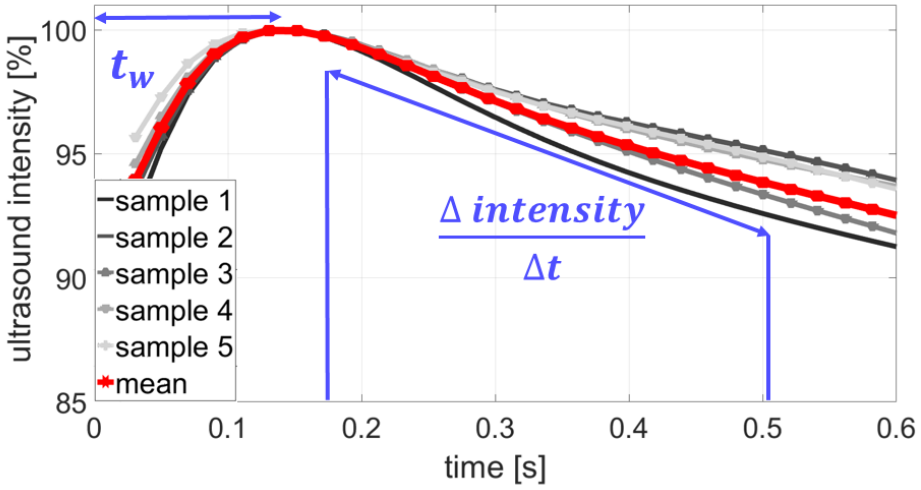


**Figure 4.3** Measurement result curve of ULP, plotting ultrasound intensity over time. The time $t_w$ [$s$] is a measure for wetting, long wetting times can be observed for bad wetting. The slope of the curve represents the penetration speed $\frac{\Delta intensity}{\Delta t}$ [$\%/s$], showing a steeper decline for faster absorption [103].

.

### 4.1.3 Bristow Wheel Absorption Test

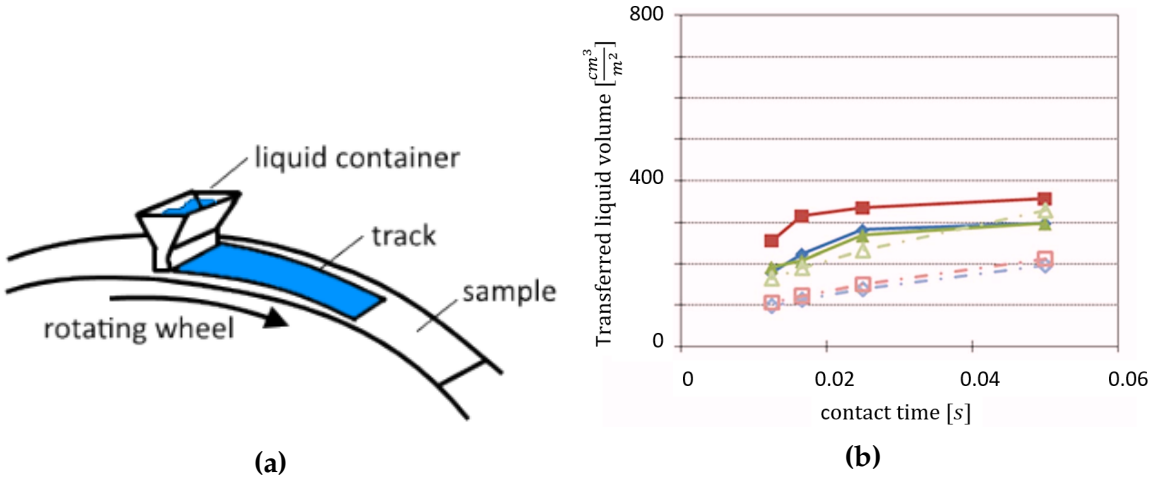


**(a)** **(b)**

**Figure 4.4** a.) The Bristow Wheel uses a nozzle to apply liquid onto a paper stripe mounted on a wheel [140]. Faster movement of the wheel results in an increased substrate velocity and is accompanied with a decrease of contact time between nozzle and paper [141]. b.) In the result curve of the Bristow Wheel absorption test, transferred liquid volume is plotted versus the contact time between nozzle and paper [140, 142]. The slope of the curve is giving liquid penetration speed. Figure adapted from Hamada et al. [142].

The Bristow Wheel absorption test is a direct measurement of imbibed liquid over time. The fluid is applied using a nozzle touching the paper. The adjustment of the contact time is done by changing the velocity of the sample holder wheel, where the paper is mounted (see Figure 4.4 a). The time scale ranges from shortly after first contact ($\sim 11\ ms$) between nozzle and paper up to 2 seconds [143]. The underlying model assumes a two-phase process: wetting the surface and penetration of the liquid into the substrate bulk [144]. The absorbed liquid is plotted versus contact time as illustrated in Figure 4.4 b. The higher the slope of this curve, the higher is the penetration of the liquid into the paper.

The Bristow Wheel was not used to capture liquid behaviour on paper during this Ph.D. thesis. However, it also employs a direct liquid application method, similar to the utilised automatic scanning absorptometer (ASA). Thus, the conclusions drawn from the ASA measurements might also apply here. The penetration detected with a direct liquid application method are suited to capture liquid penetration in the HSI field. The wetting parameter calculated with the ASA results are strongly affected by penetration and did not correlate with the contact angle values from the same liquid-paper combinations. Thus, it is not recommend to use a direct absorption measurement to quantify wettability in the HSI field (see publication II and manuscript III).

### 4.1.4 Automatic Scanning Absorptometry

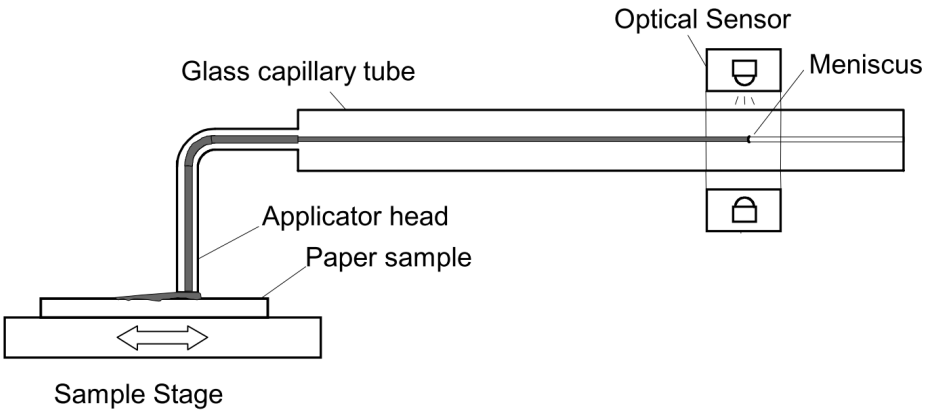


**Figure 4.5** Automatic scanning absorptometer: liquid is applied via a nozzle (applicator head) on the substrate. The transferred liquid volume is observed by the movement of the fluid's meniscus in the glass tube, detected by an optical sensor. The movement of the sample stage defines the contact time between nozzle and substrate. An increase of velocity, reduces the contact time [103, 145].

The automatic scanning absorptometer (ASA) is based on the same principle as the Bristow Wheel. A nozzle applies liquid onto paper and the transferred liquid volume is detected. The contact time is determined by the velocity of the sample stage, whereas an increased speed reduces the contact time between nozzle and paper. An illustration of the method is depicted in Figure 4.5. High fluid imbibition can be observed for strong absorbing substrates, represented by a higher amount of absorbed liquid volume per unit area. The first measurement value is obtained after approximately 10 $ms$ of contact time.

The substrates can be chosen freely as long as a sample size of A5 is provided. Liquid supply of the nozzle is ensured by a tube. High viscosity can prevent liquid movement in the tube, which restricts the selection of the liquids that can be tested with the ASA. The transferred liquid volume per unit area is plotted over time in the results curve, Figure 4.6 a, giving direct information about absorption behaviour. The slope of the curve $\frac{\Delta TLV/A}{\Delta\sqrt{t}}$ $[\frac{ml/m^2}{\sqrt{ms}}]$ represents the penetration speed, indicating higher slopes for higher imbibition rates [103, 145, 146].

The transferred liquid volume per unit area $TLV/A$ $[mm]$ can be considered as the penetration length of a liquid moving into the paper. Also the Lucas-Washburn equation describes the fluid imbibition length into the paper.

Knowing the pore diameter D of a paper and the surface tension $\gamma_{lv}$ as well as viscosity $\eta$ of the testing liquid, the ASA results can be replotted with the expression $\epsilon * \sqrt{\frac{\gamma_{vl} * D}{4 * \eta}} * \sqrt{t}$ $[mm]$ on the x-axis, which basically is a rearranged LW equation. The slope of this plot

is equal to $cos(\Theta)$ according to the Lucas-Washburn approach. This is shown in Figure 4.6 b. $cos(\Theta)_{LW}$ is a theoretical contact angle obtained from the ASA measurement and is a wetting parameter determined from liquid absorption. A detailed description of this procedure can be found in previous work of our group [103].

The ASA penetration parameter was found to reliably capture liquid imbibition behaviour into paper during HSI printing. The comparison between the contact angle from liquid drops and the calculated ASA wetting parameter $cos(\Theta)_{LW}$ from same liquid-substrate combinations resulted in a low correlation coefficient. This calculated wetting parameter is highly affected by fluid penetration into the paper, and thus is not recommended for measuring liquid wetting in the HSI related field. For further details, please see publication II and manuscript III.

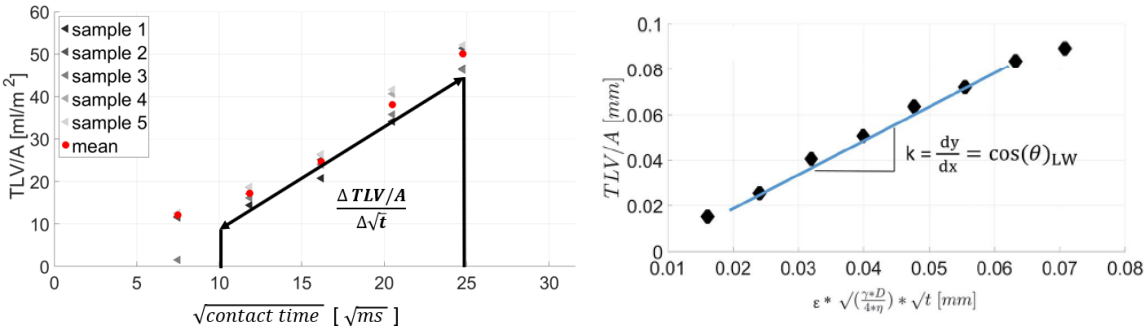


**Figure 4.6** a.) Automatic scanning absorptometer result curve. It plots the transferred liquid volume per unit area versus the root of contact time. A high slope $\frac{\Delta TLV/A}{\Delta\sqrt{t}}$ can be observed for fast liquid penetration into the paper. b.) Automatic scanning absorptometer result curve with rescaled x-axis. The rescaling of the curve was conducted via implementation of the Lucas-Washburn equation. The slope of the curve, which uses one defined paper-liquid system, represents the theoretically calculated $\cos(\Theta)_{LW}$ and can be interpreted as a wetting parameter determined from liquid absorption [103].

### 4.1.5 Hercules Size Test (HST)

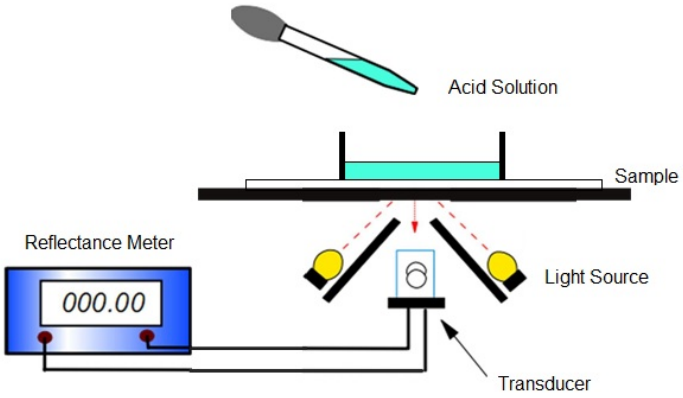


**Figure 4.7** Illustration of the Hercules Size tester. The paper sample is fixed above a light source and a transducer. After liquid application, the change in reflectance due to penetration is captured by the transducer [20, 147].

The Hercules Size test was developed by Price [148] in order to quantify the sizing degree of papers. HST measures the time required for a formic acid solution to penetrate into the substrate by detecting the change of brightness due to liquid imbibition. Various formic acid concentrations are employed depending on the sizing degree of paper. The coloured testing liquid is put on the paper and a reflectance meter detects changes in paper reflectance on the bottom side of the paper, shown in Figure 4.7. This gives a measure for resistance of paper against fluid movement into the substrate. The result curve shows the change in reflectance over time, indicating higher penetration for higher change in signal, as illustrated in Figure 4.8. The parameter obtained from the Hercules Size tester is the HST value [$s$]. This is the time it takes to reach a reflectance value of 85 % [149].

The HST was developed to quantify fluid transport resistance into sized paper, employing a time resolution in the second range [20]. Thus, the Hercules Sizing tester is not suited to capture liquid penetration and wetting in the HSI process relevant time scale.

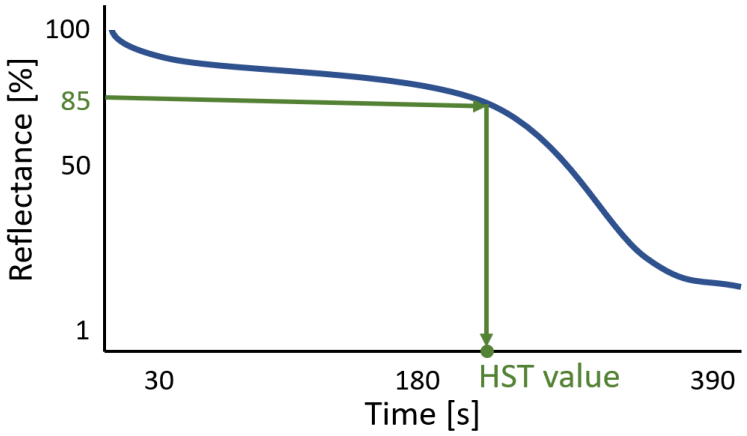


**Figure 4.8** Result curve of the Hercules Size test is shown in this diagram. Reflectance is plotted versus time. Fast penetration causes a steep slope of the curve, adapted from [147]. The time at a reflectance of 85 % is the HST value [149].

### 4.1.6 Contact Angle Measurement (CA)

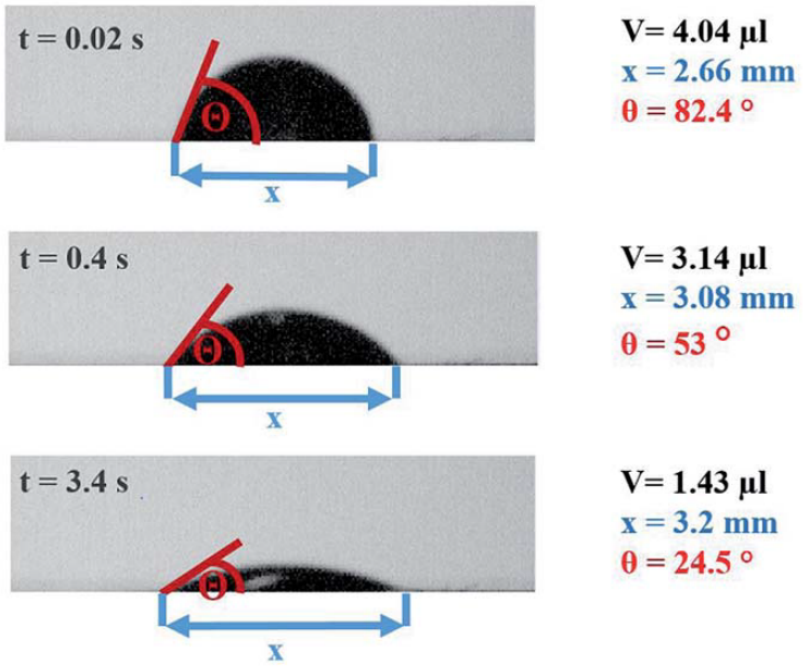


**Figure 4.9** A typical picture sequence taken by a contact angle device [103]. The calculation of the remaining drop volume (V) and drop diameter (x) is implemented for each frame the device has captured. Furthermore, a tangent is fitted onto the droplets surface at the three-phase contact point, obtaining the contact angle Θ between tangent and substrate surface. High contact angle values can be observed, when bad wetting occurs.

The pico-drop set up of the dataphysics instrument creates drop volumes in the *pl* size scale [150]. Once the drop is released onto substrates surface, the instrument starts taking

pictures, with a frame rate of 2000 frames per second. The device uses each image to fit a tangent at the droplets surface in the three phase contact point to calculate the angle $\Theta$ between tangent and substrate surface (Figure 4.9). This angle is commonly referred to as the contact angle. Thus, one obtains a series of contact angles over time, starting immediately after the drop-release. Furthermore, also the base diameter x [$mm$] of the drop and the remaining liquid volume V [$\mu l$] above the paper surface is obtained, see Figure 4.10.

The generation of drops from 0.8 to 4 $\mu l$ is mainly done with a Fibro Dat system [6, 103], following the same measurement procedure, but with lower frame rate. The results are plotted in a curve, showing calculated contact angle over time (Figure 4.10). The change of contact angle occurs due to penetration and wetting of the droplet on the paper. Thus, a high change in contact angle can be observed when the fluid drop exhibits good spreading and penetration into the paper.

A parameter often used is the initial contact angle $\Theta$, which is mainly influenced by spreading and possesses a large value in the case of bad wetting. The initial contact angle for $\mu l$ drops is measured after 50 $ms$ of contact time between paper and liquid (publication II). For $pl$ drops immediately after full liquid contact with the paper (manuscript IV).

Furthermore, drop penetration can be calculated using the results of the contact angle device. The change of remaining liquid $\Delta V$ on the paper surface is employed to calculate drop imbibition rates into the paper. Another parameter to quantify drop penetration is the transferred liquid volume per unit area (TLV/A). Here, $\Delta V$ is divided by the contact area of the drop. The contact area is assumed to be circular, having the diameter x (= drop diameter on the paper, see Figure 4.9), obtained from the contact angle measurement. The higher the TLV/A, the higher is the drop penetration into the paper.

The contact angle measurement captures the liquid wetting on paper and can be used to predict the spreading of HSI printed dots, as shown in manuscript III. In comparison to other measurement techniques for liquid penetration and wetting, the contact angle measurement is the only technique providing reliable results for capturing surface wettability (publication II). For high absorbing papers a drop size in the $\mu l$ scale should be used to quantify wetting, minimising the impact of penetration (manuscript IV). Overall, the contact angle method is a very useful instrument for capturing surface wettability and liquid spreading of drops during the HSI printing.

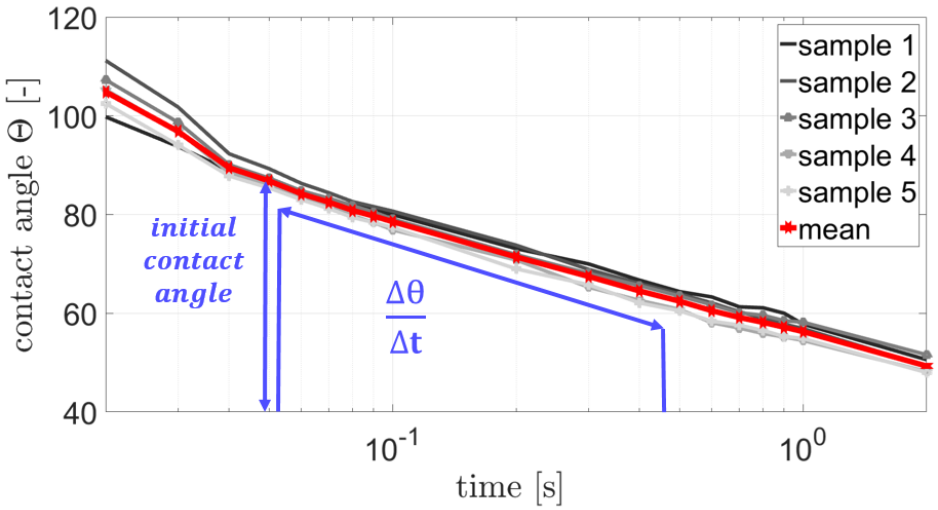


**Figure 4.10** The result plot shows the observed contact angle over time. The initial contact angle is a measure for wetting, whereas the slope of the contact angle decay captures a combination of liquid wetting and penetration into the paper [103].

## 4.2 Evaluating Penetration and Spreading of Printed Paper Samples

### 4.2.1 Ink Penetration Test

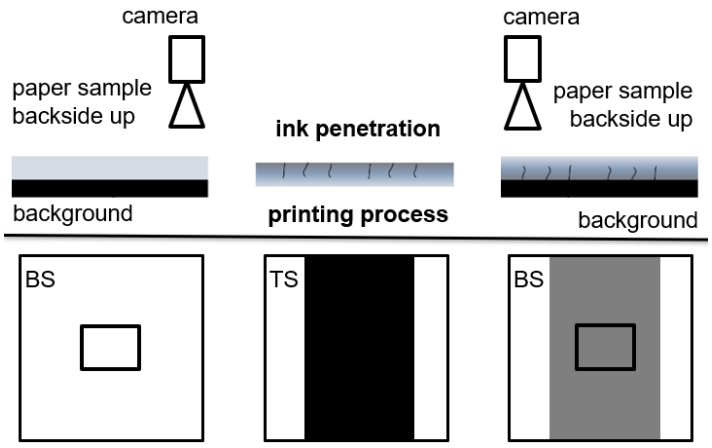


**Figure 4.11** Illustration of the ink penetration test. First, the backside (BS) of the unprinted paper is imaged. Second, the top side is printed and finally the same area of the backside of the now printed sheet is imaged again. The darkening of the paper backside caused by printing is a measure for ink penetration into the paper. A high print through value, which is defined in Equation 4.1, is accompanied with high liquid imbibition [131].

The ink penetration test directly measures the print through, which is a measure for liquid penetration into paper.

The ink penetration index PT [-] is calculated from the ratio between the gray value [8 bit gray value] of the unprinted sample backside image to the gray value of the printed sample backside image, as shown in Equation 4.1 [131]. The larger the value, the greater is the difference between the gray values, and thus the higher is the ink penetration rate. A failure of the ink penetration test might be caused by too low penetration and/or too high paper thickness.

$$PT = \frac{GV_{before\ printing}}{GV_{after\ printing}}\ [-] \tag{4.1}$$

### 4.2.2 Cross Sectioning

The investigation of ink penetration into paper is also done by microtome cross sectioning using light microscopy. The image of the paper cross section is evaluated and the average penetration depth of the ink into the paper is calculated. An example picture of a microtome recording can be seen in Figure 4.12. Here, black ink was applied on the paper, penetrating into the paper bulk. The ink coloured regions of the paper are detected by image analysis [58].

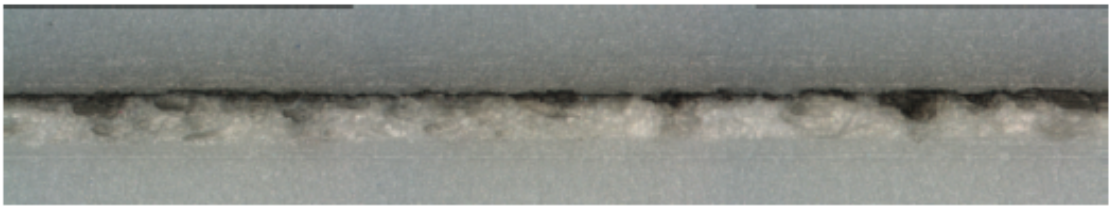

**Figure 4.12** Cross section image. The penetration of the black ink can be seen due to colouring of the paper[58].

Another method for cross sectioning is scalpel cutting [151]. Enzi [152] developed a scalpel cutting method for full tone printed paper. The method is restricted to uncoated papers and high ink penetration. The cutting is done manually using a scalpel as shown in Figure 4.13 a. The cut is examined using reflected-light microscopy, imaging the cross section. The imbibed liquid is detected by image analysis and illustrated in white (Figure 4.13 b, B). The penetration depth is determined using measurement lines with a gap of 5 $\mu m$ between them, see Figure 4.13 b, C. Thus, every 5 $\mu m$ a penetration depth value is obtained, also providing a penetration depth distribution.

However, to achieve reliable and representative results for cross sectioning, several centimetres of paper length need to be evaluated. Furthermore, it is important to take the paper cross sections at different regions of the paper [58]. The preparation and analysis of a huge amount of paper cross section to achieve good reliability of the results is very time consuming, and thus this method is not efficient enough to measure ink penetration into paper.

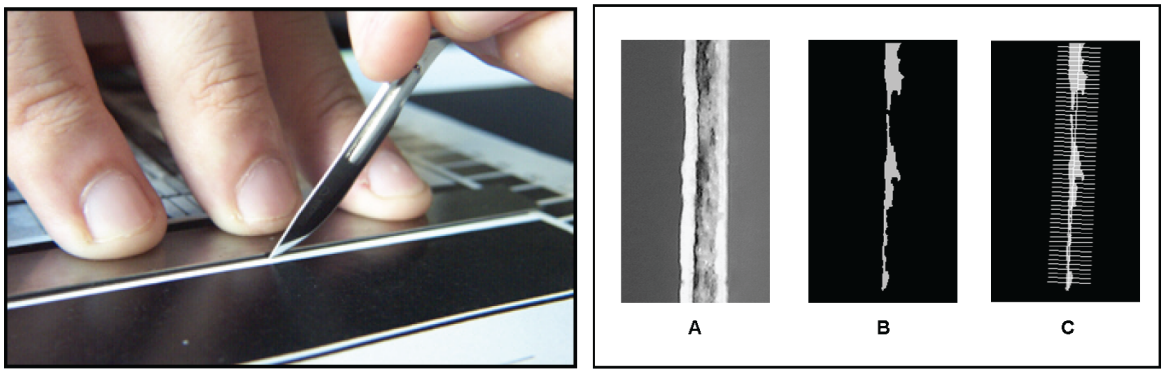


**(a)** **(b)**

**Figure 4.13** a.) Picture of the scalpel cutting process. b.) Three step evaluation of the scalpel cutted sample. b.A.) Image of the cross section is obtained using reflected-light microscopy. b.B.) Image analysis detected the ink coloured paper area b.C.) Measurement lines with a gap of 5 $\mu m$ are used to detect the penetration depth [152]. Thus, every 5 $\mu m$ a penetration depth value is obtained.

# Chapter 5

# Publication I

RSC Advances

PAPER



Cite this: *RSC Adv.*, 2018, **8**, 12861

# Short timescale wetting and penetration on porous sheets measured with ultrasound, direct absorption and contact angle†

Krainer Sarah[ab] and Hirn Ulrich *[ab]

In this study the short timescale penetration and spreading of liquids on porous sheets is investigated. Three measurement techniques are evaluated: ultrasonic liquid penetration measurement (ULP), contact angle measurement (CA) and scanning absorptiometry (SA). With each of these techniques liquid penetration as well as surface wetting can be measured. A quantitative comparison between the methods is carried out. For our studies we are using model liquids with tuneable surface tension, viscosity and surface energy which are the governing parameters for pore flow according to the Lucas–Washburn equation. Scanning absorptiometry turns out to be an adequate tool for direct measurement for liquid penetration. Ultrasonic liquid penetration showed a stable correlation ($R^2 = 0.70$) to SA and thus also gives a suitable indication on the liquid penetration behaviour. Absorption of individual microliter drops measured in the CA instrument showed different results than the other two measurements. For characterisation of the wetting behaviour the measurement techniques gave substantially different results. We thus conclude that ULP and SA do not capture the wetting behaviour of liquids on paper in the same way as conventional contact angle measurement, it is unclear if their results are meaningful. Finally we are proposing two parameters indicating a combination of liquid penetration and wetting, the slope of the contact angle over time $d\theta/dt$ and a contact angle calculated from SA. These two parameters are moderately correlated, supporting the idea that they are indeed capturing a combination of liquid penetration and wetting. While our investigations are restricted to paper, we believe that the methods investigated here are generally applicable to study liquid absorption in thin porous media like microfluidic paper based analytical devices, thin porous storage media, membranes and the like. Our findings are highlighting the importance to have a match in timescale (time for penetration and wetting) and size scale (liquid amount supplied) between the testing method and the actual use case of the material, when analyzing wetting and penetration on porous materials.

Received 14th February 2018
Accepted 26th March 2018

DOI: 10.1039/c8ra01434e

rsc.li/rsc-advances

## 1 Introduction

Wetting and liquid absorption in thin, porous materials is a relevant performance characteristic *e.g.* for microfluidic paper based analytical devices, thin porous storage media or membranes. Also High Speed Inkjet (HSI) printing is influenced by the penetration behaviour of the fluid into the printing substrate, often paper.[1,2] There are three main challenges studying liquid penetration and spreading in paper and other thin, porous media. First the thickness of the material is low, typically around 100 μm. Second paper has a high in-plane inhomogeneity which necessitates testing of either a large sample area or measurement of many specimen sampled over a large specimen area.

Finally liquid penetration and spreading in HSI printing are taking place within a few hundred milliseconds, requiring measurements with high time resolution. This has lead to the application of various analytical approaches. Commonly used techniques in paper and printing industry are ultrasound measurement (ultrasonic liquid penetration – ULP), scanning absorptiometry (SA) and contact angle measurement (CA). The application of these techniques in characterization of penetration speed and wetting was subject of several studies.[2–12] In our study we are using these instruments for both, measurement of liquid penetration and for surface wetting.

The common method to determine the wetting behaviour of liquids is the contact angle measurement (CA). The contact angle of a drop, placed on the surface of a substrate, is filmed and measured from the images. The change of contact angle over time is influenced by the spreading of the drop and by the penetration of the liquid into the paper.[13–16] Ultrasonic liquid

[a]*Institute of Paper, Pulp and Fiber Technology, TU Graz, Inffeldgasse 23, 8010 Graz, Austria. E-mail: ulrich.hirn@tugraz.at*

[b]*CD Laboratory for Fiber Swelling and Paper Performance, Inffeldgasse 23, 8010 Graz, Austria*

† Electronic supplementary information (ESI) available. See DOI: 10.1039/c8ra01434e

penetration (ULP) is delivering a measure for surface wetting by measuring the time between liquid contact and the highest signal intensity. Also scanning absorptiometry (SA) can provide information on the wetting behaviour. The wetting parameter here is a calculated contact angle, computed from the measured liquid penetration using the Lucas–Washburn equation.[17–19]

For liquid penetration ultrasonic measurement is available in different configurations. All of them indicate the liquid penetration into paper and the wetting behaviour using ultrasound intensity.[3,7–9,20–22] For example Sharma[8] showed a correlation of ULP and inkjet print quality parameters for photographic papers. Liquid penetration is also measured using scanning absorptiometry. SA evaluates the liquid absorption per unit area at a specific contact time, it is a direct measure for the penetration speed. The potential of the SA for characterising the direct liquid uptake has been studied and shows good results for measuring penetration.[6,12,17] Liquid penetration of single droplets has been investigated in this study using the contact angle instrument. The change in drop volume over time is calculated from an image sequence taken by the CA instrument.

### 1.1 Aim of the work

In this study we are comparing measurement of liquid penetration and surface wetting using ultrasonic liquid penetration measurement (ULP), contact angle measurement (CA) and scanning absorptiometry (SA). The techniques are investigated for their potential to measure penetration and wetting at different time scales, depending on the liquid (*e.g.* approximately 200 ms for fast penetration and 1.5 s for slow penetration). We are reporting results for liquid penetration in paper, however the findings should also be relevant for liquid absorption and wetting into other thin, porous materials.

For testing we are using 4 HSI inks and 5 water based model liquids with defined surface tension, viscosity and polarity in terms of Hansen solubility parameters. As discussed in Section 2.6 these three parameters are the governing features for liquid capillary penetration. The model liquids have been designed for decoupled tuning of these key liquid characteristics. The testing liquids are applied to four different papers with different degrees of liquid absorption and spreading. The chosen combination of papers and liquids are representative for the spectrum of the materials in the high speed inkjet printing process.

A quantitative comparison of the results from the different test outcomes is carried out in terms of linear regression and the suitability of the three methods to measure liquid penetration and wetting behavior is evaluated. The influence of time scale and size scale of penetration and wetting will be discussed with respect to the different measurements techniques and their results.

## 2 Materials and methods

All measurements have been conducted in a climate room under defined temperature (23 °C) and humidity (50% relative humidity) according to ISO 187:1990. The papers were then stored in the climate room for at least 24 hours to ensure they have reached equilibrium moisture content, as indicated in ISO standard 187:1990.

### 2.1 Papers

The paper grade significantly influences the penetration process. Therefore we investigated the performance of all liquids on four different wood free fine papers from an industrial supplier. These are an unsized HSI treated paper grade (DNS High Speed Inkjet CF by Mondi), an HSI unsized, pigmented paper (NEUJET Matte by Mondi) and an AKD sized paper (IQ ALLROUND by Mondi). The fourth paper, the unsized and untreated grade, is basically the unsized HSI paper grade (DNS High Speed Inkjet CF) without the surface treatment. The paper types are differing in terms of sizing (hydrophobisation) and surface treatment, covering the commercially available papers for office- and high speed inkjet printing papers.

The papers were characterized in terms of composition and pore structure, see Table 1. All of them are made of industrial bleached hardwood pulp. The common method for determination of grammage is the EN ISO 536. Filler content refers to the amount of $CaCO_3$ filler particles in the paper. The filler is a commercial PCC (precipitated calcium carbonate) grade, filler content is measured according to DIN 54370. The pigmented paper grade has a low grammage surface sizing, about 3 g $m^{-2}$ per side, consisting of a mixture of starch and clay. HSI surface treatment is a surface application of $CaCl_2$ to trigger precipitation of the ink pigments on the paper surface and reduce penetration of the pigments into the bulk of the paper. The porosity and the pore diameter was obtained from mercury intrusion porosimetry, a standard method to characterize microscale pore size distributions.[23–26] We utilized an Autopore IV 9500 from Micromeritics Instrument Corp.[27,28]

### 2.2 Testing liquids

Five water based model liquids have been prepared with respect to their viscosity, surface tension and polarity. The polarity is defined through three Hanson solubility parameters.[29] The parameters are coordinates in a three dimensional coordinate system, the HSP space. d*D* describes the dispersion forces between molecules, d*P* the dipolar forces and d*H* the forces from hydrogen bonds. The tested model liquids are DI water, 80% water/20% glycerin, 80% water/20% glycol, 50% water/40%

Table 1 Properties of the papers used: grammage, filler content, surface pigmentation, HSI-surface treatment, and porosity

| Properties | AKD sized | Unsized | Pigmented | Unsized & untreated |
|---|---|---|---|---|
| Grammage [g $m^{-2}$] | 77.2 | 78.5 | 79.89 | 97.2 |
| Filler content [%] | 13.52 | 21.51 | 22.98 | 21.51 |
| Pigmentation [g $m^{-2}$] | 0 | 0 | 4 | 0 |
| HSI surface treatment | No | Yes | Yes | No |
| Porosity [%] | 20.6 | 38.8 | 23.6 | 40.3 |
| Avg. pore diameter [μm] | 4.9 | 2.6 | 3.2 | 3.9 |

glycerin/10% hexanediol and 60% water/30%glycerin/4% hexanediol/6% diacetone alcohol. Their properties are listed in Table 2. Glycerin and glycol influence the viscosity of the liquid. Hexanediol adjusts the surface tension and diacetone alcohol changes the polarity. Furthermore 3 different grades of High Speed Inkjet (HSI) ink have been tested, 2 inks of each grade. The first type is a dye ink, where the colourants are in molecular dispersion. The second one is a pigment ink, which uses dispersed pigments as colourants. The third ink is a latex pigment ink, which contains pigments for the colouring and latex particles to enhance the ink fixation on the surface of the paper. Every measurement has been performed with two colours of each ink-type: yellow and magenta.

### 2.3 Ultrasonic liquid penetration measurement (ULP)

The Emtec Penetration Dynamics Analyser 2.0 was used for all ultrasonic measurements. Measurement frequency was set to 2 MHz. The paper samples were cut to a rectangle of 7 cm × 5 cm and fastened to the sample holder with a two sided adhesive tape. In the measurement cell an ultrasonic emitter and an ultrasonic receiver are placed to the opposite of each other, shown in Fig. 1. When the sample is released into the testing cell filled with liquid, the transmitter instantly starts to send ultrasonic waves through the sample. The receiver measures the intensity of the ultrasonic signal. Sensor area is a circle with a diameter of 35 mm. The ultrasonic waves are reflected, scattered or absorbed during the process of liquid penetration, represented through the red lines in Fig. 1. As penetration of the liquid in the substrate proceeds, the receiver records the changes in the signal. The result is the ultrasound intensity over time.[9]

A typical measurement result is shown in Fig. 2, it is from the AKD sized paper with one dye ink. The curves are results from 5 specimen of the same paper (grey) and their mean value (red). The wetting is represented as the wetting time, which is the time between liquid contact and the highest intensity (wetting time $t_w$ in Fig. 2). The longer it takes to reach 100% intensity, the lower is the wetting. The penetration speed is calculated between the time at the highest intensity and approximately 200 ms for unsized papers and around 1 s for hydrophobized papers

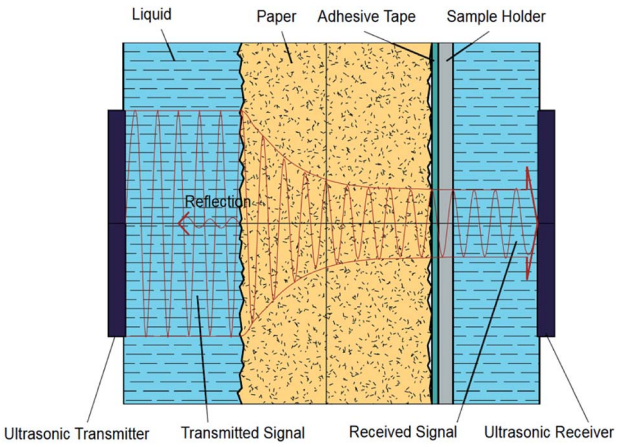


Fig. 1 Measurement principle of the ultrasonic liquid penetration (ULP) measurement, drawing not to scale.[9]

after this time. The faster the liquid penetrates into the paper, the higher is the change in ultrasound intensity and the steeper is the slope of the curve $\frac{\Delta \text{intensity}}{\Delta t}$ (Fig. 2).

### 2.4 Contact angle measurement (CA)

The contact angle measurements were performed using a Fibro DAT 1100 instrument.[30] All measurements were carried out with 4 μl drop size. Once a drop is released onto the substrate's surface, the instrument starts taking pictures of the drop, as shown in Fig. 3. A tangent is fitted to the drop's outline at the contact point between paper and liquid using digital image analysis, and the contact angle (Fig. 3, red lines) is calculated. Also the width of the drop is measured and the drop volume on the surface is calculated. This is done for every picture the camera has taken. Three pictures of the same drop and their resulting values for contact angle, volume and width are shown in Fig. 3. The contact angle is plotted over time (Fig. 4). It is also possible to evaluate the total absorbed liquid volume per unit area (TLV/$A$). This is done by calculating the volume difference of a drop between different pictures and dividing it by the area

Table 2 Testing liquids used in this study and their properties: viscosity, surface tension and polarity

| Liquids | Viscosity [mPa s] | Surface tension [mN m$^{-1}$] | d$D$ | d$P$ | d$H$ |
|---|---|---|---|---|---|
| Water | 1.004 | 72.4 | 15.5 | 16 | 42.3 |
| 80% water/20% glycerin | 1.6 | 65 | 15.9 | 15.6 | 39.3 |
| 80% water/20% glycol | 1.7 | 71 | 15.8 | 15 | 39.4 |
| 50% water/40% glycerin/10% hexanediol | 6.2 | 27.3 | 16.36 | 13.2 | 33.74 |
| 60% water/30% glycerin/4% hexanediol/ 6% diacetone alcohol | 3.45 | 33.2 | 16.1 | 13.75 | 42.9 |
| Dye ink yellow | 6.3 | 37 | — | — | — |
| Dye ink magenta | 6.3 | 35 | — | — | — |
| Pigment ink yellow | 6.3 | 36.9 | 15.8 | 13.8 | 35.6 |
| Pigment ink magenta | 6.3 | 37.4 | 15.8 | 13.8 | 35.6 |
| Latex pigment ink yellow | 5 | 32.8 | 15.8 | 13.8 | 35.6 |
| Latex pigment ink magenta | 5.3 | 33.4 | 15.8 | 13.8 | 35.6 |

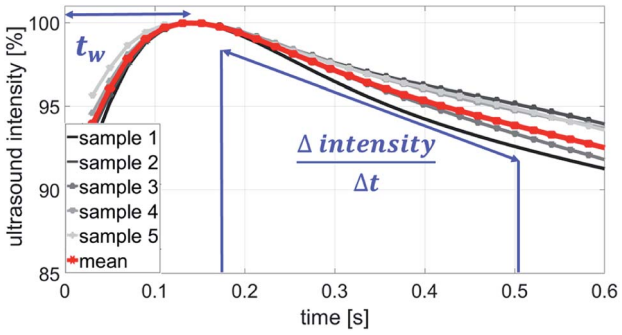


Fig. 2 The ultrasonic measurement results show the change of ultrasound intensity over time. Time at the highest intensity $t_w$ [s] is defined as wetting time of the liquid and the slope of the curve as the penetration speed $\left[\frac{\Delta\text{intensity}}{\Delta t}\right]$ of the liquid into the paper in [$s^{-1}$].

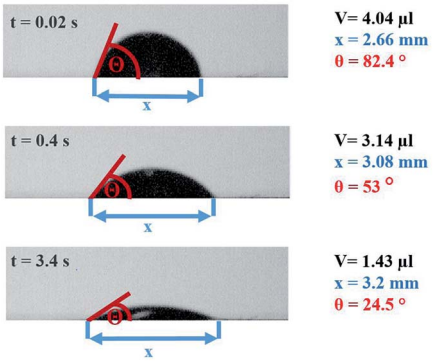


Fig. 3 Drop at different times (0.02 s, 0.4 s, 3.4 s) and the resulting values for contact angle $\theta$, width $x$ and volume $V$.

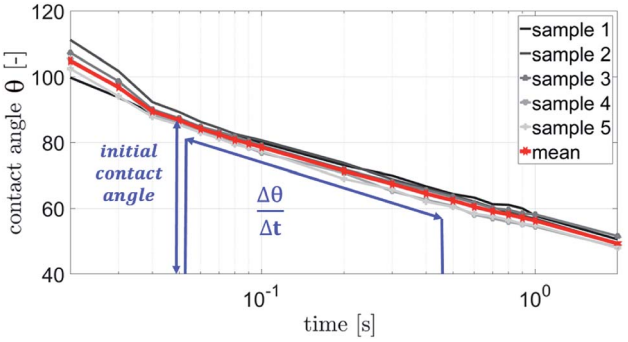


Fig. 4 The contact angle plotted over time. Initial contact angle is measured after 0.05 s and the slope is measured between 0.05 s and 0.2 s. The initial contact angle is a measure for the liquid wetting of the surface. The slope $\frac{\Delta\theta}{\Delta t}$[$s^{-1}$] is a parameter describing the combination of wetting and liquid penetration of the drop.

the drop is covering. For calculating the volume of the liquid on the surface the drop shape is assumed to be spherical. The width of the drop is used to determine the area of the droplet on the substrate surface. The change of contact angle and contact area is caused by liquid flow into the substrate (penetration) and spreading of the drop on the surface (wetting). Evaporation can be neglected at this drop size.[31–33] The initial contact angle is defined as the contact angle measured at 0.05 s after the drop has been put on the surface. A high contact angle is indicating bad wetting of the liquid on the surface. The higher the change of the contact angle over time, the faster is the liquid spreading and liquid penetration, and the steeper is the slope of the contact angle plotted over time as displayed in Fig. 4. The slope was calculated between 0.05 s and 0.2 s for the papers with treatments. The slope for the unsized & untreated paper was calculated between 0.05 s and 0.09 s, due to the fast penetration and wetting of the liquids.

### 2.5 Scanning absorptometer (SA)

The scanning absorptometer measurement, performed with a KM500win Automatic Scanning Absorptometer instrument from KRK Kumagai (Japan), provides quantitative information about the liquid absorption as a function of time on time scales of 10 ms up to 10 s.[12,17] During an SA measurement, liquid is supplied from a scanning head which moves along a spiral path on the paper. In Fig. 5 one can see the head on the paper sample surface, it is supplied with the liquid *via* a tube. The speed of the head moving over the paper surface is kept constant over a certain part of the track, then it accelerates stepwise to a higher speed which is then again kept constant. By increasing the speed the system measures the liquid penetration for different times of contact between the nozzle and the paper. The SA measures the total absorbed liquid volume per unit area. The penetration speed is represented by the slope $\frac{\Delta\text{TLV}/A}{\Delta\sqrt{t}}$ of the curve. The steeper the slope, the higher the penetration speed (Fig. 6). The slope of this curve is calculated within the same time range as the slope of the ultrasonic liquid penetration measurement is calculated *i.e.* a contact time between approximately 0.031 ms and 0.200 ms after contact between liquid and paper was made. This is done for every single liquid/paper combination. Also a parameter indicating the wetting behavior is evaluated, it is the contact angle $\cos(\theta)_{LW}$ calculated from the liquid penetration result as described in 2.6.

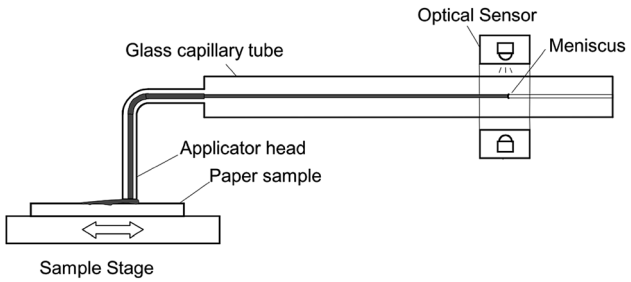


Fig. 5 The scanning absorptometer set up. The applicator head on the paper sample is moved over the paper, ink is supplied with the liquid *via* a glass tube. The meniscus sensor follows the receding meniscus and computes the amount of liquid, which is absorbed in the paper. Adapted from Enomae *et al.*[12]

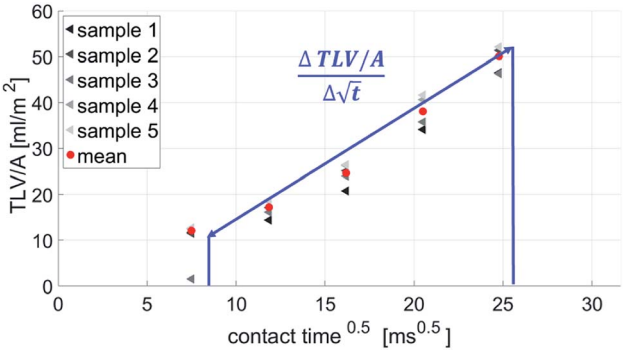


Fig. 6 SA-measurement results show the absorbed liquid volume (total transferred liquid volume per unit area TLV/A) over time. The slope of the curve $\left[\frac{\Delta TLV/A}{\Delta\sqrt{t}}\right]$ represents the penetration speed in m s$^{-1/2}$.

### 2.6 Contact angle calculated from scanning aabsorptiometry (SA) and the Lucas–Washburn equation

There are numerous theoretical studies on liquid flow into a porous system.[1,5,6,16,22,34,35] Two models are often used: the Bosanquet model and the Lucas–Washburn (LW) equation. The LW approach is a quite simplified model system, assuming straight, circular capillaries with steady state liquid flow. It describes the flow regime where the driving forces, *i.e.* the pressure difference caused by the capillary forces of the liquid in the pore, are equal to the friction forces (the viscous forces).[34,36] For penetration times below 1 ms at a pore diameters below 1 μm the LW-equations results differ from the measured values. Steady state flow is there not a valid assumption and inertial force needs to be considered for these conditions.[10,37,38] The Bosanquet model is adding the inertial forces to the Lucas–Washburn equation.[39] It has no restrictions in terms of time and pore size. However, Schoelkopf[10] and Ridgway[37] showed that the Lucas–Washburn is valid for our liquids and the pore system that we have in our papers, namely penetration times larger than 10 ms, and pore size diameters between 2.6 μm and 4.9 μm. Also earlier the Lucas–Washburn approach has successfully been used to describe the liquid flow into paper.[2,40]

$$H = \sqrt{\frac{\gamma D \cos(\theta)_{LW}}{\eta \times 4}}\sqrt{t} \quad (1)$$

Eqn (1) gives the Lucas–Washburn equation, describing the liquid uptake into a porous media modeled by cylindrical capillaries. The penetration length $H$ [m] is the distance traveled by the fluid in time $t$ [s]. The parameters that influence $H$ are the capillary diameter (pore diameter) $D$ [m], the surface tension $\gamma$ [N m$^{-1}$] and the viscosity $\eta$ [N s m$^{-2}$] of the liquid and finally the contact angle $\theta_{LW}$ [-] between the liquid and the pore material. Eqn (1) shows that according to the LW equation the penetration depth H of the liquid into the substrate is directly proportional to $\sqrt{t}$. Fig. 7 shows the results for 1 SA measurement plotted over $t$ on the left side. On the right side of Fig. 7 the

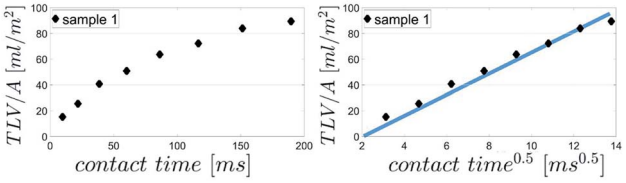


Fig. 7 Comparison of SA results plotted over $t$ (left side) and over $\sqrt{t}$ (right side). The right diagram shows that $H$ is proportional to $\sqrt{t}$ as it is the case for Lucas–Washburn flow, eqn (1).

same results are plotted over $\sqrt{t}$. A linear relation between $H$ and $\sqrt{t}$ can indeed be observed.

Please note that according to eqn (1) we can calculate the contact angle $\theta_{LW}$ when we know all the other parameters $H$, $D$, $\gamma$ and $\eta$. This is exactly the idea of our analysis, as a measure for surface wetting we are calculating the contact angle according to the Lucas–Washburn equation $\theta_{LW}$ from the scanning absorptometer measurement results.

Eqn (2) defines the volume uptake of a porous medium consisting of several parallel capillaries with the pore diameter $D$ [m]. The number of pores within an area $A$ is $N_{p,A} = N/A$ [m$^{-2}$] and each capillary has the volume $V_i = \frac{(D^2)}{4H}$ [m$^3$]. The number of capillaries (pores) $N$ multiplied with the volume $V_i$ [m$^3$] of each capillary is the total volume uptake $V$:[17,41]

$$V = NV_i = N\frac{\pi D^2}{4}H = N_{p,A}\frac{\pi D^2}{4}AH \quad (2)$$

Defining porosity $\varepsilon$ as $\frac{V_{pores}}{V_{total}}$ we find

$$\varepsilon = \frac{V_{pores}}{V_{total}} = \frac{\frac{\pi D^2}{4}H}{AH} = \frac{\frac{\pi D^2}{4}}{A} \quad (3)$$

It follows that the total absorbed liquid volume per unit area $\frac{V}{A}$ is equal to the porosity multiplied with the penetration length:

$$\frac{V}{A} = \varepsilon H \quad (4)$$

The travelled distance of the liquid flow into the porous media $H$ is described by the LW equation. Therefore the term $\frac{V}{A}$ is determined by substituting $H$, eqn (1), into eqn (4). Rearranging the resulting expression leads to

$$\frac{V}{A} = \sqrt{\cos(\theta)_{LW}}\sqrt{\frac{\gamma D}{\eta \times 4}}\varepsilon\sqrt{t}. \quad (5)$$

Eqn (5) can be re-written as a linear equation $y = kx$ with $y = \frac{V}{A}$, $x = \sqrt{t}$ and the slope as $k = \sqrt{\cos(\theta)_{LW}}\sqrt{\frac{\gamma D}{\eta \times 4}}\varepsilon$.

By plotting the result of the SA measurement $\frac{V}{A}$ on the $y$-axis and $\sqrt{\frac{\gamma D}{\eta \times 4}}\varepsilon$ on the $x$-axis we thus find $\sqrt{\cos(\theta)_{LW}}$ as the slope

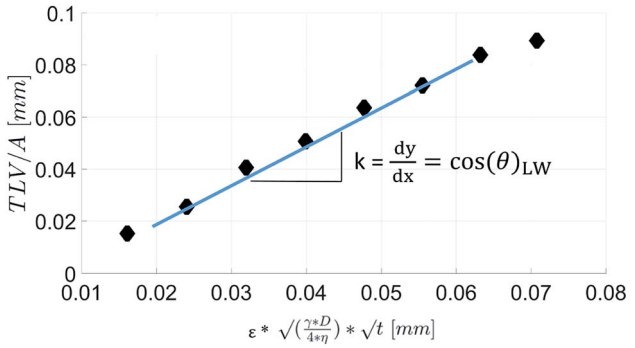


Fig. 8 The scanning absorptopmetry (SA) results are plotted over $\sqrt{\frac{\gamma D}{\eta \times 4}}\varepsilon\sqrt{t}$. The result is a straight line, indicating that the assumption of Lucas–Washburn flow is justified. The slope $k$ of the line is equivalent to $k = \sqrt{\cos(\theta)_{LW}}$, *i.e.* the square root of the contact angle.

in the resulting diagram, compare Fig. 8. The values for $t$ are taken from the SA measurements. The surface tension $\gamma$ [$N\,m^{-1}$] and the viscosity $\eta$ [N s $m^{-2}$] of the liquid have been measured for each fluid, Table 2. The parameters capillary diameter $D$ [m] and the porosity $\varepsilon$ [-] for the pore system have been measured for each paper, Table 1. Evaluating the slope of each SA penetration measurement it is possible to obtain a value for wetting, $\cos(\theta)_{LW}$, for each combination of liquid and paper from the SA. This value $\cos(\theta)_{LW}$ can be interpreted as the paper-liquid contact angle measured from the liquid penetration into the paper, under the assumption of Lucas–Washburn flow.

# 3 Results

## 3.1 Penetration speed

Fig. 9 shows the penetration speed measured by the ultrasonic measurement (ULP) plotted against the penetration speed detected by the scanning absorptometer (SA). The absorption of the model liquids water, water/glycerin and water/glycol into the untreated & unsized paper was too fast and could not be detected by the scanning absorptometer. Both measurements show for the unsized papers and the liquids without hexanediol

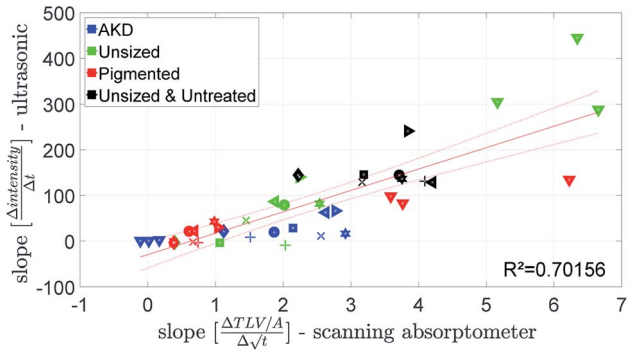


Fig. 9 Penetration speed from the ultrasonic measurement and the scanning absorptometer. For detailed description of the symbols refer to the ESI.†

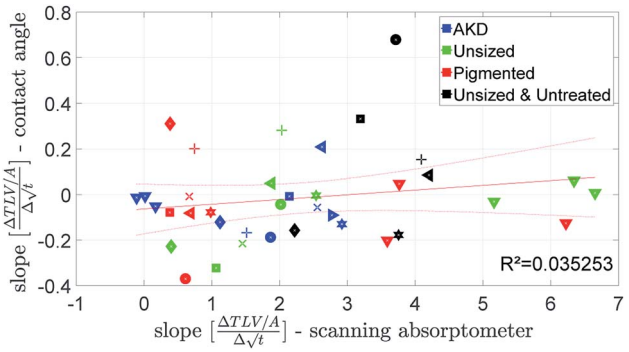


Fig. 10 Penetration speed from contact angle measurement and scanning absorptometer. Symbols are described in ESI.†

the fastest liquid uptake, followed by the liquids with hexanediol and the inks. Looking at the results for the AKD sized paper the model fluids which have a water content of 80% and 100% penetrate really slowly into the paper which is found by both techniques (Fig. 9). So, despite the totally different measurement principle, ULP and SA are delivering fairly similar results.

The penetration speed calculated from the contact angle measurement (CA) is neither correlating well to the SA, nor to the ULP data (Fig. 10 and 11). We believe the main reason is that the supplied liquid volume is comparably small (4 μl) and for the contact angle device the contact area where penetration takes place is influenced by drop spreading. In the literature[42] it has been shown that penetration into paper is considerably slower for a limited supply of liquid than for an unlimited supply. We thus believe that the differences in the measurement results represent the different penetration behavior between large amounts of liquid and small drops.

## 3.2 Wetting

The parameter for wetting from the ULP measurement is the wetting time $t_w$, see Fig. 2. The wetting parameter from the contact angle measurement is $\cos(\theta)_{50\ ms}$ the cosine of the initial contact angle measured after 50 ms, Fig. 4.

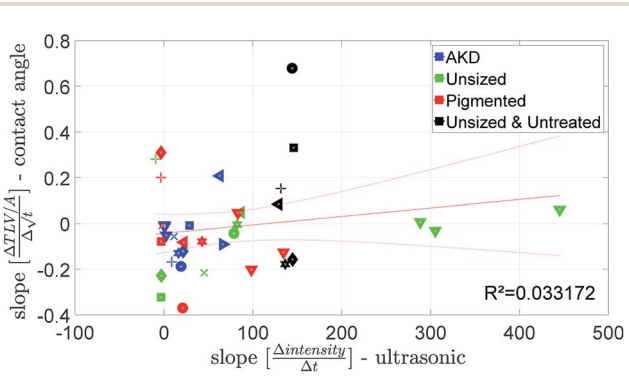


Fig. 11 Penetration speed from ultrasonic measurement and contact angle measurement. Symbols are described in ESI.†

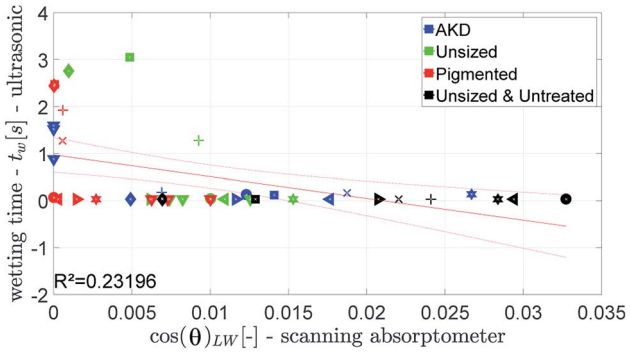


Fig. 12 Ultrasonic wetting time compared to the value for $\cos(\theta)_{LW}$ calculated from the scanning absorptometer data. Symbols are described in ESI.†

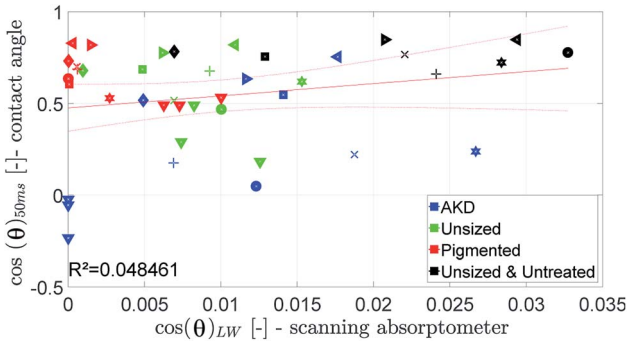


Fig. 14 Contact angle measured by the contact angle measurement at 50 ms compared to the value for $\cos(\theta)_{LW}$. Symbols are described in ESI.†

Fig. 12 and 13 show that the ultrasonic measurement is not able to capture the wetting of unsized papers. For most results the measured wetting time is zero, it cannot be determined because it takes place too fast to be detected by the ULP instrument. Also for the papers with lower wetting (AKD and pigmented paper) no correlation between ULP and the other instruments can be found. We can thus conclude that the ULP instrument is not suitable for capturing the wetting behavior of these liquids on paper.

The parameter for the spreading of the liquid measured by the SA is $\cos(\theta)_{LW}$, the contact angle calculated from the liquid penetration into the paper according to Section 2.6. It is found that the cosine of the initial contact angle directly measured by the CA instrument does not correlate well to $\cos(\theta)_{LW}$ calculated from the SA liquid penetration measurement (Fig. 14). It seems that the contact angle can not be calculated correctly using the Lucas–Washburn model. That comes somewhat surprising because the relationship between time and absorbed liquid volume was shown to have a $\sqrt{t}$ proportionality, like predicted by the Lucas–Washburn equation, compare Fig. 7. Also others have found Lucas–Washburn behavior for liquid penetration in paper.[2,40] A likely reason for the deviating results is the gross simplification of the pore system as a bundle of circular capillaries with one constant diameter. The pore system in paper has a complex geometry and a wide distribution of pore sizes.[28] It seems that while overall the penetration is following a Lucas–Washburn type time dependency, for our substrate we need a more complex pore model than the one in the Lucas–Washburn equation to successfully calculate wetting from the liquid penetration.

In conclusion we found that ULP and SA did not deliver results for the wetting behaviour that can be compared to standard contact angle measurements.

### 3.3 Combined measurement parameter for penetration speed and wetting

A combined parameter for liquid penetration and wetting is the slope of the contact angle curve. It reflects the wetting and the liquid penetration of the drop, which takes place during the time range of 0.05–0.2 s (0.05–0.09 s for fast absorbing liquids), compare Fig. 4. This parameter fits better ($R^2 = 0.35$) to the $\cos(\theta)_{LW}$ value calculated from the scanning absorptometer (Fig. 15) results. The correlation indicates that $\cos(\theta)_{LW}$ is in fact also a combined parameter which is reflecting both, the wetting on and the penetration of the fluid into the substrate. Considering that $\cos(\theta)_{LW}$ is the contact angle which has been calculated from the liquid penetration measurement, this interpretation seems plausible. The correlation between the

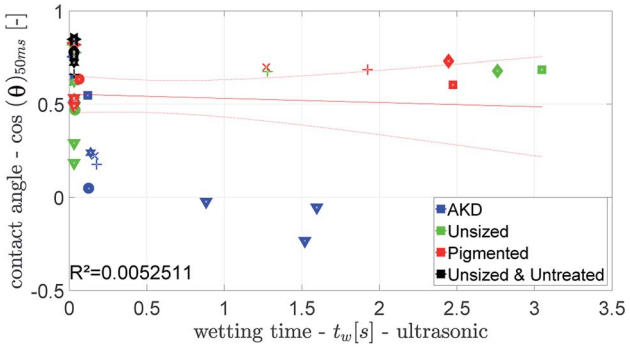


Fig. 13 Ultrasonic wetting time compared to the wetting parameter from the CA. Symbols are described in ESI.†

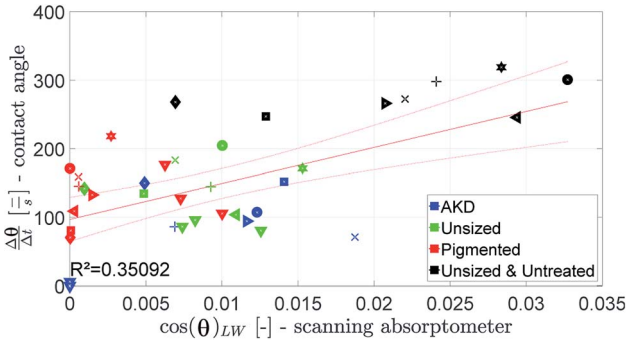


Fig. 15 The slope of the contact angle curve compared to the value for $\cos(\theta)_{LW}$ calculated from the scanning absorptometer. Symbols are described in ESI.†

measurements is low ($R^2 = 0.35$), still they somehow seem to capture similar aspects of liquid–paper interaction.

# 4 Conclusions

Ultrasonic liquid penetration measurement, contact angle measurement and scanning absorptometer are all measuring liquid penetration and surface wetting, using totally different measurement principles. In this study parameters for surface wetting and liquid penetration speed have been defined for each measurement technique and the results of the measurements have been compared. For our studies we have developed and used model liquids to independently control surface tension, viscosity and polarity of the testing fluids.

The penetration speed measurement from ULP and scanning absorptiometry showed similar results, indicating that both measurements, despite their entirely different measurement principle, are capturing the liquid penetration speed into the paper. In contrast to that liquid penetration speed measured from individual drops on the surface of the substrate gave results that differed from the other two techniques. We think that the reason might be that for the individual drops the liquid absorption is influenced by the drop spreading on the surface, while for the other two analysis techniques the contact area where penetration takes place is not influenced by wetting. We thus conclude that the penetration of small drops thus exhibits a fundamentally different penetration behavior than large amounts of liquid applied to the substrate.

For the surface wetting behaviour all three measurements techniques gave different results. We thus conclude that the well established contact angle measurement remains the most useful approach, and that ULP and SA did not provide meaningful results here.

Finally we have defined a combined parameter describing wetting and liquid penetration, it is the change in contact angle of a drop over time. This parameter is driven by both, spreading of the drop and penetration of the liquid into the substrate. A moderate correlation was found to a parameter derived from scanning absorptiometry, namely the contact angle calculated from liquid penetration using the Lucas–Washburn equation. It seems that both parameters are describing a combination of wetting and liquid penetration.

### 4.1 Implications for measurement of contact angle and liquid penetration on thin porous materials

The results have demonstrated that for measurement of wetting and liquid penetration on thin, porous materials the timescale and the size scale of the measurement is highly relevant. The time scale for all measurements was controlled it was 200 ms for fast penetration and 1.5 s for slow penetration. The size scale was differing between the measurements, excess amounts of liquids are being applied in the ultrasound measurement and for scanning absorption measurements, 4 μl drops for the contact angle measurement. Accordingly the absorption measurements of ULP and SA agree but the CA absorption is not correlated to the others. For evaluation of surface wetting only contact angle measurements are providing reasonable results. However on absorbing materials the contact angle is always a combined measurement of wetting and liquid penetration, compare Fig. 3 and 4. Thus it is particularly relevant to take drop size and measurement time into account.

The interpretation of wetting and penetration measurements on thin porous materials always has to consider the time scale of penetration and the size scale of the drop/substrate system. In the case of ink jet printing these are picoliter drops penetrating within milliseconds. In the case of other absorbing media it might be liters taken up within days. The difference in the results between the methods evaluated in this work are demonstrating the importance to carefully select the measurement method for wetting (contact angle) and liquid penetration in such a way that it reflects the time scale and size scale of the industrial application to be analyzed.

# Conflicts of interest

There are no conflicts of interest.

# Acknowledgements

The financial support for the CD Laboratory from Océ, Mondi and the Austrian Federal Ministry of Science, Research and Economy and the National Foundation for Research, Technology and Development is gratefully acknowledged.

# References

1 H. Zhou, R. Chang, E. Reichmanis and Y. Song, *Langmuir*, 2017, **33**, 130–137.
2 Y. Xu and T. a. Enomae, *RSC Adv.*, 2014, **4**, 12867.
3 M. Daun, PhD thesis, Technical University Darmstadt, 2006.
4 A. Krolle and W. Bauer, *12th TAPPI Adv. Coat. Fundam. Symp. Sept. 10-12, 2012*, Atlanta, GA USA, 2012.
5 J. Drelich, E. Chibowski, D. D. Meng and K. Terpilowski, *Soft Matter*, 2011, **7**, 9804.
6 Z. Ye, S. Li, C. Wang, R. Shen and W. Wen, *RSC Adv.*, 2016, **6**, 2774–2777.
7 L. Yang, J. Liu and X. Li, *J. Print Media Technol. Res.*, 2014, **48**, 269–273.
8 N. Sharma, MSc thesis, Miami University, 2005.
9 Y. J. Lee, J. J. Pawlak, O. Rojas and J. Skowronski, *Int. Pap. Phys. Conf.*, 2007, 143–148.
10 J. Schoelkopf, C. Ridgway, P. Gane, G. Matthews and D. Spielmann, *J. Colloid Interface Sci.*, 2000, **227**, 119–131.
11 T. Enomae, D. Ivutin and A. Isogai, *Appita Annu. Conf. Exhib.*, 2004, **2**, 577–588.
12 T. Enomae, H. Kataoka, F. Onabe, D. Papier and J. Robertson, *Sen'i Gakkaishi*, 2004, **55**, 265–291.
13 D. Kwok and A. Neumann, *Adv. Colloid Interface Sci.*, 1999, **81**, 167–249.
14 C. J. Ridgway, J. Schoelkopf, G. Matthews, P. A. Gane and P. W. James, *J. Colloid Interface Sci.*, 2001, **239**, 417–431.
15 H. B. Eral, D. J. C. M. t. Mannetje and J. M. Oh, *Colloid Polym. Sci.*, 2013, **291**, 247–260.

 

16 G. R. Willmott, C. Neto, S. C. Hendy and D. Schebarchov, *Soft Matter*, 2011, **7**, 2357–2363.
17 T. A. P. Van Stiphout, MSc thesis, Eindhoven University of Technology, 2016.
18 J. Schoelkopf, P. A. Gane, C. J. Ridgway and G. Matthews, *Colloids Surf., A*, 2002, **206**, 445–454.
19 L. Hanžič, L. Kosec and I. Anžel, *Cem. Concr. Compos.*, 2010, **32**, 84–91.
20 J. F. Oliver, E. D'Souza and R. E. Hayes, *2002 International Conference on Digital Printing Technologies*, 2002, pp. 505–508.
21 O. Amodie, *Process Prod. Qual. Conf. Trade Fair*, 1997, 59–65.
22 L. Yang, L. Jianghao and G. Lingya, *Fundam. Res. Symp.*, Cambridge, 2013, pp. 585–598.
23 M. G. Ventura, A. I. Paninho, A. V. M. Nunes, I. M. Fonseca, L. C. Branco and T. M. Aminabhavi, *RSC Adv.*, 2015, **5**, 107700–107706.
24 A. Barakat, C. Mayer-Laigle, A. Solhy, R. A. D. Arancon, H. de Vries, R. Luque, G. W. Choi, S. Rengpipat, L. Eurwilaichitr, Y. Honda and T. Watanabe, *RSC Adv.*, 2014, **4**, 48109–48127.
25 L. Roiban, G. Foray, Q. Rong, A. Perret, D. Ihiawakrim, K. Masenelli-Varlot, E. Maire, B. Yrieix, F. Fennessy, M. Sonka, J. Buatti, S. R. Aylward, J. V. Miller, S. Pieper and R. Kikinis, *RSC Adv.*, 2016, **6**, 10625–10632.
26 K. Sato, N. Ozaki, K. Nakanishi, Y. Sugahara, Y. Oaki, C. Salinas, S. Herrera, D. Kisailus and H. Imai, *RSC Adv.*, 2017, **7**, 13065–13071.
27 P. Resch, W. Bauer and U. Hirn, *Adv. Coat. Fundam. Symp.*, 2008, 58–72.
28 P. Resch, W. Bauer and U. Hirn, *Tappi*, 2010, 27–35.
29 A. Aghanouri and G. Sun, *RSC Adv.*, 2015, **5**, 1890–1892.
30 A. Hladnik, *Papier*, 1997, **25**, 44–48.
31 J. Schölkopf and P. A. C. Gane, *IPW*, 2004, 36–42.
32 V. Starov, S. Kosvintsev, V. Sobolev, M. Velarde and S. Zhdanov, *J. Colloid Interface Sci.*, 2002, **246**, 372–379.
33 B. Miller and I. Tyomkin, *J. Colloid Interface Sci.*, 1994, **162**, 163–170.
34 J. Andersson, A. Ström, T. Gebäck and A. Larsson, *Soft Matter*, 2017, **13**, 2562–2570.
35 M. Stange, *Dynamik von Kapillarströmungen in zylindrischen Rohren*, Cuvillier Verlag, Göttingen, 2004.
36 E. W. Washburn, *Phys. Rev.*, 1921, **17**, 273–283.
37 C. J. Ridgway and P. A. C. Gane, *Nord. Pulp Pap. Res. J.*, 2002, **17**, 119–129.
38 C. J. Ridgway, P. A. Gane and J. Schoelkopf, *J. Colloid Interface Sci.*, 2002, **252**, 373–382.
39 C. M. Bosanquet, *Philos. Mag.*, 1923, 525–531.
40 E. Fu, B. Lutz, P. Kauffman and P. Yager, *Lab Chip*, 2010, **10**, 918.
41 R. W. Rioux, PhD thesis, Beijing University of Chemical Technology, The University of Maine, 2003.
42 A. Marmur, *Adv. Colloid Interface Sci.*, 1992, **39**, 13–33.

# Chapter 6

# Publication II

RSC Advances

PAPER



Cite this: *RSC Adv.*, 2019, **9**, 31708

# The effect of viscosity and surface tension on inkjet printed picoliter dots†

Sarah Krainer,[ab] Chris Smit[bc] and Ulrich Hirn *[ab]

Received 2nd July 2019
Accepted 24th September 2019

DOI: 10.1039/c9ra04993b

rsc.li/rsc-advances

In this study, we investigated the effect of liquid viscosity and surface tension for inkjet printing on porous cellulose sheets. We used five model liquids, representing the operational field of an industrial high speed inkjet printer, as specified by Ohnesorge- and Reynolds number. Drops with 30 pl and 120 pl drop size were jetted with a commercial HSI printhead. We printed on four uncoated papers representing the most relevant grades on the market in terms of hydrophobisation and surface treatment. We are presenting a quantitative analysis of viscosity and surface tension on the print outcome, evaluating dot size, liquid penetration (print through) and surface coverage of the printed dots. The most important finding is that for liquids within the jetting window the variation of the liquid viscosity typically has a 2–3 times higher impact on the print outcome than variation of the liquid surface tension. Increased viscosity in all cases reduces dot area, liquid penetration and liquid surface coverage. Surface tension plays a smaller role for liquid spreading and penetration, except for hydrophobised substrates, where both are reduced for higher surface tension. Interestingly, higher surface tension consistently increases liquid surface coverage for all papers and drop sizes. A detailed analysis on the competing effect of dot spreading and liquid penetration is presented, in terms of viscosity, surface tension and surface coverage of the liquid.

## 1 Introduction

Inkjet printing on porous substrates covers a wide field of applications, from printing on paper[1,2] and other flexible substrates[3–5] to fields like metal patterning,[6–8] film creation for solar cells,[9,10] printing polymer solutions droplets[11,12] or hydrophobisation of surfaces.[13] When printing on porous substrates the resulting printing dot is affected by two competing processes, the spreading of the drop on the substrate, and the penetration of the drop into the substrate, hence both are relevant for inkjet printing.[14,15]

Capillary penetration of liquids is often taken as a model for liquid imbibition into porous sheets. The Lucas Washburn equation[16] and the Bosanquet equation[17] are commonly employed, where the latter is a generalization of the former. While the Lucas Washburn equation only considers capillary and viscous forces, the Bosanquet equation also takes inertial forces into account, a detailed analysis provides *e.g.* Schoelkopf.[18] However, the absolute experimental data reveal huge quantitative and also qualitative deviations from the calculated penetration.[19] Hence, there is ongoing refinement of these models, *e.g.* by introduction of modification factors,[20–22] like the dynamic contact angle.[23–25] Anyway, the pore system in sheet material like paper is much more complex in terms of geometry and interconnectivity than the circular tube geometry assumed for the above mentioned model equations. This is the reason why numerical simulation of pore flow is a highly relevant and increasingly important approach here.[26–29]

Analysis of drop spreading and penetration for inkjet printing is challenging due to several factors. First, the relevant drop size is in the low picoliter range, with a drop diameter around 24 μm. Yet it is common to use microliter drops[30,31] for analysis of contact angle and liquid penetration, a size scale larger by the factor $10^6$. Also evaporation plays a big role, due to the small inkjet drop size, it is limiting capillary penetration.[32] In high speed inkjet printing, a technology that is increasingly important for industrial printing, the ink setting on a porous media also happens very fast, usually within 30–100 milliseconds.[33] Capturing the relevant time- and size scale in the experimental investigations is very relevant, evaluating too large drops results in a gross oversupply on liquid on the sheet surface and in the sheet bulk, which results in unrealistic drop spreading and much too slow penetration.

Several investigations were addressing the influence of viscosity as well as surface tension on ink penetration and wetting, without capturing it quantitatively.[34,35] Here, viscosity and surface tension play a role in evaporation and penetration. An effective, increased viscosity of a water/glycerol mixture leads to a deviating penetration behaviour[34] and slows down the

[a]*Institute of Paper, Pulp and Fiber Technology, TU Graz, Inffeldgasse 23, 8010 Graz, Austria. E-mail: ulrich.hirn@tugraz.at; Tel: +43 316 87330753*

[b]*CD Laboratory for Fiber Swelling and Paper Performance, Inffeldgasse 23, 8010 Graz, Austria*

[c]*Océ, Van der Grintenstraat 1, 5914 HH, Venlo, Netherlands*

† Electronic supplementary information (ESI) available. See DOI: 10.1039/c9ra04993b

liquid flow.[35] Han and coworkers[36] found, that the higher the ratio of surface tension to viscosity is, the higher is the filling rate. The viscosity also plays a major role in the inertial selection of pores at the beginning of penetration[37,38] and during the surface wetting process.[18,39–41] Furthermore, Neogi *et al.*[42] showed that also the spreading rate of a liquid drop depends on the surface tension and viscosity.

Not only the liquid properties are responsible for wetting and penetration, but also the substrate. A lot of experimental research was done evaluating the influence of pore-size and the surface properties of liquid behaviour on cellulose material. The porous media bulk property (porosity and average pore size) plays a major role in penetration,[18,19,40,41,43] the bigger the initial pore diameter the stronger is the influence of inertia. Also the surface chemistry of the substrate has a large influence. Matching polarity of the liquid and the substrate as well as a high surface energy of the sheet material lead to stronger wetting, *i.e.* it promotes drop spreading and liquid penetration. Both of that is indicated by a lower contact angle between drop and sheet.[44]

Penetration of the color into the paper bulk reduces color density and increases print through. Hence in surface treatment for inkjet printing a common goal is to retain the coloring material on the surface, while it is necessary that ink vehicle penetrates to the paper bulk to immobilize the ink layer. This may be achieved by treating a paper surface with bivalent salts which breaks down the dispersion of pigment inks and leads to precipitation of the pigments on the surface.[45] Another approach for surface treatment is application of cationic material. This has been shown to decrease the ink penetration, but also reduces bleeding of an ink droplet.[1,46,47]

# 2 Aim of the work

As outlined in the introduction there are several important factors determining drop spreading and drop penetration in inkjet printing. Those are viscosity and surface tension of the liquid, pore system of the substrate, and the wetting behavior (contact angle) of the liquid on the substrate, which is defined by the interplay of cohesion forces in the liquid and its adhesion to the surface. The literature in the field has been addressing some of these influence factors. However, in order to draw valid conclusions for the inkjet printing process it is necessary that the research is

- considering the correct size scale, *i.e.* picoliter drops like in actual inkjet printing
- considering the correct time scale, *i.e.* setting of the liquid within the first second after drop impact
- considering liquids within the actual window of operation for inkjet printing
- considering relevant substrates.

While most of the work in the literature is considering one or maybe two of these requirements, a systematic study of the driving factors on inkjet print outcome under real process conditions is missing. This paper is aiming to fill some of that gap. It addresses the influence of liquid viscosity and surface tension on the print outcome for the industrial high speed inkjet (HSI) printing process. We are evaluating drop spreading, liquid penetration and light absorption of dots, the printing has been carried out on a test setup employing commercial high speed inkjet (HSI) printheads. We use drops in the relevant size scale, which is in the low picoliter range (30 pl and 120 pl), having liquid setting in the HSI printing time scale. This is a specific advantage of our approach in comparison to other state of the art measurement techniques. The printed liquids have been developed in such a way that viscosity and surface tension is varied as much as possible within the operating window of the printhead. As test substrates, we are using papers representing the most relevant paper grades in the market for uncoated inkjet printing papers. In this way we are able to quantify the influence of liquid surface tension and viscosity on the printing result for realistic inkjet conditions.

# 3 Materials and methods

## 3.1 HSI printhead and drop volume

For our print tests we employed a commercial inkjet print-head, like it is used in the Océ Varioprint i300 printer. It is a piezo-electric printhead, which shoots the drops on demand (Drop-on-demand method) and has a resolution of 600 dpi.[48] The model liquid drop size can be set up to a volume of 29 pl. The printhead employs frequencies of up to 30 kHz. In this work all printing tests have been carried out with 30 pl drops and 120 pl drops. We generate droplet volumes of 120 pl by shooting 4–6 droplets in a row, which coalesce to one drop before they impinge on the paper surface. For detailed information on drop volume please have a look in the ESI.†

**3.1.1 Operational field of the HSI printhead.** The Ohnesorge number (Oh), eqn (1), and the Reynolds number (Re), eqn (2), are dimensionless parameters, which can be used to indicate the jettability of a liquid. Those numbers set up the operational field of the printhead, see Fig. 1.[49,50] More information is available in the ESI.†

$$\mathrm{Oh} = \frac{\eta}{\sqrt{\gamma \rho l}} \tag{1}$$

$$\mathrm{Re} = \frac{\rho v l}{\eta} \tag{2}$$

The parameters, which have the main impact on the Oh are viscosity $\eta$ [Ns m$^{-2}$] and surface tension $\gamma$ [N m$^{-1}$] of the liquid. The density $\rho$ [kg m$^{-3}$] is roughly the same for all liquids, see Table 1, and the length $l$ [m] is the nozzle width (which is also the same for all liquids).

To take advantage of the whole operation window of the print head we tried to design liquids that possibly cover the entire printable fluid window in Fig. 1. For example, the upper-left corner has a Oh number of 1 and a Re number of 2, surface tension and viscosity of the testing liquid were chosen to best possibly obtain those values. The final testing liquids were at the very limit of (good) jet-ability, in terms of surface tension

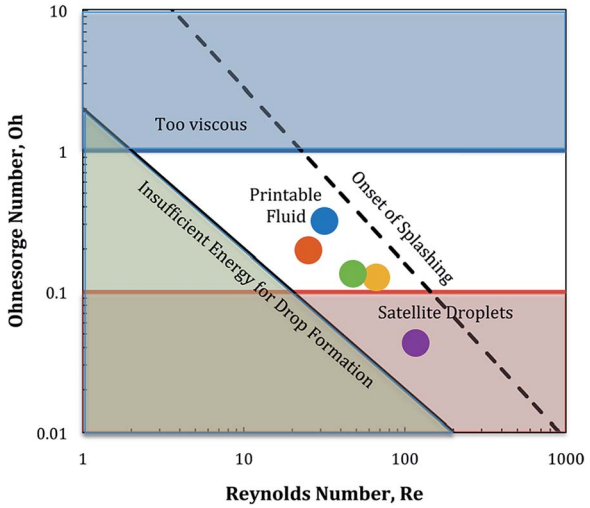


Fig. 1 Ohnesorge number plotted over Reynolds number, indicating the printable fluid window.[49] The dots indicate the position of the testing liquids used in this work.

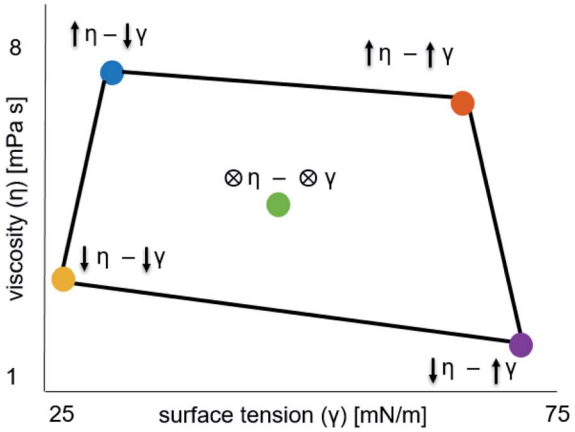


Fig. 2 The five testing liquids used in this work, with viscosity ($\eta$) plotted over surface tension ($\gamma$). In the labeling of the test points arrows are indicating low (↓) or high (↑) values. Printing of these liquids achieved stable jetting (no severe nozzle blocking, low drop splashing).

and viscosity, indicating that the actual jetting window (dots in Fig. 1) for the employed printhead is somewhat shifted from the region indicated in ref. 49.

### 3.2 Testing liquids

In order to find the actual operating window of the printhead the corner points of Fig. 1 were used as starting values. These fluids did not achieve stable jetting and showed the appearance of satellite drops and also severe nozzle blocking. Therefore an adjustment of the liquid composition, was necessary. This fine tuning was done iteratively by jetting new liquids with adapted properties followed by a visual evaluation of the printed pattern in terms of missing dots and dot splashing, done by the operator. Finally five water-based model liquids have been chosen with maximum range in viscosity and surface tension, while still having good jettability and dot quality. The dots in Fig. 1 and 2 show the actual operational window of the print-head.

Viscosity was measured at 25 °C with a Thermo Fisher Haake Rheostress 6000 instrument. The gap width was 0.5 mm, the sample amount was 2 ml and the shear rates were 10, 120, 230, 340, 450, 560, 670, 780, 890 and 1000 Hz.

Surface tension was measured at 25 °C with a Sita science line t60 tensiometer, which uses a bubble pressure method. The bubble lifetime was from 0.05 to 2 seconds. Liquid density was determined using a pyknometer with 25 $cm^3$ total volume.

The testing liquids were chosen to have a similar composition like HSI inks. These have water as a main component and also contain larger amounts of higher order alcohols.[51] We are using glycerine to adjust liquid viscosity and hexanediol to set the surface tension.[52] 0.1 weight percent of naphthol blue black (98%) were used to colour the model fluids, adding the dye, showed no impact on the liquid properties. It was found out by simple paper chromatography, that the dye travels with the liquid front into the porous media and does not separate from the liquid. Using the dye, drop spreading and penetration can be measured with image analysis. The composition of the liquids is summarized in Table 1.

### 3.3 Papers

There is a wide range of paper grades for inkjet printing available. We investigated four different wood free, fine papers from an industrial supplier, the paper properties are summarized in Table 2. The chosen substrates represent the commercially available papers in the digital printing paper market for office – and HSI papers. The papers' main component is industrial bleached hardwood pulp. The filler used in the papers is scalenohedral PCC (precipitated calcium carbonate).

• Paper. A plain paper only consisting of pulp and filler. It has no treatment and can be considered as the raw paper, which

Table 1 Testing liquids used in this study and their properties: viscosity ($\eta$), surface tension ($\gamma$) and density

| Liquid | Water [wt%] | Glycerin [wt%] | Hexanediol [wt%] | Dye [wt%] | Viscosity $\eta$ [mPa s] | Surface tension $\gamma$ [mN $m^{-1}$] | Density $\rho$ [kg $m^{-3}$] |
|---|---|---|---|---|---|---|---|
| High (↑) $\eta$–low (↓) $\gamma$ | 41.9 | 48 | 10 | 0.1 | 7.2 | 27.5 | 1.12 |
| Low (↓) $\eta$–low (↓) $\gamma$ | 64.9 | 25 | 10 | 0.1 | 3 | 26.8 | 1.06 |
| High (↑) $\eta$–high (↑) $\gamma$ | 42.4 | 57.5 | 0 | 0.1 | 7.99 | 67.6 | 1.14 |
| Low (↓) $\eta$–high (↑) $\gamma$ | 74.9 | 25 | 0 | 0.1 | 1.7 | 70.5 | 1.06 |
| Center (⊗) $\eta$–center (⊗) $\gamma$ | 53.4 | 45 | 1.5 | 0.1 | 4.23 | 43.5 | 1.12 |

Table 2 Properties of the papers used in this study

| Properties | Paper | Paper & primer | Paper & primer & pigments & starch | Hydrophobized paper & starch |
|---|---|---|---|---|
| HSI surface treatment (primer) [g m$^{-2}$] | 0 | 0 | ~0.25 | ~0.25 |
| Pigmentation [g m$^{-2}$] | 0 | 0 | 4 | 0 |
| Surface starch [g m$^{-2}$] | 0 | 0 | ~1 | ~1 |
| Hydrophobisation (AKD sizing) [kg t$^{-1}$] | 0 | 0 | 0 | 1 |
| Filler content [%] | 22 | 22 | 23 | 14 |
| Grammage [g m$^{-2}$] | 97.2 | 78.5 | 79.89 | 77.2 |
| Porosity [%] | 40.3 | 38.8 | 23.6 | 20.6 |
| Average pore diameter [μm] | 3.9 | 2.6 | 3.2 | 4.9 |
| Roughness [ml s$^{-1}$] | 321 | 50 | 78 | 191.5 |
| Dispersive surface energy [mJ m$^{-2}$] | 44 | 42 | 43 | 33 |
| Polar surface energy [mJ m$^{-2}$] | 27 | 23 | 22 | 0.1 |
| Total surface energy [mJ m$^{-2}$] | 71 | 65 | 65 | 33.1 |

is the base material for the following three commercial paper grades.

• Paper & primer. This paper has a layer of bivalent salt (=primer) on the surface. This causes faster precipitation of the ink pigments on the paper surface and minimises the travelling of the pigments into the paper bulk.

• Paper & primer & pigments & starch. This coated paper has a low surface pigmentation (4 g per m$^2$ per side) of starch and clay. It also has a primer on the surface for better ink setting and a starch layer.

• Hydrophobised paper & starch. The hydrophobised paper has a very low surface energy due to the AKD sizing (see Table 2). On the surface, starch was applied. In this article the words sized and hydrophobised are used as synonyms.

Grammage was measured according to EN ISO 536 and filler content using DIN 54370. The mean pore diameter and the porosity were evaluated with a mercury intrusion porosimetry, a common technique to characterize microscale pore size distributions.[53–55] We used an Autopore IV 9500 instrument from Micromeritics Instrument Corp.[56] The roughness was measured according to Bendtsen

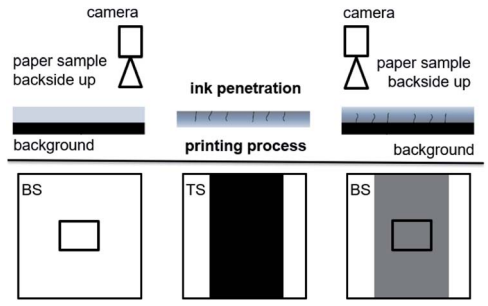


Fig. 3 Measurement principle of the print through test. An image of a 5 × 5 cm$^2$ area is taken of the backside (BS) of the paper. Then the print is applied on the topside (TS) of the paper. After printing, the exactly same 5 × 5 cm$^2$ area of the BS of the now printed sheet is imaged. The difference in gray value before and after printing is the print through.

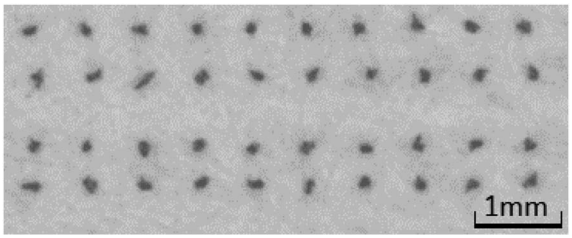


Fig. 4 Picture of the printed dot pattern. The variability of the drop area is generated by the heterogeneity of the paper.

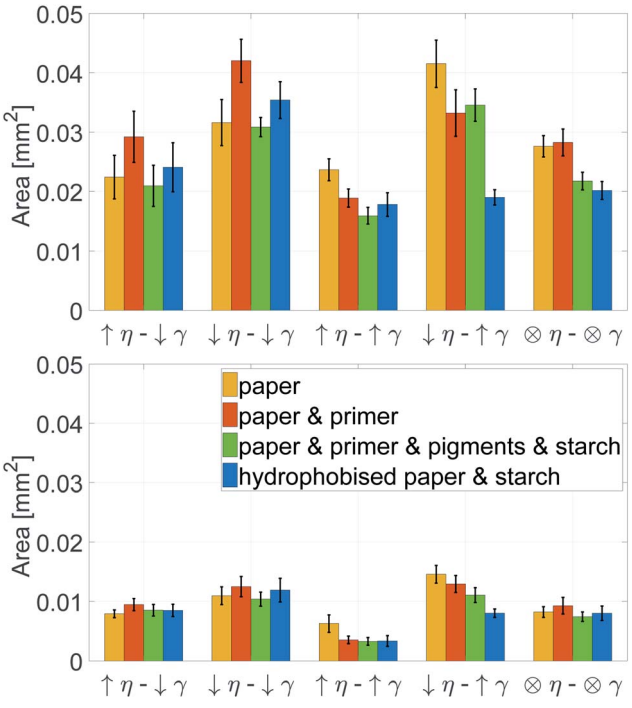


Fig. 5 Inkjet printed dot area for 120 pl (top) and 30 pl (bottom) drop size. A large dot area indicates more intense spreading of the liquid drop. The printing liquid has high (↑), medium (⊗) or low (↓) viscosity ($\eta$) and surface tension ($\gamma$) as described in Table 1. For details on the printing substrates see Table 2. Bars are 95% confidence limits. Low viscosity increases the spreading. Surface tension plays a minor role as long as the substrate is not hydrophobised. Here, low surface tension eases spreading.

method ISO 5636-3:2013. The surface energy was measured with a Kruess contact angle device applying the OWRK equation using diiodomethane and water.[57,58]

### 3.4 Print through test (PT)

The print through method is used to evaluate the print ink penetration into the paper. It measures the colour difference

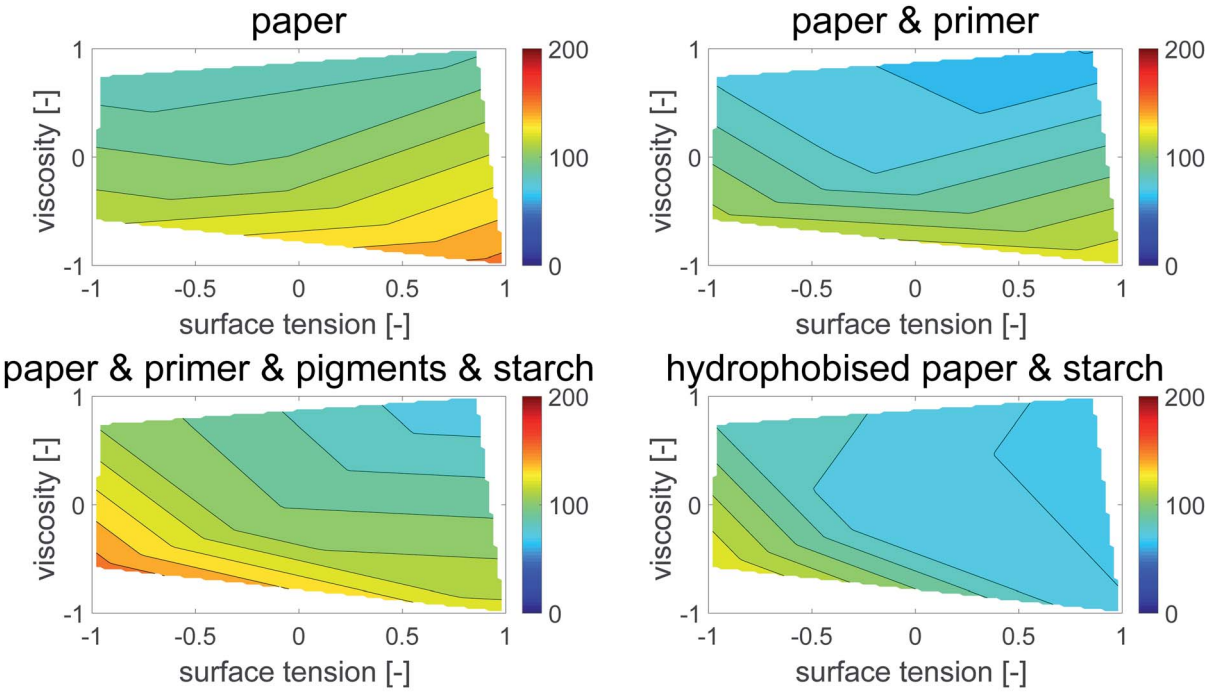


(a) 120pl

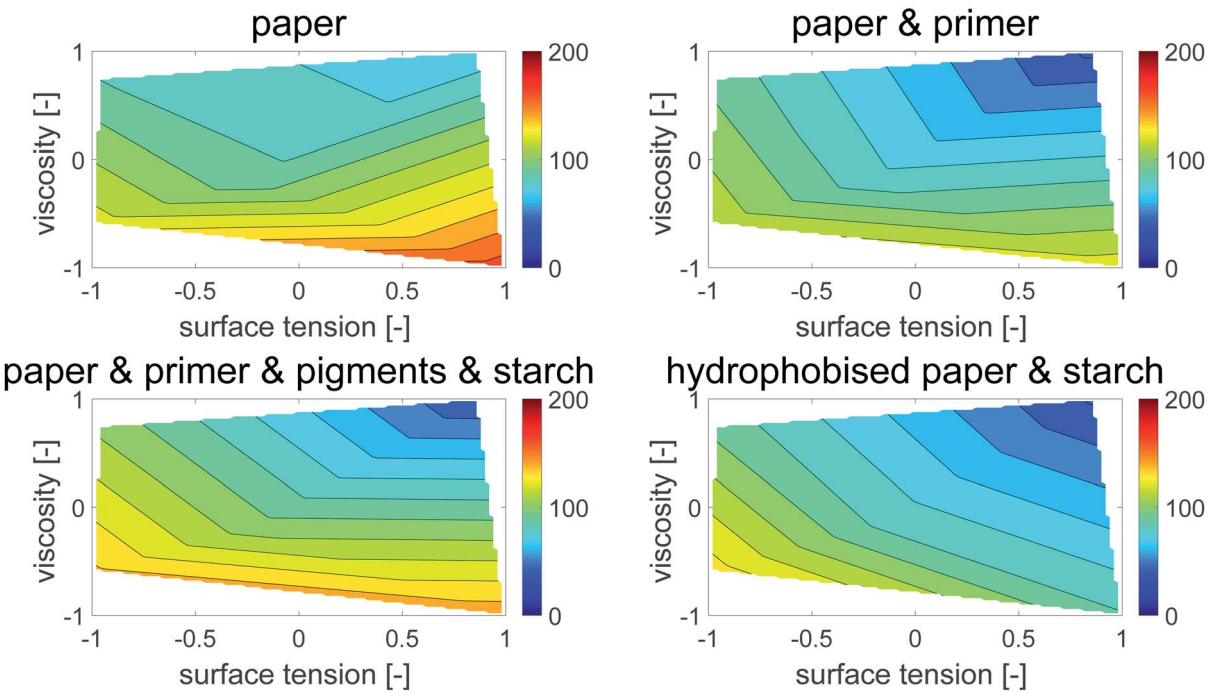


(b) 30pl

Fig. 6 Contour plots of printed dot area (in % of mean area per dot size) over dimensionless surface tension and viscosity. Each plot represents one of the papers from Table 2. The contour lines represent combinations of $\gamma$ and $\eta$ resulting in equivalent dot area. The almost horizontal lines illustrate a predominant impact of viscosity on the dot area. The surface tension effect plays a minor role except for the sized sheet (bottom, right), indicated by the changing slopes of the contour lines into a more vertical direction.

before and after printing on the backside of the paper, see Fig. 3. Before and after printing same area of the paper is investigated. The higher the difference, the higher the ink penetration into the paper. A more detailed description of this method can be found in the ESI. GV denotes the mean gray value [8 bit grayvalue] of the measurement area.

$$\mathrm{PT} = \frac{\mathrm{GV}_{\text{before printing}}}{\mathrm{GV}_{\text{after printing}}}[-] \quad (3)$$

### 3.5 Image analysis of printed dots

The ImageXpert set up uses an overhead camera with a manual stage for repeatable sample positioning.

Image analysis of the printed dots was carried out using the ImageXpert image analysis system. It records images of the print and provides fully automated digital image analysis of the printed dots. A picture of such a dot pattern can be seen in Fig. 4. For further information on image analysis and experimental error please read the ESI.† We used the parameters dot area ($A$), gray average (GA) and axis ratio (AR). Gray average GA is the mean gray value [8 bit GV] of the dot. The darker the drop, the lower is the gray average. The area of the droplet is a parameter for drop spreading. The second parameter analysed from the prints is the light absorption LA of the individual printing dots.

$$\mathrm{LA} = \Delta\mathrm{GA} \times A \text{ [8 bit grayvalue mm}^2\text{]} \quad (4)$$

We calculate the light absorption using the difference ΔGA between the (higher) gray average of the paper and the (lower) gray value of the dot, the unit of ΔGA is [8 bit grayvalue]. ΔGA is multiplied with the measured drop area $A$, which defines the unit of LA as [8 bit grayvalue mm$^2$]. Digital cameras are linear sensors, when the gamma value $\gamma$ of the camera is set to $\gamma = 1$. Hence ΔGA is linear proportional to the light remission of the dot, and $\mathrm{LA} = \Delta\mathrm{GA} \times A$ is the amount of light absorbed by the printed dot.

## 4 Results

### 4.1 Drop spreading and dot area

Fig. 5 shows the dot area for two drop sizes, 120 pl (top) and 30 pl (bottom). A larger dot area indicates more drop spreading. Generally, it can be observed that the results of 120 pl and 30 pl are very similar, indicating good repeatability and statistical significance of the measurements. The liquid, which exhibits low surface tension $\gamma$ and low viscosity $\eta$ shows the highest spreading. However, the fluid with high $\gamma$ and low $\eta$ also reveals high dot area, indicating that a low liquid viscosity is the relevant factor for drop spreading. Surface tension seems to play a much smaller role, except for the hydrophobised paper. The effect of viscosity and surface tension is much higher for the 30 pl drops, where the difference in drop size is 300% between the lowest and highest values, whereas for the 120 pl drops the maximum difference is 200%.

Contour plots were generated, where the dot area is plotted over surface tension ($x$-axis) and viscosity ($y$-axis), Fig. 6. Values between the 5 measurement points were interpolated linearly. All points with the same dot area are connected to a contour line, which represents the same dot area for different combinations of surface tension and viscosity. The impact of viscosity and surface tension on the dot area can be seen by the partial derivative (*i.e.* the slope) of the surface in $x$- and $y$-direction. A

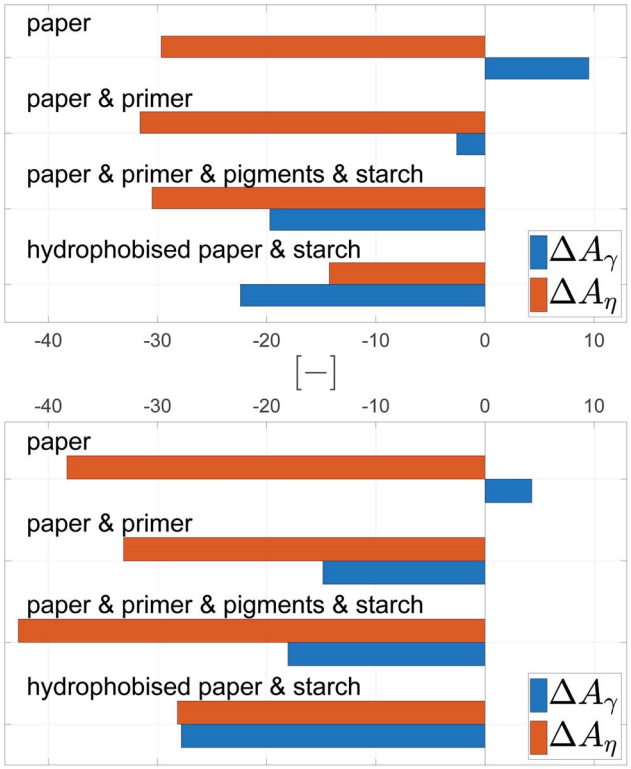


Fig. 7 Average effect of viscosity ($\Delta A_\eta$, orange bar) and surface tension ($\Delta A_\gamma$, blue bar) on printed dot area $A$ for 120 pl drops (top) and 30 pl drops (bottom). Positive values indicate an increase of the printed dot area for higher surface tension $\gamma$ and viscosity $\eta$ (negative values indicate a decrease), compare eqn (5) and (6).

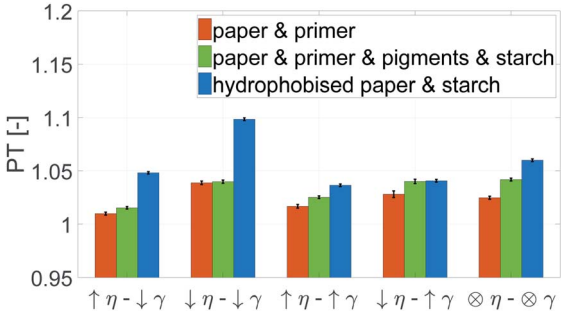


Fig. 8 Print through index PT of papers with the same grammage. A high value represents a strong penetration of the liquid into the paper. The liquid properties can be found in Table 1. Low viscosity $\eta$ increases the penetration. For the hydrophobised samples also low surface tension $\gamma$ favours strong imbibition into the paper.

high slope in $x$-direction indicates a high influence of surface tension, a high slope in $y$-direction indicates a high influence of viscosity. Also in this plot the main effect on dot area is liquid viscosity, represented by the almost horizontal contour lines. In Fig. 6 one can better see that for the hydrophobised sheets, surface tensions has a stronger influence, as indicated by the change of contour line slopes which are more tilted towards the $x$-axis.

In order to quantify the impact of surface tension and viscosity, we calculated the mean partial derivative, with respect to viscosity, eqn (5), and surface tension, eqn (6), for each point in the contour plots.

$$\Delta A_\eta = \frac{1}{n}\sum_{i=1}^{n}\frac{\partial \mathrm{Area}}{\partial \eta} \tag{5}$$

$$\Delta A_\gamma = \frac{1}{n}\sum_{i=1}^{n}\frac{\partial \mathrm{Area}}{\partial \gamma} \tag{6}$$

The mean of the partial derivatives is plotted in Fig. 7. As expected higher viscosity leads to lower dot area, indicated by the negative values. Surface tension reduces dot area, except for the plain paper, where it has a very small opposite effect. The change in viscosity has a stronger impact on the final dot area, than surface tension. This holds for both droplet sizes, except for the hydrophobised paper. Here, the surface tension plays a more important role than viscosity.

The values for surface tension and viscosity in Fig. 6 are mapped to a range from −1 to 1, representing the respective minimum/maximum values in the jetting window as shown in Fig. 2 and Table 1. The mean partial derivatives $\Delta A_\eta$ and $\Delta A_\gamma$ in eqn (5), (6) and Fig. 7 thus give the impact of surface tension and viscosity on dot area in terms of the variation possible within the jetting window. That means that *e.g.* a value of −30 for $\partial A/\partial \eta$ indicates a twice as high influence when changing viscosity from the center point to the maximum value than *e.g.* a value of −15 for $\partial A/\partial \gamma$ giving the influence of changing surface tension from the center point to the maximum value.

Three main findings for high speed inkjet printing can be derived from these results. First, viscosity has the main impact on final dot area of the printed drops, high viscosity causes low dot area. Second, surface tension plays a minor role except for liquids which are used for jetting on a hydrophobized substrate (sized paper). This reveals, that special focus needs to be put on surface tension, when printing on hydrophobised materials. Finally, the change of liquid property has an affect of up to a factor of 200% between the area of low and high surface tension and viscosity values. So by adjusting the liquid properties, a 2 times higher printed dot area can be achieved for 120 pl droplets. This effect gets even more pronounced for smaller droplets, for the 30 pl drops there is a factor of 300%.

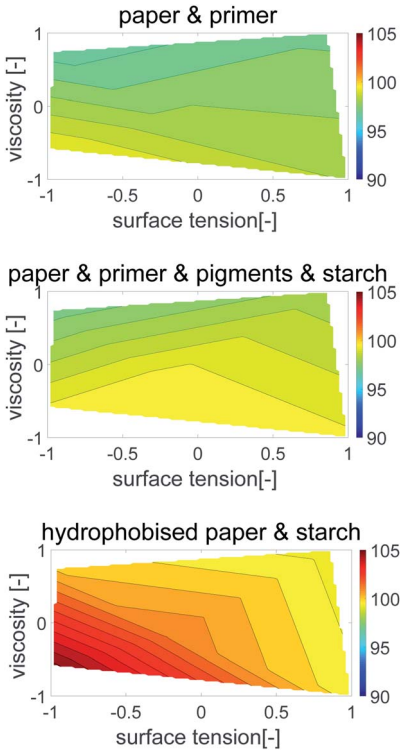


Fig. 9 Contour plots of print through value over surface tension $\gamma$ and viscosity $\eta$. Each plot illustrates one substrate from Table 2. The contour lines represent combinations of $\gamma$ and $\eta$ resulting in same print through. The horizontal lines show a strong influence of viscosity for the unsized papers. The sized sheets are influenced by both parameters, viscosity and surface tension (bottom), indicated by the changing slopes of the contour lines into a less horizontal direction.

### 4.2 Liquid penetration

The stronger the penetration into the paper, the higher is the print through (PT) value, as described in Section 3.4. Fig. 8 shows, that the liquids with low surface tension and low viscosity show the highest penetration. Especially for the hydrophobised paper, low surface tension causes a deep penetration of the liquid. The liquids with high viscosity have the smallest print through for all three substrates, indicating that low viscosity aggravates liquid penetration.

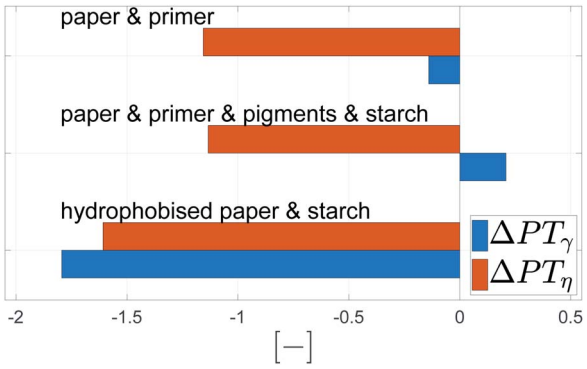


Fig. 10 Mean impact of viscosity ($\Delta PT_\eta$, orange bar) and surface tension ($\Delta PT_\gamma$, blue bar) on penetration into the paper. The bigger the bar, the stronger the influence of the represented property. Negative values show a decrease of the print through value for higher surface tension $\gamma$ and viscosity $\eta$ (positive values show an increase), compare eqn (8) and (7).

Again a contour plot was generated, now with liquid penetration over viscosity on the $y$-axis and surface tension on the $x$-axis, see Fig. 9. In a similar manner, like above, the mean partial derivative of print through $\Delta PT_\eta$ with respect to viscosity (eqn (7)) and $\Delta PT_\gamma$ with respect to surface tension (eqn (8)) was calculated from the contour plots

$$\Delta PT_\eta = \frac{1}{n}\sum_{i=1}^{n}\frac{\partial PT}{\partial \eta} \quad (7)$$

$$\Delta PT_\gamma = \frac{1}{n}\sum_{i=1}^{n}\frac{\partial PT}{\partial \gamma}. \quad (8)$$

The mean partial derivatives are plotted in Fig. 10, quantifying the influence of viscosity and surface tension change on the print through. The viscosity has a strong influence on penetration for all papers as indicated by the high slope in $y$-direction in the contour plots, Fig. 9. Low viscosity leads to high ink penetration, which is plausible. The impact of surface tension is inconsistent for the unsized papers, the contour lines are pointing upwards and downwards in these graphs, indicating a contradictive effect on liquid penetration. Consequently the mean partial derivative $\partial PT/\partial\gamma$ is low, as no systematic effect of surface tension can be found. The hydrophobised substrate shows a high impact from both parameters. Lower surface tension and lower viscosity cause an increase in penetration and thus a higher PT value.

In summary, for all substrates liquid penetration is strongly promoted by low viscosity. For hydrophobised papers, surface tension is equally important, low surface tension promotes liquid penetration.

### 4.3 Surface coverage

In order to evaluate surface coverage we measure light absorption (LA). LA of individual printing dots is calculated as the product of the area of the printed dot and the difference of the gray average (GA) between paper and printed dot, eqn (4). A high LA value corresponds to a darker colour and/or higher area of the dot. In this way LA provides information on the degree of liquid surface coverage, *i.e.* good liquid spreading with little liquid penetration.

The highest light absorption is obtained by liquids with low viscosity and high surface tension, see Fig. 11. This is valid for big and small droplet sizes. For the small drops high viscosity and high surface tension causes an extremely low light absorption. For light absorption, the substrate influence is of lower importance, the values are fairly similar for all investigated papers.

Also here contour plots were made, see Fig. 12. For all different paper treatments and the drop sizes the shape of the contour plots is similar, the lines are fairly horizontal,

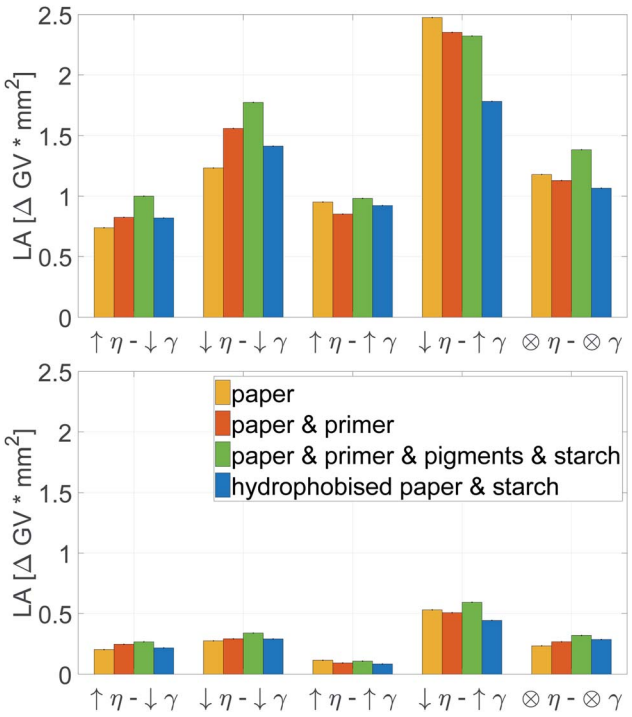


Fig. 11 Light absorption for 120 pl (top) and 30 pl (bottom) drop size. The printing liquid has high (↑) or low (↓) viscosity ($\eta$) and surface tension ($\gamma$) as described in Table 1. The ⊗ sign represents viscosity and surface tension value from the center point. For details on the printing substrates see Table 2. Bars are 95% confidence limits. The viscosity has a major impact on all substrates and droplet sizes. Low viscosity favors high LA.

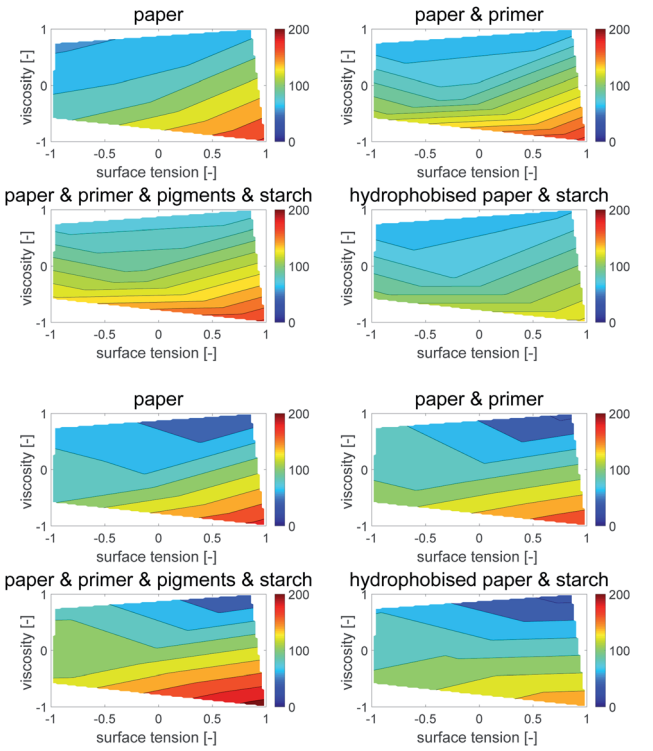


Fig. 12 Contour plots of light absorption over surface tension $\gamma$ and viscosity $\eta$. (120 pl dots top, 30 pl dots bottom) Each plot illustrates one of the papers from Table 2. The contour lines represent combinations of $\gamma$ and $\eta$ resulting in equivalent light absorption. The fairly horizontal lines show a strong impact of viscosity on the light absorption.

indicating the predominant influence of viscosity on dot light absorption. Again the mean partial derivatives with respect to viscosity (eqn (9)) and surface tension (eqn (10)) of the data points in the contour plots were computed.

$$\Delta \mathrm{LA}_{\eta} = \frac{1}{n}\sum_{i=1}^{n}\frac{\partial \mathrm{LA}}{\partial \eta} \tag{9}$$

$$\Delta \mathrm{LA}_{\gamma} = \frac{1}{n}\sum_{i=1}^{n}\frac{\partial \mathrm{LA}}{\partial \gamma} \tag{10}$$

Fig. 13 gives the mean values $\Delta \mathrm{LA}_{\eta}$ and $\Delta \mathrm{LA}_{\gamma}$, quantifying the impact of viscosity and surface tension on dot light absorption. All substrates show the predominant influence of the viscosity, Fig. 13, $\Delta \mathrm{LA}_{\eta}$ is at least by the factor 3 higher than $\Delta \mathrm{LA}_{\gamma}$. However, the surface tension still has an impact on the light absorption, especially for the bigger droplet size. A decrease of viscosity causes an increase of light absorption, whereas an increase in surface tension results in a light absorption increase. This observations hold for all four substrates, irrespective of the surface treatment of the paper.

For increasing color density in low and medium printing tone values in HSI printing reduction of liquid viscosity (and to a lower extent increase of liquid surface tension) is a promising strategy. In order to develop the full tone density, however our results suggest to increase viscosity, and for sized papers also increase surface tension, as this will reduce liquid penetration. In terms of print gamut, our results suggest that liquid viscosity governs a tradeoff between higher gamut in the light and middle tones (low viscosity) and higher gamut in the full tones (high viscosity).

In summary, the liquid surface coverage (light absorption) is mainly influenced by viscosity, to some extent surface tension is also relevant, especially for larger drops. Higher LA is achieved by reducing viscosity and increasing surface tension. The substrate plays a minor role, especially for small droplets. It is remarkable that, irrespective of surface treatment (hydrophobisation – paper sizing, pigmentation and inkjet surface treatment with salt) the effect of viscosity on dot light absorption is stable and nearly equally strong.

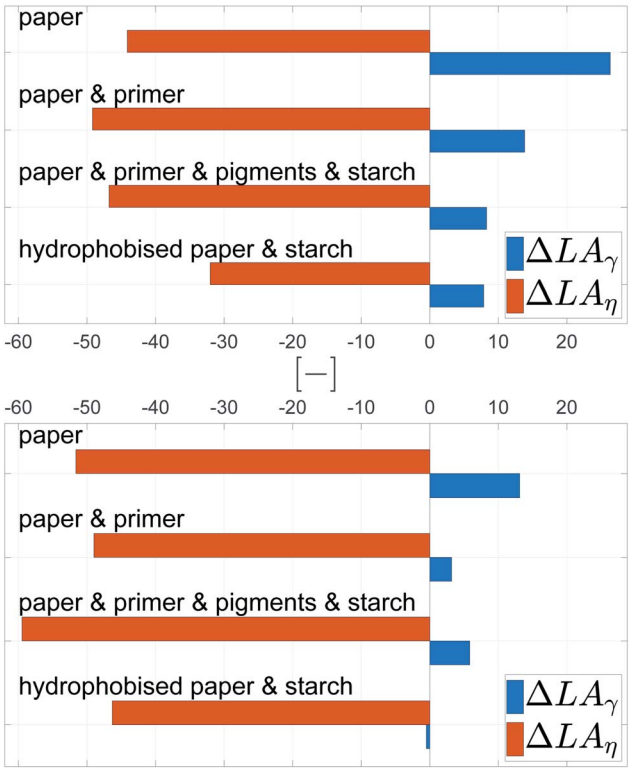


Fig. 13 Average influence of viscosity $\Delta \mathrm{LA}_{\eta}$ and surface tension $\Delta \mathrm{LA}_{\gamma}$ on the light absorption for 120 pl (top) and 30 pl (bottom) drops. Light absorption is a measure for good surface coverage. The positive values for $\Delta \mathrm{LA}_{\gamma}$ indicate a moderate increase of dot light absorption for higher surface tension $\gamma$, especially for the larger drops. The negative values for $\Delta \mathrm{LA}_{\eta}$ demonstrate a considerable negative impact of viscosity on dot light absorption.

# 5 Conclusions

In the current work we have investigated the influence of liquid- and substrate properties on high speed inkjet printing outcome. We have chosen representative process conditions within the inkjet operating window in terms of picoliter drop size, liquid surface tension and viscosity.

Three main characteristics of the resulting inkjet printing have been analyzed: drop spreading on the surface (dot area), liquid penetration (print through) and the surface coverage of the individual printing dots, measured by light absorption.

## 5.1 Drop spreading

Altogether, the measured dot area showed that for both picoliter droplet sizes, the viscosity is the main impact factor. Lower viscosity results in higher spreading and thus a larger dot area. Only for the hydrophobised substrate (sized paper), the surface tension has a considerable influence. Here, the decrease of surface tension causes an increase in spreading.

## 5.2 Liquid penetration

The print through shows a strong dependence on viscosity, except for the hydrophobised sample which, again, is heavily influenced by surface tension. Similar to dot spreading, high viscosity causes low penetration of the liquid.

## 5.3 Surface coverage

Surface coverage is the combination of good liquid spreading with little liquid penetration into the substrate, we measured it with light absorption. Again viscosity turned out to be most important, it reduces the surface coverage. However, also a decrease in surface tension was found to cause a decrease in surface coverage. These findings are equivalent for all four substrates and for all drop sizes, however the influence of surface tension is less for smaller drops.

The surface coverage (light absorption) is a result of two competing processes, dot spreading and liquid penetration. As shown above both of these factors are promoted by the same

 

liquid properties, mostly low viscosity but also low surface tension. Considering that low viscosity is also the driving factor for surface coverage of the printed dot it becomes clear, that the increase in dot spreading is clearly dominating over the increase in liquid penetration for the investigated dot sizes. That means that in order to obtain a good surface coverage in an inkjet printing process on porous substrates, reducing the viscosity and increasing the surface tension is a promising strategy. These findings can also be transferred to other inkjet applications on porous surfaces like printed electronics,[9] patterning of microfluidic sensors,[59,60] or membrane functionalisation.[61]

### 5.4 Surface tension and viscosity

We would like to point out, that our results provide a quantitative analysis of viscosity and surface tension impact on HSI print. The most important general finding here is that for liquids within the jetting window the variation of the liquid viscosity typically has a 2–3 times higher impact on the print outcome than variation of the liquid surface tension. Viscosity in all cases reduces dot area, liquid penetration and dot surface coverage. Surface tension significantly reduces dot spreading and liquid penetration of hydrophobised substrates, however it consistently increases dot surface coverage for all papers and drop sizes.

## Conflicts of interest

There are no conflicts to declare.

## Acknowledgements

The financial support by the Austrian Federal Ministry for Digital and Economic Affairs and the National Foundation for Research Technology and Development is gratefully acknowledged. Furthermore the authors want to thank Océ, Mondi, Kelheim Fibres and SIG Combibloc for their financial support. Special thanks to Pim du Buf for his support during the printing trials.

## Notes and references

1 T. Lamminmäki, J. Kettle, P. Puukko, C. Ridgway and P. Gane, Short timescale inkjet ink component diffusion: An active part of the absorption mechanism into inkjet coatings, *J. Colloid Interface Sci.*, 2012, **365**(1), 222–235.
2 J. Kettle, T. Lamminmäki and P. Gane, A review of modified surfaces for high speed inkjet coating, *Surf. Coat. Technol.*, 2010, **204**(12–13), 2103–2109.
3 R. Singh, E. Singh and N. Hari Singh, Inkjet printed nanomaterial based flexible radio frequency identification (rfid) tag sensors for the internet of nano things, *RSC Adv.*, 2017, **7**, 48597–48630.
4 K. E. Belsey, A. V. S. Parry, C. V. Rumens, M. A. Ziai, S. G. Yeates, J. C. Batchelor and S. J. Holder, Switchable disposable passive rfid vapour sensors from inkjet printed electronic components integrated with pdms as a stimulus responsive material, *J. Mater. Chem. C*, 2017, **5**, 3167–3175.
5 K. Venkata, *et al.*, Conductive silver inks and their applications in printed and flexible electronics, *RSC Adv.*, 2015, **5**, 77760–77790.
6 H. Ning, R. Tao, Z. Fang, W. Cai, J. Chen, Y. Zhou, Z. Zhu, Z. Zheng, R. Yao, M. Xu, L. Wang, L. Lan and J. Peng, Direct patterning of silver electrodes with 2.4 μm channel length by piezoelectric inkjet printing, *J. Colloid Interface Sci.*, 2017, **487**, 68–72.
7 N. Zhang, *et al.*, Tannic acid stabilized silver nanoparticles for inkjet printing of conductive flexible electronics, *RSC Adv.*, 2016, **6**, 83720–83729.
8 Y. Farraj, M. Bielmann and S. Magdassi, Inkjet printing and rapid ebeam sintering enable formation of highly conductive patterns in roll to roll process, *RSC Adv.*, 2017, **7**, 15463–15467.
9 I. Bernacka-Wojcik, P. Wojcik, H. Aguas, E. Fortunato and R. Martins, Inkjet printed highly porous $TiO_2$ films for improved electrical properties of photoanode, *J. Colloid Interface Sci.*, 2016, **465**, 208–214.
10 Y. Sun and Y. Zhang, Solvent inkjet printing process for the fabrication of polymer solar cells, *RSC Adv.*, 2013, **3**, 11925–11934.
11 R. K. Holman, M. J. Cima, S. A. Uhland and E. Sachs, Spreading and Infiltration of Inkjet-Printed Polymer Solution Droplets on a Porous Substrate, *J. Colloid Interface Sci.*, 2002, **249**(2), 432–440.
12 Y. Lin and C. Liu, Improved performances of inkjet-printed poly(3-hexylthiophene) organic thin-film transistors by inserting an ionic self-assembled monolayer, *RSC Adv.*, 2016, **6**, 40970–40974.
13 J. Sun, *et al.*, Facile fabrication of a superhydrophilic–superhydrophobic patterned surface by inkjet printing a sacrificial layer on a superhydrophilic surface, *RSC Adv.*, 2016, **6**, 31470–31475.
14 H. Zhou, R. Chang, E. Reichmanis and Y. Song, Wetting of Inkjet Polymer Droplets on Porous Alumina Substrates, *Langmuir*, 2017, **33**(1), 130–137.
15 A. Lundberg, J. Örtegren, E. Alfthan and G. Ström, Paper-ink interactions: Microscale droplet absorption into paper for inkjet printing, *Nord. Pulp Pap. Res. J.*, 2011, **26**(1), 142–150.
16 E. W. Washburn, The Dynamics of Capillary Flow, *Phys. Rev.*, 1921, **17**(3), 273–283.
17 C. Bosanquet, On the Flow of Liquids into Capillary Tubes, *Philos. Mag.*, 1923, **45**(S6), 525.
18 J. Schoelkopf, P. A. C. Gane, C. J. Ridgway and G. P. Matthews, Practical observation of deviation from Lucas-Washburn scaling in porous media, *Colloids Surf., A*, 2002, **206**(1–3), 445–454.
19 J. Andersson, A. Ström, T. Gebäck and A. Larsson, Dynamics of capillary transport in semi-solid channels, *Soft Matter*, 2017, **13**(14), 2562–2570.
20 R. L. Hoffman, A study of the advancing interface: II. Theoretical prediction of the dynamic contact angle in liquid-gas systems, *J. Colloid Interface Sci.*, 1983, **94**(2), 470–486.

21 T. Jiang, O. H. Soo-Gun and J. C. Slattery, Correlation for dynamic contact angle, *J. Colloid Interface Sci.*, 1979, **69**(1), 74–77.

22 E. Rillaerts and P. Joos, The Dynamic contact angle, *Chem. Eng. Sci.*, 1980, **35**(4), 883–887.

23 A. Hamraoui, K. Thuresson, T. Nylander and V. Yaminsky, Can a Dynamic Contact Angle Be Understood in Terms of a Friction Coefficient?, *J. Colloid Interface Sci.*, 2000, **226**(2), 199–204.

24 M. Heshmati and M. Piri, Experimental Investigation of Dynamic Contact Angle and Capillary Rise in Tubes with Circular and Noncircular Cross Sections, *Langmuir*, 2014, **30**(47), 14151–14162.

25 M. Hilpert, Effects of dynamic contact angle on liquid infiltration into inclined capillary tubes: (Semi)-analytical solutions, *J. Colloid Interface Sci.*, 2009, **337**(1), 138–144.

26 D. Siregar, J. Kuerten and C. van der Geld, Numerical simulation of the drying of inkjet-printed droplets, *J. Colloid Interface Sci.*, 2013, **392**, 388–395.

27 N. Karami, M. H. Rahimian and M. Farhadzadeh, Numerical simulation of droplet evaporation on a hot surface near Leidenfrost regime using multiphase lattice Boltzmann method, *Appl. Math. Comput.*, 2017, **312**, 91–108.

28 C. Diddens, Detailed finite element method modeling of evaporating multi-component droplets, *J. Comput. Phys.*, 2017, **340**, 670–687.

29 S. Jaganathan, H. V. Tafreshi and B. Pourdeyhimi, A realistic modeling of fluid infiltration in thin fibrous sheets, *J. Appl. Phys.*, 2009, **105**(11), 113522.

30 K. Mielonen, S. Ovaska, T. Laukala and K. Backfolk, Three-Layered Polyelectrolyte Structures as Inkjet Receptive Coatings: Part 2. Interaction With Pigment-based Inks, *J. Imaging Sci. Technol.*, 2016, **60**(3), 1–9.

31 K. Mielonen, P. l. Geydt, M. Österberg, L. S. Johansson, K. Backfolk, S. Ovaska and T. Laukala, Inkjet ink spreading on polyelectrolyte multilayers deposited on pigment coated paper, *J. Colloid Interface Sci.*, 2015, **438**(3), 179–190.

32 M. Liu, J. Wu, Y. Gan, D. A. H. Hanaor and C. Q. Chen, Evaporation limited radial capillary penetration in porous media, *Langmuir*, 2016, **32**(38), 9899–9904.

33 K. L. Yip, A. R. Lubinsky, D. R. Perchak and K. C. Ng, Measurement and Modeling of Drop Absorption Time for Various Ink-Receiver Systems, *J. Imaging Sci. Technol.*, 2003, **47**(5), 378–393.

34 M. O'Loughlin, K. Wilk, C. Priest, J. Ralston and M. Popescu, Capillary rise dynamics of aqueous glycerol solutions in glass capillaries: A critical examination of the Washburn equation, *J. Colloid Interface Sci.*, 2013, **411**, 257–264.

35 L. Yang, J. Liu and X. Li, Dynamics of ink absorption of packaging paper, *Journal of Print and Media Technology Research*, 2014, **48**(4), 269–273.

36 A. Han, G. Mondin, N. G. Hegelbach, N. F. de Rooij and U. Staufer, Filling kinetics of liquids in nanochannels as narrow as 27 nm by capillary force, *J. Colloid Interface Sci.*, 2006, **293**(1), 151–157.

37 L. R. Fisher and P. D. Lark, An experimental study of the washburn equation for liquid flow in very fine capillaries, *J. Colloid Interface Sci.*, 1979, **69**(3), 486–492.

38 L. Hanžič, L. Kosec and I. Anžel, Capillary absorption in concrete and the Lucas-Washburn equation, *Cem. Concr. Compos.*, 2010, **32**(1), 84–91.

39 S. M. Kumar and A. P. Deshpande, Dynamics of drop spreading on fibrous porous media, *Colloids Surf., A*, 2006, **277**(1–3), 157–163.

40 C. J. Ridgway and P. A. C. Gane, Dynamic absorption into simulated porous structures, *Colloids Surf., A*, 2002, **206**, 217–239.

41 C. J. Ridgway, P. A. C. Gane and J. Schoelkopf, Effect of Capillary Element Aspect Ratio on the Dynamic Imbibition within Porous Networks, *J. Colloid Interface Sci.*, 2002, **252**(2), 373–382.

42 P. Neogi and C. Miller, Spreading kinetics of a drop on a rough solid surface, *J. Colloid Interface Sci.*, 1983, **92**(2), 338–349.

43 C. Kappel, U. Hirn, M. Donoser and W. Bauer, Measurement of Printing Ink Penetration in Uncoated Papers and Its Influence on Print Quality, *94th Annual Meeting*, Pulp and Paper Technical Association of Canada, 2008, pp. 539–542.

44 J. Restolho, J. L. Mata and B. Saramago, On the interfacial behavior of ionic liquids: Surface tensions and contact angles, *J. Colloid Interface Sci.*, 2009, **340**(1), 82–86.

45 G. Wypych, Typical Primer Formulations and Applications to Different Substrates, in *Handbook of Adhesion Promoters*, ChemTec Publishing, 2018, pp. 77–91.

46 T. Lamminmäki, J. Kettle and P. Gane, Absorption and adsorption of dye-based inkjet inks by coating layer components and the implications for print quality, *Colloids Surf., A*, 2011, **380**(1–3), 79–88.

47 K. Mielonen, P. l. Geydt, C. l. Tåg and K. Backfolk, Inkjet ink spreading, absorption and adhesion on substrates coated with thin layers of cationic polyelectrolytes, *Nord. Pulp Pap. Res. J.*, 2015, **30**(2), 179–188.

48 D. Zwang, *Production Inkjet—The Next Wave: Canon Océ VarioPrint i300 Sheetfed Inkjet Press and More - WhatTheyThink*, http://whattheythink.com/articles/72603–production, 05.04.2019.

49 G. H. McKinley and M. Renardy. Wolfgang von Ohnesorge, *Phys. Fluids*, 2011, **23**, 127101.

50 W. Ohnesorge, Formation of Drops by Nozzles and the Breakup of Liquid Jets, *Appl. Math. Mech.*, 1936, **16**, 355–358.

51 C. Schmid, Formulation and Properties of Waterborne Inkjet Inks, in *The Chemistry of Inkjet Inks*, ed. Shlomo Magdassi, World Scientific Publishing Co. Pte. Ltd., 2010, pp. 123–140.

52 K. Sarah and H. Ulrich, Short timescale wetting and penetration on porous sheets measured with ultrasound, direct absorption and contact angle, *RSC Adv.*, 2018, **8**(23), 12861–12869.

53 M. G. Ventura, A. I. Paninho, A. V. M. Nunes, I. M. Fonseca and L. C. Branco, Biocompatible locust bean gum mesoporous matrices prepared by ionic liquids and a scCO 2 sustainable system, *RSC Adv.*, 2015, **5**(130), 107700–107706.


 

54 A. Barakat, C. Mayer-Laigle, A. Solhy, R. A. D. Arancon, H. de Vries and R. Luque, Mechanical pretreatments of lignocellulosic biomass: towards facile and environmentally sound technologies for biofuels production, *RSC Adv.*, 2014, **4**(89), 48109–48127.
55 L. Roiban, G. Foray, Q. Rong, A. Perret, I. Dris, K. Masenelli-Varlot, E. Maire and B. Yrieix, Advanced three dimensional characterization of silica-based ultraporous materials, *RSC Adv.*, 2016, **6**(13), 10625–10632.
56 P. Resch, W. Bauer and U. Hirn, Calendering effects on coating pore structure and ink setting behavior, *Tappi J.*, 2010, **9**(1), 27–35.
57 D. K. Owens and R. C. Wendt, Estimation of the surface free energy of polymers, *J. Appl. Polym. Sci.*, 1969, **13**(8), 1741–1747.
58 Y. Luo, Y. Zhao, Y. Duan and S. Du, Surface and wettability property analysis of CCF300 carbon fibers with different sizing or without sizing, *Mater. Des.*, 2011, **32**(2), 941–946.
59 R. Koivunen, E. Jutila, R. Bollström and P. Gane, Hydrophobic patterning of functional porous pigment coatings by inkjet printing, *Microfluid. Nanofluid.*, 2016, **20**(6), 83.
60 X. Li, J. Tian, G. Garnier and W. Shen, Fabrication of paper-based microfluidic sensors by printing, *Colloids Surf., B*, 2010, **76**(2), 564–570.
61 Y. Chen, P. Gao, M. J. Summe, W. A. Phillip and N. Wei, Biocatalytic membranes prepared by inkjet printing functionalized yeast cells onto microfiltration substrates, *J. Membr. Sci.*, 2018, **550**, 91–100.

# Chapter 7

# Manuscript III

Sarah Krainer,[a‡] Louis Saes,[b] and Ulrich Hirn*[a‡]

# Predicting Inkjet Dot Spreading and Print Through from Liquid Penetration- and Picoliter Contact Angle Measurement †

In this study we have evaluated the suitability of laboratory testing methods to predict inkjet printing results. We have developed and used testing liquids that are spanning the operational window of industrial High Speed Inkjet (HSI) printers while still covering the maximum possible range of viscosity and surface tension. First we correlated liquid penetration measured with ultrasound (ULP) and direct absorption (ASA) to print through from HSI prints. The best correlation ($R^2 \approx 0.7$ ) was found for the sized paper. For papers with increasing liquid penetration speed we found a decreasing ability of both testing methods to predict print through, for the strong absorbing paper the correlation drops to $R^2 \approx 0.2$. Second we correlated contact angle and drop diameter to the dot area from HSI prints. Contact angle turned out to be a better predictor for printed dot area than drop diameter. Evaluating the change in contact angle over time we found the highest correlation to the dot area in the print when measuring the contact angle as soon as possible, in our case 1ms after deposition of the drop on the paper. We also compared contact angle with microliter drops to picoliter drops, which are in the size scale of the actual inkjet droplet. To our great surprise correlations for microliter drops were equal or better than for picoliter drops, particularly for highly absorbing papers. Thus in order to predict dot spreading on paper our results suggest to measure the contact angle with microliter drops. Overall we found that, using laboratory testing methods, print through and dot spreading for HSI printing can be quite well predicted for slow absorbing papers but not very well for fast absorbing papers.

**Keywords:** inkjet, paper, wetting, penetration, contact angle, ultrasonic liquid penetration

## 1 Introduction

The relevance of High Speed Inkjet (HSI) printing is rapidly growing in the publishing industry. While the overall printing market is declining, the HSI sector is expanding [1–4]. The method combines the advantages of digital printing, e.g. no print form and flexible change of the print subject, with increasing print speed [2,3,5]. Preferred applications thus are products that are time critical or require only a small amount of copies. With higher printing speed increasingly large print runs are becoming profitable, making HSI a more and more relevant printing technique.

HSI is a non-contact printing method [5]. Industrial production of droplets is achieved using the drop on demand method (DOD). Here, droplets are created only when actually printing a dot on the paper, as opposed to continuous inkjet where a permanent stream of drops is created, but not all of them are deposited to the paper [1,6–8]. An ink droplet created by an HSI printhead has a typical volume between ∼1pl and ∼29pl depending on printer settings and printer design [9,10]. Once the droplet has been applied onto the paper surface, an ink setting time of 30-100ms is achieved [11], depending on the absorption

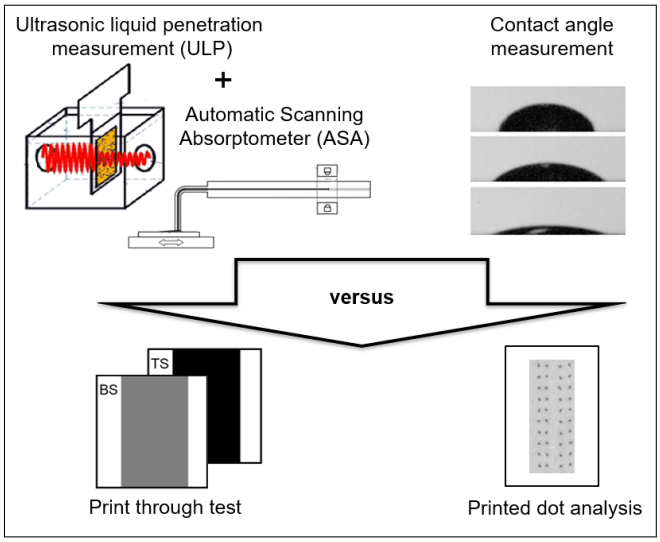


**Fig. 1** In this work we are predicting ink penetration (print through) and dot spreading (dot area) for industrial High Speed Inkjet (HSI) printing. First we are evaluating the ability of laboratory liquid penetration tests (ULP and ASA) to predict HSI print through. Second we are evaluating the ability of picoliter- and microliter contact angle measurements to predict spreading of HSI printing dots.

[a] *Institute of Paper, Pulp and Fiber Technology, TU Graz, Inffeldgasse 23, 8010 Graz, Austria; E-mail: ulrich.hirn@tugraz.at, phone:+43(316)87330753.*
[b] *Océ, Van der Grintenstraat 1, 5914 HH, Venlo, Netherlands.*
† Electronic Supplementary Information (ESI) available, see DOI: 00.0000/00000000.
‡ CD Laboratory for Fiber Swelling and Paper Performance, Inffeldgasse 23, 8010 Graz, Austria.

rate of the paper[6]. HSI print applications attain print velocities up to 300 meters per minute[1,10]. This requires fast ink drying to prevent smearing or ink transfer to the backside of other prints. Thus, rapid ink setting constitutes a fundamental necessity in HSI printing[10,12–16].

Generally it can be assumed that with faster liquid penetration, drop drying and ink setting will also be faster. This can be explained by faster transport of the ink solvent into the paper bulk[6,17]. Fast imbibition of the ink vehicle also leads to ink colourants travelling with the carrier liquid into the paper bulk. This usually deteriorates colour density in the full tones[18,19] and may lead to an increase in print mottle[10,13]. Another drawback of high penetration rates is low drop spreading due to rapid liquid absorption to the paper bulk. This reduces print quality by increasing print mottle and reducing colour density in the light tones[20,21]. Thus, good HSI print results require a well-tuned combination of liquid spreading and penetration, providing good ink setting and at the same time strong ink drop spreading on the surface while preventing excessive printing ink penetration[4,21–23].

A key paper treatment for inkjet printing is aiming to improve ink colourant fixation to the paper surface in order to prevent penetration of the dyestuff into the paper. For pigment inks a widespread approach is to apply a layer of bivalent salt on the paper surface. This treatment causes a destabilisation of the ink particle suspension, it leads to rapid agglomeration of the pigments on the paper surface[24,25]. For dye inks, cationic polymers applied to the paper surface are used to fixate the anionic dye molecules from the ink to the paper surface[12]. Both approaches also lead to a decrease in colour bleeding, in addition to the reduced ink penetration.

Inkjet printer developers seek for methods enabling to print faster using less ink. This leads to changes in HSI-printer design but also modifications of the inks[5,10]. One possibility for ink adjustment is adding latex particles to enhance the ink rub-off resistance on paper[6,26].

Changes in surface energy and polarity of both, paper and ink, are affecting surface wetting and liquid penetration. Consequently it is the *combination* of both factors that controls drop spreading and penetration[27,28]. Thus, for good runnability print quality modifications of ink or paper always require an adaption of the other component. As a consequence continuing, extensive print trials are performed to tune paper-ink combinations fulfilling the necessary quality requirements with respect to ink penetration and spreading.

Laboratory measurements are aiming to mimic the HSI printing process providing insights into relevant penetration and wetting behaviour. For example, ultrasonic liquid penetration testing captures the penetration of a liquid into the paper by measuring the change of ultrasonic intensity during fluid wetting and penetration into the substrate. Fast attenuation of the signal, reflected by a steep slope of the result curve, can be observed for papers with strong absorption[29,30]. Also direct liquid absorption measurements are often used to quantify fluid penetration into paper. Here liquid is applied to the paper via a nozzle for different contact times and the absorption rate is measured. The transferred liquid volume per area is plotted versus the contact time and provides information about liquid penetration behaviour[29,31,32]. Surface wetting is typically quantified by measuring the contact angle of a drop on the paper, where a high contact angle indicates bad wetting[29,33,34]. Mielonen et al.[20,35] investigated the impact of paper treatment on print outs printed with ink, analysing print density, mottling, bleeding and wicking of the printed sheets. The change of paper surface wettability was investigated by contact angle measurement with $\mu l$ droplets, using deionized water, ethylene glycol and diiodomethane. The measurement of the contact angle was done using different fluids than utilized for printing and printout analysis. Thus, the results capture the variation in liquid behaviour due to paper adjustment, but do not provide a quantitative comparison between contact angle and print results.

Our work provides a direct relation between print results and lab testing. First, we are investigating the direct correlation between liquid penetration speed and print through. Second, we are studying the correlation between contact angle measurements and dot spreading. In order to provide a direct relation to the printing process we designed testing liquids that are covering the jetting window for an industrial inkjet printhead. Those testing liquids are having a maximum variation in viscosity and surface tension, while still being jettable with an industrial HSI printer. It is the aim of the work to clarify how well the laboratory testing methods (liquid penetration and contact angle) can predict the actual inkjet print result (in terms of print through and dot area).

Figure 1 provides an overview of the printed analysis and the lab testing instruments. The printed dot area is measured to capture the drop spreading during the industrial process. Laboratory devices commonly use the contact angle of droplets in the $\mu l$ size scale to predict liquid wetting of HSI printed pl droplets, the actual inkjet printing droplets are smaller by a factor $10^6$ than $\mu l$ drops. We are utilizing both, picoliter and microliter drops, for contact angle measurement. We compare the contact angle of $2\mu l$ and $4\mu l$ as well as 30pl and 60pl drops to the dot area of HSI printed 30pl and 60pl dots. This experiment clarifies if contact angle measurements with picoliter drops can better predict HSI drop spreading than microliter drop contact angle measurements.

The investigation of liquid penetration during the industrial process is done by analyzing full-tone HSI printed sheets, evaluating the print through. The fluid imbibition using laboratory conditions is quantified utilizing ultrasonic liquid penetration measurements (ULP)[29,36,37] and a direct absorption measurement device (similar to the Bristow Wheel), called Automatic Scanning Absorptiometer (ASA). The outcome of the print through method is compared to the ULP and ASA result, providing information about the ability of laboratory measurements to forecast liquid penetration during the HSI printing.

In summary, our study investigates the applicability of laboratory methods to predict ink spreading and penetration during industrial HSI printing.

## 2 Materials and Methods

All contact angle, ultrasonic liquid penetration and direct imbibition measurements have been carried out in a climate room under defined temperature (23°C) and humidity (50% relative humidity). The substrates have been stored in the climate room at least 24 hours to reach equilibrium moisture content, as required by ISO 187:1990.

### 2.1 Papers and paper properties

The papers used in this study exhibit different bulk and surface modifications to capture the effects of paper treatments on liquid behaviour during HSI printing. The paper grades are representing the most relevant paper grades on the market for uncoated HSI printing papers. We use an all purpose office paper (AKD sized paper), an uncoated HSI paper (paper & primer) and a pigmented HSI paper (pigmented paper & primer). The fourth grade can be seen as the raw material of the others, it is an untreated and unsized office base paper. The absorption tendency of the papers varies, ranging from very strongly absorbing (plain paper) to hardly absorbing (AKD sized paper). All papers are made of fully bleached eucalyptus hardwood pulp. The filler is a scalenohedral precipitated calcium carbonate, it is the same type in all four papers. All papers have been produced in an industrial papermill.

- Plain paper. Plain office base paper made of pulp and filler, being the raw material of the other papers. It has the strongest absorption.
- Paper & primer. A layer of bivalents salts (=primer) is applied on the paper surface causing faster precipitation of ink-pigments. The layer thickness is approximately $\sim 0.25$ $g/m^2$. This reduces the colourant movement into the paper bulk resulting in a higher colour density[24,38]. This paper has neither internal nor surface sizing and fast liquid penetration can be observed.
- Pigmented paper & primer. This paper is slightly pigmented in a size press using a surface coating of $4\,g/m^2$ per side consisting of starch and clay for improved surface quality. Better ink setting is achieved applying $\sim 0.25$ $g/m^2$ of bivalent salt primer to the paper surface[24,38].
- AKD sized paper. The sizing of the paper causes hydrophobization and a reduction in the surface energy of the paper (see Table 1). Additionally size press surface starch is applied. The sizing results in the lowest liquid absorption of all evaluated papers.

A full summary of the relevant paper properties can be found in Table 1. Grammage was measured according to EN ISO 536, filler content according to DIN 54370. The porosity was determined via mercury porosimetry[39,40] using an Autopore IV 9500 from Micrometics Instruments, which is commonly used in the paper industry[41–43]. The roughness was evaluated using a Bendtsen tester following the ISO 8791-2:2013 standard. Surface energy was captured using Kruess contact angle measurement set-up, employing the OWRK equation and $4\mu l$ drops of diiodomethane and water[44,45]. The transferred water volume in Table 1 was quantified using the ASA direct absorption tester[29,32] which is described below.

### 2.2 Printing liquids and liquid properties

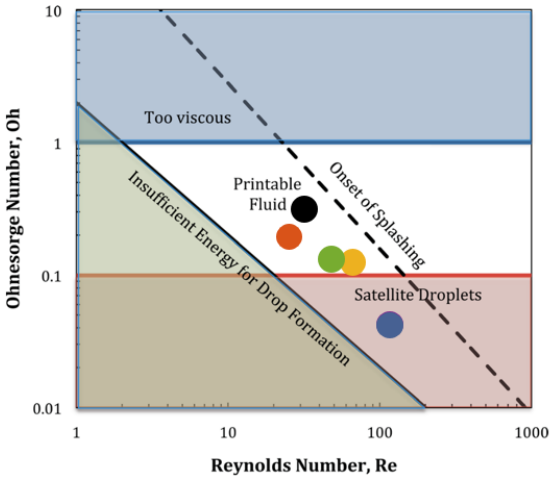


**Fig. 2** Ohnesorge Number versus Reynolds Number, representing the inkjet jettable fluid window[46]. The dots illustrate the position of the model liquids employed in this study[9].

We have been aiming to vary the liquid properties within the operational window of an industrial inkjet printer, Figure 2, which is defined by Ohnesorge and Reynolds Number to predict jettability of liquids[6,46,47]. The model liquids have highest possible variation in viscosity and surface tension, while still printable in an HSI printer. The liquids are based on deionized water, viscosity was adjusted by addition of glycerol and surface tension was tuned by adding hexanediol. To ease print analysis, naphthol blue black was added as a dye, travelling with the liquid front and facilitating print out evaluation. Simple paper chromatography showed that the dye travels with the liquid front into the paper. The corner points of Figure 2 were used as starting values for the development of the test fluids. However, these model liquids were not suitable for jetting in practice, showing drop splashing and missing dots. For this reason, further experimental liquid development with test prints utilising the print head was carried out. Finally, five water-based test fluids with maximum range in viscosity and surface tension have been selected, Figure 3, which have good jettability and high printing dot quality, Figure 4. For detailed description of liquid development, please refer to our earlier work[9]. A summary of the fluid properties can be found in Table 2 and Figure 3.

Liquid viscosities were obtained using a Thermo Fisher Haake Rheostress 6000, using a gap width of 0.5mm. The liquid volume was 2ml and the shear rates were 10, 120, 230, 340, 450, 560, 670, 780, 890 and 1000 Hz at 25°C. Surface tension was determined using a Sita Science Line T60 tensiometer, employ-

**Table 1** Properties of the four papers investigated in this study.

| | plain paper | paper & primer | pigmented paper & primer | AKD sized paper |
|---|---|---|---|---|
| primer (primer) $[g/m^2]$ | - | - | $\sim 0.25$ | $\sim 0.25$ |
| Pigmentation $[g/m^2]$ | - | - | 4 | - |
| Surface starch $[g/m^2]$ | - | - | $\sim 1$ | $\sim 1$ |
| Hydrophobisation (AKD sizing) $[kg/t]$ | - | - | - | 1 |
| Filler content [%] | 22 | 22 | 23 | 14 |
| Grammage $[g/m^2]$ | 97.2 | 78.5 | 79.89 | 77.2 |
| Porosity [%] | 40.3 | 38.8 | 23.6 | 20.6 |
| Average pore diameter $[\mu m]$ | 3.9 | 2.6 | 3.2 | 4.9 |
| Roughness $[ml/s]$ | 321 | 50 | 78 | 191.5 |
| Dispersive surface energy $[mJ/m^2]$ | 44 | 42 | 43 | 33 |
| Polar surface energy $[mJ/m^2]$ | 27 | 23 | 22 | 0.1 |
| Total surface energy $[mJ/m^2]$ | 71 | 65 | 65 | 33.1 |
| absorbed water volume $[ml/m^2 100ms]$ | 71 | 48 | 37.9 | 0.6 |

ing the bubble pressure method. The bubble lifetime lasted from 0.05 to 2 seconds. Liquid density was determined using a pycnometer, which had total volume of $25cm^3$.

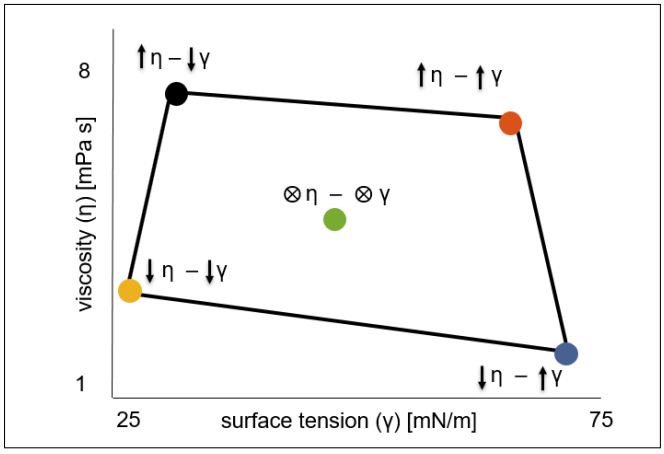


**Fig. 3** The five model fluids employed in this study, covering the maximum HSI jettable range in terms of viscosity ($\eta$) versus surface tension ($\gamma$). Low property values are indicated with an arrow pointing downwards (↓), high values with (↑)[9].

### 2.3 Measurement techniques

**Ultrasonic liquid penetration measurement (ULP)** is commonly used in the paper industry to measure liquid penetration[29,30]. For our experiments, an Emtec PDA 2.0 was used. The instrument measures the attenuation of ultrasound waves transmitted through the paper sample while liquid is penetrating into the paper. The faster the liquid penetration the faster is the change in the ultrasound transmittance. Ultrasound transmittance is recorded over time while the liquid penetrates into the paper, the slope of the recorded curve provides a value for the penetration rate. The faster the observed signal change, as reflected by the slope, the higher the penetration speed. The slope was calculated from the curve segment starting from the highest ultrasound intensity till the following 3s or to the end of the measurement time. For a detailed description of the measurement please refer to the electronic supplementary information (ESI) or to earlier publications[29].

The **Automatic Scanner Absorptometer(ASA)** is also utilized to quantify liquid penetration[29,32]. The ASA instrument measures the absorption of liquid delivered to the paper surface via a nozzle moving over the paper surface, similar like the Bristow Wheel. Contact time between paper and liquid is varied by changing the speed of the moving sample stage. The transferred liquid volume is than plotted versus the square root of contact time. The faster the liquid imbibition into the paper the higher is the observed slope of the result curve. For a detailed description of the measurement please refer also here to the electronic supplementary information (ESI) or to earlier publications[29].

The **contact angle measurement (CA)** is the standard method for determining the wetting of a given liquid - substrate combination. The typical measurement procedure involves putting a drop of liquid on the substrate and recording images of this droplet over time. The angle between the outline of the drop in the contact point and the substrate represents the contact angle. The higher the contact angle, the worse is the wetting of the liquid on the surface. In this work we are producing drops on two size scales, picoliter and microliter.

First we utilize a dataphysics instrument with a picoliter head to generate droplets with a size of 30pl and 60pl, the spreading and penetration of the drops is imaged at a frame rate of 2000 frames per second. The test liquid is sucked through a orifice into a cartridge using a standard micro-pipet combined with a special dataphysics attachment. The cartridge is than inserted into the dosing head of the picoliter head. This dosing element is positioned on the membrane cap of the cartridge, enabling to create a pulse which squeezes out the liquid through the orifice of the cartridge (Figure 6 in the ESI). The diameter of this opening can be adjusted by using cartridges with different sized orifices. The parameters pulse amplitude, pulse duration and pulse frequency of the pulse can be varied for the individual dosing processes, depending on the used testing fluid and drop size. The sensor treshold is a measure for the applied negative pressure, in the cartridge to prevent liquid leakage through the orifice. The higher this value, the higher will be the negative pressure in the nozzle, being zero for ambient conditions in the cartridge. The parameters are adjusted in order to guarantee a

**Table 2** Liquid composition properties: viscosity ($\eta$), surface tension ($\gamma$) and density.

| Liquid | water [$w\%$] | glycerol [$w\%$] | hexanediol [$w\%$] | dye [$w\%$] | viscosity $\eta$ [$mPas$] | surface tension $\gamma$ [$mN/m$] | density $\rho$ [$kg/m^3$] |
|---|---|---|---|---|---|---|---|
| High (↑) $\eta$ - Low (↓)) $\gamma$ | 41.9 | 48 | 10 | 0.1 | 7.2 | 27.5 | 1.12 |
| Low (↓) $\eta$ - Low (↓) $\gamma$ | 64.9 | 25 | 10 | 0.1 | 3 | 26.8 | 1.06 |
| High (↑) $\eta$ - High (↑) $\gamma$ | 42.4 | 57.5 | 0 | 0.1 | 7.99 | 67.6 | 1.14 |
| Low (↓) $\eta$ - High (↑) $\gamma$ | 74.9 | 25 | 0 | 0.1 | 1.7 | 70.5 | 1.06 |
| center(⊗) $\eta$ - center(⊗) $\gamma$ | 53.4 | 45 | 1.5 | 0.1 | 4.23 | 43.5 | 1.12 |

stable drop production. The optimal settings can be found in the ESI Table 1-5 for each liquid. The paper, 90 mm x 50 mm in size, is clamped centrally on the self-built specimen holder using four magnets to fixate it, illustrated in Figure 7a in the ESI. Here, it is important that the paper area, were the liquid is applied on the surface, is not in contact with the sample holder (Figure 7b).

Second we are employing a standard instrument used in the paper industry, the Fibro DAT 1100 instrument[48]. It generates droplets with a liquid volume of $2\mu l$ and $4\mu l$, a size scale larger by the factor of $10^6$ compared to HSI printed droplets. Both instruments evaluate the contact angle over time, starting with the first image where the entire drop is deposited on the paper surface.

The Fibro and the dataphysics instrument employ different time resolution, whereas the Fibro has a logarithmic frame rate starting with a frame rate of 100 frames per second for the first 100ms, the dataphysics instrument takes pictures every 0.5ms.

The **print through test** is a measure for the penetration depth of the printing liquid into the paper. For this purpose, the backside of the unprinted sheet is imaged behind a coloured background. This background has the same colour as the print. Subsequently, the sheet is full-tone printed on the top side. Finally, the exact same position of the backside of the printed paper is imaged again, measuring the mean gray value [8 bit grayvalue] of the measurement area. The difference of the gray values before- and after printing represents the print through value. The measurement procedure is described in detail elsewhere[9] and the electronic supplementary information.

The **printed dot analysis** is used to evaluate the printed dots with regard to drop area [$mm^2$] and the aspect ratio [-]. The dot area captures the liquid spreading during the industrial HSI printing. A high dot area, indicates high spreading of the liquid drop. In our study, the ImageXpert Stand-Alone Audit Station was used, taking pictures of the dot pattern and measuring the relevant parameters of the detected dots using digital image analysis. Dots originating from drop splashing, satellite drops or a combination of both are distorting the overall result and need to be excluded from the evaluation. The aspect ratio (AR) of the dot is used as a filter and is a measure for the roundness of the drop. A perfectly circular dot has an AR value of 1. We are filtering out all dots with a value below 0.85, which are produced by bad jetting or insufficient detection from the measurement device. A typical dot pattern is shown in Figure 4, discarded dots are circled red. For detailed explanation of the dot analysis please have look at Krainer et al.[9].

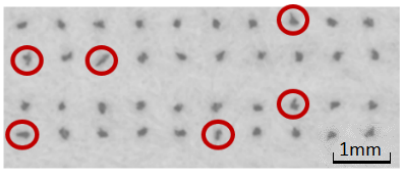


**Fig. 4** Printed dot pattern for dot area measurement. The red circled dots have an aspect ratio below 0.85, being excluded from evaluation.

### 2.4 High Speed Inkjet printing

Liquid application on paper was done utilizing an industrial HSI printhead in a laboratory printing setup. Such a printhead is e.g. built in the Océ VarioPrint i300 HSI printer from Canon[49].

## 3 Results and discussion

### 3.1 Penetration speed

Figure 5 illustrates correlations between ULP penetration speed and print through for the five used model liquids on two different papers. The papers are a pigmented, medium absorbing HSI paper grade (Figure 5a) and plain paper without any treatment, exhibiting very strong penetration (Figure 5b). The same symbols represent the same liquid, but tested on top side and bottom side of the paper. Figure 5a shows a coefficient of determination $R^2 = 0.68$, representing a reasonable ability of the ULP to predict liquid penetration into the pigmented paper during HSI printing. Figure 5b for the untreated paper exhibits $R^2 = 0.18$, ULP fails to predict HSI-print penetration.

The coefficient of determination for each paper between ultrasonic liquid penetration measurement and print through test for all five liquids is shown in Figure 6a. The sized paper with very low absorption, results in the highest $R^2 = 0.71$, similar like for the pigmented paper with $R^2 = 0.68$. The paper with only primer treatment has higher absorption and a significantly lower coefficient of determination. For the paper with the strongest penetration, the completely untreated one, the correlation $R^2 = 0.18$ is the worst. With increasing absorption tendency of the paper, the correlation between penetration behaviour during the industrial process and the ULP measurement decreases. Looking at the correlation between the ASA penetration parameter and the print through of HSI full-tone printed sheets, Figure 6b, we find similar results, the prediction power of the ASA measurement decreases for increasingly strong absorbing paper. Thus, it can be concluded, that the stronger the observed liquid penetration into the paper, the less the laboratory tests have been able to

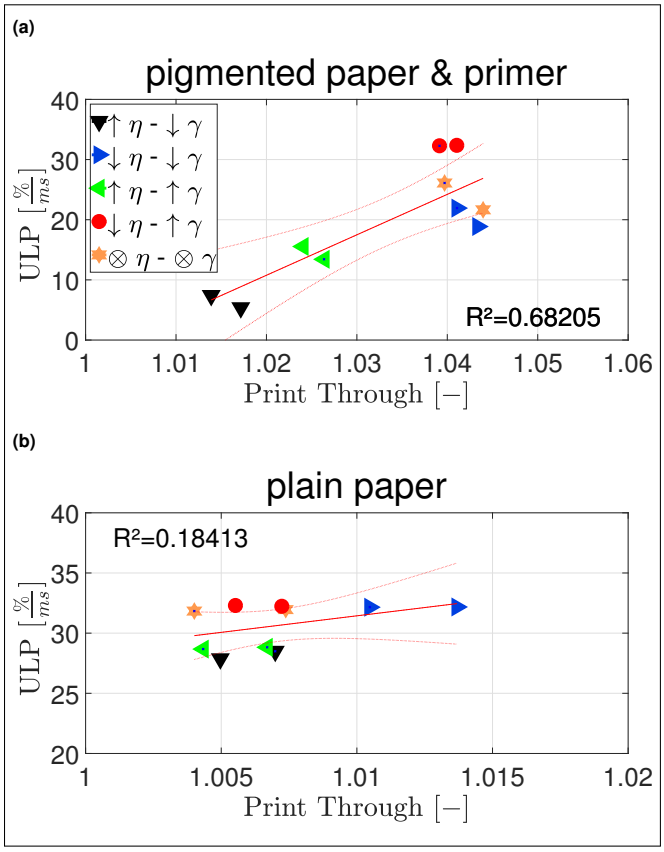


**Fig. 5** ULP value for penetration speed plotted versus print through measured on full tone HSI printed sheets. The symbols represent the model liquids, using same symbols for top and bottom side of the paper. The papers are a pigmented, medium absorbing HSI paper grade (a) and a plain paper without any treatment, having strong absorption (b). The correlation in Subfigure (a) indicates a good prediction of HSI liquid penetration by the laboratory test ULP. In contrast to that, part (b) shows a low correlation, revealing a failure in forecasting HSI-print penetration by ULP for the high absorbing paper.

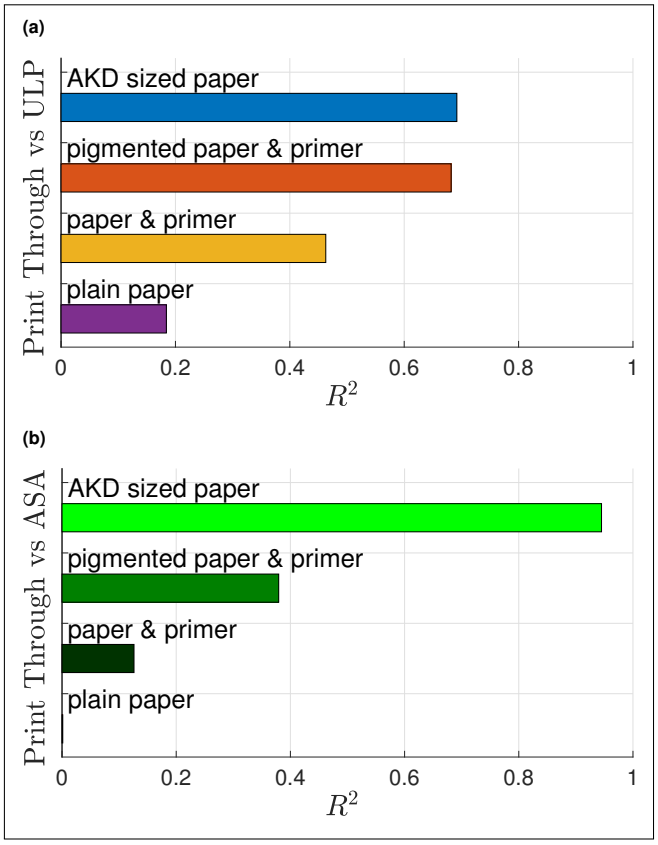


**Fig. 6** Coefficient of determination $R^2$ between print HSI print through values and liquid penetration measured by (a) ultrasonic liquid penetration ULP and (b) automatic scanning absorptometer (ASA) values. Both show that the slower the liquid penetration into the paper, the higher is the observed ability of the instrument to predict fluid imbibition during HSI printing, as indicated by increasing $R^2$. The laboratory tests can quite well predict HSI liquid penetration for low absorbing paper, but not for high absorbing paper.

predict fluid imbibition during the HSI print process.

This can be rationalized assuming, that ULP and ASA measurements apply a virtually unlimited amount of liquid, for penetration into the paper. In contrast to that, during HSI printing thousands of tiny drops in the lower picoliter range are shot onto the paper, providing a very limited fluid supply on the paper surface. For papers exhibiting low absorption tendency, the liquid oversupply is not so prominent as they saturate with a smaller amount of liquid. This causes less difference in imbibed liquid between printing and laboratory measurement. For the highly absorbing, completely untreated paper, the difference between the imbibed liquid during ULP or ASA measurement und printing is high. This causes an enormous difference between absorbed liquid during the HSI process and ULP or ASA measurement, resulting in a low prediction potential.

Another reason for the low prediction power of the untreated paper might be the 20% higher grammage compared to the other three grades. The print through might be not sensible enough to capture liquid penetration in high grammage paper due to too low relative penetration depth. Overall the ULP showed slightly higher correlations to print through than the ASA measurement.

### 3.2 Wetting

Figure 7 shows the contact angle plotted versus the HSI printed dot area, in both cases for 60pl drops. The contact angle was measured immediately after the complete liquid was deposited on the paper surface. The symbols represent the five model liquids, same symbols indicate top- and bottom side of the paper. The substrates in Figure 7 are the pigmented HSI grade with moderate small absorption (a) and the untreated paper with fast imbibition (b). The slower absorbing pigmented paper exhibits a better correlation coefficient $R^2 = 0.64$ between contact angle and printed dot area than the fast absorbing untreated paper $R^2 = 0.22$.

The penetration and wetting of picoliter droplets during the printing process is completed after 30-100ms of liquid application [11] and thus the final dot shape is achieved shortly after the printhead. The measured contact angle is highly affected by the contact time between fluid and substrate, it changes due to pen-

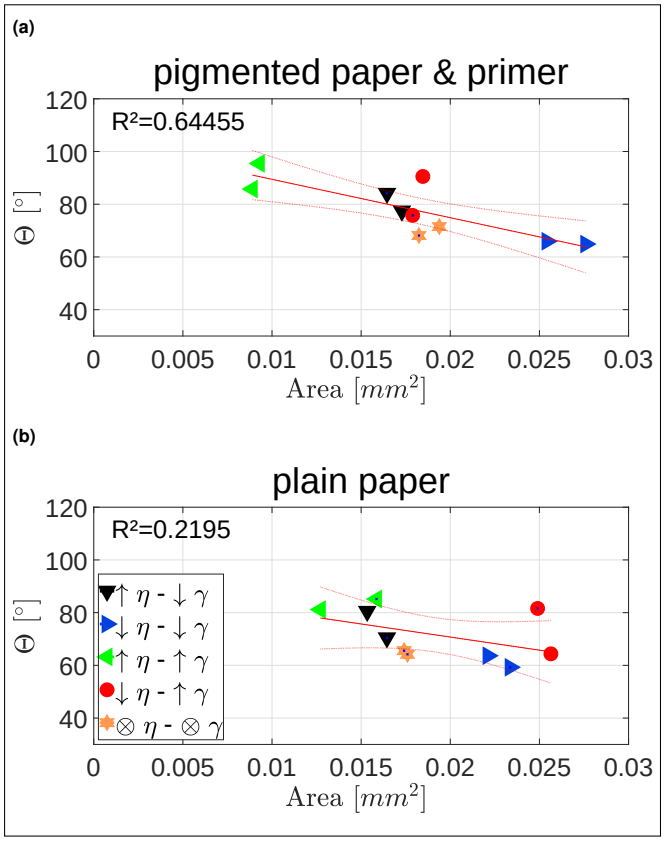


**Fig. 7** Contact angle vs. HSI printed dot area for 60pl droplets measured immediately after drop deposition. The symbols represent the model liquids, using same symbols for top and bottom side of the paper. The contact angle predicts liquid spreading quite well on pigmented, medium absorbing paper (top, $R^2 = 0.64$), but not so well for untreated, high absorbing papers (bottom, $R^2 = 0.22$).

etration and spreading of the liquid on the paper. This contact angle change over time is particularly relevant for small (picoliter) drops, which is aggravated for highly absorbing papers[29]. Most commonly microliter drops are used for contact angle measurement. These big drops are often evaluated after longer contact times between fluid and paper[50], due to drop oscillation after liquid deposition. Thus it is relevant to evaluate the optimal moment for contact angle measurement when trying to correlate the contact angle to the spreading behavior of the HSI drops. The coefficients of correlation using contact angle at different measurement times and the HSI printed dot area (which is always the same as it is measured on the HSI prints) are illustrated in Figure 8, 10 and 11. The first point in each graph is around 0.5ms which is the first image after drop deposition which is delivered by the contact angle instruments, later values are measured from subsequent images. Each dot in the graph is the $R^2$ value from a similar correlation plot as shown in Figure 7.

#### 3.2.1 Correlation between picoliter drops for printing and contact angle measurement

Figure 8 shows the correlation coefficient $R^2$ between contact angle and dot area over different measurement times, using droplets of identical size. That means that both, contact angle and dot area, were measured and printed with the same volume (squares are 60pl and triangles are 30pl). The correlation generally decreases from little absorbing (AKD sized paper) to highly absorbing (unsized and untreated) papers. For the former the contact angle quite well predicts HSI printed dot area, the latter has only a low correlation between these parameters. In Figure 9 we see the correlation coefficient between the base diameter of the contact angle drop and the final printed dot area. The idea behind this is that the drop diameter in the contact angle measurement should directly reflected drop spreading, which could be a better predictor for the dot area of the actual HSI print. Comparing Figures 8 and 9 however reveals that the base diameter of the contact angle in every case predicts the final printing dot area not as good as the contact angle. Both measurement parameters (contact angle and drop diameter) have less correlation to printed dot area when paper absorption is increasing. By calculating the volume of the remaining drop on the surface we also found that for the fast absorbing paper in the first image (after 0.5ms) already $\sim$ 65% of the total drop volume has penetrated into the paper, highlighting the influence of penetration on the measurement.

Drop size has an influence on the correlations, in every case the 60pl drops have a significantly higher correlation between contact angle measurements and printed dot size. Interestingly the difference between the correlation coefficients of 30pl contact angle and 30pl printed area and 60pl contact angle and 60pl printed dot area is small for the sized paper and the raw paper, whereas, the papers exhibiting moderate penetration (pigmented paper & primer and paper & primer) show a higher gap between the $R^2$ values of 30pl and 60pl drop sizes (compare triangles and squares Figures 8 and 9). This suggests that for papers exhibiting either very low penetration or rapid imbibition the drop volume is not so relevant. Another explanation might be the fact that 30 picoliter drops are so small (they have a height of about 10 micrometers) that surface roughness is starting to play a role. A considerable amount of the drop volume disappears in the surface roughness, which leads to variations in the apparent contact angle. Furthermore the influence of absorption on the contact angle measurement is larger for the smaller drops, which is likely to also decrease the correlation to printed dot area.

In summary, it can be concluded that stronger penetration and lower liquid volume on the paper surface makes picoliter contact angle measurements less suitable to predict spreading of HSI printed picoliter drops. Contact angle is a better predictor for printed dot area than the drop diameter in the contact angle instrument, also 60pl drops have clearly higher correlations than 30pl drops. Also it can be concluded that the correlation between contact angle and dot size is the best at 1ms after drop application, thus it is recommended to measure the contact angle

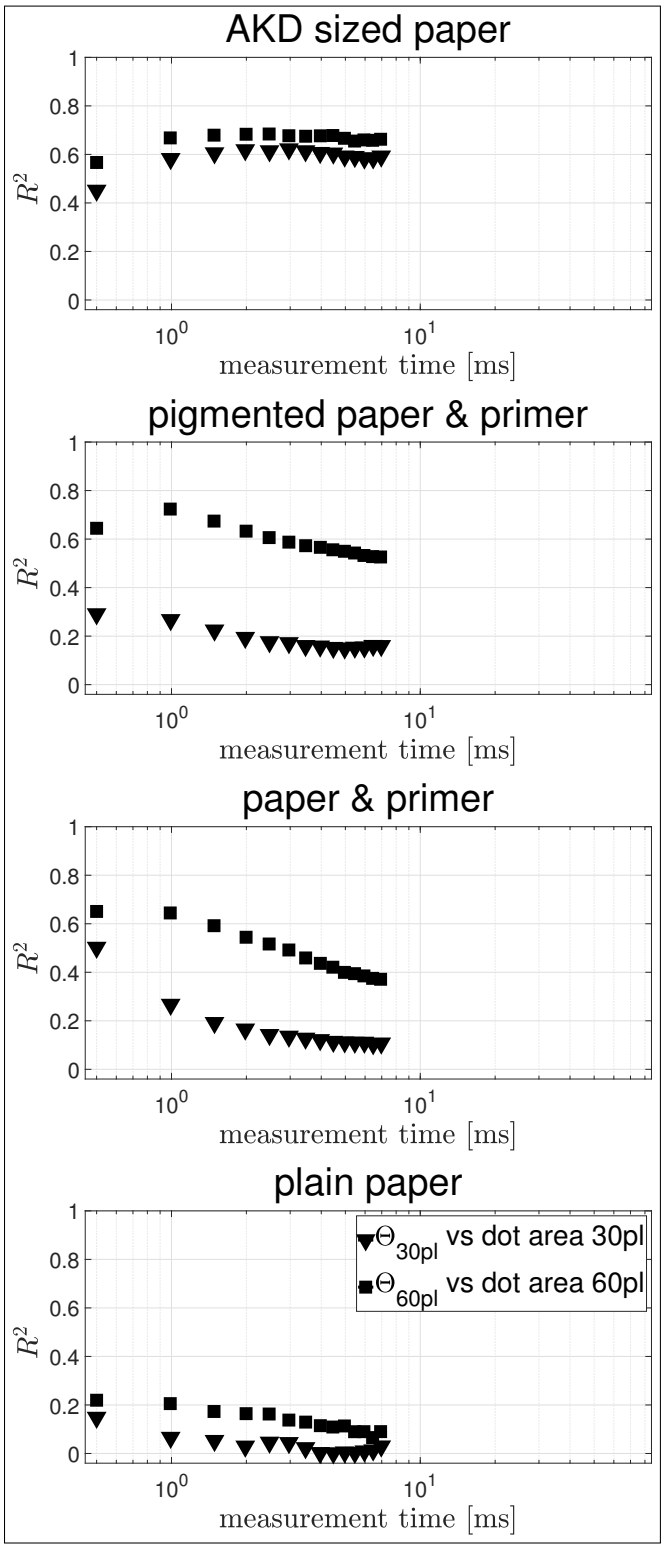


**Fig. 8** Correlation between the contact angle and the printed dot area of 30pl (squares) and 60pl (triangles) droplets plotted versus measurement time. For the sized paper $R^2$ is high. With increasing water absorption the predictive power $R^2$ of the contact angle for the printed dot area decreases. Measurement of the contact angle at 1ms gives a better correlation to the printed dot area than measurement at a later time.

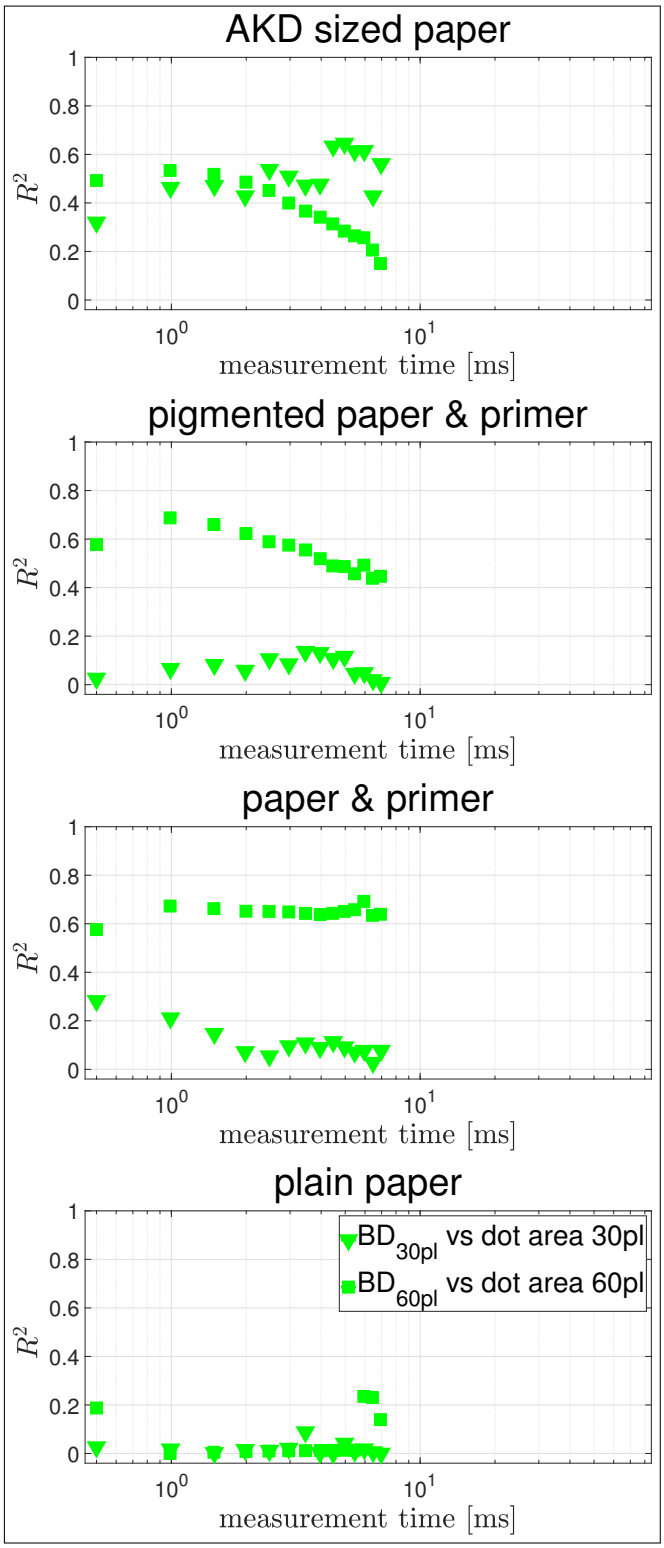


**Fig. 9** The coefficient of determination between the base diameter obtained from the contact angle measurement and the printed dot area of droplets with identical drop volume is calculated and plotted versus the measurement time of the contact angle measurement. The liquid volume applied on the paper was 60pl (square) and 30pl (triangle). For the sized paper $R^2$ is high, decreasing with increasing water absorption.

immediately after the drop's impact oscillation has dampened out.

#### 3.2.2 Correlation between picoliter drops for printing and other drop sizes for contact angle measurement

Finally we studied the effect of varying the drop size for the contact angle measurement and analyzing the effect on the correlation between contact angle measurements and the spreading (printing dot area) of inkjet printed dots. Correlations to 30pl printed dots are plotted in Figure 10, correlations to 60pl printed dots are shown in Figure 11. Due to differences between the measurement instruments, microliter droplets are recorded at lower frame rates than picoliter drops, leading to different measurement times.

It can be observed that the first (for unsized papers) or second (for sized papers in combination with dot area of pl drops) measurement value exhibits the highest coefficient of determination, see Figure 10 and 11. This is the case for all drop sizes, picoliter like microliter drops. Apparently the initial contact angle, or at least the earliest measurable contact angle, is best suited for predicting the area of the final printing dot.

One key finding is that contact angle measurements from small (picoliter) drops are not working better than large (microliter drops). Small and large drops have similar $R^2$ values in Figures 10 and 11. For the highly absorbing untreated paper the microliter drops are even clearly better suited to predict the printing dot area, indicated by the higher $R^2$. We had expected that contact angle measurement on the same size scale like in the inkjet process, i.e. in the low picoliter range, could lead to a better prediction for the actual inkjet print. Microliter drops, having the size of several times the paper thickness, clearly are hardly effected by e.g. surface roughness and liquid penetration, whereas the picoliter drops are highly affected by both. Nevertheless correlations between drop area of picoliter printed dots and contact angle of various drop volumes from 30pl, 60pl, $2\mu l$ and $4\mu l$ show similar coefficients of determination for all drop sizes. Our results suggest no benefit of using picoliter contact angle measurement over microliter measurements. In fact large drops are much easier to handle, the measurement instruments are simpler and cheaper and measurement standards have been established (e.g. Tappi T558). Anyway we would like to point out that in the current work we have covered the full range of jettable liquids, it would be interesting to investigate if similar results can be found for smaller variations in the liquid properties.

Finally we have also evaluated if the drop diameter measured in the contact angle instrument is a suitable predictor for the area of the printed dot. It turned out that the correlation of the drop diameter is in all cases lower than for the contact angle, the contact angle is the better predictor. For detailed plots on these results please refer to the electronic supplementary information (Figures 8 and 9).

## 4 Conclusions

In this study we have evaluated the suitability of laboratory testing methods to predict inkjet printing results. We have developed and used testing liquids that are spanning the operational window of industrial HSI printers while still covering the maximum possible range of viscosity and surface tension. In order to find correlations between test prints and laboratory tests, both were performed with these testing liquids. We tested four papers representative for the uncoated high speed inkjet paper market, these papers exhibited large differences in terms of water absorption. First we correlated liquid penetration measured with ultrasound (ULP) and direct absorption (ASA) to print through from HSI prints. Second we correlated contact angle and drop diameter to the dot area from HSI prints.

**Print through and liquid penetration.** The print through measurements capturing liquid penetration in HSI printed sheets were first correlated with liquid penetration speed measured by ultrasonic liquid penetration (ULP). The best correlation ($R^2 = 0.71$ ) was found for the sized paper. For papers with increasing liquid penetration speed we found a decreasing ability of the laboratory testing methods to predict print through, for the strong absorbing paper the correlation drops to $R^2 = 0.18$. Similar results, although with somewhat lower correlations, were found for the direct absorption tester (ASA). We can thus conclude that the investigated liquid penetration measurement techniques can well predict the print through for little absorbing papers but not so well for highly absorbing papers.

**Dot spreading and contact angle.** We compared the dot area of HSI printed 30pl and 60pl drops to contact angle measurements from picoliter- and microliter drops. Also here better correlations were found for little absorbing paper than for strongly absorbing papers. Contact angle turned out to be a better predictor for printed dot area than the diameter of the drops on the paper. A key finding is that the correlation between contact angle and dot size is the best at about 1ms after drop deposition, thus it is recommended to measure the contact angle as soon as possible after application.

Furthermore, the contact angle of picoliter drops (30pl and 60pl) and microliter drops ($2\mu l$ and $4\mu l$) drops was compared to the dot area of 30pl and 60pl HSI prints. Surprisingly, contact angle measurements from small (picoliter) drops were *not* better able to predict inkjet dot spreading than contact angle measurements with large (microliter) drops. Correlations for microliter drops were equal or better than for picoliter drops, particularly for highly absorbing papers. Thus in order to predict dot spreading on paper our results suggest to measure the contact angle with microliter drops. This is a highly unexpected finding. We had assumed that picoliter measurements, being in the same size scale like the drops in the inkjet printing process, would deliver better results, particularly because picoliter drops are highly affected by paper surface roughness and liquid absorption and microliter drops, being one million times larger, are not.

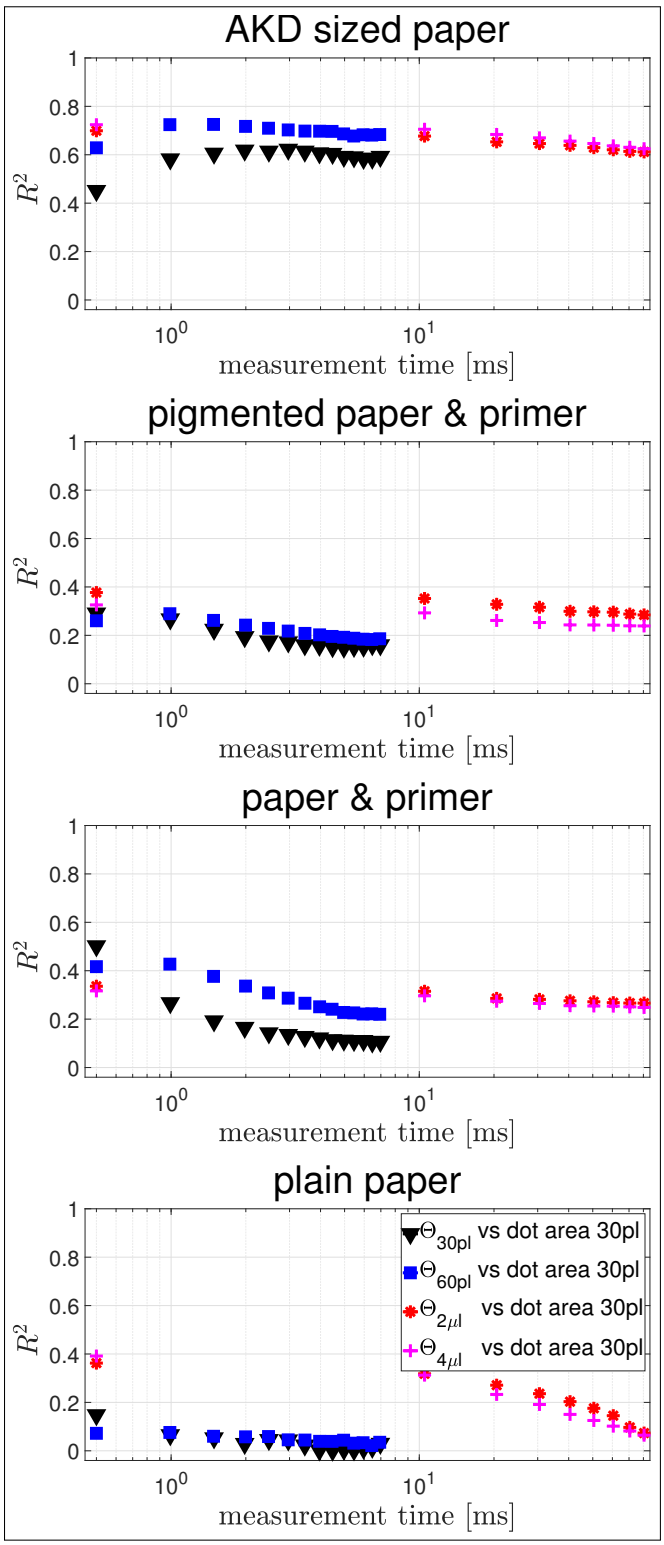


**Fig. 10** Correlation between the contact angle measured with 30pl, 60pl, $2\mu l$ and $4\mu l$ drops and the dot area printed with 30pl droplets. The $R^2$ of dot area versus contact angle is plotted over measurement time. The contact angle measured with large (microliter) drops is equally or better suited to predict printed dot area than small (picoliter) drops. Low absorbing papers (AKD sized) have much better correlation than high absorbing papers (unsized and untreated).

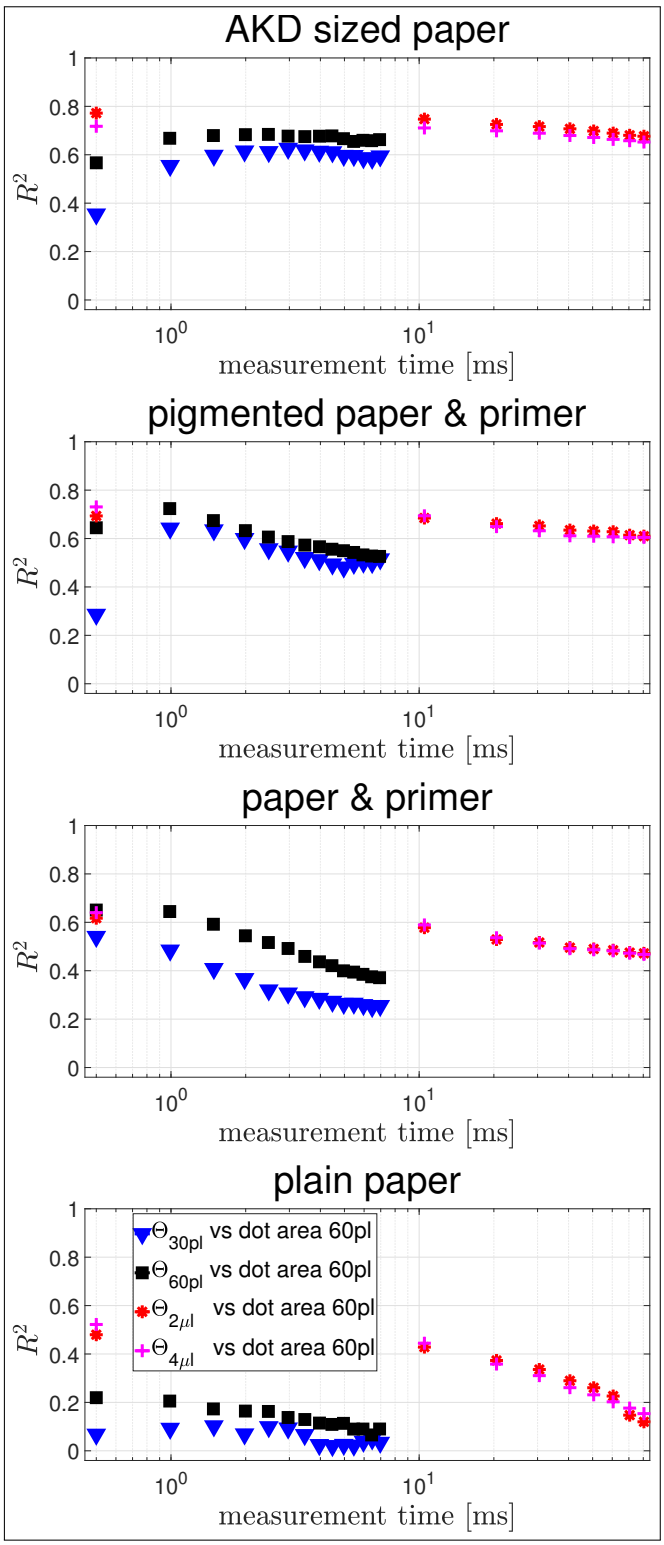


**Fig. 11** Correlation between the contact angle measured with 30pl, 60pl, $2\mu l$ and $4\mu l$ drops and the dot area printed with 60pl droplets. The $R^2$ of dot area versus contact angle is plotted over measurement time. The contact angle measured with large (microliter) drops is equally or better suited to predict printed dot area than small (picoliter) drops. Low absorbing papers (AKD sized) have much better correlation than high absorbing papers (unsized and untreated).

## Conflicts of interest

There are no conflicts to declare.

## 5 Acknowledgements

The financial support by the Austrian Federal Ministry for Digital and Economic Affairs and the National Foundation for Research Technology and Development is gratefully acknowledged. Furthermore the authors want to thank Océ, Mondi, Kelheim Fibres and SIG Combibloc for their financial support. Special Thanks to Pim du Buf for his support during the printing trials and Rob van Os for his help with the ASA measurements.

## Notes and references

1 S. S. Ovaska and K. Backfolk. The versatility of the Bristow absorption tester - A review. *Nordic Pulp and Paper Research Journal*, 33(2):279–296, 2018.

2 H. Kipphan. *Heidelberger Handbuch der Printmedien*. Springer-Verlag, 2000.

3 J. Blechschmidt. *Taschenbuch der Papiertechnik*. Carl Hanser Verlag München, 2013.

4 U. Lindqvist, L. Hakola, J. Heilmann, B. Zhmud, and E. Wallström. Interaction Characteristics in Different Applications of Ink- Jet Printing. *TAGA Journal*, 2:99–109, 2006.

5 U. Lindqvist, L. Hakola, Z. Boris, and E. Wallstrom. Advances in Printing Science and Technology. In *Proceedings of the 31st International iarigai Research Conference*, page 260. Acta Craphica Publishers, 2004.

6 C. Schmid and A. Hudd. Formulation and Properties of Waterborne Inkjet Inks. In S. Magdassi, editor, *The Chemestry of Inkjet Inks*, pages 123 –140. World Scientific Publishing Co. Pte. Ltd., 2010.

7 L. Neimo and S. P.-I. Yhdistys. *Papermaking Chemistry*, volume 4. 1999.

8 H. Dong, W. W. Carr, and J. F. Morris. An experimental study of drop-on-demand drop formation. *Physics of Fluids*, 18(7), 2006.

9 S. Krainer, C. Smit, and U. Hirn. The effect of viscosity and surface tension on inkjet printed picoliter dots. *RSC Advances*, 9(54):31708–31719, 2019.

10 E. P. Furlani. *Fundamentals of Inkjet Printing: The Science of Inkjet and Droplets*, volume 1. Wiley-VCH Verlag, 2016.

11 K. L. Yip, A. R. Lubinsky, D. R. Perchak, and K. C. Ng. Measurement and Modeling of Drop Absorption Time for Various Ink-Receiver Systems. *Journal of Imaging Science and Technology*, 47(5):378–393, 2003.

12 T. Lamminmäki, J. Kettle, and P. Gane. Absorption and adsorption of dye-based inkjet inks by coating layer components and the implications for print quality. *Colloids and Surfaces A: Physicochemical and Engineering Aspects*, 380(1-3):79–88, 2011.

13 J. Kettle, T. Lamminmäki, and P. Gane. A review of modified surfaces for high speed inkjet coating. *Surface and Coatings Technology*, 204(12-13):2103–2109, 2010.

14 K. Mielonen, S. S. Ovaska, T. Laukala, and K. Backfolk. Three-Layered Polyelectrolyte Structures as Inkjet Receptive Coatings: Part 2. Interaction With Pigment-based Inks. *Journal of Imaging Science and Technology*, 60(3):1–9, 2016.

15 D. Siregar, J. G. Kuerten, and C. van der Geld. Numerical simulation of the drying of inkjet-printed droplets. *Journal of Colloid and Interface Science*, 392(1):388–395, feb 2013.

16 C. Diddens, J. G. Kuerten, C. W. van der Geld, and H. M. Wijshoff. Modeling the evaporation of sessile multi-component droplets. *Journal of Colloid and Interface Science*, 487:426–436, 2017.

17 A. Marmur. Penetration and displacement in capillary systems of limited size. *Advances in Colloid and Interface Science*, 39:13–33, 1992.

18 R. Li, Y. Zhang, Y. Cao, and Z. Liu. Ink Penetration of Uncoated Inkjet Paper and Impact on Printing Quality. *BioResources*, 10(4), 2015.

19 E. Svanholm. *Printability and ink-coating interactions in inkjet printing*. PhD thesis, Karlstad University, 2007.

20 K. Mielonen, P. Geydt, C.-M. Tåg, and K. Backfolk. Inkjet ink spreading, absorption and adhesion on substrates coated with thin layers of cationic polyelectrolytes. *Nordic Pulp & Paper Research Journal*, 30(2):179–188, 2015.

21 L. Yang. *Ink-Paper Interaction: A study in ink-jet color reproduction*. PhD thesis, Linkoping University, 2003.

22 C. J. Ridgway and P. A. C. Gane. Controlling the absorption dynamic of water-based ink into porous pigmented coating structures to enhance print performance. *Nordic Pulp and Paper Research Journal*, 17(2):119–129, 2002.

23 J. Gigac, M. Kasajov, M. Maholyiov, M. Stankovsk, and M. Letko. Prediction of surface structure of coated paper and of ink setting time by infrared spectroscopy. *Nordic Pulp and Paper Research Journal*, 28(2):274–281, 2013.

24 G. Wypych. Typical Primer Formulations and Applications to different substrates. In *Handbook of Adhesion Promoters*, pages 77–91. ChemTec Publishing, 2018.

25 T. Lamminmäki, J. Kettle, P. Puukko, C. Ridgway, and P. Gane. Short timescale inkjet ink component diffusion: An active part of the absorption mechanism into inkjet coatings. *Journal of Colloid and Interface Science*, 365(1):222–235, 2012.

26 D. R. Karsa. *Surfactants in Polymers, Coatings, Inks and Adhesives*. Blackwell Pub., 2003.

27 J. B. Rosenholm. Liquid spreading on solid surfaces and penetration into porous matrices: Coated and uncoated papers. *Advances in Colloid and Interface Science*, 220:8–53, 2015.

28 E. Bohlin. *Surface and porous structure of pigment coatings: Interactions with flexographic ink and effects on print quality*. PhD thesis, Karlstad University, 2013.

29 K. Sarah and H. Ulrich. Short timescale wetting and penetration on porous sheets measured with ultrasound, direct absorption and contact angle. *RSC Adv.*, 8(23):12861–12869, 2018.

30 D. Yang, M. Krasowska, C. Priest, M. N. Popescu, and J. Ral-

ston. Dynamics of capillary-driven flow in open microchannels. *Journal of Physical Chemistry C*, 115(38):18761–18769, 2011.

31 J. A. Bristow. Liquid absorption into paper during short time intervals. *Svensk papperstidning*, 70(19):623–629, 1967.

32 C. Kuijpers, T. van Stiphout, H. Huinink, N. Tomozeiu, S. Erich, and O. Adan. Quantitative measurements of capillary absorption in thin porous media by the Automatic Scanning Absorptometer. *Chemical Engineering Science*, 178:70–81, 2018.

33 R. Hebbar, A. Isloor, and A. Ismail. Contact Angle Measurements. *Membrane Characterization*, pages 219–255, 2017.

34 K. Y. Law and H. Zhao. *Surface wetting: Characterization, Contact Angle, and Fundamentals*. 2015.

35 K. Mielonen, P. Geydt, M. Österberg, L. S. Johansson, K. Backfolk, S.-S. Ovaska, T. Laukala, and K. Backfolk. Inkjet ink spreading on polyelectrolyte multilayers deposited on pigment coated paper. *Journal of Colloid and Interface Science*, 438(3):179–190, 2015.

36 M. Daun. *Model for the dynamics of liquid penetration into porous structures and its detection with the help of changes in ultrasonic attenuation*. Dissertation, Technical University Darmstadt, 2006.

37 L. Yang, L. Jianghao, and G. Lingya. Detailed insights to liquid absorption and liquid - paper interaction. In *XV Fundamental Research Symposium*, pages 585–598, Cambridge, 2013.

38 H. Holik. *Recycled Fibre and Deinking*. Helsinki, 2009.

39 K. Sato, N. Ozaki, K. Nakanishi, Y. Sugahara, Y. Oaki, C. Salinas, S. Herrera, D. Kisailus, and H. Imai. Effects of nanostructured biosilica on rice plant mechanics. *RSC Adv.*, 7(22):13065–13071, 2017.

40 P. Resch, W. Bauer, and U. Hirn. Calendering effects on coating pore structure and ink setting behavior. *Tappi Journal*, 9(1):27–35, 2010.

41 M. G. Ventura, A. I. Paninho, A. V. Nunes, I. M. Fonseca, and L. C. Branco. Biocompatible locust bean gum mesoporous matrices prepared by ionic liquids and a scCO2 sustainable system. *RSC Advances*, 5(130):107700–107706, 2015.

42 A. Barakat, C. Mayer-Laigle, A. Solhy, R. A. D. Arancon, H. de Vries, and R. Luque. Mechanical pretreatments of lignocellulosic biomass: towards facile and environmentally sound technologies for biofuels production. *RSC Adv.*, 4(89):48109–48127, 2014.

43 L. Roiban, G. Foray, Q. Rong, A. Perret, D. Ihiawakrim, K. Masenelli-Varlot, E. Maire, and B. Yrieix. Advanced three dimensional characterization of silica-based ultraporous materials. *RSC Advances*, 6(13):10625–10632, 2016.

44 D. K. Owens and R. C. Wendt. Estimation of the surface free energy of polymers. *Journal of Applied Polymer Science*, 13(8):1741–1747, 1969.

45 Y. Luo, Y. Zhao, Y. Duan, and S. Du. Surface and wettability property analysis of CCF300 carbon fibers with different sizing or without sizing. *Materials & Design*, 32(2):941–946, 2011.

46 G. H. McKinley and M. Renardy. Wolfgang von Ohnesorge. *Physics of Fluids*, 23, 2011.

47 W. V. Ohnesorge. Formation of Drops by Nozzles and the Breakup of Liquid Jets. *Applied Mathematics and Mechanics*, 16:355–358, 1936.

48 A. Hladnik. Dynamic wetting and liquid sorption in paper - FIBRO 1100 DAT measuring. *Papier*, 25((3-4)):44–48, 1997.

49 David Zwang. Production Inkjet—The Next Wave: Canon Océ VarioPrint i300 Sheetfed Inkjet Press and More - WhatTheyThink, 2015.

50 M. Von Bahr, R. Seppänen, F. Tiberg, and B. Zhmud. Dynamic wetting of AKD-sized papers. *Journal of Pulp and Paper Science*, 30(3):74–81, 2004.

# Chapter 8

# Manuscript IV

# Contact Angle Measurement on Porous Substrates: Effect of Liquid Absorption and Drop Size

Sarah Krainer[1,2], Ulrich Hirn[1,2,*]

**Abstract**

**Hypothesis:** Liquid absorption has a strong impact on the contact angle Θ measured on absorptive substrates. Hence liquid absorption rate, drop size and contact time are relevant influencing factors on the measured contact angle. We will demonstrate that the impact of these three parameters is fully captured by the relative absorbed drop volume i.e. the percentage of the drop volume penetrated into the substrate.

**Experiments:** The wetting studies were carried out applying a wide range of drop volumes between 30 $pl$ to 4 $\mu l$ (spanning a factor $10^5$) using water. Furthermore, the effects of surface tension (26.8 $mN/m$ - 73 $mN/m$) and the substrate absorption rate (0.6 $ml/(m^2 100ms)$ to 71 $ml/(m^2 100ms)$) have also been tested. We employed non-contact drop deposition methods.

**Findings:**
We observed three regimes of liquid penetration impact on Θ, determined by the absorption rate of the substrate and drop size. Here, strong, low and no reduction of the drop volume takes place corresponding to high, low and no penetration impact on the contact angle. Investigation of liquid surface tension impact shows, that for high values the average contact angle of the $pl$ sizes is 10° to 15° lower than obtained from $\mu l$ drop contact angles. Our results suggest the measuring of the contact angle with large droplets and immediately after the drop application to minimize the impact of penetration on the wetting process. Independent of drop size, absorption rate and measurement time the contact angle decreases between ∼0.5° to ∼1.2° for each percentage of relative absorbed drop volume V. Thus, V fully captures the combined effect of drop size, contact time and substrate absorption rate.

*Keywords:* drop size, relative absorbed drop volume, surface tension, drop spreading, absorption rate, picoliter, nanoliter, microliter

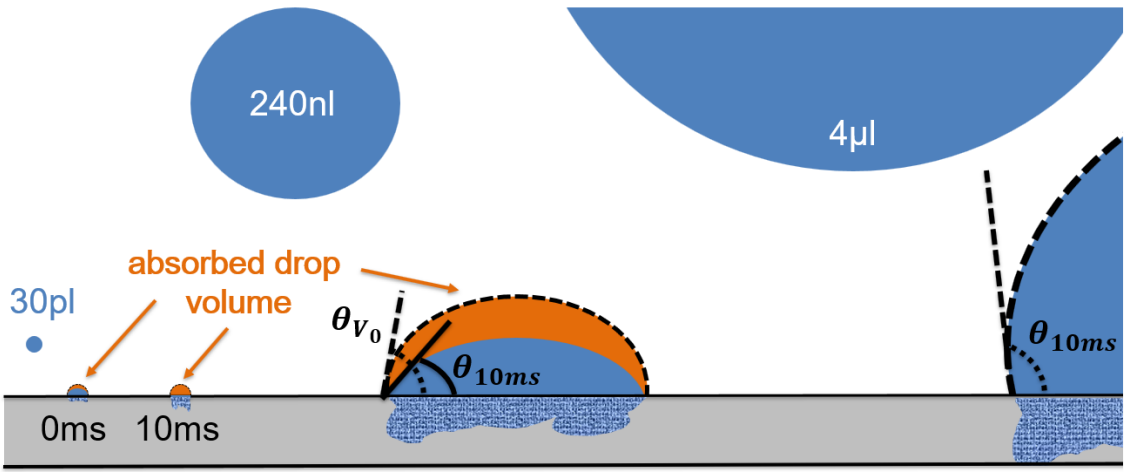


*corresponding author
*Email address:* ulrich.hirn@tugraz.at,phone:+43(316)87330753 (Ulrich Hirn )
[1]Institute of Paper, Pulp and Fiber Technology, TU Graz, Inffeldgasse 23, 8010 Graz, Austria
[2]CD Laboratory for Fiber Swelling and Paper Performance, Inffeldgasse 23, 8010 Graz, Austria

## 1. Introduction

Liquid behaviour on porous substrate is determined simultaneously by spreading on the substrate's surface and penetration into the bulk of the absorptive substrate [1, 2]. A parameter, affected by both, fluid and substrate, is the contact angle $\Theta$ of a liquid drop applied on the flat, horizontal substrate [3]. The $\Theta$ is defined as the angle between the drops outline tangent at the three-phase contact point and the substrate. It is affected by the liquid surface tension $\gamma_{lv}$, the interfacial tension between liquid and substrate $\gamma_{sl}$ and by the surface energy of the substrate $\gamma_{sv}$ [4], surrounded by a vapour phase $v$ (= air). Young [5], described the equilibrium between contact angle and these parameters for a three-phase system, exhibiting a thermodynamic equilibrium, according to:

$$\cos(\Theta) = \frac{\gamma_{sv} - \gamma_{sl}}{\gamma_{lv}}. \quad (1)$$

$\Theta$ is used for capturing the wettability of fluid-substrate systems in many applications. In the High Speed Inkjet field, the contact angle measurement of $\mu l$ drops of, for example, water is employed to quantify liquid behaviour during the printing process [6]. Furthermore, for wetting studies in the coating field [7, 8] the water contact angle is utilized to capture the change of surface characteristics by coating. Here, the water repellent behaviour is proven if water droplets exhibit a high $\Theta$ on the treated surface. In characterisation of membrane separation efficiency [9, 10] or for capturing membrane fouling [11, 12] the contact angle is a widely used and very popular parameter to quantify liquid-substrate interaction. A low $\Theta$ of a liquid drop on the membrane is observed for components, desired to move into the membrane. A high contact angle of fluids indicates low penetration tendency into the membrane. Also in quantification of liquid behaviour in and on powder packages this parameter is used to capture the interaction, showing sensitivity to powder compact preparation [13, 14].

Surprisingly, various drop sizes and measurement times are employed and this, following no strict regulations, during quantification of $\Theta$ in both industry and research. The variation of drop size, contact time between liquid and substrate and the deposition method of the liquid drop is given even within one research field. For example, liquids and drop sizes differ greatly in the characterisation of metal surfaces [15, 16]. Wettability studies using different drop sizes showed a size impact on the contact angle $\Theta$. Kumar et al. [17] gave insights in volume influence between $\sim 21\,\mu l$ and $\sim 35\ \mu l$ observing, that contact angle change on porous substrate is slightly slower for bigger droplets. Wang et al. [18] provided information about higher volume variation, ranging from $\sim 1\,nl$ to 6 $\mu l$ on textured substrate. He investigated rough surfaces showing prominent volume impact on $\Theta$ below $\mu l$ size scale, confirmed by results from Drelich et al. [19]. Thus, direct and quantitative comparison using the results of various drop sizes might deliver deviating characterisation of the wetting behaviour and will therefore need to be considered.

Furthermore, the absorption behaviour of the substrate with regard to the used liquid also affects $\Theta$ [13, 3, 20]. Researcher captured the substrate absorption impact on the contact angle by changing the porosity [21], pore diameter [22] or the effective permeability [23] of the absorptive substrate. They showed, that the higher these parameters are the higher was the contact angle decrease and liquid imbibition into the substrate. However, for deviating surface morphologies (isotropic open-porous structure, anisotropic structure, array of pillars, et cetera), the liquid behaviour changes, despite similar porosity or pore size [24, 25]. Thus, the porosity, pore diameter and the permeability are not suited to capture the absorption impact on $\Theta$.

Furthermore, surface tension affects the liquid when spreading on solids [26, 27]. Previous studies have carried out experiments to quantify the impact of this property on the liquid behaviour [28]. The investigation of surface tension impact was done between $50\,mN/m$ and $73\,mN/m$, indicating only minor effect on drop spreading within this range [29, 30].

It can be noted, that the substrate surface roughness affects $\Theta$ [31, 32]. Soltman et al. showed that an increase of roughness causes sharper drop corners, and thus impacts $\Theta$ hysteresis [33]. Also single contact angle values are affected by surface inhomogeneity. It was demonstrated, that lower substrate roughness leads to a decrease of the contact angle, measured from water droplets [34]. Thus, an increased hydrophobicity can be observed for higher roughness [35]. A common equation taking the unevenness of the substrate into account is the Wenzel law [31]. Here, the contact angle of the liquid is measured on the same surface, but being perfectly smooth. The cosine of this angle is then multiplied with a roughness parameter r, whereas $r > 1$. High r indicates high unevenness of the solid. The substrate roughness exaggerates the wetting properties [36]. The Wenzel equation is valid as long as the surface pattern dimension is lower than the liquid drop scale [37, 38, 39]. In our study, all substrates exhibit similar roughness parameter $S_q$, and thus roughness effects can be considered as similar on each of the used porous sheets.

### *1.1. Aim of the Work*

This study provides information about how to correctly capture the contact angle on absorptive substrates studying wettability. It highlights the influence of droplet size, fluid absorption, change of $\Theta$ over time and surface tension.

The particular advantage of our work is the investigation of an especially wide range of drop volumes covering three size scales of magnitude, from picoliter ($pl$) over nanoliter ($nl$) to microliter ($\mu l$) volume. This provides a quantitative analysis of drop size impact on contact angle.

Furthermore, the drop volumes are studied on four substrates with different absorption rates. Starting from almost non-absorbing ($0.6\ ml/(m^2 100ms)$) to strongly absorbing ($71\ ml/(m^2 100ms)$), capturing the impact of absorption behaviour on $\Theta$.

The wetting studies were carried out utilising liquids, which cover a surface tension region between 26.8 $mN/m$ and 73 $mN/m$ to capture the impact on liquid behaviour. The contact angle is investigated comparing an average contact angle for the $pl$ drop size range ($\Theta_{pl}$) and an average contact angle in the $\mu l$ size scale ($\Theta_{\mu l}$). This is especially helpful, since different liquid volumes are employed during industry liquid application and laboratory wettability quantification, capturing the impact of fluid quantity and surface tension on $\Theta$.

Furthermore, our approach provides an estimation of the contact angle change caused by increasing relative absorbed drop volume, capturing the combined effect of contact time, absorption rate and drop size.

## 2. Material and Methods

### *2.1. Testing Liquids*

We studied the impact of droplet size from 30 $pl$ to 4 $\mu l$ and substrate property with deionised water to capture the effect of drop size and fluid imbibition on the contact angle. The impact of surface tension was investigated, providing insights of drop size and surface tension impact on the contact angle. Five model fluids on a water base have been developed, covering a viscosity range from 1 $mPas$ to 8 $mPas$ and surface tension from 26.8 $mN/m$ to 73 $mN/m$. The liquid viscosity was adjusted using glycerol, surface tension was decreased utilizing hexanediol [3, 40]. 0.1 weight percent of naphthol blue black (98 %) were added to colour the liquids, showing no impact on liquid properties. For detailed liquid properties please have a look at Table 1.

A Thermo Fisher Haake Rheostress 6000 instrument was used to measure viscosity at 25°C, with a gap width of 0.5mm. 2ml were used at different shear rates: 10, 120, 230, 340, 450, 560, 670, 780, 890 and 1000 Hz. Surface tension was measured at 25 °C with a Sita science line t60 tensiometer, utilizing bubble pressure method. The bubble lifetime was from 0.05 to 2 seconds. A 25 $cm^3$ pyknometer was utilised to measure density.

### *2.2. Substrates*

In this study, the absorption rate is used to characterise the substrate, providing direct information about the liquid uptake. Four types of cellulose sheets are employed ranging from almost non-absorbing (0.6 $ml/(m^2 100\ ms)$) to strongly absorbing (71 $ml/(m^2 100\ ms)$) to capture the impact of absorption rate on the contact angle. Substrate properties are presented in Table 2, a more detailed description can be found in Table 1 in the electronic supplementary information (ESI). The quantification of the absorption rate is explained in section 2.2.1. The four cellulose sheets are classified in:

- strongly absorbing, the absorption rate is 71 $ml/m^2$ of water within 100 $ms$.
- Moderately absorbing, the substrate shows reduced liquid absorbency, due to lower porosity [41]. Water imbibition reduces to a value of 47 $ml/(m^2 100\ ms)$.
- Weakly absorbing. Surface modification decreases the water uptake to 39 $ml/m^2$ per 100 $ms$.
- Almost non-absorbing. This substrate was heavily treated employing sizing agents, reducing the surface free energy (see Table 2). This bulk sizing causes a hydrophobisation of the cellulose sheet. The absorption rate of water was 0.6 $ml/m^2$ within 100 $ms$. The word hydrophobised is used as a synonym for sized in this publication.

The pore size distribution was measured with mercury intrusion porosimetry, commonly used to characterize microscale pore size distribution [42, 43]. We employed an Autopore IV 9500 instrument from Micromeritics Instrument Corp [44]. Surface free energy was calculated applying the Owens-Wendt-Rabel-Kaelble (OWRK) method utilizing a Kruess device [45, 46] measuring droplets with a volume of 4 $\mu l$. The liquids used for the surface energy determination were diiodomethane and water. The roughness parameter $S_q$ captures the quadratic mean height of the substrate surface and was evaluated using an IFM alicona roughness measurement device, capturing the size scale of surface roughness. A fast Fourier transformation (FFT) - highpass filtering was used, applying a threshold wavelength of 3.5 $mm$.

#### *2.2.1. Liquid Absorption Rate*

The absorbing tendency of the investigated substrates was quantified employing a direct absorption measurement device, the automatic scanning absorptometer (ASA) [47]. Liquid is applied through a nozzle onto the substrate, detecting the direct transferred liquid volume into the substrate at different contact times between nozzle and porous sheet. The contact time between nozzle and substrate was reduced by the increase of the sample stage velocity. The liquid uptakes within 100 $ms$ are shown in Figure 1. Further measurement description can be found in the electronic supplementary information or in previous work of our group [3].

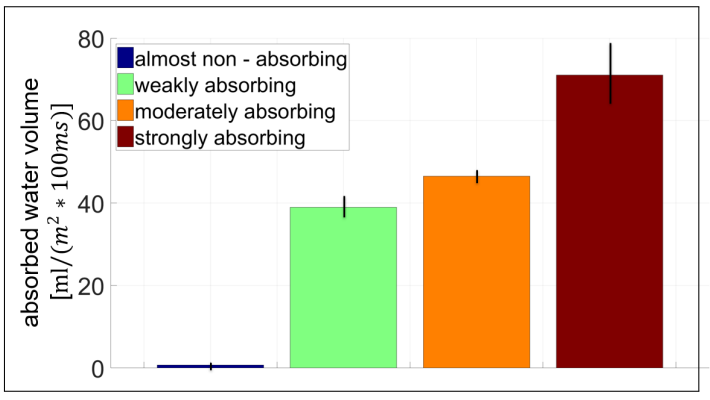


Figure 1: The absorbed water volume was measured with a direct absorption measurement device. The transferred liquid volume within 100 $ms$ is plotted for each substrate. The strongly absorbing sheet shows the highest liquid uptake. By contrast, the almost non-absorbing substrate exhibits a very low imbibed water volume within 100 $ms$.

Table 1: Properties of liquids used in this study. The surface tension ($\gamma$) of the liquids covers a value range from 28.8 $mN/m$ to 73 $mN/m$.

| Liquid | surface tension $\gamma$ $[mN/m]$ | viscosity $\eta$ $[mPas]$ | density $\rho$ $[kg/m^3]$ | water $[w\%]$ | glycerol $[w\%]$ | hexanediol $[w\%]$ | dye $[w\%]$ |
|---|---|---|---|---|---|---|---|
| $\gamma_{low}$ | 26.8 | 3 | 1.06 | 64.9 | 25 | 10 | 0.1 |
| | 27.5 | 7.2 | 1.12 | 41.9 | 48 | 10 | 0.1 |
| | 43.5 | 4.23 | 1.12 | 53.4 | 45 | 1.5 | 0.1 |
| | 67.6 | 7.99 | 1.14 | 42.4 | 57.5 | 0 | 0.1 |
| | 70.5 | 1.7 | 1.06 | 74.9 | 25 | 0 | 0.1 |
| $\gamma_{high}$ | 73 | 1 | 1 | 100 | - | - | - |

Table 2: Properties of the used substrates, classified by the absorption rate.

| Properties | strongly absorbing | moderately absorbing | weakly absorbing | almost non-absorbing |
|---|---|---|---|---|
| Absorbed water volume $[ml/(m^2 100ms)]$ | 71 | 47 | 39 | 0.6 |
| Porosity [%] | 40.3 | 38.8 | 23.6 | 20.6 |
| Average pore diameter $[\mu m]$ | 3.9 | 2.6 | 3.2 | 4.9 |
| Roughness parameter $S_q$ $[\mu m]$ | 3.6 | 2.4 | 3.1 | 4 |
| Dispersive surface energy $[mJ/m^2]$ | 44 | 42 | 43 | 33 |
| Polar surface energy $[mJ/m^2]$ | 27 | 23 | 22 | 0.1 |
| Total surface energy $[mJ/m^2]$ | 71 | 65 | 65 | 33.1 |

### *2.3. Contact Angle Measurement*

The **contact angle measurement** is the standard method for determining the wettability of a given liquid-substrate combination. The typical measurement procedure involves putting a drop of liquid on the substrate and recording images of this droplet over time. The angle between the tangent of the drop outline in the three-phase contact point and the substrate represents the contact angle. The higher $\Theta$, the worse is the wetting of the liquid on the surface. In this work we are creating drops of three size scales, picoliter ($pl$), nanoliter ($nl$) and microliter ($\mu l$). This provides information of drop size impact on contact angle utilizing a huge range of fluid volumes accompanied with a high size resolution. We employ different measurement setups for each of the three size scales in this study, always using a non-contact deposition method.

- Picoliter drops: The $pl$ contact angle measurements were performed using a dataphysics OCA200. The picoliter setup of this instrument creates drops of different sizes: 30 $pl$, 60 $pl$, 120 $pl$, 240 $pl$, 480 $pl$ and 960 $pl$. Generation of 960 $pl$ drops was done shooting two droplets in a row, coalescing before impingement on the surface of the substrate. A cartridge is filled with the test liquid and inserted into the dosing element of the $pl$ head. The dosing head creates a pulse, which squeezes out the liquid. The parameters pulse amplitude, pulse width and pulse frequency of the pulse can be varied, depending on the used testing fluid and drop size. The optimal settings can be found in the ESI in Table 2-7 for each used liquid. Further to this, a more detailed description of the $pl$ drop production is also available in the electronic supplementary information, section 3 and section 4.

- Nanoliter drops: $nl$ drops are created employing the OCA200 nanoliter setup. We create drops with a volume of: 5 $nl$, 15 $nl$, 30 $nl$, 60 $nl$, 120 $nl$, 240 $nl$ and 480 $nl$. This setup utilizes a tube with a shutter, generating a falling liquid beam. For detailed description please see ESI, section 3 and section 4.

- Microliter drops: The measurement of $\mu l$ drops was carried out with a Fibro DAT 1100 instrument [48], often used in industry. It generates droplets by pushing the liquid out of a tube with defined void volume creating volumes of 1 $\mu l$, 2 $\mu l$ or 4 $\mu l$. The collected fluid at the end of the tube creates a hanging drop and is slashed off with a spring, falling on the substrate. A detailed description of this procedure can be found in the previous work of our group [3].

All three measurement setups employ a camera recording images of the drop and use the same approach to evaluate the pictures: Once the liquid is released onto the substrate surface, the instrument starts image acquisition of the drop at different time rates, depending on the used device and drop size. The frame rate per second is 2000 for the lower $pl$ droplet sizes, 1000 for the $nl$ drops and 100 frames per second for the $\mu l$ volumes.

For each liquid, substrate and drop size combination, 40-95 drops were investigated with a distance of roughly 1 cm between them, utilizing at least four different sheets of the same substrate.

Furthermore, the image analyse of a contact angle measurement device also calculates the drop volume on the substrate over time. Thus, not only the contact angle is evaluated for each frame taken, but also the remaining quantity of liquid on the substrate.

## 3. Results

### *3.1. Impact of Drop Size and Absorption Rate*

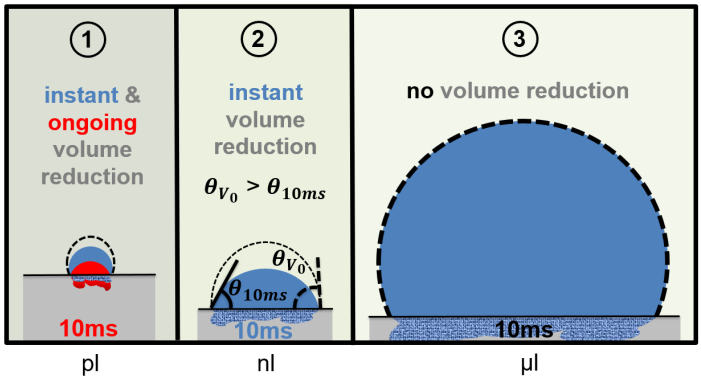


Figure 2: The contact angle on absorptive substrate for droplets within the *pl* scale is affected by instant and ongoing volume reduction, regime 1. Instant absorption reduces the originally created liquid volume $V_0$ (dashed line) already during liquid impingement on the porous sheet, and is thus not recorded. In the *nl* scale, $\Theta$ is only affected by instant volume reduction, regime 2. For $\mu l$ drops, regime 3, the imbibition does not influence the contact angle. The penetrated liquid quantity is so small in comparison to the applied volume, that it does not impact the contact angle.

Our results show three regimes of absorption impact on the contact angle. The liquid behaviour in each of these regimes is illustrated in Figure 2.

- Regime 1: In this liquid penetration regime, the drop is affected by instant absorption and ongoing penetration. Instant volume reduction is caused by roughness filling and liquid movement into the pore structure of the cellulose sheet during liquid arrival on the substrate. Thus, the originally applied/created volume (dashed line, $V_0$ in Figure 2) is not recorded. The moment at complete liquid application on the substrate is referred to as 0 *ms*. In regime 1 the ongoing drop penetration into the substrate strongly impacts the contact angle. The higher the absorption rate, the higher the fluid movement into the paper and the higher is the difference in absorbed drop volume between different contact times (red-part of liquid in Figure 2, regime 1).

  Drop sizes showing similar relative absorbed drop volumes for different contact times indicate regime 2.

- Regime 2: In this region, only instant volume reduction affects the contact angle. The theoretical contact angle $\Theta_{V_0}$ of a created volume $V_0$ without penetration impact is bigger than the contact angle $\Theta_{10ms}$, determined after 10 *ms* of contact time (see Figure 2). The bigger the applied drop volume, the more alike is the recorded drop volume on the substrate compared to the originally created volume $V_0$.

- Regime 3: Droplet volumes with a relative absorbed drop volume of around zero, even after longer contact, indicate regime 3. Here, no absorption impact on the contact angle occurs.

The absorbed drop volume over the originally produced liquid quantity $V_0$ is illustrated in Figure 3. Here, the absorbed volume [%] is the imbibed volume, normalised by initially created drop volume. The results immediately after full contact between substrate and liquid are represented by magenta squares ($= 0\ ms$). The relative imbibed liquid after roughly 10 *ms* of contact time between substrate and fluid is illustrated by red diamonds. The higher the absorption rate and/or the longer the contact time, the smaller the quantity of fluid on the absorptive substrate, and thus the higher is the relative absorbed volume.

As long as the relative absorbed drop volume between 0 *ms* and 10 *ms* shows a difference, the instant and ongoing volume reduction affects $\Theta$, regime 1. The liquid penetration regime 2 shows the same relative absorbed drop volume for 0 *ms* and 10 *ms* of contact time. Here, only instant volume reduction impacts the contact angle. Big drop volumes showing no detected instant and ongoing volume reduction, and thus no penetration effect on $\Theta$, indicate regime 3.

It can be observed, that the smallest droplet size ($30\,pl$), exhibits the highest relative absorbed drop volume ($\sim 55\,\%$) (Figure 3) and the lowest contact angle (Figure 4) for all four substrates compared to other volumes. This is valid for each of the tested sheets, regardless the absorption rate. The similar size scale of the substrate roughness ( $S_q \sim 5\ \mu m$) and the drop (sphere diameter $\sim 38\,\mu m$) might cause the high relative absorbed drop volume due to levelling out the inhomogeneity of the substrate surface.

Figure 4 shows the contact angle of water plotted over initially generated drop size on each of the four investigated substrates. The two signs illustrate two different contact times between substrate and liquid drop. 0 *ms* (blue square) represents the moment at drop impact, when the complete liquid is collected on the absorptive substrate surface. 10 *ms* (green diamond) reflects the results at a contact time of roughly 10 *ms* between sheet and fluid.

Interestingly, in the case of a great change in the relative absorbed drop volume, also a great difference in the contact angle can also be observed, decreasing with less relative absorbed volume. The absorbed liquid quantity of the different contact times converge for higher drop volumes with increasing absorption rate of the porous sheets.

The volume reduction can be neglected for $\mu l$ drops in comparison to the originally created volume. Here, the contact angle of all three $\mu l$ drop sizes is not affected by penetration within the first 10 *ms* of contact time. However, the contact angles differ between $\sim 2°$ and $\sim 10°$ for the three droplet sizes, showing that also additional effects, which are not captured e.g. the application method, causing a change in contact angle.

### *3.2. Contact Angle of pl and µl Volumes - Impact of Surface Tension on Θ*

Figure 5 shows the average contact angle $\Theta_{pl}$ of the *pl* range (60 *pl* - 480 *pl*, black circle immediately after impact and grey

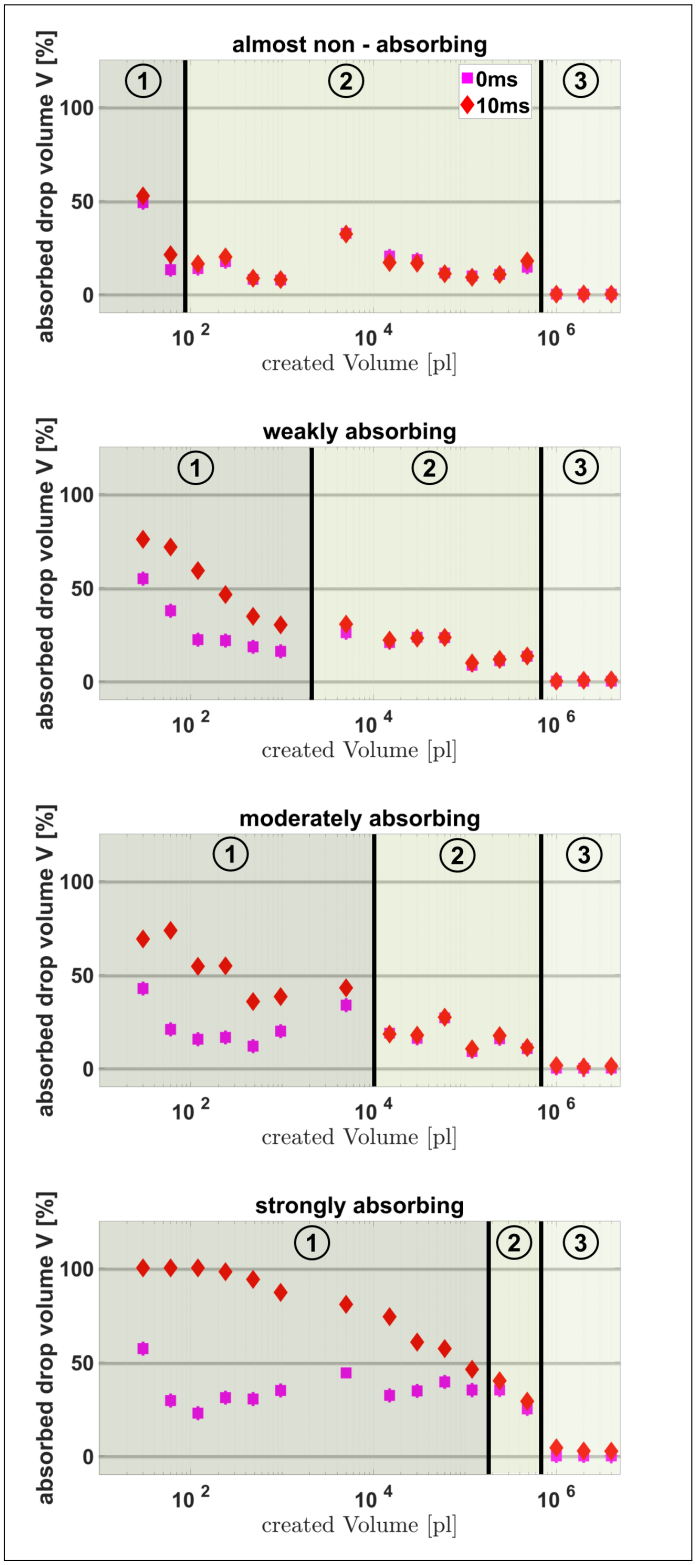


Figure 3: The absorbed drop volume [%] is the imbibed volume normalised by the created drop volume. This figure shows the absorbed drop volume at first full liquid contact with the sheet (0 $ms$) over generated drop size, represented by magenta squares. The errorbars represent a 95% confidence interval. Regime 1, regime 2 and regime 3 indicate three different absorption impacts on the contact angle, illustrated in Figure 2. The absorbed fluid quantity after roughly 10 $ms$ is represented by the red diamonds. The higher the absorption and/or the longer the contact time, the smaller is the fluid quantity above the substrate surface. And subsequently, the higher the relative absorbed drop volume. For the strongly absorbing substrate the 30 $pl$ - 240 $pl$ are completely absorbed after 10 $ms$, resulting in 100 % imbibed liquid volume.

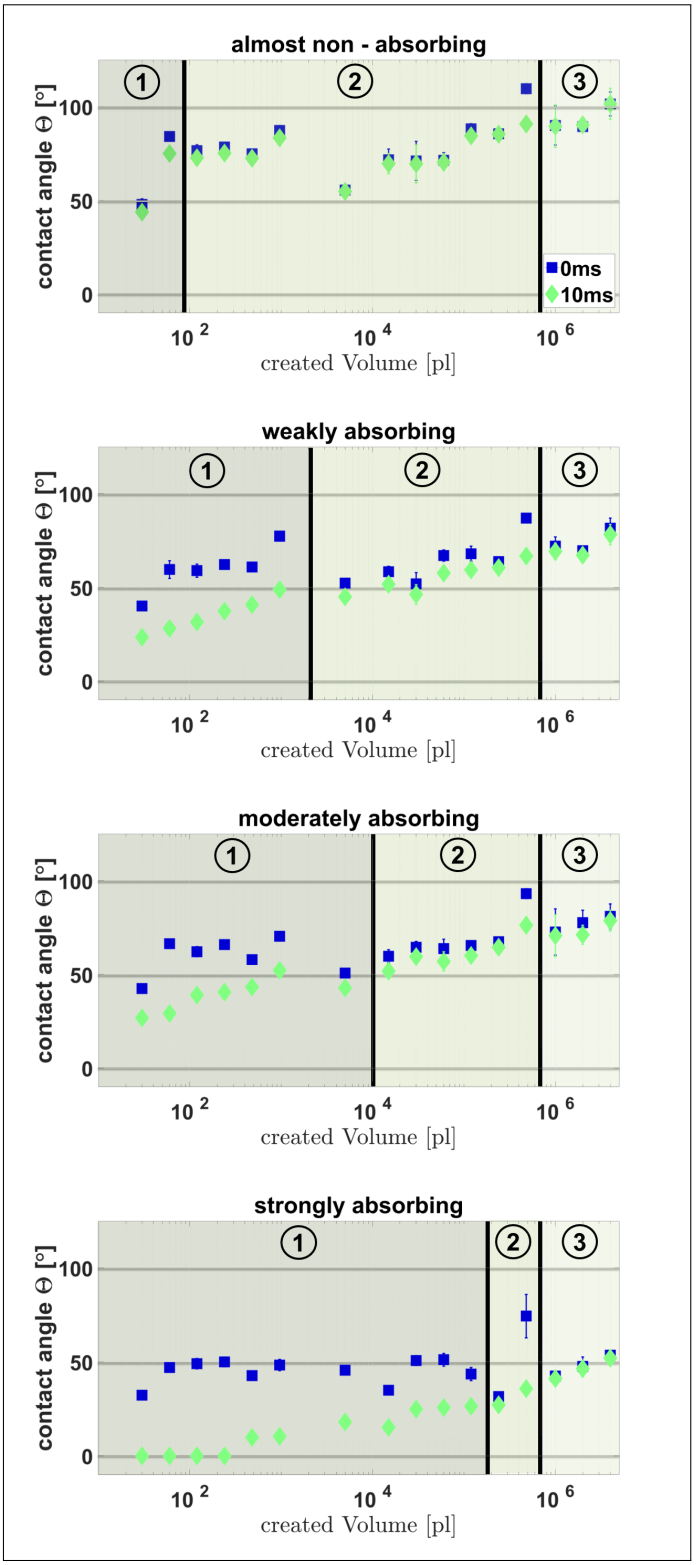


Figure 4: Contact angle at drop impact (0 $ms$, blue square) and after 10 $ms$ of contact time (green diamonds) are plotted versus created drop volume on each of the four investigated substrates. The errorbars represent a 95 % confidence interval. The absorption rate has a great impact on the change of contact angle with increased liquid volume. The longer the drop is in contact with the substrate, the higher the absorbed volume and the lower is the contact angle. For the strongly absorbing substrate the 30 $pl$ - 240 $pl$ are completely absorbed after 10 $ms$, thus no $\Theta$ can be measured and the values are set to zero. Regime 1, regime 2 and regime 3 indicate three different absorption impacts on the contact angle, illustrated in Figure 2.

square after 10 $ms$ of contact time) and the average value $\Theta_{\mu l}$ for the $\mu l$ region (1 $\mu l$ - 4 $\mu l$, dark blue triangle pointing left directly after drop application and green triangle pointing right after 10 $ms$ of contact between fluid and substrate). Looking at Figure 5, the results show a higher $\Theta_{pl}$ in comparison to $\Theta_{\mu l}$, focusing on liquids with low surface tension. Interestingly, the behaviour is reversed for liquids exhibiting high surface tension. The $\Theta$ values and 95 % of confidence interval values for $\mu l$ and $pl$ region are listed in the ESI, Table 9-12.

After 10 $ms$ of contact time, the behaviour of all liquids show the same tendency. The $pl$ contact angle is smaller than the $\mu l$ parameter $\Theta_{\mu l}$. This might be caused by the highly increased relative absorbed drop volume of the $pl$ drops, leading to a decrease in the contact angle.

### *3.3. Impact of Relative Absorbed Drop Volume on the Contact Angle (Time Independent)*

The contact angle is plotted versus the relative absorbed drop volume for all used substrates in Figure 6. The symbols coloured in blue are illustrate the contact angle of 4 $\mu l$ drops and symbols in black 60 $pl$ droplets.

It can be noted, that the same absorbed drop volumes are captured at different contact times between sheet and liquid. For example, the 4 $\mu l$ drop on the strongly absorbing substrate is observed for roughly 30 $s$ and the relative absorbed volume V reduces from 0 % to 60 % within this measurement time. In contrast to that, the first contact angle of the 60 $pl$ droplet is measured at V $\sim$ 30 % and is fully absorbed after $\sim$ 10 $ms$.

The slope k $[\frac{^\circ}{\%}]$ of the contact angle decay is expressed in Equation 2.

$$k = \frac{\Delta\Theta}{\Delta V} \tag{2}$$

Here, the difference in contact angle $\Delta\Theta$ [°] is divided by the change of the relative absorbed drop volume $\Delta V$ [%], grey lines in Figure 6.

V captures the combined effect of absorption rate, drop volume and contact time om $\Theta$. $R^2$ is the coefficient of determination for the regression line used to obtain k, showing high values ($\geq$ 0.95). The exact values for each drop size-porous sheet combination can be found in Table 3. The drop volumes and contact times for the slope k are similar for the investigated absorption rates. Independent of drop size, absorption rate and measurement time the contact angle decreases between $\sim$ 0.5° and 1.2° for an increase of 1 % in relative absorbed drop volume.

## 4. Conclusion

**Drop Size and Absorption Rate Impact on Contact Angle.** The main goal of this study was to investigate the impact of droplet size and substrate absorption rate on the contact angle $\Theta$. We use drop sizes spanning a factor $10^5$ in

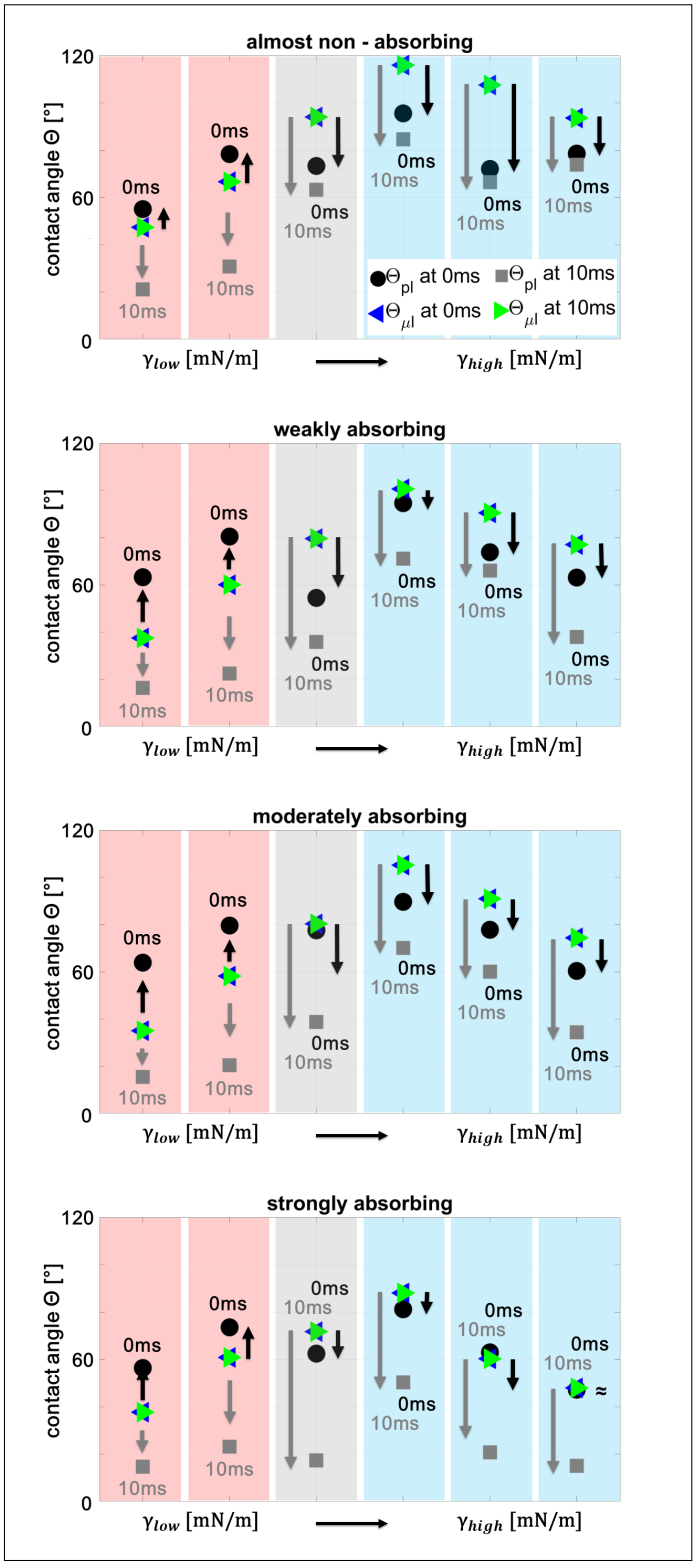


Figure 5: Effect of surface tension on contact angle change due to drop penetration. Average contact angle $\Theta_{pl}$ of 60 $pl$, 120 $pl$, 240 $pl$ and 480 $pl$ (black circle) and average contact angle $\Theta_{\mu l}$ of 1 $\mu l$, 2 $\mu l$ and 4 $\mu l$ drops (dark blue triangle pointing left) immediately after liquid application (0 $ms$) are plotted for liquids with different surface tension ($\gamma$). Also $\Theta_{pl}$ (grey square) and $\Theta_{\mu l}$ (green triangle) are plotted after 10 $ms$ of contact time. Low surface tension causes a lower $\Theta_{pl}$ in comparison to the $\Theta_{\mu l}$, whereas for high surface tensions, this behaviour is reversed. For 10 $ms$ of contact time between liquid and substrate the $\Theta_{pl}$ is for all liquids lower than $\Theta_{\mu l}$.

Table 3: The contact angle decay exhibits a slope k $[\frac{^\circ}{\%}]$, similar for all investigated drop size-porous sheet combinations. $R^2$ is the coefficient of determination for the regression line used to calculate k.

| created drop volume | strongly absorbing | | moderately absorbing | | weakly absorbing | | almost-non absorbing | |
|---|---|---|---|---|---|---|---|---|
| parameter | k $[\frac{^\circ}{\%}]$ | $R^2$ [-] | k $[\frac{^\circ}{\%}]$ | $R^2$ [-] | k $[\frac{^\circ}{\%}]$ | $R^2$ [-] | k $[\frac{^\circ}{\%}]$ | $R^2$ [-] |
| 60 $pl$ | 0.53 | 0.99 | 0.61 | 0.97 | 0.81 | 0.96 | 0.51 | 0.997 |
| 4 $\mu l$ | 0.43 | 0.99 | 1.11 | 0.95 | 1.40 | 0.95 | - | - |

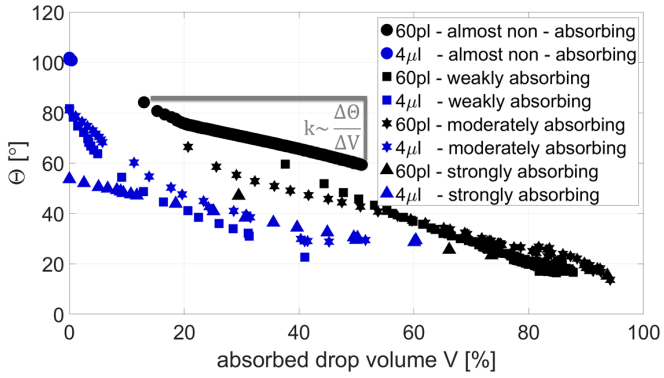


Figure 6: The contact angle Θ is plotted versus the relative absorbed drop volume V. The higher V, the lower is the contact angle, independent of the absorption rate, drop volume and contact time.

drop volume, starting from 30 $pl$ to 4 $\mu l$. Θ is measured immediately after first contact and after 10 $ms$ of contact between liquid and substrate.

Three regimes of liquid absorption impact can be observed. Regime 1, where the contact angle is affected by instant and ongoing volume reduction. Here, instant volume reduction is caused by roughness filling and liquid movement into the pore structure of the cellulose sheet during liquid arrival on the substrate. This regime can be observed for small droplets and high absorptive sheets. In regime 2, Θ is only affected by the instant volume reduction. Here, either the liquid penetration is so small or the liquid volume is so large that no visible loss in drop volume can be observed. In the case of big droplets ($\mu l$) the drop volume is so large, that the contact angle is not affected by absorption, regime 3.

The wetting studies are carried out on four substrates exhibiting different water absorption rates, ranging from almost non-absorbing (0.6 $ml/(m^2 100ms)$) to strongly absorbing (71 $ml/(m^2 100ms)$). Several researchers studied Θ on absorptive substrates tuning the absorption behaviour by changing the porosity [21] and pore diameter [22]. They showed, that the higher these parameters are the greater the contact angle decrease and liquid imbibition into the substrate. However, for deviating surface morphologies, bulk and surface chemistry treatments, the liquid behaviour changes, despite similar porosity or pore size [24, 25]. Our results suggest, that the quantification of the absorption rate captures the substrate impact on the liquid behaviour very well. Considering the strong relationship between relative absorbed drop volume and contact angle, one of our conclusions is that the absorption rate of the substrate is the underlying impact factor on the measured contact angle, which explains the earlier observed influence of pore size distribution and surface chemistry.

**Surface Tension Impact on Contact Angle for $pl$ and $\mu l$ Drops.** We investigated the average $pl$ contact angle $\Theta_{pl}$ of 60 $pl$, 120 $pl$, 240 $pl$ and 480 $pl$ and the average $\mu l$ contact angle $\Theta_{\mu l}$ of 1 $\mu l$, 2 $\mu l$ and 4 $\mu l$ drops. Whereas investigation of surface tension within 50 $mN/m$ and 73 $mN/m$ showed slight differences on contact angle [29, 30], we noticed for a property window between 26 $mN/m$ and 73 $mN/m$ strong influence. For high surface tension we find a $\sim 10^\circ$ to $\sim 15^\circ$ higher contact angle for $\mu l$ drops than for $pl$ droplets. This behaviour is reversed for low surface tension values. Our results show a $\sim 10^\circ$ to $\sim 15^\circ$ lower contact angle for $\mu l$ drops than for $pl$ droplets using a liquid with low surface tension.

**Impact of Relative Absorbed Drop Volume on the Contact Angle** Independent of drop size, absorption rate and measurement time the contact angle decreases between $\sim 0.5^\circ$ to $\sim 1.2^\circ$ for each percentage of relative absorbed drop volume V. Thus, V fully captures the combined effect of drop size, contact time and substrate absorption rate. An increase of 10 % absorbed drop volume cause a contact angle decrease of $\sim 5^\circ$ to $\sim 12^\circ$, which is a considerably quantity.

In summary our results show, that the drop volume as well as the absorption rate of the substrate affect the contact angle, highlighting the importance of liquid penetration impact.

Thus, for a correct and stable measurement of the contact angle, it is necessary to use high drop volumes and capture Θ immediately after drop application, eliminating the penetration impact. If the absorption rate is too high or the drop size is restricted to a specific value, however we recommend calculating the relative absorbed drop volume V and obtaining the contact angle always at same values for V. Thus, the relative absorbed drop volume fully captures the combined effect of drop volume, contact time and substrate absorption rate.

*Outlook.* We wish to further investigate the liquid polarity impact on contact angle, on self hydrophobised substrates.

## 5. Acknowledgements

The financial support by the Austrian Federal Ministry for Digital and Economic Affairs and the National Foundation for Research Technology and Development is gratefully acknowledged. Furthermore, the authors wish to thank Océ -Canon, Mondi, Kelheim Fibres and SIG Combibloc for their financial support. Special Thanks to Anna Fellner and Johann

Schwarzl for the support during the work on over 18000 drop measurements.

## References


[1] H. Wijshoff. Drop dynamics in the inkjet printing process. *Current Opinion in Colloid & Interface Science*, 36:20–27, 2018.

[2] R. K. Holman, M. J. Cima, S. A. Uhland, and E. Sachs. Spreading and Infiltration of Inkjet-Printed Polymer Solution Droplets on a Porous Substrate. *Journal of Colloid and Interface Science*, 249(2):432–440, 2002.

[3] K. Sarah and H. Ulrich. Short timescale wetting and penetration on porous sheets measured with ultrasound, direct absorption and contact angle. *RSC Adv.*, 8(23):12861–12869, 2018.

[4] K. Y. Law and H. Zhao. *Surface wetting: Characterization, Contact Angle, and Fundamentals*. Springer, 2016.

[5] T. Young. An Essay on the Cohesion of Fluids. *Philosophical Transactions of the Royal Society of London*, 95(65), 1805.

[6] K. Mielonen, P. Geydt, M. Österberg, L. S. Johansson, K. Backfolk, S.-S. Ovaska, T. Laukala, and K. Backfolk. Inkjet ink spreading on polyelectrolyte multilayers deposited on pigment coated paper. *Journal of Colloid and Interface Science*, 438(3):179–190, 2015.

[7] J. Wang, H. Guo, X. Shi, Z. Yao, W. Qing, F. Liu, and C. Y. Tang. Fast polydopamine coating on reverse osmosis membrane: Process investigation and membrane performance study. *Journal of Colloid and Interface Science*, 535:239–244, 2019.

[8] W. Li, X. Zhang, X. Yu, G. Wu, Y. Lei, G. Sun, and B. You. Journal of Colloid and Interface Science Near infrared light responsive self-healing superhydrophobic coating based on solid wastes. *Journal of Colloid And Interface Science*, 560:198–207, 2020.

[9] L. Shen, Y. Zhang, W. Yu, R. Li, M. Wang, Q. Gao, J. Li, and H. Lin. Fabrication of hydrophilic and antibacterial poly(vinylidene fluoride) based separation membranes by a novel strategy combining radiation grafting of poly(acrylic acid) (PAA) and electroless nickel plating. *Journal of Colloid and Interface Science*, 543:64–75, 2019.

[10] N. Subramanian, A. Qamar, A. Alsaadi, A. Gallo, M. G. Ridwan, J. G. Lee, S. Pillai, S. Arunachalam, D. Anjum, F. Sharipov, N. Ghaffour, and H. Mishra. Evaluating the potential of superhydrophobic nanoporous alumina membranes for direct contact membrane distillation. *Journal of Colloid and Interface Science*, 533:723–732, 2019.

[11] S. Muthu, A. Childress, and J. Brant. Propagation-of-uncertainty from contact angle and streaming potential measurements to XDLVO model assessments of membrane-colloid interactions. *Journal of Colloid and Interface Science*, 428:191–198, 2014.

[12] J. M. Dickhout, E. Virga, R. G. Lammertink, and W. M. de Vos. Surfactant specific ionic strength effects on membrane fouling during produced water treatment. *Journal of Colloid and Interface Science*, 556:12–23, 2019.

[13] L. Susana, F. Campaci, and A. C. Santomaso. Wettability of mineral and metallic powders: Applicability and limitations of sessile drop method and Washburn's technique. *Powder Technology*, 226:68–77, 2012.

[14] S. Kirdponpattara, M. Phisalaphong, and B.-m. Z. Newby. Applicability of Washburn capillary rise for determining contact angles of powders/porous materials. *Journal of Colloid and Interface Science*, 397:169–176, 2013.

[15] D. Megias-Alguacil, E. Tervoort, C. Cattin, and L. J. Gauckler. Contact angle and adsorption behavior of carboxylic acids on $\alpha$-Al2O3 surfaces. *Journal of Colloid and Interface Science*, 353(2):512–518, 2011.

[16] J. Sun, C. Chen, J. Song, J. Liu, X. Yang, J. Liu, X. Liu, and Y. Lu. A universal method to create surface patterns with extreme wettability on metal substrates. *Journal of Colloid and Interface Science*, 535:100–110, 2019.

[17] S. M. Kumar and A. P. Deshpande. Dynamics of drop spreading on fibrous porous media. *Colloids and Surfaces A: Physicochemical and Engineering Aspects*, 277:157–163, 2006.

[18] R. Wang and S. Bai. Effect of droplet size on wetting behavior on laser textured SiC surface. *Applied Surface Science*, 353:564–567, 2015.

[19] J. Drelich, J. D. Miller, and J. Hupka. The Effect of Drop Size on Contact Angle over a Wide Range of Drop Volumes. *Journal of Colloid and Interface Science*, 155(2):379–385, 1993.

[20] L. L. Popovich, D. L. Feke, and I. Manas-Zloczower. Influence of physical and interfacial characteristics on the wetting and spreading of fluids on powders. *Powder Technology*, 104(1):68–74, 1999.

[21] J. B. Lee, D. Derome, and J. Carmeliet. Drop impact on natural porous stones. *Journal of Colloid and Interface Science*, 469:147–156, 2016.

[22] A. Clarke, T. D. Blake, K. Carruthers, and A. Woodward. Spreading and imbibition of liquid droplets on porous surfaces. *Langmuir*, 18(8):2980–2984, 2002.

[23] L. Espín and S. Kumar. Droplet spreading and absorption on rough, permeable substrates. *Journal of Fluid Mechanics*, 784:465–486, 2015.

[24] T. Gambaryan-Roisman. Liquids on porous layers: Wetting, imbibition and transport processes, aug 2014.

[25] L. Bacri and F. Brochard-Wyart. Droplet suction on porous media. *European Physical Journal E*, 3(1):87–97, 2000.

[26] P. Letellier, A. Mayaffre, and M. Turmine. Drop size effect on contact angle explained by nonextensive thermodynamics. Young's equation revisited. *Journal of Colloid and Interface Science*, 314(2):604–614, 2007.

[27] A. Mohammad Karim, J. P. Rothstein, and H. P. Kavehpour. Experimental study of dynamic contact angles on rough hydrophobic surfaces. *Journal of Colloid and Interface Science*, 513:658–665, 2018.

[28] A. Han, G. Mondin, N. G. Hegelbach, N. F. de Rooij, and U. Staufer. Filling kinetics of liquids in nanochannels as narrow as 27 nm by capillary force. *Journal of Colloid and Interface Science*, 293(1):151–157, 2006.

[29] M. Toivakka. Numerical investigation of droplet impact spreading in spray coating of paper. In *Symposium TAPPI Advanced Coating Fundamentals Symposium*, 2003.

[30] M. Pasandideh-Fard, Y. M. Qiao, S. Chandra, and J. Mostaghimi. Capillary effects during droplet impact on a solid surface. *Physics of Fluids*, 8(3):650–659, 1996.

[31] R. N. Wenzel. Resistance of solid surfaces to wetting by water. *Industrial and Engineering Chemistry*, 28(8):988–994, 1936.

[32] B. D. Cassie and S. Baxter. Wettability of porous surfaces. *RSC*, (5):546–551, 1944.

[33] D. Soltman, B. Smith, S. J. Morris, and V. Subramanian. Inkjet printing of precisely defined features using contact-angle hysteresis. *Journal of Colloid and Interface Science*, 400:135–139, 2013.

[34] A. Terriza, R. Álvarez, A. Borrás, J. Cotrino, F. Yubero, and A. R. González-Elipe. Roughness assessment and wetting behavior of fluorocarbon surfaces. *Journal of Colloid and Interface Science*, 376(1):274–282, 2012.

[35] R. Kaltenbach, D. Diehl, and G. E. Schaumann. Links between nanoscale and macroscale surface properties of natural root mucilage studied by atomic force microscopy and contact angle. *Journal of Colloid and Interface Science*, 516:446–455, 2018.

[36] Z. Cao, M. J. Stevens, J. M. Y. Carrillo, and A. V. Dobrynin. Adhesion and wetting of soft nanoparticles on textured surfaces: Transition between Wenzel and Cassie-Baxter states. *Langmuir*, 31(5):1693–1703, 2015.

[37] A. Marmur and E. Bittoun. When Wenzel and Cassie are right: Reconciling local and global considerations. *Langmuir*, 25(3):1277–1281, 2009.

[38] X. Yong and L. T. Zhang. Nanoscale wetting on groove-patterned surfaces. *Langmuir*, 25(9):5045–5053, 2009.

[39] E. M. Grzelak and J. R. Errington. Nanoscale limit to the applicability of Wenzel's equation. *Langmuir*, 26(16):13297–13304, 2010.

[40] S. Krainer, C. Smit, and U. Hirn. The effect of viscosity and surface tension on inkjet printed picoliter dots. *RSC Advances*, 9(54):31708–31719, 2019.

[41] P. Resch, W. Bauer, and U. Hirn. Calendering effects on coating pore structure and ink setting behavior. *Tappi Journal*, 9(1):27–35, 2010.

[42] M. G. Ventura, A. I. Paninho, A. V. Nunes, I. M. Fonseca, and L. C. Branco. Biocompatible locust bean gum mesoporous matrices prepared by ionic liquids and a scCO2 sustainable system. *RSC Advances*, 5(130):107700–107706, 2015.

[43] L. Roiban, G. Foray, Q. Rong, A. Perret, D. Ihiawakrim, K. Masenelli-Varlot, E. Maire, and B. Yrieix. Advanced three dimensional characterization of silica-based ultraporous materials. *RSC Advances*, 6(13):10625–10632, 2016.

[44] P. Resch, W. Bauer, and U. Hirn. Pore Structure Change due to Calendering and its Effect on Ink Setting Behaviour – Review and Novel Findings. In *Advanced Coating Fundamentals Symposium*, pages 58 – 72, 2008.

[45] D. K. Owens and R. C. Wendt. Estimation of the surface free energy of polymers. *Journal of Applied Polymer Science*, 13(8):1741–1747, 1969.

[46] Y. Luo, Y. Zhao, Y. Duan, and S. Du. Surface and wettability property analysis of CCF300 carbon fibers with different sizing or without sizing. *Materials & Design*, 32(2):941–946, 2011.

[47] C. Kuijpers, T. van Stiphout, H. Huinink, N. Tomozeiu, S. Erich, and O. Adan. Quantitative measurements of capillary absorption in thin porous media by the Automatic Scanning Absorptometer. *Chemical Engineering Science*, 178:70–81, 2018.

[48] A. Hladnik. Dynamic wetting and liquid sorption in paper - Fibro 1100 Dat measuring. *Papier*, 25:44–48, 1997.

## List of Figures



## List of Tables

Chapter 9

# Conclusions

Liquid penetration and wetting on paper during High Speed Inkjet (HSI) printing was investigated in this work. Four main findings have been reported.

Laboratory measurements were employed to quantify liquid behaviour during industrial printing processes, providing valuable insights into the determining process parameters of wetting and penetration. Three commonly used measurement methods have been compared: Ultrasonic liquid penetration measurement (ULP), contact angle measurement and automatic scanning absorptometer (ASA) measurement. These techniques also implement three different measurement principles, and thus render the comparison of the predictive quality among these devices a challenging task. Parameters for liquid spreading and absorption speed for each of the three methods have been introduced. The penetration parameter detected by the ultrasonic liquid penetration measurement and the automatic scanning absorptometer are similar to each other. In contrast to that, the penetration speed of single 4 $\mu l$ drops showed no correlation to the ULP values, neither to the ASA results. A possible reason for this might be the difference of applied liquid quantity. A limited drop volume is used for the contact angle measurements, whereas the ASA and the ULP use a virtually unlimited liquid supply. Thus, it is concluded that the penetration behaviour of droplets and unlimited liquid supply follow different mechanism, also found by Danino [63]. Regarding the wetting, we did not find any correlation between the three measurement techniques. The ULP is not able to detect the fast wetting of unsized papers. Furthermore, the ASA wetting parameter calculated from the imbibed liquid volume is strongly

influenced by penetration, affecting the spreading quantification. Thus, the very popular contact angle measurement seems to be the best choice capturing the wettability. Subsequently, we also introduced a parameter analysing wetting and penetration, the contact angle curve decay. Here, a moderate correlation between the calculated wetting parameter from the ASA measurements and the slope of the contact angle curve is obtained.

Five model liquids with different surface tensions and viscosities were created. Their development was guided by the Ohnesorge number and the Reynolds number to ensure that these fluids can be used for jetting with a HSI printhead. Four paper grades, which posses different bulk and surface treatments were investigated with regard to the impact of liquid imbibition and wetting during the HSI printing. These four grades were an all purpose office paper with AKD bulk sizing, an uncoated HSI paper, a pigmented HSI paper and a base paper. The base paper grade has been treated as the raw material of the others. The papers varied in surface treatment and sizing, representing the uncoated paper grades on the market for HSI printing papers.

The investigation of wetting and spreading during the HSI printing process was done by evaluation of printed single dot pattern and full-tone printed sheets. The impact of liquid property, paper property and two droplet sizes (30 *pl* and 120 *pl*) on the High Speed Inket (HSI) print was evaluated. Dot area is a measure for drop spreading and the print through of full-tone printed sheets quantifies the liquid penetration. The evaluated light absorption captures the surface coverage of printed dots. Our results show that viscosity is the parameter of highest impact for drop spreading, penetration and surface coverage. An increase of viscosity results in a reduced value for these parameters. When dealing with sized paper, surface tension is important as well due to the changed surface energy of the sized paper. Here, an increase in surface tension reduces dot spreading and liquid penetration. In terms of surface coverage, not only viscosity but also surface tension had an effect on the results of all papers. Increased surface coverage was achieved for higher surface tension, independent of drop size and paper grade. The observations made are valid for 30 *pl* and 120 *pl* droplet sizes.

The prediction power of laboratory devices in terms of wetting and penetration was quantified by direct comparison of results achieved from the print analysis and the laboratory measurement results. The dot spreading was evaluated by comparing the dot area of

printed 30 *pl* and 60 *pl* drops to the contact angle of 30 *pl*, 60 *pl*, 2 $\mu l$ and 4 $\mu l$ volumes. Here, the correlation between *pl* drop contact angle and the printed dot area and $\mu l$ drop contact angle and dot area were similar.

It can be observed that the predictability decreases with an increase in absorption rate of the paper and longer contact times. The penetration during HSI-printing was quantified with the print through value and compared to the penetration speed measured by the ultrasonic liquid penetration measurement and the automatic scanning absorptometer. A high correlation was found for sized papers, decreasing with increasing absorption rate of the paper.

Finally, the impact of droplet size, surface tension and paper absorption rate was investigated. Therefore, the water contact angle between 30 *pl* and 4 $\mu l$ was evaluated. The higher the absorption rate of the paper, the bigger was the observed drop size impact on the contact angle. The liquid surface tension impact was screened by calculating an average *pl* contact angle and an average $\mu l$ contact angle. This study (manuscript IV) showed how to correctly measure the contact angle on absorptive media, highlighting the impact of fluid absorption and contact angle change over time. It is recommended to use the contact angle of $\mu l$ drops immediately after drop application to quantify wetting, minimising the influence of penetration on the spreading process. However, for substrates with a too high absorption rate and/or small drop volumes the contact angle needs to be measured at the same relative absorbed drop volume V. V captures the combined impact of liquid volume, paper absorption rate and contact time.

Furthermore, for high values of liquid surface tension, a higher contact angle was observed for $\mu l$ droplets compared to results of the *pl* range. This behaviour was reversed for liquids with low surface tension.

# Chapter 10

# Appendix

# Electronic Supplementary Information to "The Effect of Viscosity and Surface Tension on High Speed Inkjet Printed Picoliter Dots"

## 1 Materials and Methods

### 1.1 HSI printhead and drop volume

Evoked from the different viscosity and surface tension of the liquids, the produced droplets have some deviation in their volume when using the same print head settings as frequency and electric wave form. Therefore it was necessary to measure the exact drop volume at each print setting. 500 sheets were printed with a defined dot pattern. The difference in reservoir liquid before and after printing divided by the amount of droplets was used to calculate the actual average drop volume for each setting. The deviation from the target drop size was at maximum 5% for the 30pl drops and 3.3% for the 120pl drops.

#### 1.1.1 Operational Field of the HSI printhead

The Oh number helps to predict fluid flow break up and thus droplet formation. It is the ratio between viscous forces to surface tension and inertia. A higher value indicates a danger for nozzle blocking due to e.g. a too viscous liquid (Figure 1 in the main article, blue region), where as a too low Oh might cause drop splashing and satellite drops (Figure 1 in the main article, red region and area between dashed line and right corner)). According to literature, fluids with an Ohnesorge value Oh between 0.1 and 1 are jetable in HSI printing. The Reynolds (Re) number relates the inertial to the viscous forces. The characteristic length l [m] is the nozzle width (0.02 mm). The speed of the droplets was constant at circa $8m/s$. Above the critical Re number the laminar flow turns into a turbulent flow, the critical value for a tube flow is around 2300. In the HSI field, the Re number is stated to be between 2 and 160 to have a printable fluid (see Figure 1 in the main article) [1]. A too low Reynolds number can result in a continuous liquid jet without separation of the drops, see Figure 1 in the main article, green region, in the main article.

### 1.2 Print through test (PT)

First a quadratic 5x5cm$^2$ square on the backside (BS in Figure 3 in the main article) of the unprinted paper is imaged in front of a coloured background. It is important that the colour of this background is identical to the colour of the test ink. This image gives the pure shine through of the coloured background without any ink penetration. Then the paper is printed on the top side (TS

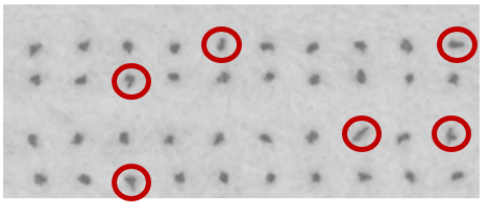

Figure 1: Picture of the printed dot pattern. The dots with an axis ratio below 0.85 are excluded and marked with a red circle. The variability of the drop area is generated by the heterogeneity of the paper.

in Figure 3 in the main article) and the same 5x5cm$^2$ area of the backside of the now printed paper is imaged again (shown on the right side of Figure 3 in the main article). The images are taken using a microscope (Alicona Infinite Forcus) with diffusive illumination to eliminate surface shading effects due to the paper roughness. The final image of size 5x5cm$^2$ is stitched together from 10x10 overlapping images taken by the instrument. Illumination artifacts were removed by frequency domain image filtering.

The ink penetration index PT [-] is calculated from the ratio between the gray value of the unprinted sample backside image to the gray value of the printed sample backside image, Equation 3 in the main article.

## 1.3 Image analysis of printed dots

The used papers have a gray average of around 220. Axis ratio AR is a shape descriptor of the dot, where two perpendicular axes are fit to the dot area and AR [-] is the ratio of the shorter axis length to the longer axis length. A value of 1 describes a perfectly round object, increasingly lower values indicate a more and more elongated shape.

A printed drop pattern is shown in Fig. 1. Despite detailed evaluation of the printed dot pattern for developing liquids with good jetability, there is still some drop splashing. Another point, which needs to be considered is, that due to small droplet size and low color density of the dots, the dot area on the paper surface is not always detected correctly. Thus we decided to only evaluate dots with an aspect ratio higher than 0.85. This filter eliminates all dots which are fragmented due to image segmentation problems or exhibit drop splashing (i.e. dots with satellite drops), which are diluting the measurement results. Figure 1 shows the dots as printed in the trial. The picture also indicates drops with AR below 0.85 (red circles), which are not included in the evaluation. The area of the droplet is a parameter for drop spreading.

Please note that liquid penetration and liquid spreading have the opposite effect on light absorption, LA increases with drop spreading (higher dot area $A$) and decreases with liquid penetration (lighter dot, hence lower $\Delta GA$).

### 1.3.1 Experimental Error

Local variation of paper properties within one sheet is large, leading to large variations in the local print appearance [2], which has e.g. been shown for local print density [3] and local printing ink penetration [4]. Thus for quantitative evaluation of print results it is mandatory to test a large enough specimen area or several smaller areas sampled from different regions of the paper. We printed each liquid on 6 different sheets from the same paper grade and analysed 3 to 7 regions of this printed area with at least 1.5 centimeters space between these regions. Excluding droplets with an aspect ratio less than 0.85, we ended up with an average amount of 200-600 droplets per liquid paper combination. The difference is caused by the droplet size itself, bigger droplets need more area than the smaller ones and thus less drops can be printed in one region with one nozzle firing. We computed 95% confidence limits for each test result by counting each evaluated region as one specimen, the number of independent samples per test point therefore was between 18 and 42, considering that we tested 6 sheets with 3-7 regions each.

# References


[1] G. H. McKinley and M. Renardy. Wolfgang von Ohnesorge. *Physics of Fluids*, 23(127101), 2011.

[2] U. Hirn, M. Lechthaler, and W. Bauer. Registration and point wise correlation of local paper properties. *Nordic Pulp and Paper Research Journal*, 23(4):374–381, 2008.

[3] W. Fuchs, M. Dauer, U. Hirn, and W. Bauer. A memory effect in sheet-fed offset printing. In *Paper Conference and Trade Show, PaperCon 2017: Renew, Rethink, Redefine the Future*, volume 2, page 1098, 2017.

[4] C. Kappel, U. Hirn, M. Donoser, and W. Bauer. Measurement of Printing Ink Penetration in Uncoated Papers and Its Influence on Print Quality. *94th Annual Meeting, Pulp and Paper Technical Association of Canada*, pages 539–542.

# Electronic Supplementary Information to "Predicting High Speed Inkjet dot spreading and penetration from ultrasonic and direct absorption testing and picoliter contact angle"

## 1. Ultrasonic Liquid Penetration Measurement (ULP)

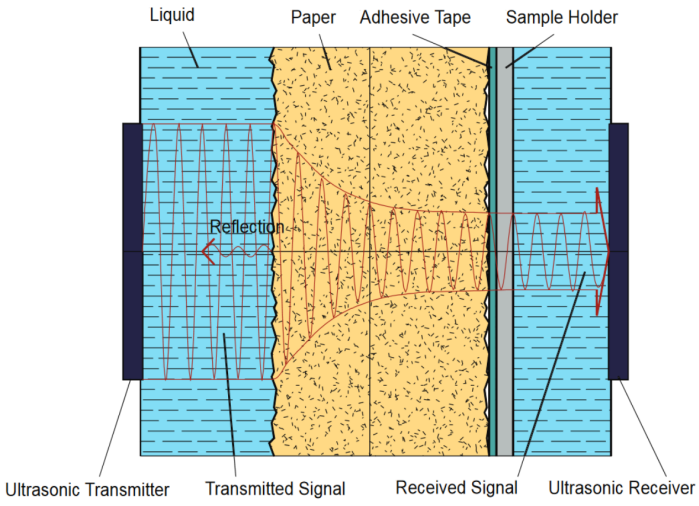


Figure 1: Measurement principle of the ultrasonic liquid penetration (ULP) measurement, drawing not to scale [1, 2].

The Emtec Penetration Dynamics Analyser 2.0 was used for all ultrasonic measurements. Measurement frequency was set to 2 MHz. The paper samples were cut to a rectangle of 7cm×5cm and fastened to the sample holder with a two sided adhesive tape. In the measurement cell an ultrasonic emitter and an ultrasonic receiver are placed to the opposite of each other, shown in Figure 1. When the sample is released into the testing cell filled with liquid, the transmitter instantly starts to send ultrasonic waves through the sample. The receiver measures the intensity of the ultrasonic signal. Sensor area is a circle with a diameter of 35mm. The ultrasonic waves are reflected, scattered or absorbed during the process of liquid penetration, represented through the red lines in Figure 1. As penetration of the liquid in the substrate proceeds, the receiver records the changes in the signal. The result is the ultrasound intensity over time [1].

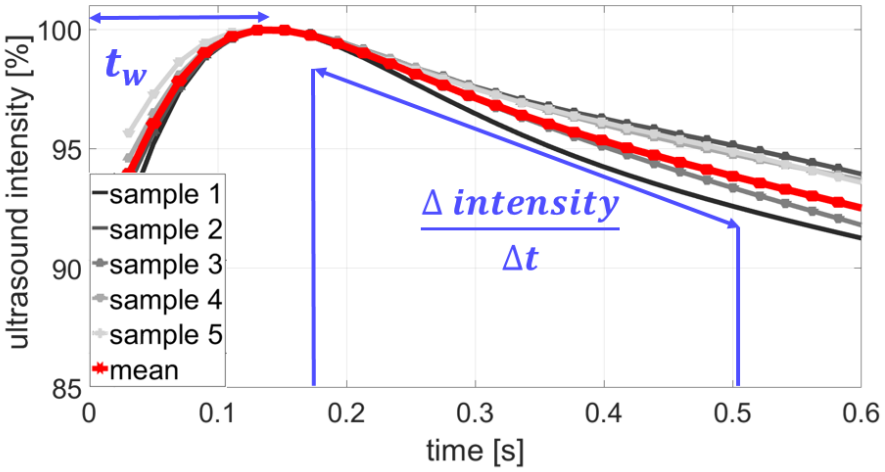


Figure 2: The ultrasonic measurement results show the change of ultrasound intensity over time. Time at the highest intensity $t_w[s]$ is defined as wetting time of the liquid and the slope of the curve as the penetration speed $[\frac{\Delta intensity}{(\Delta t)}]$of the liquid into the paper in $[\frac{1}{s}]$ [2].

A typical measurement result is shown in Figure 2, it is from the AKD sized paper with one dye ink. The curves are results from 5 specimen of the same paper (grey) and their mean value (red). The wetting is represented as the wetting time, which is the time between liquid contact and the highest intensity. (wetting time $t_w$ in Figure 2). The longer it takes to reach 100% intensity, the lower is the wetting. The penetration speed is calculated between the time at the highest intensity and approximately 200ms for unsized papers and around 1s for hydrophobized papers after this time. The faster the liquid penetrates into the paper, the higher is the change in ultrasound intensity and the steeper is the slope of the curve $\frac{\Delta intensity}{\Delta t}$ (Figure 2). This is also available in previous work of our group [2].

## 2. Automatic Scanning Absorptometer (ASA)

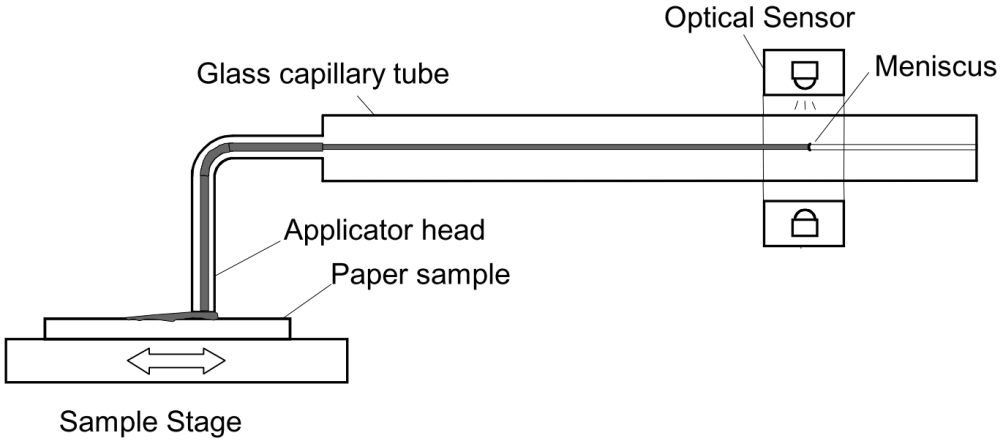


Figure 3: The automatic scanning absorptometer set up. The applicator head on the paper sample is moved over the paper, ink is supplied with the liquid via a glass tube. The meniscus sensor follows the receding meniscus and computes the amount of liquid, which is absorbed in the paper. Adapted from Enomae et al. [3, 2]

The Automatic Scanning Absorptometer measurement, performed with a KM500win Automatic Scanning Absorptometer instrument from KRK Kumagai (Japan), provides quantitative information about the liquid absorption as a function of time on time scales of 10 ms up to 10 s.[3, 4] During an SA measurement, liquid is supplied from a scanning head which moves along a spiral path on the paper. In Figure 3 one can see the head on the paper sample surface, it is supplied with the liquid via a tube. The speed of the head moving over the paper surface is kept constant over a certain part of the track, then it accelerates stepwise to a higher speed which is then again kept constant. By increasing the speed the system measures the liquid penetration for different times of contact between the Orifice and the paper. The ASA measures the total absorbed liquid volume per unit area. The penetration speed is represented by the slope $\frac{\Delta TLV/A}{\Delta\sqrt{t}}$ of the curve. The steeper the slope, the higher the penetration speed (Figure 4). The slope of this curve is calculated within the same time range as the slope of the Ultrasonic liquid penetration measurement is calculated i.e. a contact time between approximately 0.031ms and 0.200ms after contact between liquid and paper was made. This is done for every single liquid/paper combination [2].

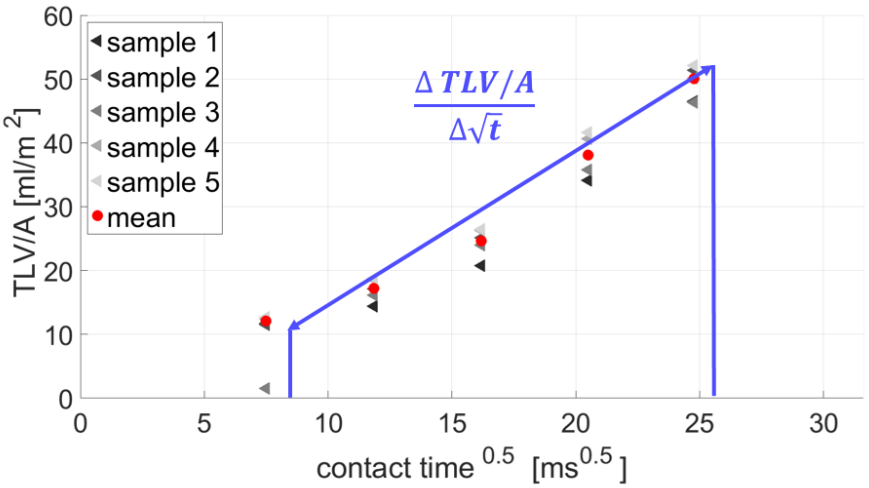


Figure 4: ASA - Measurement results show the absorbed liquid volume (Total Transferred Liquid Volume per unit Area TLV/A) over time. The slope of the curve $[\frac{\Delta TLV/A}{\Delta\sqrt{t}}]$ represents the penetration speed in $[\frac{m}{\sqrt{s}}]$ [2].

## 3. Print through test

The print through test can be used as a measure for the penetration depth of the printed liquid into the paper. For this purpose, the backside of the unprinted sheet is imaged behind a coloured background. This background has the same colour as the liquid used for the printing. Subsequently, the sheet is fully printed on the top side. Finally, the exact same position of the backside of the printed paper is imaged again. The difference of the grey values between the images represents the print through value. The measurement procedure is illustrated in Figure 5.

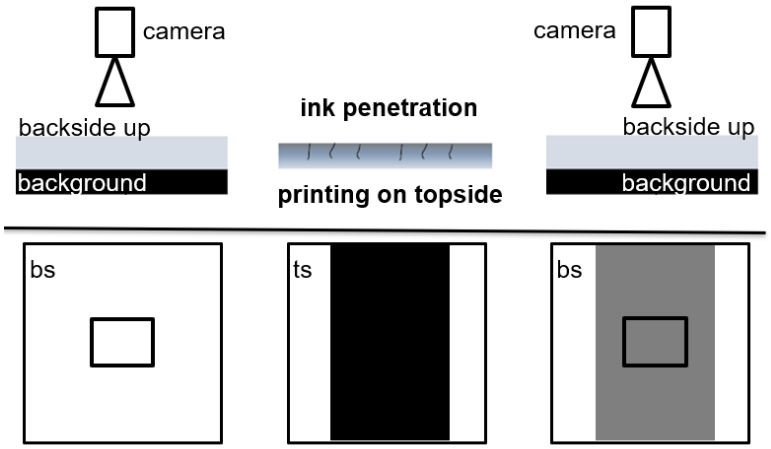


Figure 5: print through test: first the backside of the sample is imaged. Second, the topside of this paper sheet is fully printed. And third, the same area location of the backside, from the now printed sheet is imaged again. The higher the penetration depth is, the higher is the difference in gray value of those two images.

## 4. Sample Preparation for the Ppicoliter Head Contact Angle Measurement


Figure 6: The cartridge is inserted into the dosing head of the picoliter head. This dosing element is positioned on the membrane cap of the cartridge, enabling to create a pulse which presses the liquid through the orifice of the cartridge.

(a)

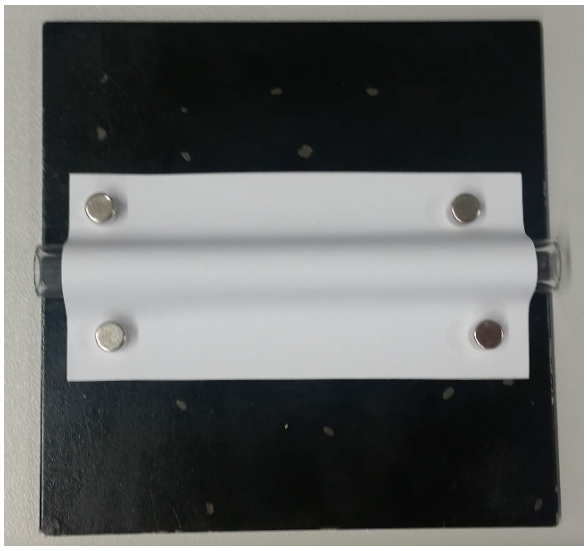

(b)

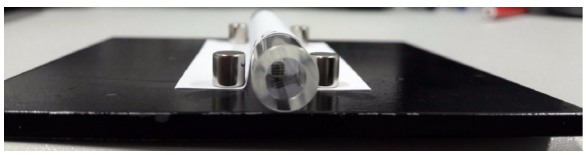

Figure 7: The paper, 90 mm x 50 mm in size, is clamped centrally on the specimen holder using four magnets to fixate it (Subfigure a). The outer diameter of the plexiglas cylinder is 1cm. Importantly can be noted, that the region of the paper where the liquid is applied, is not in contact with the sample holder (Subfigure b).

## 5. Picoliter Head Settings for Contact Angle Measurement

Table 1: The settings for the pl dot - production vary with viscosity ($\eta$), surface tension ($\gamma$) and drop size. Picoliter head settings for droplet generation using the liquid High ($\uparrow$) $\eta$ - Low ($\downarrow$) $\gamma$ are listed in this table.

| dropsize | 30pl | 60pl |
|---|---|---|
| Orifice diameter | $30\mu m$ | $50\mu m$ |
| Pulse amplitude | 92 | 70 |
| Pulse width | 55 | 52 |
| Pulse frequency | 100 | 100 |
| Sensor treshold | 3 | 3 |
| Number of drops | 1 | 1 |

Table 2: The settings for the pl dot - production vary with viscosity ($\eta$), surface tension ($\gamma$) and drop size. Picoliter head settings for droplet generation using the liquid Low ($\downarrow$) $\eta$ - Low ($\downarrow$) $\gamma$ are listed in this table.

| dropsize | 30pl | 60pl |
|---|---|---|
| Orifice diameter | $30\mu m$ | $30\mu m$ |
| Pulse amplitude | 85 | 100 |
| Pulse width | 40 | 50 |
| Pulse frequency | 100 | 100 |
| Sensor treshold | 2 | 2 |
| Number of drops | 1 | 1 |

Table 3: The settings for the pl dot - production vary with viscosity ($\eta$), surface tension ($\gamma$) and drop size. Picoliter head settings for droplet generation using the liquid High ($\uparrow$) $\eta$ - High ($\uparrow$) $\gamma$ are listed in this table.

| dropsize | 30pl | 60pl |
|---|---|---|
| Orifice diameter | $30\mu m$ | $50\mu m$ |
| Pulse amplitude | 100 | 100 |
| Pulse width | 100 | 100 |
| Pulse frequency | 100 | 100 |
| Sensor treshold | 0 | 0 |
| Number of drops | 1 | 1 |

Table 4: The settings for the pl dot - production vary with viscosity ($\eta$), surface tension ($\gamma$) and drop size. Picoliter head settings for droplet generation using the liquid Low ($\downarrow$) $\eta$ - High ($\uparrow$) $\gamma$ are listed in this table.

| dropsize | 30pl | 60pl |
|---|---|---|
| Orifice diameter | $30\mu m$ | $30\mu m$ |
| Pulse amplitude | 30 | 30 |
| Pulse width | 65 | 39 |
| Pulse frequency | 100 | 100 |
| Sensor treshold | 0 | 0 |
| Number of drops | 1 | 1 |

Table 5: The settings for the pl dot - production vary with viscosity ($\eta$), surface tension ($\gamma$) and drop size. Picoliter head settings for droplet generation using the liquid center($\otimes$) $\eta$ - center($\otimes$) $\gamma$ are listed in this table.

| dropsize | 30pl | 60pl |
|---|---|---|
| Orifice diameter | $30\mu m$ | $30\mu m$ |
| Pulse amplitude | 85 | 90 |
| Pulse width | 40 | 60 |
| Pulse frequency | 100 | 100 |
| Sensor treshold | 0 | 0 |
| Number of drops | 1 | 1 |

## 6. Correlation between Base Diameter of the Drop and HSI Printed Dot Area

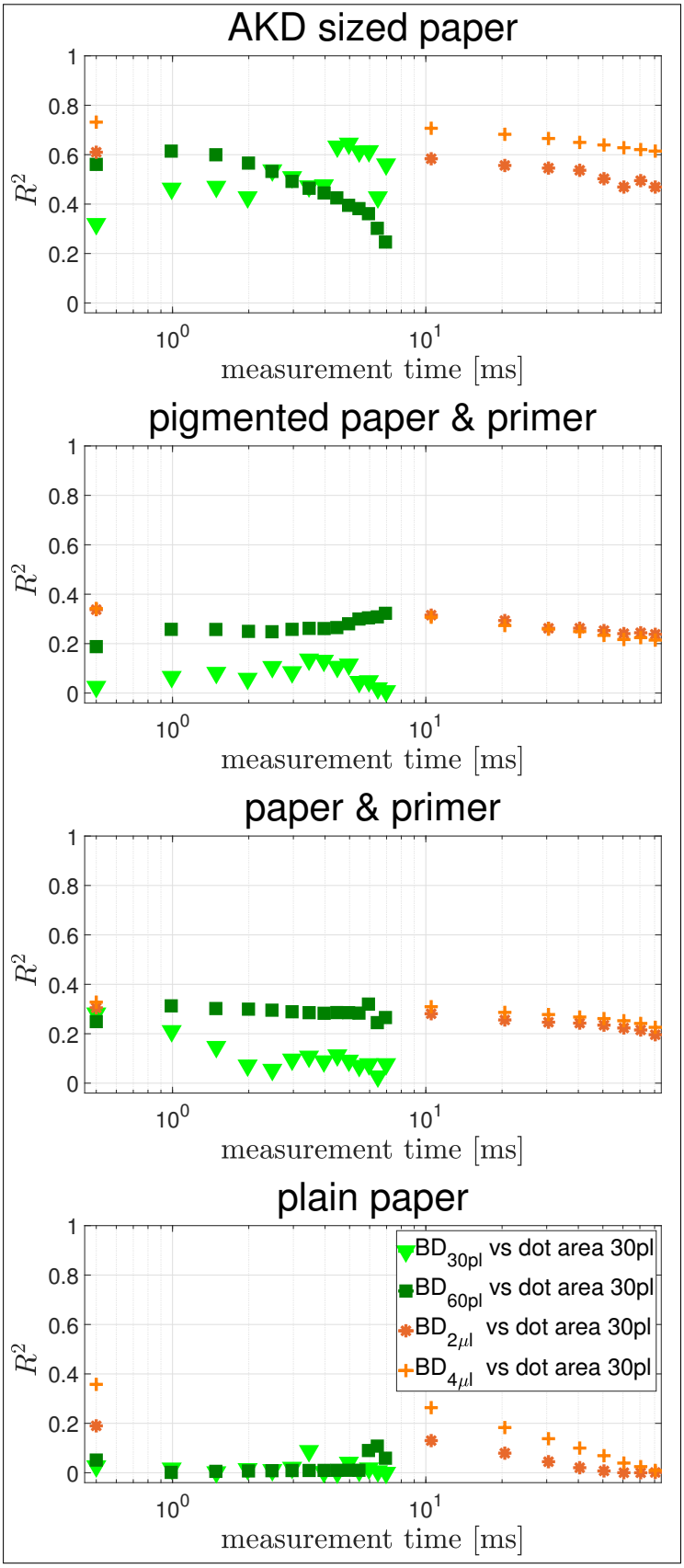


Figure 8: The coefficient of determination of 30pl HSI printed dot area compared to the base diameter of 30pl, 60pl, 2$\mu l$ and 4$\mu l$ drops at advancing contact time between drop and paper of the contact angle measurement device.

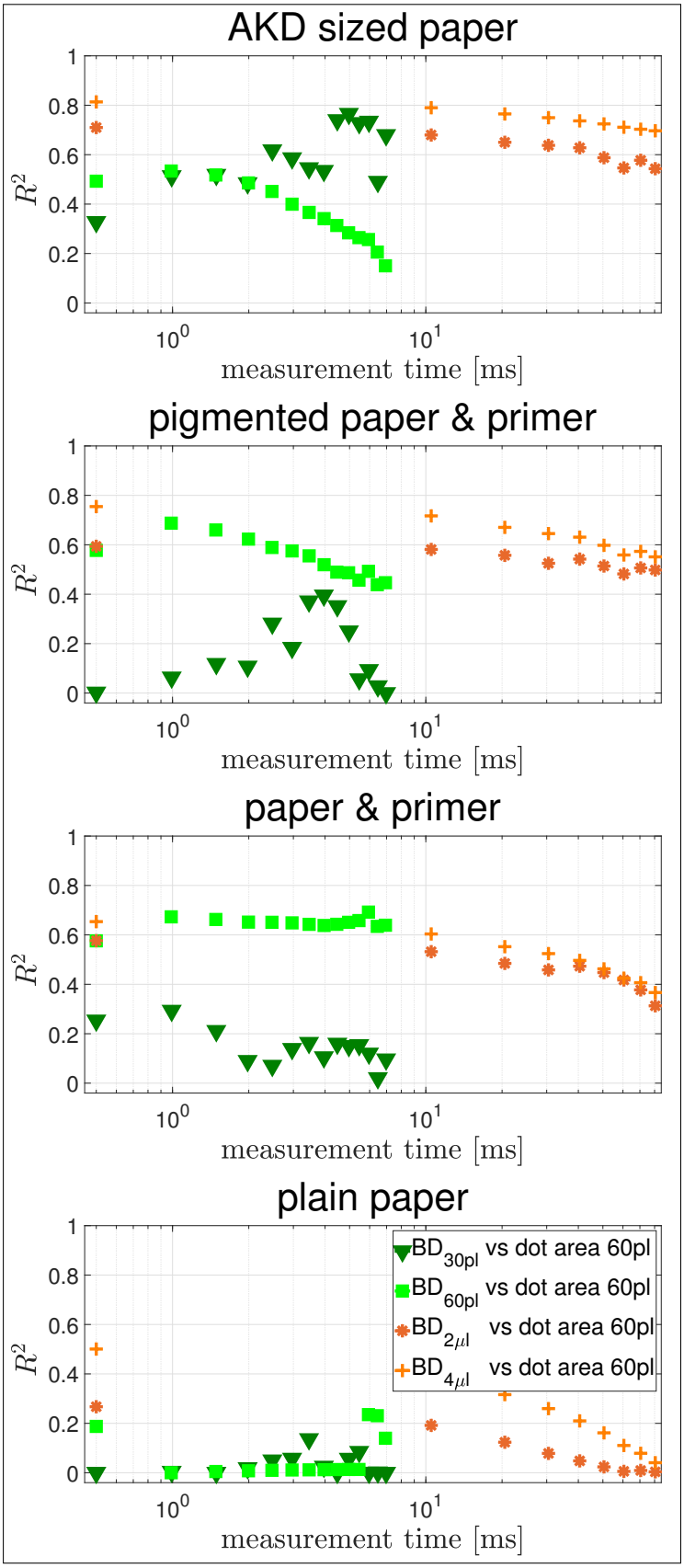


Figure 9: The coefficient of determination of 60pl HSI printed dot area compared to the base diameter of 30pl, 60pl, $2\mu l$ and $4\mu l$ drops at advancing contact time between liquid paper.

## References


[1] Y J Lee, J J Pawlak, O Rojas, and J Skowronski. Paper and paper machine variables affecting the attenuation of ultrasonic signals during wetting. In *Int. Paper Physics Conference*, pages 143–148, 2007.

[2] Krainer Sarah and Hirn Ulrich. Short timescale wetting and penetration on porous sheets measured with ultrasound, direct absorption and contact angle. *RSC Adv.*, 8(23):12861–12869, 2018.

[3] Toshiharu Enomae, Hiroshi Kataoka, Fumihiko Onabe, Das Papier, and J Robertson. In-Plane Distribution of Paper Absorbency Measured by Liquid Absorption Profilometer. *Sen'i Gakkaishi*, 55(2):265–291, 2004.

[4] Thijs Andrew Per Van Stiphout. *Liquid Absorption in porous Media studied by Automatic Scanning Absorptometer*. PhD thesis, Eindhoven University of Technology, 2016.

# Electronic Supplementary Information to "Contact Angle Measurement on Porous Substrates: Effect of Liquid Absorption and Drop Size"

## 1. Detailed Substrate Description

Liquid behaviour is studied on a wide field of substrates [1, 2, 3]. In this study four types of cellulose sheets are used ranging from strong absorbency to poor absorption ability, capturing the impact of substrate absorption on liquid behaviour. Those medias are woodfree papers from an industrial supplier and the raw material of these. Detailed paper properties are shown in Table 1. The papers consists of industrial bleached hardwood pulp mainly, filler is scalenohedral PCC (precipitated calcium carbonate).

- strongly absorbing. Plain paper made of pulp and filler, having no treatment. This strongly absorbing media is the raw material of the following three cellulose sheets, being commercial available.
- moderately absorbing. This paper shows reduced liquid absorbency, due to densification of the bulk by passing the sheet through rolls compressing the sheet (calendaring). This causes a more closed surface [4]. Bivalents salts (=primer) have been applied on the substrate surface, increasing ink-pigment precipitation. Thus, reduction of ink particle movement into media bulk can be observed [5, 6].
- weakly absorbing. 4 $g/m^2$ per side of starch and clay were applied to create a more homogeneous surface, reducing and uniforming liquid penetration into paper [7, 8]. A primer was applied too, increasing ink quality due to improved ink-particle fixation on substrate-surface [5, 6].
- almost non-absorbing. This substrate was heavily treated employing sizing agents, reducing the surface free energy (see Table 1). This bulk sizing hydrophobised the paper. Furthermore, a layer consisting of starch was put on the substrate surface. The words hydrophobised and sized are used as synonyms in this publication.

For determination of grammage and filler the EN ISO 536 and the DIN 54370 were followed. Roughness was determined using the Bendtsen Method ISO 5636-3:2013. The mean hight of ten highest points within the measured area was evaluated using a IFM alicona roughness measurement device, capturing the size scale of surface roughness. A fast fourier transformation (FFT) - highpass filtering was used, applying a threshold wavelength of 3.5 $mm$.

Table 1: Properties of the used substrates, similar to [9].

| Properties | strong absorbing | moderately absorbing | weakly absorbing | almost non -absorbing |
|---|---|---|---|---|
| Bivalent salt $[g/m^2]$ | - | - | $\sim 0.25$ | $\sim 0.25$ |
| Pigmentation $[g/m^2]$ | - | - | 4 | - |
| Surface starch $[g/m^2]$ | - | - | $\sim 1$ | $\sim 1$ |
| Hydrophobisation $[kg/t]$ (AKD sizing) | - | - | - | 1 |
| Filler content [%] | 22 | 22 | 23 | 14 |
| Grammage $[g/m^2]$ | 97.2 | 78.5 | 79.89 | 77.2 |
| Porosity [%] | 40.3 | 38.8 | 23.6 | 20.6 |
| Average pore diameter $[\mu m]$ | 3.9 | 2.6 | 3.2 | 4.9 |
| Roughness $[ml/s]$ | 321 | 50 | 78 | 192 |
| Roughness parameter $S_q$ $[\mu m]$ | 3.6 | 2.4 | 3.1 | 4 |
| Mean height of ten highest peaks in evaluated area$[\mu m]$ | 35 | 46 | 35 | 40 |
| Dispersive surface energy $[mJ/m^2]$ | 44 | 42 | 43 | 33 |
| Polar surface energy $[mJ/m^2]$ | 27 | 23 | 22 | 0.1 |
| Total surface energy $[mJ/m^2]$ | 71 | 65 | 65 | 33.1 |
| absorbed water volume $[ml/(m^2 100ms)]$ | 71 | 48 | 38 | 0.6 |

## 2. Automatic Scanning Absorptometer (ASA)

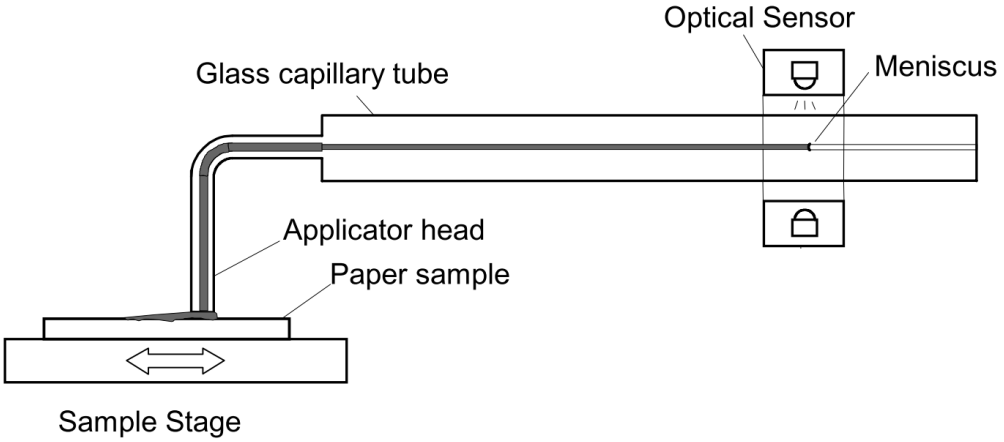


Figure 1: The automatic scanning absorptometer set up. The applicator head on the paper sample is moved over the paper, ink is supplied with the liquid via a glass tube. The meniscus sensor follows the receding meniscus and computes the amount of liquid, which is absorbed in the paper. Adapted from Enomae et al. [10].

The Automatic Scanning Absorptometer measurement, performed with a KM500 win Automatic Scanning Absorptometer instrument from KRK Kumagai (Japan), provides quantitative information about the liquid absorption as a function of time on time scales of 10 $ms$ up to 10 $s$ [10, 11]. During an SA measurement, liquid is supplied from a scanning head which moves along a spiral path on the paper. In Figure 2 one can see the head on the paper sample surface, it is supplied with the liquid via a tube. The speed of the head moving over the paper surface is kept constant over a certain part of the track, then it accelerates stepwise to a higher speed which is then again kept constant. By increasing the speed the system measures the liquid penetration for different times of contact between the nozzle and the paper. The ASA measures the total absorbed liquid volume per unit area. The penetration speed is represented by the slope $\frac{\Delta TLV/A}{\Delta\sqrt{t}}$ of the curve. The steeper the slope, the higher the penetration speed (Figure 3).

The highest slope is observed for the absorptive media exhibiting the highest absorption rate. The hydrophobised media shows almost no liquid uptake, regardless of the contact time, reflected by the very low absorbed water volumes.

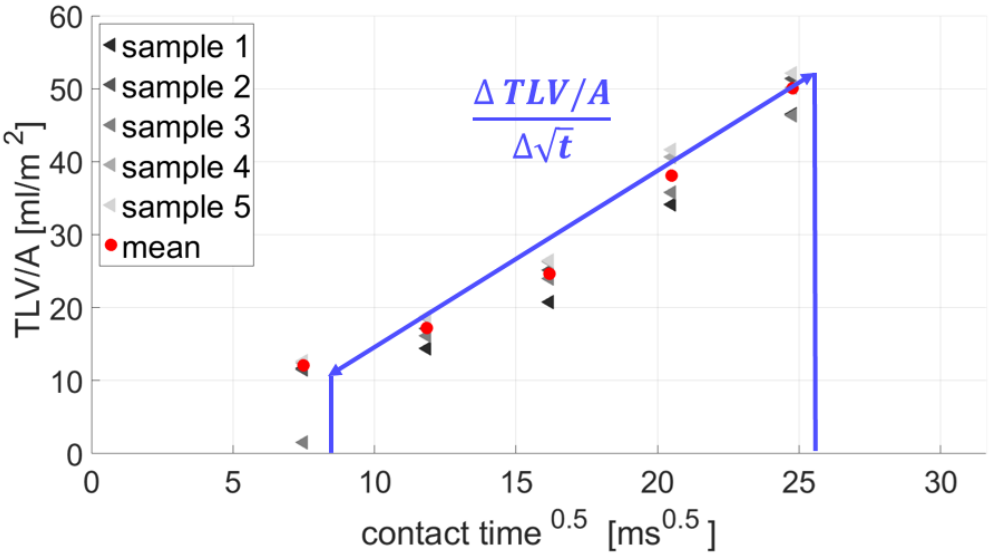


Figure 2: ASA-Measurement results show the absorbed liquid volume (Total Transferred Liquid Volume per unit Area TLV/A) over time. The slope of the curve $[\frac{\Delta TLV/A}{\Delta\sqrt{t}}]$ represents the penetration speed in $[\frac{m}{\sqrt{ms}}]$. The higher the slope, the higher the detected liquid movement into the paper.

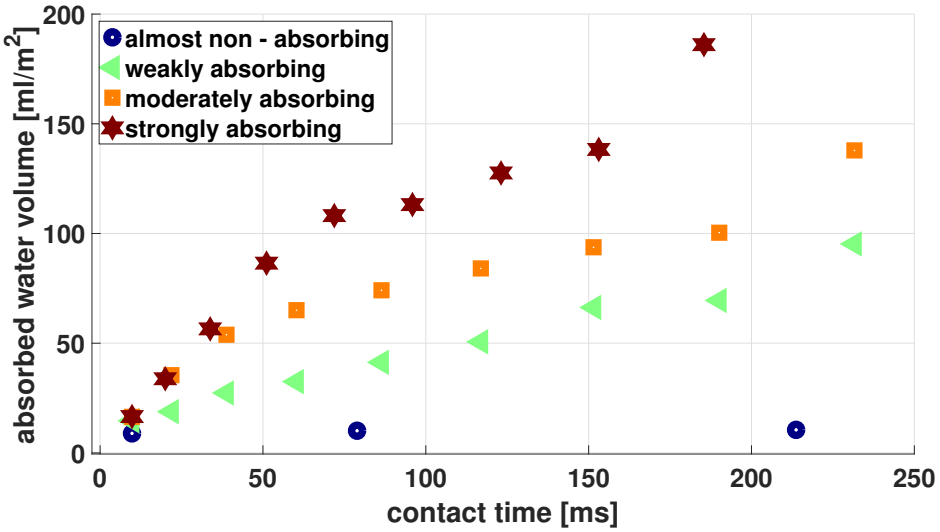


Figure 3: The transferred liquid volume is plotted versus the contact time between applicator head (nozzle) and substrate. The strongly absorbing sheet shows the highest liquid uptake, independent of the contact time. In contrast to that, the almost non-absorbing media exhibits a very low imbibed water volume.

## 3. Sample Preparation for the Picoliter Head and Nanoliter Setup Contact Angle Measurement


Figure 4: The cartridge is inserted into the dosing head of the picoliter head. This dosing element is positioned on the membrane cap of the cartridge, enabling to create a pulse which presses the liquid through the orifice of the cartridge.

(a)

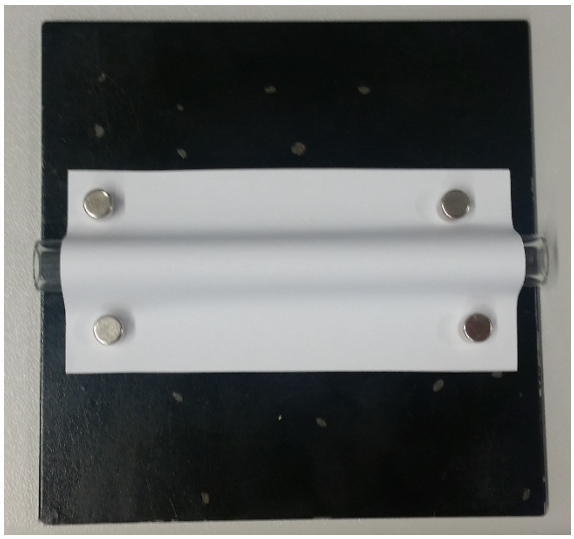

(b)

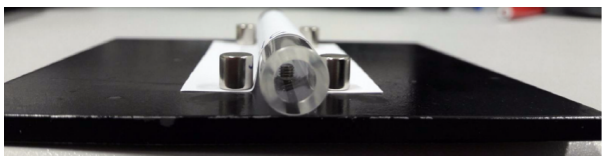

Figure 5: The paper, 90 mm x 50 mm in size, is clamped centrally on the specimen holder using four magnets to fixate it (Subfigure a). The outer diameter of the plexiglas cylinder is 1 cm. Importantly can be noted, that the region of the paper where the liquid is applied, is not in contact with the sample holder (Subfigure b).

## 4. Detailed Description of Drop Production

- Picoliter drops: The *pl* contact angle measurements were performed using a dataphysics OCA200. The picoliter setup of this instrument creates drops of different sizes: $30\,pl$, $60\,pl$, $120\,pl$, $240\,pl$, $480\,pl$ and $960\,pl$. Generation of $960\,pl$ drops was done shooting two droplets in a row, coalescing before impingement on the surface of the substrate. The test liquid is sucked through an orifice into a cartridge using a standard micro-pipet combined with a special dataphysics attachment. The cartridge is then inserted into the dosing element of the *pl* head. This dosing element is positioned on the membrane cap of the cartridge, enabling to create a pulse which squeezes out the liquid through the orifice of the cartridge (Figure 3). The diameter of this opening can be adjusted by using cartridges with different sized orifices. Any liquid can be used for *pl* droplet generation as long as it can be sucked and squeezed out of the cartridge. The parameters pulse amplitude, pulse width and pulse frequency of the pulse can be varied for the individual dosing processes, depending on the used testing fluid and drop size. The sensor threshold is a measure for the applied negative pressure, in the cartridge to prevent liquid leakage through the orifice. The higher this value, the higher will be the negative pressure in the cartridge, being zero for ambient conditions. The parameters are adjusted in order to guarantee a stable drop production. The settings are varied as long as the desired drop volume applied on a non-absorbing aluminium foil is achieved, without having liquid volume reduction by absorption. The optimal settings can be found in Table 2-7 for each used liquid. The paper, 90 mm x 50 mm in size, is clamped centrally on the self-built specimen holder using four magnets to fixate it, illustrated in Figure 4a. Here, it is important that the paper area, were the liquid is applied on the surface, is not in contact with the sample holder (Figure 4b).

- Nanoliter drops: *nl* drops are created employing the OCA200 nanoliter setup. We create drops with a volume of: $5\,nl$, $15\,nl$, $30\,nl$, $60\,nl$, $120\,nl$, $240\,nl$ and $480\,nl$. This set up utilizes a tube with a shutter, generating a falling liquid beam. The longer the pulse time $[ms]$, and thus the longer the valve is open, the bigger is the liquid volume released by the *nl*-setup. The liquid volume is applied on a non-absorbing aluminium foil to obtain the corresponding settings, without having liquid volume reduction by absorption. This system only operates with water. The settings for the individual drop sizes are listed in Table 8. The substrate sample is put on the same sample holder as utilized during the *pl* measurement, illustrated in Figure 4a in the ESI, also guaranteeing no contact between liquid application area on the sheet and sample holder (Figure 4b).

- Microliter drops: The measurement of $\mu l$ drops was carried out with a Fibro DAT 1100 instrument [12], often used in industry due to the easy drop production. It generates droplets by pushing out the liquid drop of a tube with defined void volume, now filled with the tested fluid. Thus, a liquid drop of $1\,\mu l$, $2\,\mu l$ or $4\,\mu l$ is created. Detailed description of this procedure can be found in previous work of our group [13]. Any liquid can be used for drop production in the lower $\mu l$ range as long as it does not clog the tube. The collected fluid at the end of the tube creates a hanging drop and is slashed off with a spring, falling on the substrate. Also here, the region of paper were the liquid is applied is not in contact with the sample holder.

## 5. Picoliter Head Settings for Contact Angle Measurement

Table 2: Picoliter head settings for droplet generation using water are listed in this table.

| Drop size [pl] | 30 | 60 | 120 | 240 | 480 | 960 |
|---|---|---|---|---|---|---|
| Orifice diameter [$\mu m$ ] | 30 | 30 | 70 | 70 | 100 | 100 |
| Pulse amplitude | 83 | 66 | 65 | 93 | 88 | 88 |
| Pulse width | 27.5 | 30.6 | 29.4 | 38.8 | 41.5 | 41.5 |
| Pulse frequency [$Hz$] | 100 | 100 | 100 | 100 | 100 | 9500 |
| Sensor treshold | 0 | 0 | 0 | 0 | 0 | 0 |
| Number of drops | 1 | 1 | 1 | 1 | 1 | 2 |

Table 3: The settings for the pl dot-production vary with viscosity ($\eta$), surface tension ($\gamma$) and drop size. Picoliter head settings for droplet generation using the liquid with the lowest surface tension $\gamma = 26.8$ [$mN/m$] are listed in this table.

| Drop size [pl] | 60 | 120 | 240 | 480 |
|---|---|---|---|---|
| Orifice diameter [$\mu m$ ] | 30 | 100 | 100 | 100 |
| Pulse amplitude | 100 | 80 | 95 | 100 |
| Pulse width | 50 | 45 | 68.5 | 88 |
| Pulse frequency [$Hz$] | 100 | 100 | 100 | 100 |
| Sensor treshold | 2 | 3 | 3 | 3 |
| Number of drops | 1 | 1 | 1 | 1 |

Table 4: The settings for the pl dot-production vary with viscosity ($\eta$), surface tension ($\gamma$) and drop size. Picoliter head settings for droplet generation using the liquid with a surface tension $\gamma$ of 27.5 [$mN/m$] are listed in this table.

| Drop size [pl] | 60 | 120 | 240 | 480 |
|---|---|---|---|---|
| Orifice diameter [$\mu m$ ] | 50 | 50 | 100 | 100 |
| Pulse amplitude | 70 | 85 | 87 | 87 |
| Pulse width | 52 | 60 | 50 | 70 |
| Pulse frequency [$Hz$] | 100 | 100 | 100 | 100 |
| Sensor treshold | 3 | 4 | 3 | 3 |
| Number of drops | 1 | 1 | 1 | 1 |

Table 5: The settings for the pl dot-production vary with viscosity ($\eta$), surface tension ($\gamma$) and drop size. Picoliter head settings for droplet generation using the liquid with a surface tensions of $\gamma = 43.5\ [mN/m]$ are listed in this table.

| Drop size [pl] | 60 | 120 | 240 | 480 |
|---|---|---|---|---|
| Orifice diameter [$\mu m$ ] | 30 | 30 | 100 | 100 |
| Pulse amplitude | 90 | 95 | 95 | 95 |
| Pulse width | 60 | 86 | 50 | 53 |
| Pulse frequency [$Hz$] | 100 | 100 | 100 | 100 |
| Sensor treshold | 0 | 0 | 0 | 0 |
| Number of drops | 1 | 1 | 1 | 1 |

Table 6: The settings for the pl dot-production vary with viscosity ($\eta$), surface tension ($\gamma$) and drop size. Picoliter head settings for droplet generation using the liquid with a surface tension of $\gamma = 67.6\ [mN/m]$ are listed in this table.

| Drop size [pl] | 60 | 120 | 240 | 480 |
|---|---|---|---|---|
| Orifice diameter [$\mu m$ ] | 50 | 70 | 100 | 100 |
| Pulse amplitude | 100 | 100 | 90 | 90 |
| Pulse width | 100 | 70 | 60 | 55 |
| Pulse frequency [$Hz$] | 100 | 100 | 100 | 100 |
| Sensor treshold | 0 | 0 | 0 | 0 |
| Number of drops | 1 | 1 | 1 | 1 |

Table 7: The settings for the pl dot-production vary with viscosity ($\eta$), surface tension ($\gamma$) and drop size. Picoliter head settings for droplet generation using the liquid with a liquid surface tension of $\gamma = 70.5\ [mN/m]$ are listed in this table.

| Drop size [pl] | 60 | 120 | 240 | 480 |
|---|---|---|---|---|
| Orifice diameter [$\mu m$ ] | 30 | 30 | 70 | 100 |
| Pulse amplitude | 30 | 5 | 95 | 85 |
| Pulse width | 39 | 50 | 30 | 35.5 |
| Pulse frequency [$Hz$] | 100 | 100 | 100 | 100 |
| Sensor treshold | 0 | 0 | 0 | 0 |
| Number of drops | 1 | 1 | 1 | 1 |

## 6. Nanoliter Dispenser Settings for Contact Angle Measurement

Table 8: The settings for the nl dot-production vary with drop size. Nanoliter head settings for droplet generation using water are listed in this table.

| Drop size $[nl]$ | 5 | 15 | 30 | 60 | 120 | 240 | 480 |
|---|---|---|---|---|---|---|---|
| Pulse time $[ms]$ | 0.988 | 1.5 | 3 | 6 | 12.5 | 26 | 52 |

## 7. Values of the Mean pl and $\mu l$ Contact Angle

Table 9: Contact angle of mean pl and mean $\mu l$ and the corresponding 95 % confidence intervals of the used liquids, scaling with the surface tension ($\gamma$) on the almost non-absorbing substrate.

| time $[ms]$ | 0 | 0 | 0 | 0 | 10 | 10 | 10 | 10 |
|---|---|---|---|---|---|---|---|---|
| $[^\circ]$ | $\Theta_{pl}$ | 95% CI | $\Theta_{\mu l}$ | 95% CI | $\Theta_{pl}$ | 95% CI | $\Theta_{\mu l}$ | 95% CI |
| $\gamma_{low}$ | 55.81 | 9.24 | 47.35 | 13.1 | 21.1 | 5.9 | 47.4 | 9.10 |
| | 79.00 | 7.31 | 66.63 | 15.70 | 30.80 | 5.99 | 66.6 | 15.70 |
| | 73.91 | 7.40 | 94.10 | 7.75 | 63.4 | 15.9 | 94.1 | 7.80 |
| | 95.92 | 5.80 | 116.04 | 4.76 | 85.00 | 12.1 | 116.04 | 4.70 |
| | 71.85 | 19.58 | 107.63 | 4.80 | 66.40 | 13.5 | 107.6 | 4.80 |
| $\gamma_{high}$ | 78.77 | 5.37 | 94.00 | 9.20 | 74.10 | 2.00 | 94 | 9.20 |

Table 10: Contact angle of mean pl and mean $\mu l$ and the corresponding 95 % confidence intervals of the used liquids, scaling with the surface tension ($\gamma$) on the weakly absorbing substrate.

| time $[ms]$ | 0 | 0 | 0 | 0 | 10 | 10 | 10 | 10 |
|---|---|---|---|---|---|---|---|---|
| $[^\circ]$ | $\Theta_{pl}$ | 95% CI | $\Theta_{\mu l}$ | 95% CI | $\Theta_{pl}$ | 95% CI | $\Theta_{\mu l}$ | 95% CI |
| $\gamma_{low}$ | 63.26 | 13.21 | 37.53 | 8.00 | 16.38 | 4.30 | 37.53 | 8.00 |
| | 80.50 | 9.50 | 60.10 | 13.20 | 22.48 | 6.43 | 60.10 | 13.20 |
| | 54.50 | 26.89 | 79.63 | 7.50 | 35.84 | 21.16 | 79.63 | 7.45 |
| | 94.65 | 11.13 | 100.67 | 1.80 | 71.10 | 4.55 | 100.67 | 1.75 |
| | 73.85 | 16.61 | 90.52 | 6.70 | 66.10 | 16.20 | 90.52 | 6.73 |
| $\gamma_{high}$ | 63.12 | 4.86 | 77.08 | 7.30 | 38.00 | 7.53 | 77.10 | 7.23 |

Table 11: Contact angle of mean pl and mean $\mu l$ and the corresponding 95 % confidence intervals of the used liquids, scaling with the surface tension ($\gamma$) on the moderately absorbing substrate.

| time $[ms]$ | 0 | 0 | 0 | 0 | 10 | 10 | 10 | 10 |
|---|---|---|---|---|---|---|---|---|
| $[^\circ]$ | $\Theta_{pl}$ | 95% CI | $\Theta_{\mu l}$ | 95% CI | $\Theta_{pl}$ | 95% CI | $\Theta_{\mu l}$ | 95% CI |
| $\gamma_{low}$ | 63.94 | 8.10 | 35.10 | 9.850 | 15.56 | 3.46 | 35.10 | 9.85 |
| | 79.65 | 14.15 | 68.24 | 12.22 | 20.50 | 5.43 | 58.24 | 12.22 |
| | 77.62 | 16.70 | 80.38 | 8.92 | 38.85 | 47.06 | 80.38 | 8.92 |
| | 89.70 | 12.50 | 105.23 | 1.90 | 70.15 | 3.56 | 105.27 | 1.90 |
| | 77.86 | 17.72 | 91.01 | 5.23 | 60.13 | 8.19 | 91.01 | 5.23 |
| $\gamma_{high}$ | 60.40 | 1.76 | 74.44 | 11.02 | 34.47 | 6.96 | 17.44 | 11.02 |

Table 12: Contact angle of mean pl and mean $\mu l$ and the corresponding 95 % confidence intervals of the used liquids, scaling with the surface tension ($\gamma$) on the strongly absorbing substrate.

| time $[ms]$ | 0 | 0 | 0 | 0 | 10 | 10 | 10 | 10 |
|---|---|---|---|---|---|---|---|---|
| $[^\circ]$ | $\Theta_{pl}$ | 95% CI | $\Theta_{\mu l}$ | 95% CI | $\Theta_{pl}$ | 95% CI | $\Theta_{\mu l}$ | 95% CI |
| $\gamma_{low}$ | 56.37 | 7.70 | 35.10 | 9.850 | 14.72 | 1.92 | 37.70 | 9.14 |
| | 73.55 | 11.09 | 68.24 | 9.22 | 23.10 | 5.87 | 60.85 | 9.54 |
| | 62.45 | 42.29 | 80.38 | 8.92 | 17.30 | 4.91 | 71.76 | 6.67 |
| | 81.19 | 20.36 | 105.23 | 1.90 | 50.30 | 28.96 | 88.08 | 4.00 |
| | 62.97 | 18.03 | 91.01 | 5.23 | 20.77 | 6.74 | 60.29 | 6.11 |
| $\gamma_{high}$ | 47.20 | 3.98 | 74.44 | 11.02 | 10.04 | 8.74 | 47.95 | 9.64 |

## References


[1] I. Bernacka-Wojcik, P. Wojcik, H. Aguas, E. Fortunato, and R. Martins. Inkjet printed highly porous TiO2 films for improved electrical properties of photoanode. *Journal of Colloid and Interface Science*, 465:208–214, 2016.

[2] H. Ning, R. Tao, Z. Fang, W. Cai, J. Chen, Y. Zhou, Z. Zhu, Z. Zheng, R. Yao, M. Xu, L. Wang, L. Lan, and J. Peng. Direct patterning of silver electrodes with 2.4 $\mu$m channel length by piezoelectric inkjet printing. *Journal of Colloid and Interface Science*, 487:68–72, 2017.

[3] R. K. Holman, M. J. Cima, S. A. Uhland, and E. Sachs. Spreading and Infiltration of Inkjet-Printed Polymer Solution Droplets on a Porous Substrate. *Journal of Colloid and Interface Science*, 249(2):432–440, 2002.

[4] P. Resch, W. Bauer, and U. Hirn. Calendering effects on coating pore structure and ink setting behavior. *Tappi Journal*, 9(1):27–35, 2010.

[5] G. Wypych. Typical Primer Formulations and Applications to different substrates. In *Handbook of Adhesion Promoters*, pages 77–91. ChemTec Publishing, 2018.

[6] H. Holik. *Recycled Fibre and Deinking*. Fapet OY, 2009.

[7] H. Aslannejad, S. M. Hassanizadeh, A. Raoof, D. A. de Winter, N. Tomozeiu, and M. T. van Genuchten. Characterizing the hydraulic properties of paper coating layer using FIB-SEM tomography and 3D pore-scale modeling. *Chemical Engineering Science*, 160:275–280, 2017.

[8] H. Aslannejad, S. M. Hassanizadeh, and M. A. Celia. Characterization of the Interface Between Coating and Fibrous Layers of Paper. *Transport in Porous Media*, 127(1):143–155, 2019.

[9] S. Krainer, C. Smit, and U. Hirn. The effect of viscosity and surface tension on inkjet printed picoliter dots. *RSC Advances*, 9(54):31708–31719, 2019.

[10] T. Enomae, H. Kataoka, F. Onabe, D. Papier, and J. Robertson. In-Plane Distribution of Paper Absorbency Measured by Liquid Absorption Profilometer. *Sen'i Gakkaishi*, 55(2):265–291, 2004.

[11] T. A. P. Van Stiphout. *Liquid Absorption in porous Media studied by Automatic Scanning Absorptometer*. Master thesis, Eindhoven University of Technology, 2016.

[12] A. Hladnik. Dynamic wetting and liquid sorption in paper - Fibro 1100 Dat measuring. *Papier*, 25:44–48, 1997.

[13] K. Sarah and H. Ulrich. Short timescale wetting and penetration on porous sheets measured with ultrasound, direct absorption and contact angle. *RSC Adv.*, 8(23):12861–12869, 2018.

# List of Figures

# Bibliography


[1] E. P. Furlani. *Fundamentals of Inkjet Printing: The Science of Inkjet and Droplets*, volume 1. Wiley-VCH Verlag, 2016.

[2] J. Kettle, T. Lamminmäki, and P. Gane. A review of modified surfaces for high speed inkjet coating. *Surface and Coatings Technology*, 204(12-13):2103–2109, 2010.

[3] C. Schmid and A. Hudd. Formulation and Properties of Waterborne Inkjet Inks. In S. Magdassi, editor, *The Chemestry of Inkjet Inks*, pages 123 –140. World Scientific Publishing Co. Pte. Ltd., 2010.

[4] A. Marmur. Penetration and displacement in capillary systems of limited size. *Advances in Colloid and Interface Science*, 39:13–33, 1992.

[5] T. Lamminmäki, J. Kettle, and P. Gane. Absorption and adsorption of dye-based inkjet inks by coating layer components and the implications for print quality. *Colloids and Surfaces A: Physicochemical and Engineering Aspects*, 380:79–88, 2011.

[6] K. Mielonen, S. S. Ovaska, T. Laukala, and K. Backfolk. Three-Layered Polyelectrolyte Structures as Inkjet Receptive Coatings: Part 2. Interaction With Pigment-based Inks. *Journal of Imaging Science and Technology*, 60(3):1–9, 2016.

[7] D. Siregar, J. G. Kuerten, and C. van der Geld. Numerical simulation of the drying of inkjet-printed droplets. *Journal of Colloid and Interface Science*, 392(1):388–395, 2013.

[8] C. Diddens. Detailed finite element method modeling of evaporating multicomponent droplets. *Journal of Computational Physics*, 340:670–687, 2017.

[9] S. S. Ovaska and K. Backfolk. The versatility of the Bristow absorption tester - A review. *Nordic Pulp and Paper Research Journal*, 33(2):279–296, 2018.

[10] R. Li, Y. Zhang, Y. Cao, and Z. Liu. Ink Penetration of Uncoated Inkjet Paper and Impact on Printing Quality. *BioResources*, 10(4), 2015.

[11] E. Svanholm. *Printability and ink-coating interactions in inkjet printing*. PhD thesis, Karlstad University, 2007.

[12] K. Mielonen, P. Geydt, C.-M. Tåg, and K. Backfolk. Inkjet ink spreading, absorption and adhesion on substrates coated with thin layers of cationic polyelectrolytes. *Nordic Pulp & Paper Research Journal*, 30(2):179–188, 2015.

[13] J. Järnström, M. Järn, C. M. Tåg, J. Peltonen, and J. B. Rosenholm. Liquid spreading on ink-jet paper evaluated by the hydrodynamic and molecular-kinetic models. *Journal of Adhesion Science and Technology*, 25(6-7):761–779, 2010.

[14] L. Yang. *Ink-Paper Interaction: A study in ink-jet color reproduction*. PhD thesis, Linköping University, 2003.

[15] H. Wijshoff. Personal Communcication with Prof.dr.ir. H.M.A. (Herman) Wijshoff, 2019.

[16] U. Lindqvist, L. Hakola, J. Heilmann, B. Zhmud, and E. Wallström. Interaction Characteristics in Different Applications of Ink- Jet Printing. *TAGA Journal*, 2:99–109, 2006.

[17] C. J. Ridgway and P. A. C. Gane. Controlling the absorption dynamic of water-based ink into porous pigmented coating structures to enhance print performance. *Nordic Pulp and Paper Research Journal*, 17(2):119–129, 2002.

[18] J. Gigac, M. Kasajov, M. Maholyiov, M. Stankovsk, and M. Letko. Prediction of surface structure of coated paper and of ink setting time by infrared spectroscopy. *Nordic Pulp and Paper Research Journal*, 28(2):274–281, 2013.

[19] Y. Yuan and T. R. Lee. Contact Angle and Wetting Properties. In G. Bracco and B. Holst, editors, *Springer Series in Surface Sciences*. Springer-Verlag, 2013.

[20] R. J. Roberts. *Liquid penetration into paper*. PhD thesis, The Australian National University, 2004.

[21] J. Schoelkopf, C. Ridgway, P. Gane, G. Matthews, and D. Spielmann. Measurement and Network Modeling of Liquid Permeation into Compacted Mineral Blocks. *Journal of colloid and interface science*, 227(1):119–131, 2000.

[22] T. Lamminmäki, J. Kettle, P. Puukko, C. Ridgway, and P. Gane. Short timescale inkjet ink component diffusion: An active part of the absorption mechanism into inkjet coatings. *Journal of Colloid and Interface Science*, 365(1):222–235, 2012.

[23] K. Mielonen, P. Geydt, M. Österberg, L. S. Johansson, K. Backfolk, S.-S. Ovaska, T. Laukala, and K. Backfolk. Inkjet ink spreading on polyelectrolyte multilayers deposited on pigment coated paper. *Journal of Colloid and Interface Science*, 438(3):179–190, 2015.

[24] G. Wedler and H.-J. Freund. *Lehrbuch Physikalische Chemie*. Wiley-VCH, 2012.

[25] A. Adamson. *A Textbook of Physical Chemistry; Theory and Practise*. Elsevier Inc., 1973.

[26] T. Young. An Essay on the Cohesion of Fluids. *Philosophical Transactions of the Royal Society of London*, 95(65), 1805.

[27] K. L. Mittal, editor. *Contact Angle, Wettability and Adhesion*, volume 6. CRC Press, 2009.

[28] P.-G. de Gennes, F. Brochard-Wyart, D. Quéré, P.-G. de Gennes, F. Brochard-Wyart, and D. Quéré. Wetting and Long-Range Forces. In *Capillarity and Wetting Phenomena*, pages 87–105. Springer New York, New York, NY, 2004.

[29] B. Bhushan and Y. C. Jung. Wetting, adhesion and friction of superhydrophobic and hydrophilic leaves and fabricated micro/nanopatterned surfaces. *Journal of Physics Condensed Matter*, 20(22), 2008.

[30] D. Quéré. Wetting and Roughness. *Annual Review of Materials Research*, 38(1):71–99, 2008.

[31] K. Y. Law and H. Zhao. *Surface wetting: Characterization, Contact Angle, and Fundamentals*. Springer, 2016.

[32] Z. Cao, M. J. Stevens, J. M. Y. Carrillo, and A. V. Dobrynin. Adhesion and wetting of soft nanoparticles on textured surfaces: Transition between Wenzel and Cassie-Baxter states. *Langmuir*, 31(5):1693–1703, 2015.

[33] D. Quéré. Non-sticking drops. *Reports on Progress in Physics*, 68(11):2495–2532, 2005.

[34] A. Marmur. Wetting on hydrophobic rough surfaces: To be heterogeneous or not to be? *Langmuir*, 19(20):8343–8348, 2003.

[35] B. D. Cassie and S. Baxter. Wettability of porous surfaces. *RSC*, (5):546–551, 1944.

[36] R. N. Wenzel. Resistance of solid surfaces to wetting by water. *Industrial and Engineering Chemistry*, 28(8):988–994, 1936.

[37] A. Marmur and E. Bittoun. When Wenzel and Cassie are right: Reconciling local and global considerations. *Langmuir*, 25(3):1277–1281, 2009.

[38] L. Gao and T. J. McCarthy. How Wenzel and Cassie were wrong. *Langmuir*, 23(7):3762–3765, 2007.

[39] G. McHale. Cassie and Wenzel: Were they really so wrong? *Langmuir*, 23(15):8200–8205, 2007.

[40] M. Nosonovsky. On the range of applicability of the Wenzel and Cassie equations. *Langmuir*, 23(19):9919–9920, 2007.

[41] C. W. Extrand. Contact angles and hysteresis on surfaces with chemically heterogeneous islands. *Langmuir*, 19(9):3793–3796, 2003.

[42] X. Yong and L. T. Zhang. Nanoscale wetting on groove-patterned surfaces. *Langmuir*, 25(9):5045–5053, 2009.

[43] E. M. Grzelak and J. R. Errington. Nanoscale limit to the applicability of Wenzel's equation. *Langmuir*, 26(16):13297–13304, 2010.

[44] A. Dupre. Theorie Mécanique de la Chaleur. *Gauthier-Villars*, 1869.

[45] M. J. Barbarisi. Relationship between wettability and adhesion of polyethylene. *Nature*, 215(5099):383–384, 1967.

[46] L. K. Koopal. Wetting of solid surfaces: Fundamentals and charge effects. *Advances in Colloid and Interface Science*, 179-182:29–42, 2012.

[47] M. E. Schrader. Young-Dupre Revisited. *Langmuir*, 11(9):3585–3589, 1995.

[48] D. K. Owens and R. C. Wendt. Estimation of the surface free energy of polymers. *Journal of Applied Polymer Science*, 13(8):1741–1747, 1969.

[49] W. Rabel. Einige Aspekte der Benetzungstheorie und ihre Anwendung auf die Untersuchung und Veränderung der Oberflächeneigenschaften von Polymeren. *Farbe und Lack*, 77:997–1005, 1971.

[50] F. M. Fowkes. Determination of interfacial tensions, contact angles, and dispersion forces in surfaces by assuming additivity of intermolecular interactions in surfaces. *Journal of Physical Chemistry*, 66(2):382, 1962.

[51] F. M. Fowkes. Attractive forces at interfaces. *Industrial & Engineering Chemistry*, 56(12):40–52, 1964.

[52] F. M. Fowkes. Donor-acceptor interactions at interfaces. *The Journal of Adhesion*, 4(2):155–159, 1972.

[53] L. A. Girifalco and R. J. Good. A Theory for the Estimation of Surface and Interfacial Energies. I. Derivation and Application to Interfacial Tension. *Journal of Physical Chemistry*, 61(7):904–909, 1957.

[54] J. H. Hildebrand and R. Scott. *The Solubility of Nonelectrolytes*. Reinhold, 1950.

[55] J. H. Hildebrand and R. Scott. *Regular solutions*. Prentice-Hall, 1962.

[56] DIN 55660-2: Beschichtungsstoffe - Benetzbarkeit - Teil 2: Bestimmung der freien Oberflächenenergie fester Oberflächen durch Messung des Kontaktwinkels, 2011.

[57] C. J. Biermann. Papermaking Chemistry. In *Handbook of Pulping and Papermaking*, pages 438–462. Fapet Oy, Helsinki, 1996.

[58] C. Voura. *Untersuchung des Penetrationsverhaltens von niedrigviskosen Druckfarben in CaCO3-hältige Papierstrukturen*. PhD thesis, Graz University of Technology, 2012.

[59] H. J. Kent and M. B. Lyne. On the Penetration of Printing Ink into Paper. *Nordic Pulp and Paper Research Journal*, 2:141–145, 1989.

[60] K. Niskanen. *Paper Physics*, volume 16. Paperi ja Puu, Helsinki, 2008.

[61] F. J. Schmied, C. Teichert, L. Kappel, U. Hirn, W. Bauer, and R. Schennach. What holds paper together: Nanometre scale exploration of bonding between paper fibres. *Scientific Reports*, 3(1):2432, dec 2013.

[62] H. Kipphan. *Heidelberger Handbuch der Printmedien*. Springer-Verlag, 2000.

[63] D. Danino and A. Marmur. Radial capillary penetration into paper: Limited and unlimited liquid reservoirs. *Journal of Colloid And Interface Science*, 166(1):245–250, 1994.

[64] H. Aslannejad, S. M. Hassanizadeh, A. Raoof, D. A. de Winter, N. Tomozeiu, and M. T. van Genuchten. Characterizing the hydraulic properties of paper coating layer using FIB-SEM tomography and 3D pore-scale modeling. *Chemical Engineering Science*, 160:275–280, 2017.

[65] T. Senden, A. Bauer, and R. Roberts. Experimental imaging of fluid penetration into papers. In *Appita Conference*, pages 149–153, 2007.

[66] J. Andersson, A. Ström, T. Gebäck, and A. Larsson. Dynamics of capillary transport in semi-solid channels. *Soft Matter*, 13(14):2562–2570, 2017.

[67] J. Schoelkopf. *Observation and Modelling of Fluid Transport into Porous Paper Coating Structures*. PhD thesis, University of Plymouth, 2002.

[68] P. A. C. Gane, M. Salo, J. P. Kettle, and C. J. Ridgway. Comparison of Young-Laplace pore size and microscopic void area distributions in topologically similar structures: a new method for characterising connectivity in pigmented coatings. *Journal of Materials Science*, 44(2):422–432, 2008.

[69] H. Aslannejad and S. M. Hassanizadeh. Study of Hydraulic Properties of Uncoated Paper: Image Analysis and Pore-Scale Modeling. *Transport in Porous Media*, 120(1):67–81, 2017.

[70] H. Aslannejad, S. M. Hassanizadeh, and M. A. Celia. Characterization of the Interface Between Coating and Fibrous Layers of Paper. *Transport in Porous Media*, 127(1):143–155, 2019.

[71] E. Bohlin. *Surface and porous structure of pigment coatings: Interactions with flexographic ink and effects on print quality*. PhD thesis, Karlstad University, 2013.

[72] D. M. Desjumaux, D. W. Bousfield, and P. Aurenty. Dynamics of ink gloss: Influence of ink rheology on leveling. In *Proceedings of the Technical Association of the Graphic Arts, TAGA*, pages 618–637, 1998.

[73] P. A. Gane and C. J. Ridgway. Interactions between flexographic ink and porous coating structures. In *TAPPI 2nd Annual PaperCon'09 Conference - Solutions for a Changing World*, 2009.

[74] J. S. Preston, A. G. Hiorns, D. J. Parsons, and P. J. Heard. Design of coating structure for flexographic printing. *Paper Technology*, 49(1):27–36, 2008.

[75] G. R. Ström, J. Borg, and E. Svanholm. Short-time water absorption by model coatings. In *TAPPI Advanced Coating Fundamentals Symposium Proceedings*, pages 204–216, 2008.

[76] J. S. Aspler, S. Davis, and M. B. Lyne. Surface chemsistry of paper in realtion to dynamic wetting and sorption of water and lithographic fountain solutions. *Journal of Pulp and Paper Science*, 13(2):55–60, 1987.

[77] E. Kenttä, T. Pöhler, and K. Juvonen. Latex uniformity in the coating layer of paper. *Nordic Pulp and Paper Research Journal*, 21(5):665–669, 2006.

[78] L. R. Fisher and P. D. Lark. An experimental study of the washburn equation for liquid flow in very fine capillaries. *Journal of Colloid And Interface Science*, 69(3):486–492, 1979.

[79] L. Hanžič, L. Kosec, and I. Anžel. Capillary absorption in concrete and the Lucas-Washburn equation. *Cement and Concrete Composites*, 32(1):84–91, 2010.

[80] S. M. Kumar and A. P. Deshpande. Dynamics of drop spreading on fibrous porous media. *Colloids and Surfaces A: Physicochemical and Engineering Aspects*, 277:157–163, 2006.

[81] K. Li, D. Zhang, H. Bian, C. Meng, and Y. Yang. Criteria for applying the lucas-washburn law. *Scientific Reports*, 5(1):14085, 2015.

[82] M. Liu, J. Wu, Y. Gan, D. A. Hanaor, and C. Q. Chen. Evaporation limited radial capillary penetration in porous media. *Langmuir*, 32(38):9899–9904, 2016.

[83] A. Marmur. Capillary Rise in Thin Porous Media. *J. Phys. Chem*, 93:4813–4811, 1989.

[84] A. Marmur and R. D. Cohen. Characterization of porous media by the kinetics of liquid penetration: the vertical capillaries model. *Journal of Colloid and Interface Science*, 189(2):299–304, 1997.

[85] J. Oliver, L. . Agbezuge, and K. Woodcock. A diffusion approach for modelling penetration of aqueous liquids into paper. *Colloids and Surfaces A: Physicochemical and Engineering Aspects*, 89:213–226, 1994.

[86] M. O'Loughlin, K. Wilk, C. Priest, J. Ralston, and M. Popescu. Capillary rise dynamics of aqueous glycerol solutions in glass capillaries: A critical examination of the Washburn equation. *Journal of Colloid and Interface Science*, 411:257–264, 2013.

[87] A. Perez-Cruz, I. Stiharu, and A. Dominguez-Gonzalez. Two-dimensional model of imbibition into paper-based networks using Richards' equation. *Microfluidics and Nanofluidics*, 21(5):98, 2017.

[88] J. Songok and M. Toivakka. Modelling of capillary-driven flow for closed paper-based microfluidic channels. *Journal of Micromechanics and Microengineering*, 27(6):065001, 2017.

[89] V. Starov, S. Kostvintsev, V. Sobolev, M. Velarde, and S. Zhdanov. Spreading of Liquid Drops over Dry Porous Layers: Complete Wetting Case. *Journal of Colloid and Interface Science*, 252(2):397–408, 2002.

[90] D. Yang, M. Krasowska, C. Priest, M. N. Popescu, and J. Ralston. Dynamics of capillary-driven flow in open microchannels. *Journal of Physical Chemistry C*, 115(38):18761–18769, 2011.

[91] H. Zhou, R. Chang, E. Reichmanis, and Y. Song. Wetting of Inkjet Polymer Droplets on Porous Alumina Substrates. *Langmuir*, 33(1):130–137, 2017.

[92] J. Drelich, E. Chibowski, D. D. Meng, and K. Terpilowski. Hydrophilic and superhydrophilic surfaces and materials. *Soft Matter*, 7(21):9804–9828, 2011.

[93] L. Yang, L. Jianghao, and G. Lingya. Detailed insights to liquid absorption and liquid - paper interaction. In *XV Fundamental Research Symposium*, pages 585–598, Cambridge, 2013.

[94] G. R. Willmott, C. Neto, and S. C. Hendy. Uptake of water droplets by non-wetting capillaries. *Soft Matter*, 7(6):2357–2363, 2011.

[95] Z. Ye, S. Li, C. Wang, R. Shen, W. Wen, B. Zhao, J. S. Moore, D. J. Beebe, W. L. Hsu, D. W. Inglis, H. Jeong, D. E. Dunstan, M. R. Davidson, E. M. Goldys, D. J. E. Harvie, R. Karnik, K. Castelino, A. Majumdar, R. Qiao, N. R. Aluru, L. Xu, S. Davies, A. B. Schofield, D. A. Weitz, L. Xu, A. Bergès, P. J. Lu, A. R. Studart, A. B. Schofield, H. Oki, S. Davies, D. A. Weitz, M. A. Unger, H. P. Chou, T. Thorsen, A. Scherer, S. R. Quake, M. W. Prins, W. J. J. Welters, J. W. Weekamp, R. Qiao, N. R. Aluru, E. W. Wasburn, S. Kelly, M. T. Balhoff, C. Torres-Verdín, N. A. Mortensen, A. Kristensen, J. Haneveld, N. R. Tas, N. Brunets, H. V. Jansen, L. H. Thamdrup, F. Persson, H. Bruus, A. Kristensen, Y. Zhu, K. Petkovic-Duran, J. N. Kuo, W. K. Wang, M. N. Hamblin, A. R. Hawkins, D. Murray, D. Maynes, M. L. Lee, A. T. Woolley, H. D. Tolley, N. R. Tas, M. Escalante, J. W. van Honschoten, H. V. Jansen, M. Elwenspoek, V. N. Phan, N. T. Nguyen, C. Yang, P. Joseph, L. Djeghlaf, D. Bourrier, A. Gue, J. W. Suk, and J. H. Cho.

Capillary flow control in nanochannels via hybrid surface. *RSC Adv.*, 6(4):2774–2777, 2016.

[96] M. Stange. *Dynamik von Kapillarströmungen in zylindrischen Rohren*. Cuvillier Verlag Göttingen, 2004.

[97] E. W. Washburn. The dynamics of capillary flow. *Physical Review*, 17(3):273–283, 1921.

[98] J. Szekely, A. W. Neumann, and Y. K. Chuang. The rate of capillary penetration and the applicability of the washburn equation. *Journal of Colloid And Interface Science*, 35(2):273–278, 1971.

[99] J. Schoelkopf, P. A. Gane, C. J. Ridgway, and G. P. Matthews. Practical observation of deviation from Lucas-Washburn scaling in porous media. *Colloids and Surfaces A: Physicochemical and Engineering Aspects*, 206(1-3):445–454, 2002.

[100] S. Levine and G. H. Neale. Theory of the rate of wetting of a porous medium. *Journal of the Chemical Society, Faraday Transactions 2: Molecular and Chemical Physics*, 71(0):12–21, 1975.

[101] A. Cerepi, L. Humbert, and R. Burlot. Dynamics of capillary flow and transport properties in porous media by time-controlled porosimetry. *Colloids and Surfaces A: Physicochemical and Engineering Aspects*, 206(1-3):425–444, 2002.

[102] A. Lundberg, J. Ö. Örtegren, E. Alfthan, and G. Ström. Paper-ink interactions: Microscale droplet absorption into paper for inkjet printing. *Nordic Pulp & Paper Research Journal*, 26(1):142–150, 2011.

[103] K. Sarah and H. Ulrich. Short timescale wetting and penetration on porous sheets measured with ultrasound, direct absorption and contact angle. *RSC Adv.*, 8(23):12861–12869, 2018.

[104] G. Liu, S. Fu, Z. Lu, M. Zhang, C. Ridgway, and P. Gane. Contrasting liquid imbibition into uncoated versus pigment coated paper enables a description of imbibition into new-generation surface-filled paper. *European Physical Journal E*, 40(12), 2017.

[105] J. Schoelkopf, P. A. Gane, C. J. Ridgway, and G. P. Matthews. Influence of inertia on liquid absorption into paper coating structures. In *Nordic Pulp and Paper Research Journal*, volume 15, pages 422–430, 2000.

[106] C. Bosanquet. On the Flow of Liquids into Capillary Tubes. *Philosophical Magazine*, (45):525, 1923.

[107] M. A. Hubbe, D. J. Gardner, and W. Shen. Contact Angles and Wettability of Cellulosic Surfaces. *BioResources*, 10(4):8657–8749, 2015.

[108] A. Hamraoui, K. Thuresson, T. Nylander, and V. Yaminsky. Can a Dynamic Contact Angle Be Understood in Terms of a Friction Coefficient? *Journal of Colloid and Interface Science*, 226(2):199–204, 2000.

[109] M. Heshmati and M. Piri. Experimental Investigation of Dynamic Contact Angle and Capillary Rise in Tubes with Circular and Noncircular Cross Sections. *Langmuir*, 30(47):14151–14162, dec 2014.

[110] M. Hilpert. Effects of dynamic contact angle on liquid infiltration into inclined capillary tubes: (Semi)-analytical solutions. *Journal of Colloid and Interface Science*, 337(1):138–144, 2009.

[111] R. L. Hoffman. A study of the advancing interface. I. Interface shape in liquid—gas systems. *Journal of Colloid and Interface Science*, 50(2):228–241, 1975.

[112] R. L. Hoffman. A study of the advancing interface: II. Theoretical prediction of the dynamic contact angle in liquid-gas systems. *Journal of Colloid and Interface Science*, 94(2):470–486, 1983.

[113] T.-S. Jiang, O. Soo-Gun, and J. C. Slattery. Correlation for dynamic contact angle. *Journal of Colloid and Interface Science*, 69(1):74–77, 1979.

[114] P. Joos, P. Van Remoortere, and M. Bracke. The kinetics of wetting in a capillary. *Journal of Colloid and Interface Science*, 136(1):189–197, 1990.

[115] E. Rillaerts and P. Joos. The Dynamic contact angle. *Chemical Engineering Science*, 35(4):883–887, 1980.

[116] A. Siebold, M. Nardin, J. Schultz, A. Walliser, and M. Oppliger. Effect of dynamic contact angle on capillary rise phenomena. *Colloids and Surfaces A: Physicochemical and Engineering Aspects*, 161(1):81–87, 2000.

[117] A. Han, G. Mondin, N. G. Hegelbach, N. F. de Rooij, and U. Staufer. Filling kinetics of liquids in nanochannels as narrow as 27 nm by capillary force. *Journal of Colloid and Interface Science*, 293(1):151–157, 2006.

[118] C. J. Ridgway and P. A. Gane. Dynamic absorption into simulated porous structures. *Colloids and Surfaces A: Physicochemical and Engineering Aspects*, 206(1-3):217–239, 2002.

[119] P. Neogi and C. Miller. Spreading kinetics of a drop on a rough solid surface. *Journal of Colloid and Interface Science*, 92(2):338–349, 1983.

[120] H. Aslannejad, H. Fathi, S. M. Hassanizadeh, A. Raoof, and N. Tomozeiu. Movement of a liquid droplet within a fibrous layer: Direct pore-scale modeling and experimental observations. *Chemical Engineering Science*, 191:78–86, 2018.

[121] A. Basit, K. Kushaari, P. Siwayanan, and B. Azeem. Effect of process parameters on droplet spreading behaviour over porous surface. *Canadian Journal of Chemical Engineering*, 96(1):352–359, 2018.

[122] A. Asai, M. Shioya, S. Hirasawa, and T. Okazaki. Impact of an ink drop on paper. *Journal of Imaging Science and Technology*, 37(2):205–207, 1993.

[123] P. Alam, M. Toivakka, K. Backfolk, and P. Sirviö. Impact spreading and absorption of Newtonian droplets on topographically irregular porous materials. *Chemical Engineering Science*, 62(12):3142–3158, 2007.

[124] M. Toivakka. Numerical investigation of droplet impact spreading in spray coating of paper. In *Symposium TAPPI Advanced Coating Fundamentals Symposium*, 2003.

[125] M. Pasandideh-Fard, Y. M. Qiao, S. Chandra, and J. Mostaghimi. Capillary effects during droplet impact on a solid surface. *Physics of Fluids*, 8(3):650–659, 1996.

[126] B. L. Scheller and D. W. Bousfield. Newtonian drop impact with a solid surface. *AIChE Journal*, 41(6):1357–1367, 1995.

[127] X. Zhang and O. Basaran. Dynamic Surface Tension Effects in Impact of a Drop with a Solid Surface. *Journal of colloid and interface science*, 187(1):166–78, 1997.

[128] U. Lindqvist, L. Hakola, Z. Boris, and E. Wallstrom. Advances in Printing Science and Technology. In *Proceedings of the 31st International iarigai Research Conference*, page 260. Acta Craphica Publishers, 2004.

[129] David Zwang. Production Inkjet—The Next Wave: Canon Océ VarioPrint i300 Sheetfed Inkjet Press and More - WhatTheyThink, 2015.

[130] E. Hakola and P. Oittinen. Principles of digital printing. In P. Oittinen and H. Saarelma, editors, *Print Media – Principles , Processes and Quality*, chapter 4. Paper Engineers' Association, 2 edition, 2009.

[131] S. Krainer, C. Smit, and U. Hirn. The effect of viscosity and surface tension on inkjet printed picoliter dots. *RSC Advances*, 9(54):31708–31719, 2019.

[132] Hue P. Le. Progress and Trends in Ink-jet Printing Technology. *Journal of Imaging Science and Technology*, 42(1):49–62, 1998.

[133] W. V. Ohnesorge. Formation of Drops by Nozzles and the Breakup of Liquid Jets. *Applied Mathematics and Mechanics*, 16:355–358, 1936.

[134] J. . M. and fluid transport Kettle. Moisture and fluid transport. In K. Niskanen, editor, *Paper Physics in Papermaking Science and Technology*, pages 265– 294. Tappi Press, 2008.

[135] H. Ok, H. Park, W. W. Carr, J. F. Morris, and J. Zhu. Particle-laden drop impacting on solid surfaces. *Journal of Dispersion Science and Technology*, 25(4):449–456, 2004.

[136] W. Fuchs. *Investigation of Paper - and Printing Process Related Reasons for Print Unevenness*. PhD thesis, Graz University of Technology, 2016.

[137] L. T. Creagh-Dexter. Applications in Commercial Printing for Hot Melt Ink Jets. In *Societey for Imagging Science and Technology*, page 3, 1994.

[138] J. Blechschmidt. *Taschenbuch der Papiertechnik*. Carl Hanser Verlag München, 2013.

[139] M. Daun. *Model for the dynamics of liquid penetration into porous structures and its detection with the help of changes in ultrasonic attenuation*. PhD thesis, Technical University Darmstadt, 2006.

[140] J. F. Waterhouse. Mechanical and Physical Properties of Paper Surfaces. In T. E. Conners and S. Banerjee, editors, *Surface Analysis of Paper*, chapter 3, page 372. CRC Press, 1995.

[141] T. A. P. Van Stiphout. *Liquid Absorption in porous Media studied by Automatic Scanning Absorptometer*. Master thesis, Eindhoven University of Technology, 2016.

[142] H. Hamada, D. W. Bousfield, and W. T. Luu. Absorption mechanism of aqueous and solvent inks into synthetic nonwoven fabrics. *Journal of Imaging Science and Technology*, 53(5):0502011–0502016, 2009.

[143] J. A. Bristow. Liquid absorption into paper during short time intervals. *Svensk papperstidning*, 70(19):623–629, 1967.

[144] J. A. Bristow. The absorption of water by sized papers. *Svensk papperstidning*, 71(2):33–39, 1968.

[145] T. Enomae, H. Kataoka, F. Onabe, D. Papier, and J. Robertson. In-Plane Distribution of Paper Absorbency Measured by Liquid Absorption Profilometer. *Sen'i Gakkaishi*, 55(2):265–291, 2004.

[146] C. Kuijpers, T. van Stiphout, H. Huinink, N. Tomozeiu, S. Erich, and O. Adan. Quantitative measurements of capillary absorption in thin porous media by the Automatic Scanning Absorptometer. *Chemical Engineering Science*, 178:70–81, 2018.

[147] ADERHOLD FIRM. Hercules Sizing Tester Taf 300 Series - Instruction Manual, 2015.

[148] D. Price, R. Osborn, and J. Davis. A liquid penetration test formeasuring the sizing of paper. *Tappi Journal*, 36(1):42–46, 1953.

[149] P. Lopes, C. Preciso, A. Mendes De Sousa, and P. Ferreira. SIZING EVALUATION OF UNCOATED FINE PAPERS. In *XXI TECNICELPA Conference and Exhibition*, 2010.

[150] A. Oko. *Spontaneous imbibition and colloidal aspects of inkjet printing*. PhD thesis, KTH Royal Institute of Technology, 2014.

[151] J. Lipponen, T. Lappalainen, J. Astola, and J. Grön. Novel method for quantitative starch penetration analysis through iodine staining and image analysis of cross-sections of uncoated fine paper. *Nordic Pulp and Paper Research Journal*, 19(3):300–308, 2004.

[152] S. Enzi. *Skalpellschnittverfahren - Messmethode zur Beurteilung der Druckfarbenpenetration bei SC-Papier*. Master thesis, Graz University of Technology, 2002.